ANNUAL REPORT
of
THE INSTITUTE OF PHYSICS
ACADEMIA SINICA

VOLUME 14 DECEMBER 1984

THE INSTITUTE OF PHYSICS, ACADEMIA SINICA
TAIPEI, TAIWAN, REPUBLIC OF CHINA

Annual Report
of
The Institute Of Physics
Academia Sinica

Volume 14 December 1984

The Institute of Physics, Academia Sinica
Taipei, Taiwan, Republic of China

中央究研院物理研究所集刊

發 行 人 (Publisher)
林 爾 康 (E. K. Lin)

執行編輯 (Executive Editor)
任 源 盛 (S.-U. Jen)

The Annual Report is published annually by the Institute of Physics, Acadmia Sinica, Taipei Taiwan, 115, Republic of china.

中央研究院物理研究所集刊

第十四卷

中央研究院物理研究所印行

CONTENTS 目 錄

ARTICLES

FLUID MECHANICS AND ATMOSPHERIC PHYSICS

ABSTRACT

THEORETICAL PHYSICS

NUCLEAR PHYSICS

SOLID STATE PHYSICS AND BIPHYSICS

NOTE ON THE EFFECT OF AN ELECTRIC DIPOLE MOMENT IN THE ELECTRON ON THE GROUND STATE OF THE HYDROGEN ATOM*

Ta-You Wu

ABSTRACT

Recently the question of the effect of the existence of an electric dipole moment in the electron on the energy levels of a hydrogenic atom (especially the effect on the Lamb shift and the lifetime of the $2^2S_{1/2}$ state, etc.) has been examined by a number of authors [G. Feinberg Phys. Rev. 112, 1637 (1958); E.F. Salpeter, Phys. Rev. 112, 1642, (1958)]. The present note is concerned with the question whether such a dipole moment in the electron leads to a detectable effect by an atomic beam experiement on the hydrogen atom in the ground state.

INTRODUCTION

An electron having an electric dipole moment violates the requirement of invarince of the system (electron) under time reversal. For this reason, such an electron is not described by the Dirac equation. We shall assume, however, that a modified Dirac equation can be employed to describe such an electron. For this purpose we shall go back to the usual Dirac equation.

For an electron in an electromagnetic field the Dirac equation is

$$(\pi_\mu \gamma^\mu - imc)\psi = 0 \qquad (1)$$

where

$$\pi_\kappa = \frac{\hbar}{i} \frac{\partial}{\partial x_\kappa} + \frac{e}{c} A_\kappa, \quad k = 1,2,3, \quad \pi_4 = \frac{\hbar}{i} \frac{\partial}{ic\partial t} + \frac{e}{c} i\phi$$

γ^μ are the Dirac matrices, and the summation convention is used. The first order equation (1) when transformed into one of the second order, is

* This note was written, but unpublished, in 1958 when the writer was with the National Research Counal of Canada, Ottawa. In view of some recent interest in the problem and the possibilities of experimental measurements not conceivable in 1958, if has been suggested by some colleagues that the note be now published, in the form in which it was written.

$$(\pi^2 + m^2c^2 + \frac{m\mu}{i} \gamma^\mu\gamma^\nu F_{\mu\nu})\psi = 0 \qquad (2)$$

where

$$F_{\mu\nu} = \frac{\partial A_\nu}{\partial x_\mu} - \frac{\partial A_\mu}{\partial x_\nu} , \qquad \mu_o = \frac{e\hbar}{2mc}$$

The results of the Dirac theory of the electron are well known: it leads, among other things, to the electron spin, with the correct gyromagnetic ratio (without the correction factor $(1 + \frac{\alpha}{2\pi} + \ldots .)$ arising from radiative effects in a many-particle, rather than one-particle, theory).

It is known that one can add an additional term to (1) and still retain the invariance property under Lorentz and gauge transformations. Thus

$$(\pi_\mu \gamma^\mu - imc) \psi = G\psi , \qquad G = g_1 \frac{\mu_o}{2c} \gamma^\mu \gamma^\nu F_{\mu\nu} \qquad (3)$$

where g_1 is an arbitrary number. Such a term G represents an extra (Pauli) magnetic moment in addition to the "intrinsic" one already contained in (1). The second-order equation for (3) corresponding to (2) is

$$\{ \pi_\mu^2 + m^2c^2 + (1+g_1)\frac{m\mu_o}{i} \gamma^\mu\gamma^\nu F_{\mu\nu} \}\psi = \{ G^2 + [\gamma^\mu \pi_\mu, G] \} \psi , \qquad (4)$$

where $[\, , \,]$ is the commutator. On neglecting the terms on the righthand side, it is seen that the effect of the Pauli moment in (3) is to increase the gryomagnetic ratio by the factor $1+g_1$. Historically, it is of interest to note that it was a search for such a Pauli moment by Kusch (in a discussion with Breit and Rabi) that led to the empirical result which was the radiative correction predicted by the covariant formulation of quantum electrodynamics (Schwinger).

For the purpose of making more readily recognizable the nature of the Dirac equation (1), we shall use the form in which the two small components of ψ are expressed in terms of the two big components. Thus for (4) we have, for an electron in a hydrogenic atom,

$$Hu = Eu$$

where

$$H = \frac{p^2}{2m} - \frac{Ze^2}{r} - \frac{p^2p^2}{8m^3c^2} + eZE_o + \frac{e}{mc}(A\cdot p) + \frac{e^2}{2mc^2}A^2 + \frac{\mu_o}{2mc}(\sigma\cdot[E \times p])$$

$$- \frac{i\mu_o}{2mc}(E\cdot p) + g_N \frac{m}{M}\frac{\mu_o^2}{r^3}\{(\sigma_I\cdot\sigma) + \frac{3}{r^2}(\sigma_I\cdot r)(\sigma\cdot r)\} + g_N\frac{m}{M}\mu_o(\sigma_I\cdot\mathcal{H})$$

$$+ g_1\mu_o\{(\sigma\cdot\mathcal{H}) + \frac{1}{2mc}(\sigma\cdot[Exp]) - \frac{i}{2mc}(E\cdot p)\} , \qquad (5)$$

where σ_1 is the Pauli matrix for nuclear spin, The magnetic field, and

$$E = E_i + E_o , \qquad E_i = \frac{Ze}{r^3}\vec{r} ,$$

E_i being the Coulomb field due to the nucleus, and E_o, the external field. It is well known that

$$\frac{\mu_o}{2mc}(\sigma\cdot[E_i x p]) = \frac{2Z\mu_o^2}{r^3}(\ell\cdot s) , \qquad s = \frac{1}{2}\sigma , \qquad (6)$$

is the spin-orbit interaction, and $-\frac{i\mu_o}{2mc}(E_i\cdot p)$ is the so-called s-state correction [See, for example, Condon-Shortley].

ELECTRON WITH AN ELECTRIC DIPOLE MOMENT

For such an electron, we assume the equation

$$(\pi_\mu\gamma^\mu - imc)\psi = \xi\frac{\mu_o}{2c}\gamma^5\gamma^\mu\gamma^\nu F_{\mu\nu}\psi . \qquad (7)$$

The γ^5, being a pseudoscalar, corresponds to the parity non-conserving dipole. ξ is a numerical parameter. The equation corresponding to (5) now is

$$(H_I + H_{II} + H_{III} + H_{IV})\, u = E\, u , \qquad (8)$$

$$H_I = \frac{p^2}{2m} - \frac{Ze^2}{r} - \frac{p^2p^2}{8m^3c^2} + \frac{2Z\mu_o^2}{r}(\ell\cdot s) - \frac{i\mu_o}{2mc}(E_i\cdot p)$$

$$+ g_N\frac{m}{M}\mu_o^2\frac{1}{r^3}\{(\sigma_I\cdot\sigma) + \frac{3}{r^2}(\sigma_I\cdot r)(\sigma\cdot r)\} ,$$

$$H_{II} = eZE_o + \frac{\mu_o}{2mc}(\sigma \cdot E_o x p) - i\frac{\mu_o}{2mc}(E_o \cdot p) ,$$

$$H_{III} = \mu_o(\ell \cdot \mathfrak{H}) + \mu_o(\sigma \cdot \mathfrak{H}) + g_N \frac{m}{M}\mu_o(\sigma_i \cdot \mathfrak{H}) + \frac{e^2\mathfrak{H}^2}{8mc^2} r^2 \sin^2\theta ,$$

$$H_{IV} = \xi\mu_o\{(\sigma \cdot E_i) + (\sigma \cdot E_o) - \frac{1}{2mc}(\sigma \cdot [\mathfrak{H} x p]) + \frac{i}{2mc}(\mathfrak{H} \cdot p)\} , \qquad (9)$$

H_I gives the fine structure and hyperfine structure levels of the atom; H_{II} the effect of the external electric field, H_{III} that of the external magnetic field; H_{IV} the interactions from the electric dipole moment ξ (ξ is the electric moment in units of $e\lambda_C = \frac{e\hbar}{mc}$).

In an atomic beam experiment, the hydrogen atom is in an electric field E_o + a magnetic field $\mathfrak{H}$. The hfs levels are perturbed by H_{II}, H_{III}, H_{IV}, We shall consider their effects as follows. We shall be primarily interested in the $1^2S_{\frac{1}{2}}$ state.

$$H_{II,1} = ezE_o$$

If we denote a state by $<n, j, \ell, m_j|$, then it is well known that the only non-vanishing elements are, for $1^2S_{\frac{1}{2}}$,

$$< 1, \tfrac{1}{2}, 0, m_j \quad |z| \quad n, \tfrac{1}{2}, 1, m_j > \neq 0,$$

$$< 1, \tfrac{1}{2}, 0, m_j \quad |z| \quad n, \tfrac{3}{2}, 1, m_j > \neq 0,$$

Thus for $1^2S_{\frac{1}{2}}$, there is only a second-order (non-relativistic) Stark effect.

$$H_{II,2} = \frac{\mu_o}{2mc}(\sigma \cdot [E_o x p])$$

The diagonal element of $H_{II,2}$ vanishes on account of p. Thus $H_{II,2}$ gives only a second-order, relativistic Stark effect. The magnitude of this can be estimated by noting that, from (6), even for $E_o \simeq 5\times10^4$ volts/cm,

$$\frac{H_{II,2}}{H_{I,4}} = \frac{H_{II,2}}{\text{fine structure seperation}} = \frac{E_o}{E_i} \simeq 10^{-5}$$

That $H_{II,2}$ contributes only to the second order $|<1S|H_{II,2}|np>|^2/(E_{1s}-E_{np})$ means that the energy change from $H_{II,2}$ is of the order 10^{-15} times the fine structure shift and is entirely negligible.

$$H_{II,3} = -i\frac{\mu_o}{2mc}(E_o \cdot p)$$

Entirely similar arguments show this to be negligibly small compared with the S-state correction $-i\frac{\mu_o}{2mc}(E_i \cdot p)$ which is of the order of fine structure separations. H_{III} gives the Zeeman effect of the hfs , and the diamagnetic effect, which are well known.

$$H_{IV,1} = \xi\mu_o(\sigma \cdot E_i), \qquad E_i = \frac{Ze}{r^3}\vec{r} ,$$

This is the interaction of the electric dipole with the Coulomb field due to the nucleus. The only non-vanishing matrix elements are

$$<n, j, \ell = j \pm \tfrac{1}{2}, m_j|\sigma \cdot r|n', j, \ell = j \mp \tfrac{1}{2}, m_j> = \tfrac{1}{2}(1 - \delta_{n,n'}) ,$$

For the $1^2S_{\frac{1}{2}}$ state, there is no diagonal element and $H_{IV,1}$ has only a second order effect, which is (Salpeter)

$$E_{1S_{\frac{1}{2}}} = -\frac{\xi^2\alpha^2}{2}\ \text{rydberg} = -8.7\times10^4\xi^2\ \text{MC/sec} \qquad (10)$$

$$H_{IV,2} = \xi\mu_o(\sigma \cdot E_o)$$

This has a diagonal element equal to $\xi\mu_o E_o$ and hence a first-order effect (in both ξ and E_o). Since $H_{II,1}$ and $H_{IV,1}$ both have a second order effect, one has to consider the second-order energy change

$$\sum_n \frac{|<1S_{\frac{1}{2}}|\ H_{II,1} + H_{IV,1}|\ nP_{\frac{1}{2}}>|^2}{E_{1S} - E_{nP}}$$

The contribution from the cross terms, which is proportional to ξE_o, has been shown (Salpeter) to cancel exactly that from $H_{IV,2}$. Thus there is no energy change linear in ξ .

$$H_{IV,3} = -\xi \frac{\mu_o}{2mc} (\sigma \cdot [\mathscr{H} \times p])$$

This has the same structure as $H_{II,2}$. The magnitudes of these are similar when E (in volts/cm) is of the same order as $\mathscr{H}$ (in gauss). Hence $H_{IV,3}$ is negligibly small.

$$H_{IV,4} = i\xi \frac{\mu_o}{2mc} (p \cdot \mathscr{H})$$

This is similar to $H_{II,3}$, and for the same reason as above for $H_{IV,3}$, is negligibly small.

Thus, up to this order (9) (higher order relativistic effects and higher orders in α are neglected), the only effect of the dipole moment ξ is to shift the whole hfs .* pattern of $1^2S_{\frac{1}{2}}$ downward by (10)

$$\Delta E = -8.7 \times 10^4 \xi^2 \text{ MC/sec} \qquad (10')$$
$$= -2.9\ \xi^2 \text{cm}^{-1}$$

[in opposite direction to the Lamb shift]. Since the optical method for the Lyman α-line can detect perhaps at best a shift of $\sim 0.01 \text{cm}^{-1}$, it is not sensitive enough to put an upper limit to ξ which is < 0.1. From the Lamb shift of $1S_{\frac{1}{2}}$, however, a considerably lower value ($\xi < 0.004$) can be concluded for the upper limit of ξ (Salpeter).

* Since the dipole moment ξ cannot cause any further splitting of the Zeeman pattern of the hfs levels (the ground state of the electron around a proton of spin ½ has only 4 states), and since the interaction between ξ and the magnetic moment of the nucleus is a higher order effect which is certainly small, the change in the separations of the hfs Zeeman levels is too small to be considered.

A NOTE ON CORRELATED PERCOLATION AND REVERSIBLE SOL-GEL PHASE TRANSITIONS

Chin-Kun Hu
Institute of Physics, Academia Sinica
Nankang, Taipei, Taiwan 115
Republic of China

ABSTRACT

Using Hu's idea to establish the connection between the percolation transition and the thermal phase transition, in this paper we formulate a percolation theory of reversible sol-gel phase transitions in solvent. Our theory does not have certain phenomenological parameter introduced in Coniglio, Stanley and Klein's theory.

In 1941, Flory[1] considered the random process, which corresponds to the bond percolation process[2], on a Bethe lattice as a model for the sol-gel phase transition. Flory ignored effects of solvent molecules and correlations between the monomers in his model. In 1979, Coniglio, Stanley and Klein (CSK)[3] proposed a site-bond-correlated percolation model of reversible sol-gel phase transition, hereafter referred to as CSK model, in which effects of solvent molecules and correlations between monomers are taken into account. In the CSK model, each lattice site is occupied by either a solvent (A site) or a monomer molecule (B site) as shown in FIG. 1c of Ref. 3. The nearest-neighbour (NN) pairs of solvent-solvent, monomer-solvent, and monomer-monomer molecules have interaction energies $-W_{AA}$, $-W_{AB}$, and $-\varepsilon_{BB}$, respectively. CSK introduced a phenomenological parameter ρ_μ to distinguish two possible cases for $-\varepsilon_{BB}$: van der Waals interaction $-W_{BB}$ with weight ρ_μ and bonding energy $-E$ with weight $1-\rho_\mu$. In the CSK model, the probability p_B that a bond is present between two NN monomers is

$$P_B = \frac{(1-\rho_\mu)\exp(\beta E)}{\exp(\beta W_{BB}) + (1-\rho_\mu)\exp(\beta E)} \quad ,$$

Here $\beta = \frac{1}{kT}$; k is the Boltzmann constant.

In recent papers [4-8], we have shown that the partition functions of many Ising-like spin models are the generating functions of the corresponding percolation models. From such connections, we could physically understand many properties of the studied spin models, e.g. the finite-size scaling and broadening[5,7], the increase of the specific heat exponent α with q in the q-state Potts model[7]. We have also applied this approach to formulate a theory[8] of hydrogen-bonding in H_2O and D_2O to explain the unusual behaviour of supercooled water, in which certain assumptions made in Stanley and his coworkers' papers[9] do not present but could be derived directly from the theory. In this paper, we will apply our approach[4-8] to formulate a percolation theory of reversible sol-gel phase transitions in solvent. Our theory does not have the phenomenological paramer ρ_μ introduced in the CSK theory[3].

As in the CSK theory, we assume that each site of a lattice G with N sites and E bonds, such as the square lattice of FIG. 1, is occupied by either a solvent or a monomer. However, we also assume that each monomer has f arms to form bonds with its nearest-neighbor (NN) monomers. A monomer at a given lattice site could have q different orientations, represented by a variable s having q different values: s = 1, 2, ..., q. To distinguish the sites with a monomer and the sites with a solvent, we introduce another variable t for each lattice site, which is 1 for a lattice site with a monomer and 0 for a lattice site with a solvent. Without loss of generality, we take the monomer-solvent pair interaction energy $-W_{AB}$ to be zero. We assume that two NN monomers always have a van der Waals energy $-W_{BB}$; in addition to that, they also have a bonding energy -J when and only when both of them have a bonding arm lying on the NN bond between them, which will be called the monomer boding condition (MBC). The Hamiltonian of the system is given by:

$$H = -J \sum_{<ij>} g(s_i, s_j)\, t_i\, t_j - W_{BB} \sum_{<ij>} t_i\, t_j - W_{AA} \sum_{<ij>} (1-t_i)(1-t_j) - \mu \sum_i t_i \qquad (1)$$

Here the first three sums are over all NN bonds of the lattice, the last sum is over all sites of the lattice, and μ is the chemical potential; $g(s_i, s) = 1$ when the bond <ij> satisfies the MBC and $g(s_i, s_j) = 0$ when the bond <ij> does not satisfies the MBC.

The partition function Z_N for H of (1) may be wirtten as:

$$Z_N = \sum_{s_1 \cdots s_N} \sum_{t_1 \cdots t_N} e^{-\beta H}$$

$$= \sum_{s_1 \cdots s_N} \sum_{t_1 \cdots t_N} \exp\Big[\Delta \sum_i t_i + \beta W_{BB} \sum_{<ij>} t_i t_j + \beta W_{AA} \sum_{<ij>} (1-t_i)(1-t_j)\Big] \times \prod_{<ij>} [1 + (e^K - 1) g(s_i, s_j)] \quad , \qquad (2)$$

where $K=\beta J$, $\Delta=\beta\mu$ and the product extends over only those NN bonds <ij> such that $t_i = t_j = 1$. As in Ref. 6, we first carry out the configuration sum over $t_1 \cdots t_N$ and use the section graphs G' of G to represent states in the summation such that occupied (unoccupied) sites in G' correspond sites with t = 1 (t=0). For a given G', there corresponds a subgraph $G^* \supset G$ which is generated from G' by attaching bonds to every pair of the NN occupied sites in G'. Now we expand the product in (2) and use the subgraphs $G'' \subset G^*$ to represent the terms in the expansion. In each G" there are e(G") bonds which are attached by the factor $(e^K - 1)\, g(s_i, s_j)$ in the the expansion. The sites connected by occupied sites and attached bonds of G" are said to be in the same cluster. For a given G", we can sum over all monomer states at occupied sites, and in such a summation only the terms where each attached bond satisfies the condition MBC have non-zero contributions. Thus Z_N may be rewritten as:

$$Z_N = \sum_{G' \subset G} \exp[\Delta v(G') + \beta W_{BB} M(G') + \beta W_{AA} S(G')]$$

$$\times \sum_{G'' \subset G^*} (e^K - 1)^{e(G'')} \prod_c D_c$$

$$= (e^\Delta + 1)^N \sum_{G' \subset G} p_s^{v(G')} (1-p_s)^{N-v(G')} \exp[\beta W_{BB} M(G') + \beta W_{AA} S(G') + KM(G')] \times \sum_{G'' \subset G^*} p_b^{e(G')} (1-p_b)^{M(G')-e(G')} \prod_c D_c \; . \qquad (2)$$

Here v(G'), M(G'), and S(G') are the numbers of occupied sites, monomer-monomer pairs, and solvent-solvent pairs in G', respectively. The product Π_c extends over all clusters in G". D_c is the total number of configurations of the molecules in cluster c in which each bond satisfies the condition MBC. For isolated cluster, i.e. sites without any attached bonds, $D_c = q$; p_s and p_b are given by:

$$p_s = \frac{e^{\Delta}}{1 + e^{\Delta}} \tag{3}$$

$$p_b = 1 - e^{-K} \tag{4}$$

It is clear from Eq.(2)' that Z_N is the generating function of the following site-bond-correlated percolation model (SBCPM) on G:

1. The sites of G are occupied with a site probability p_s. This process generates section graphs G'⊆G. Attaching bonds tc each pair of the NN occupied sites of G' constitutes G*⊆G.

2. All bonds of G* are attached with a bond probability p_b. This generates subgraphs G"⊆G*.

3. The overall probability of a subgraph G" is enhanced by a factor $\exp(\beta W_{BB} + K)$ for each NN pair of occupied sites and by a factor $\exp[\beta W_{AA}]$ for each NN pair of vacant sites.

For small p_s and p_b, we only have small clusters of bonded monomers., i.e. we have the sol phase. For large p_s and p_b, besides the small clusters of bonded monomers, we also have a percolation cluster, i.e. we have the gel phase. For p_s=1, i.e. there is no solvent molecules, there is a critical bond probability:

$$p_{b,c} = 1 - \exp[-J/kT_{max}] \tag{5}$$

Such that for $p_b < p_{b,c}$, i.e. $T > T_{max}$, there is no gel phase. When T decreases from $T > T_{max}$ to $T < T_{max}$, there is a sol-gel phase transition. When we increase the concentration of solvent molecules (i.e. decrease p_s), critical probability and the sol-gel transition temperature will decrease. Thus we have a site-bond-correlated percolation model (SBCPM) of the reversible sol-gel phase transition. In our model, there is no phenomenological parameter ρ_μ introduced in the CSW model.

Our model could also allow solvent-monomer phase separation, which could correspond certain geometrical properties of our SBCPM. The detail is under investigation.

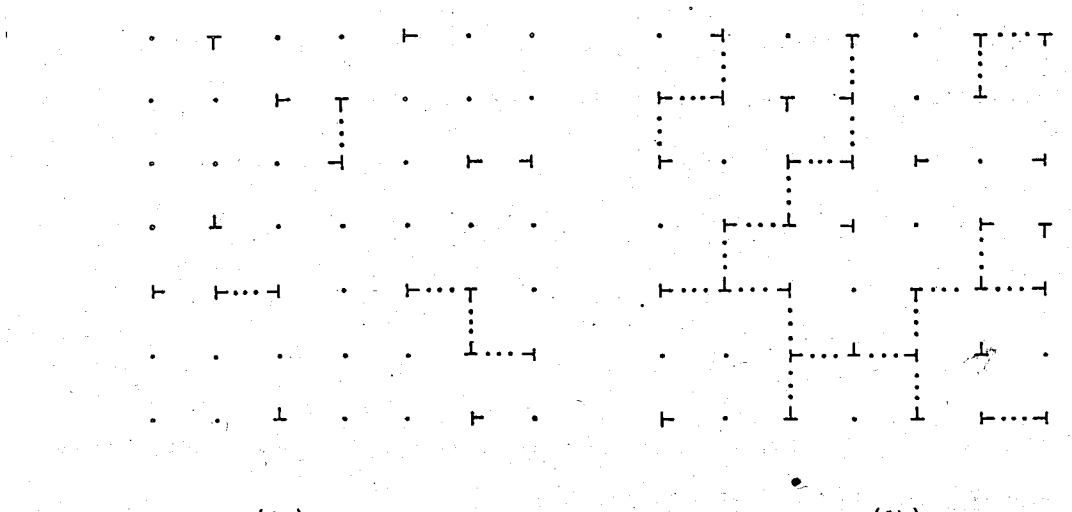

(1a) (1b)

Fig. 1. Each lattice site is occupied by either a solvent (.) or a monomer (⊥) with f bonding arms. In the figure we use f=3. If and only if both NN monomers have a bonding arm on the NN bond connecting them, they have a bond probabiligy p_b to bond together (represented by dotted line). For small site probability p_s and/or bond probability p_b, the system has only small clusters and is in the sol phase (1a). For large p_s and p_b, the system has a percolation cluster besides small clusters and is in the gel phase (1b).

This work was supported by the National Science Council of the Republic of China under contract No. NSC73-0204-M001-03.

REFERENCES

1. P.J. Flory, J. Am. Chem. Soc. 63, 3083, 3091, 3096 (1941).
2. For recent reviews on percolation problems, see articles in Percolation structures and Process, edited by G. Deutscher, R. Zallen, and J. Adler (AIP, New York, 1983).
3. A. Coniglio, H. E. Stanley, and W. Klein, Phys. Rev. Lett. 42, 518 (1979).
4. C.K. Hu, Physica 119A, 609 (1983).
5. C.K. Hu, Phys. Rev. 29, 5103 (1984).

6. C.K. Hu, Phys. Rev. 29, 5109 (1984).

7. C.K. Hu, Chin. J. Phys. (Taipei) 22, 1 (1984).

8. C.K. Hu, J..Phys. A 16, L321 (1983).

9. H. E. Stanley, J. Phys. A 12, L329 (1979); H.E. Stnaley and J. Teixeria, J. Chem. Phys. 73, 3404 (1981); H. E. Stanley, J. Teixeria, A. Geiger, and R.L. Blumberg, Physica 106A, 260 (1981).

GAMMA TRANSITIONS AND STRENGTHS IN $^{160}_{66}$Dy FOLLOWING THE BETA DECAY OF ^{160}Tb

E. K. Lin, D. Wang, G. C. Jon,
and
C. W. Wang

The $^{160}_{66}$Dy nucleus has been intensively investigated by several authors. The experimental results such as evergy levels, spins and parities, gamma transition intensities and branching ratios etc. have been collected by Leaderer and Shirley[1]. The energy eigenstates of this nucleus have been determined below 3.8 MeV. Among these determined energy states, spin and parity of the most of these states have been assigned. From the known information, the dynamics of this nucleus are vibrational in nature for low lying states. However, there are still some spins or parities have not been determined, and some inconsistency between experiments that determining the branching ratios of gamma decay for several states. Recently, Krane[2] investigated angular distribution of 19 gamma transitions by using oriented $^{160}_{65}$Tb nucleus. He found that the spin and parity of the 1386 keV level is 4^- rather than $(3)^-$ which was listed in ref.1. A calculation based on interacting boson approximation has been performed by Ibrahim and Stewart.[3] That calculation presented results by considering the Z=50 and N=82 shell closure and the Z=64 subshell closure. The result of subshell closure at Z=64 gave a somewhat better consistency with the experimental result.

Recently, we obtained the single spectrum, the coincidence spectrum, and the angular correlation function of gamma transitions from excited states of $^{160}_{66}$Dy. The experimental set up had been described in some detail in the previous report[4]. The energy resolution of the Ge(Li) detector was measured to be 2.8 keV for 1.333 MeV gamma. The gating signal of the coincidence and the angular correlation measurements was 964±60 keV. The time resolution was measured to be better than 15ns. And the real to random coincidence was about 5 to 1. This result was estimated by comparing the

relative intensities of the single and coincidence-spectra.

Twenty-nine gammas were observed in addition to the nature background of the lab. The energy of these gamma rays ranged from 197 keV to 1312 keV. The energy levels that correspond to these gamma transitions were also assigned as listed in Table 1. The intensity of these observed gammas, also listed in the table, was corrected with detector efficiency and was normalized to the absolute intensities of 299 keV, 879 keV, and 1178 keV gammas whose absolute intensities were well measured. Both single spectrum and coincidence spectrum show that the intensities we measured are consistent with the previous measurements to within 10% for gammas whose absolute intensities are greater than 0.3%. The intensity of weaker transitions was checked with coincidence measurement. The consistency between our results and previous experiments is better than 50% except for the 350 keV one (1399 kev → 1049 keV). The branching ratios of the gamma decay from specific states were also deduced. They are also in good agreement with previous results.

Several angular correlation functions were also measured. Three of them have been analyzed. These are 1765 keV → 966 keV → 0, 1359 keV → 1049 keV → 87 keV, and 1386 keV → 1049 keV → 87 keV. The spins and parities of the 1359 keV, 1049 keV, and 87 keV levels are 2^-, 3^+, and 2^+ respectively. The posible multipolarities of the 1359 keV → 1049 keV are E1, M2, etc. The M2 admixture is expected to be small. From this arguement we found that the 1049 keV → 87 keV transition is E2 plus 14% M1. This result was used for the analysis of the caseade 1386 keV → 1049 keV → 87 keV. The preliminary analysis shows that the spin of the 1386 keV state is likely to be 4. The parity of this state is known to be negative[1]. Further analysis gave the multipolarity of the 1386 keV → 1049 keV transition to be E1 plus 1.7% M2. The assignment of the spin of the 1386 keV state is consistent with the result of ref. 2. The 1265 keV → 966 keV → 0 angular correlation function gives the spin of the 1265 keV level to be 2, and the multipolarity of the 1265 keV → 966 keV transition to be E1 plus 0.26% M2.

We are indebted to Mr. G. C. Kiang for the discussion.

This work was supported by the NSC. ROC.

REFERENCES

1. M. C. Lederer and V. S. Shirley. Table of isotopes (7th ed.), John Wiley & Sons, Inc., New York, 1978.
2. K. S. Krane, Nuclear Phys., A377 (1982) 176.
3. N. Ibrahim and N. M. Stewart, J. Phys. G: Nucl. Phys. 9 (1983) L 195.
4. D. Wang et al., Ann. Rept., Inst. Phys., Acad. Sin. Vol. 13(1983)29.

Table 1. Energies, intensities, and branching ratios of the transitions in ^{160}Dy

Initial state	Gamma energy	Final state	Intensity (%)		Branching ratio (%)	
Ei (keV)	Er (keV)	Ef (keV)	Present work	Ref. 1	Present work	Ref. 1
283.8	197	86.8	4.78	5.2		
966.2	682	283.8	0.55		0.98	1.1
	879	86.8	29.6	30	52.9	54
	966	0	25.8		46.1	45
1049.1	765	283.8	2.1		18.1	19
	962	86.8	9.5	9	81.9	81
1155.9	872	283.8	0.15	0.21	61.2	66
	1069	86.8	0.095		38.8	34
1264.7	216	1049.1	3.8		8.3	8.6
	299	966.2	27.0	27	58.7	59
	1178	86.8	15.2		33.0	32
1286.7	238	1049.1	0.019		0.55	0.4
	1003	283.8	1.06		30.	30
	1200	86.8	2.4	2.4	69.	70
1358.7	310	1049.1	0. 9		9.	9
	392	966.2	1.34		13.	14
	1272	86.8	7.7	7.5	78.	76
1386.4	231	1155.9	0.041		4.2	8
	337	1049.1	0.38		38.7	35
	1103	283.8	0.56	0.57	57.	56
1398.9	350	1049.1	0.11		2.4	0.4
	433	966.2	0.022		0.5	0.5
	1115	283.8	1.46		32.	33
	1312	86.8	2.98	2.9	65.1	66
1535.1	246	1288.2	0.019		8.7	12
	379	1155.9	0.013		6.1	8
	486	1049.1	0.098		44.	38
	1251	283.8	0.098	0.1	44.2	40

抑制康普吞邊緣的伽瑪能譜的設置

仲　國　慶
中央研究院物理研究所

江　紀　成
中央研究院物理研究所

摘　要

我們在量度伽瑪單能譜時，都會因康普吞邊緣之作用而使得在較低能量且相對強度較弱之伽瑪射線不易顯現，若要改正這種缺失須利用抑制康普吞邊緣之技術，本報告即是討論此種技術之設備與方法。

壹、前　言

伽瑪射線在穿過晶體偵檢器時，會與偵檢器內之晶體生(1)光電效應(2)偶生效應(3)康普吞效應等三種效應，我們利用這三種效應，以量取入射的伽瑪能譜，由能譜上顯現的能峯的位置及高度，來表示此伽瑪射線的能量及强度。由於有康普吞效應，部份入射的伽瑪射線由於與晶體中的原子散射而損失能量，會在能譜中顯現所謂"康普吞邊緣"（Compton edge），通常多出現在某主能峯附近之低能區，且呈連續分佈[1][2]，當我們須要找出只有較低收集比（Counting rate）的伽瑪射線時，必須利用抑制康普吞邊緣的技術，以降低此康普吞背景。目前常用來抑制康普吞邊緣的方式是以反符合（Anti-Coincidence）電路來配合量取伽瑪能譜，稱作Compton Suppression Spectrometer。

但是此種設備中使用巨大的NaI（Tℓ）晶體來包住有較佳能量分解度的Ge（Li）偵檢器，並且此種大型NaI（Tℓ）晶體須加4～6個光電倍增管[3]，所以所費不貲。同時又由於放射源須放在Ge（Li）偵檢器和NaI（Tℓ）偵檢器之共同的前方，再以反符合方式來度量，故收集比將大大的降低，可至原來的3～10倍，故有人認爲傳統的方式要仔細的考慮[4]。

本組此次所設置完成的抑制康普吞邊緣的設備，NaI（Tℓ）偵檢器構造簡化了許多，外觀只是一個直徑6吋，長8.5吋之圓柱體，中間有一直徑3吋，長4吋之圓柱孔，以便放置Ge（Li）偵檢器及放射性試料，NaI（Tℓ）偵檢器外殼包以鋁合金，以保護偵檢器之晶體，NaI（Tℓ）偵檢器只有一個光電倍增管放置於NaI（Tℓ）晶體之後。儀器配

置我們亦作了少許修改，但是抑制康普吞邊緣之效果仍然很理想，而收集比只降低了原來的 2～3 倍！

貳、實驗方法與結果

因爲放射源（放射性試料）須放置在NaI（Tℓ）偵檢器和Ge（Li）偵檢器之間，故放射源之活性（Activity）不宜超過 2 μci ，外型由二片扁平之膠片把點狀之放射性試料夾往，以免放射性物質洩漏。將放射源放置在Ge（Li）偵檢器和NaI（Tℓ）偵檢器之間（如圖 1 所示），放射源置於Ge（Li）偵檢器正前方約 2 公分處，目的是使放射源可當作點放射源看待（若放射源和偵檢器距離能大於十倍放射源本身形狀之最大距離就可以當作點放射源[5]），以減少幾何誤差。這種安排方式較傳統之方法也因爲放射源與Ge（Li）偵檢器之間無伽瑪射線之屏蔽，可減少伽瑪射線因屏蔽而產生之偏折所產生之誤差。

電子綫路如圖 1 所示，我們先使得兩組AMP（AMPlifier）有信號輸出，令輸出之類此信號在 0 －10伏之間，再把兩組的TSCA（Timing Single-Channel Anlyzer）的Lower Level均降爲0 伏，Upper Level均爲10伏，以便由AMP輸出的信號經過TSCA均有邏輯輸出，再同時調整兩組TSCA之時間差，使得NaI（Tℓ）偵檢器和Ge（Li）偵檢器之信號取得同步（因儀器不可避免之誤差，二者時間差100 nsec就算是同步），我們認爲此同步信號，分別是由經過Ge（Li）偵檢器之伽瑪射線碰撞電子而使得電子得到能量而被收集之信號，以及伽瑪射線在Ge（Li）偵檢器內經康普吞散射而逸出Ge（Li）偵檢器而被NaI（Tℓ）偵檢器所收集之信號，我們不希望此有與NaI（Tℓ）偵檢器信號同步之Ge（Li）偵檢器信號顯現在能譜中，故將NaI（Tℓ）偵檢器之信號與Ge（Li）偵檢器作反符合綫路之反閘門信號，這個TAC（Time Analyzer）來完成，在Ge（Li）偵檢器之邏輯信號所附加的Delay，此綫路只是爲了利用TAC作反符合綫路。我們將 TAC之輸出之邏輯信號取出和Ge（Li）偵檢器之類比信號比較時間關係，須在Ge（Li）偵檢器之類比信號加以延遲才可以取得同步，再以TAC之輸出作閘門信號去開啟Ge（Li）偵檢器之類比信號，這個由LG（Linear Gate）來完成。在 LG 所輸出之類比信號將是抑制康普吞效應之信號，我們將之送入ADC 和MCA，就可以在MCA顯現出此抑制康普吞邊緣的伽瑪能譜了。

我們爲了比較這種抑制康普吞邊緣設備的效用，就同時量取兩種伽瑪能譜，一種是經由此種抑制康普吞邊緣設備之伽瑪能譜（如圖 1 上之 A 信號之能譜），和另一種是未經過此設備之伽瑪能譜（B 信號之能譜），並電子儀器不加調整只改換標準放射源 Co－60和 Cs－137 之伽瑪能譜，分別顯示於圖 2，3，4，5 。發覺確實把康普吞邊緣改善了許多。再把主能峯之收集數與康普吞邊緣之收集數兩者作一比較，列於表 1 和表 2 。發覺只使得收集比降低約一半，而康普吞邊緣抑制改進了 2～3 倍！

參考文獻

1. Jan Krugers, Instrumentation in Applied Nuclear Chemistry, 1973, p128.
2. 河田　燕，放射線計測技術，東京大學出版會（1981）p79 。
3. CANBERRA INDUSTRIES, Catalog, 1983, p22.
4. 河田　燕，放射線計測技術，東京大學出版會（1981）p85 。
5. 原子能委員會，非醫用游離輻射防護講習教材，p41 。
6. J. Simpson and P.A. Butler, L.P. Ekstrom, Nucl. Instr. and Meth. 204 (1983) p463-469.
7. R.A. Meyer, Phys. Rev. 170 4, (1968) p1089-1107.

表 1 ：標準放射源 Co － 60 抑制康普吞邊緣之收集數的比較

能　量 (Mev)	主能峯之收集數 (A)	康普吞邊緣之收集數平均 (B)	(A)÷(B)	
1.17	2501 (1428), (716)	37	67.6	圖 2 之能譜
1.33	1936 (801), (1159)	27	71.7	
1.17	5465 (1845), (3060)	224	24.4	圖 3 之能譜
1.33	3816 (1151), (3651)	189	20.2	

( )內表示主能峯前或後一個 channel 的收集數

表 2 ：標準放射源 Cs － 137 抑制康普吞邊緣之收集數的比較

能　量 (Mev)	主峰之收集數 (A)	康普吞邊緣之收集數平均 (B)	(A)÷(B)	
662	1736 (599), (1709)	10.3	168.6	圖 4 之能譜
662	1952 (1098), (1121)	54.3	36	圖 5 之能譜

( )內表示主能峯前或後一個 channel 的收集數

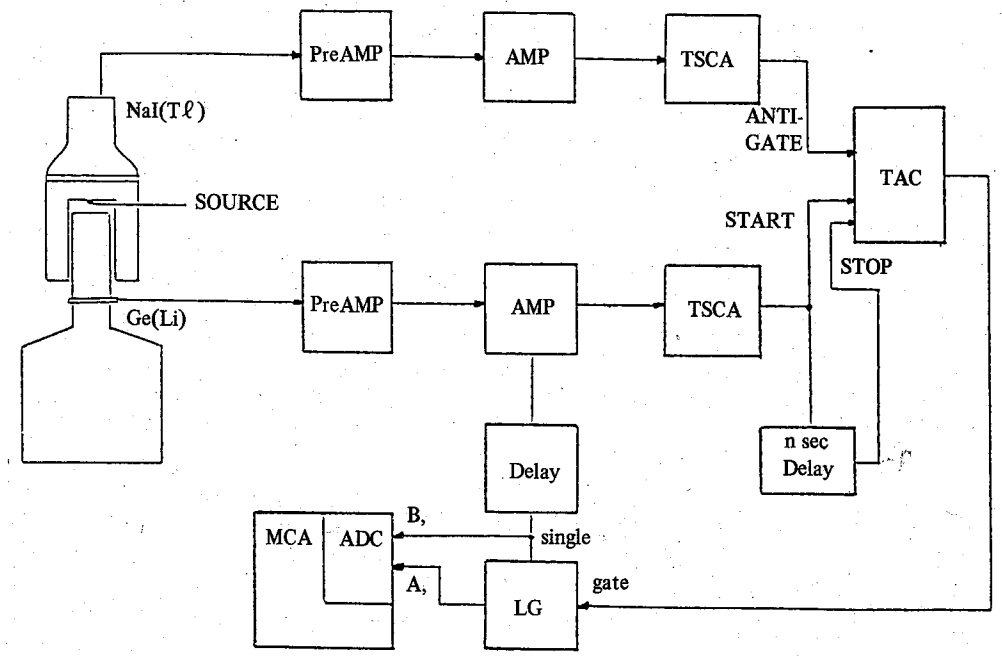

圖 1　抑制康普吞邊緣設備之儀器配置圖

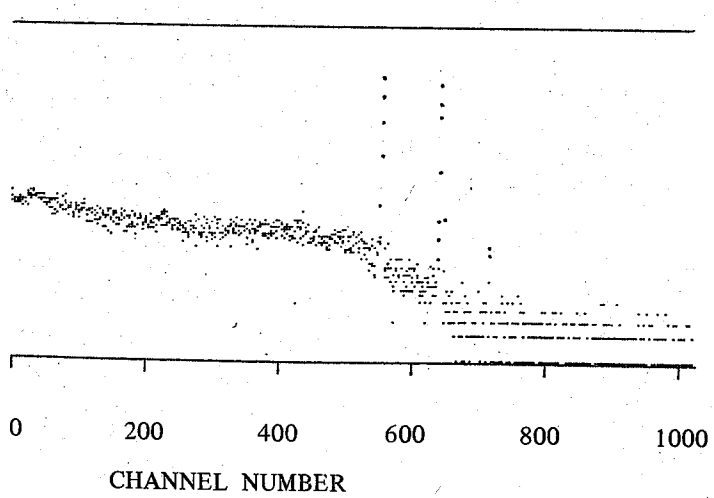

圖 2　標準放射源 Co － 6o 之抑制康普吞邊緣伽瑪能譜

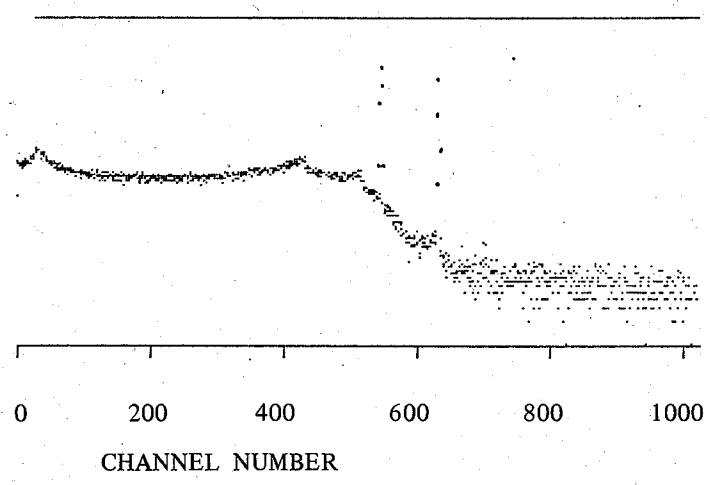

圖3　標準放射源Co－6o之伽瑪能譜

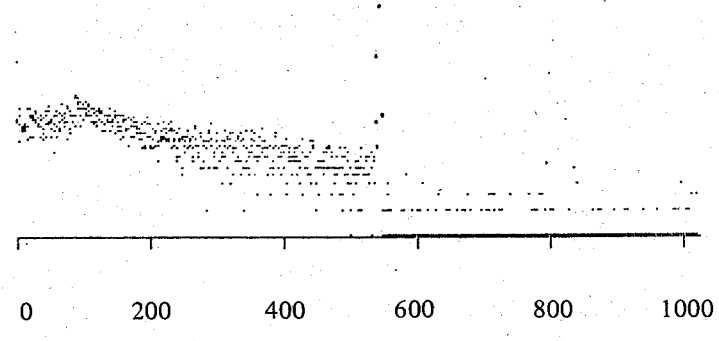

圖4　標準放射源Cs－137之抑制康普吞邊源伽瑪能譜

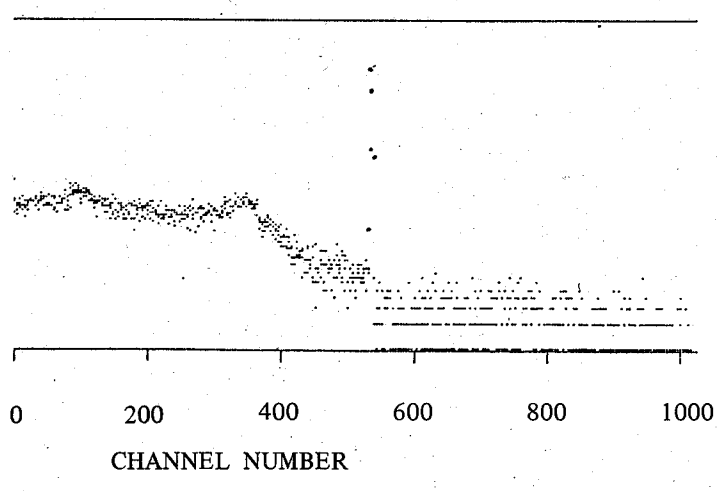

圖5　標準放射源Cs－137之伽瑪能譜

微電腦多波道分析儀之研究

程　斌　慶
仲　國　遠
陳　志
中央研究院物理研究所

摘　要

本文報導由我們自行發展成功之微型實驗數據收集系統，此系統可用於核物理，固態物理及其他如化學，生物，醫學等實驗數據之收集、儲存、分析之用。

在原子核物理實驗的研究上，傳統的數據之獲得是由MCA（Multichannel Analyzer）擔任核譜（Nuclear Spectra）的記錄，儲存或分析的主角。近年來國外大型實驗室多以迷你或中，大型計算機擔任此項工作。即是將所需的多組反應訊號經由若干ADC 轉成數位訊號後經過介面裝置輸入計算機中以作爲線上（on-line）或離線（off-line）計算及處理之用，這種系統十分方便快速，可是所費不貲，一般小型實驗室是無法負擔的。市面上雖然已有附加微處理機的MCA，這種MCA 雖也可作若干初步的分析工作，但售價頗昂，同時也有若干機能的限制（Function limit），例如只能記錄一組核譜資料。本文報導以市售廉價之微電腦，如Apple Ⅱ等，爲主的Data Acqusition system設計。它的前端機（ADC Memory Interface Unit），簡稱ADC MIU，最多可有六具ADC MIU與微處理機相連接（也就是1至6個前端機可以 on-line）。ADC MIU能夠與8位元或16位元或32位元電腦配合以適當之軟體及該電腦之週邊設備而工作。其功能不僅取代目前廣泛使用的MCA，且可與大型的DAS 比美，用記錄在軟性磁碟中的多組核譜資料可供 on-line 或 off-line 分析之用。

本系統中之前端機（ADC MIU）裡所包含之精密ADC（不同於一般之ADC）大部分參考Wilkingson type之1 K，2 K位址方式所製成，而整個ADC MIU之工作情形簡略來說是外加訊號經過 ADC 後快速的存入記憶電路中，等候微處理機命令經由介面取走，或是讀入ADC MIU。本前端機有1 K位址，每個位址有24個 bit（即最高可收集1.6 M個 counts）。前端機中含有脈高分析及複計數器之功能。另外可由光電管輸出之信號直接加於本系統來分析處理。前端機中有預置時間，可設定時間在一天以上，含有Add-Sub，Channel offset，上下限之切除，dead time indicator等，一應俱備。另有一項功能可在電腦之螢幕上完成之 live display。

工作穩定度方面，本系統之前端機（ADC MIU）24小時內，在室溫25 ℃，外線電壓115 ± 10 V變化下之Channel Shift 只有± 1 CH。

用途方面，本系統可將任何具有脈高變化之脈波信號予以精確的分析及記錄，組合運算及輸出或送入大型電腦，也可由顯示螢光幕、印字機及磁碟機輸出。所以除了原子核物理實驗方面之應用外，尚有化學、農業、醫學等方面均可以利用。

我們除已發展上述硬體外，對於本系統應用之軟體一併研究完成。用於本系統在ADC MIC與Apple Ⅱ連接作業之程式之如下：

```
30      HOME : HGR2
60      CALL 4096
90      HGR : HCOLOR = 7
100     FOR I = 0 TO 1023
200     HPLOT PEEK (20480 + I), INT
        (I / 6)
300     NEXT I: CLEAR
390     LOMEM: 24576
400     DIM A(1040): VTAB (22): HTAB
        8: FLASH : PRINT "CONVERTING
          DATA"
500     FOR J = 0 TO 1023
550     LET A(J) = PEEK (16384 + J)
        * 65536 + PEEK (18432 + J)
        * 256 + PEEK (20480 + J)
600     NEXT J
650     VTAB (21): PRINT : PRINT"
          INSERT DATA DISC --〉PRESS
          ANY KEY";: GET T$: HOME : NORMAL
        : VTAB (22): PRINT" ENTER
          FILE NAME : ";: INPUT F$
660     PRINT CHR$ (4) "OPEN" F$: PRINT
          CHR$ (4) "DELETE" F$: PRINT CHR$
        (4) "OPEN" F$: PRINT CHR$ (4)
        "WRITE" F$
700     FOR K = 0 TO 1027: PRINT A(K),:
        NEXT K
750     PRINT CHR$ (4) "CLOSE" F$
900     TEXT
```

為了配合將前端機內所附有的記憶體所存的資料取出，放置在個人電腦中再加處理，所用的程式由組合語言和培基語言交互寫成。當前端機在收集資料同時能很快的搬取前端機的資料至Apple Ⅱ個人電腦中，並把資料轉換成能譜顯示出來。當收集終了可以把資料轉換成數據再存貯磁碟片中，以便日後列印，畫圖和數據分析。本文所附的程式，能有以上的功能。(1)在60行是將前端機內之記憶體的資料取出，搬至Apple Ⅱ個人電腦。(2)100 至 300 行是把能譜顯現出來。(3) 400 至 600 行是將資料轉換成數據。(4) 650 至 700 行是把數據存入磁碟片。本程式執行完畢後尚有一些程式可資應用，使得MCA所能作的幾乎都已包含，而且速度也不慢。

本系統有體積小、成本低、效能高的優點。所用的微電腦亦不失其原有功能；除了DAS 時用作記憶、儲存、分析數據外，也可用作其他的計算工作，存於軟性磁碟中的資料經過轉換，可存於磁帶再輸入大型電腦作離線分析之用，應可推廣至一般實驗室廣泛使用。

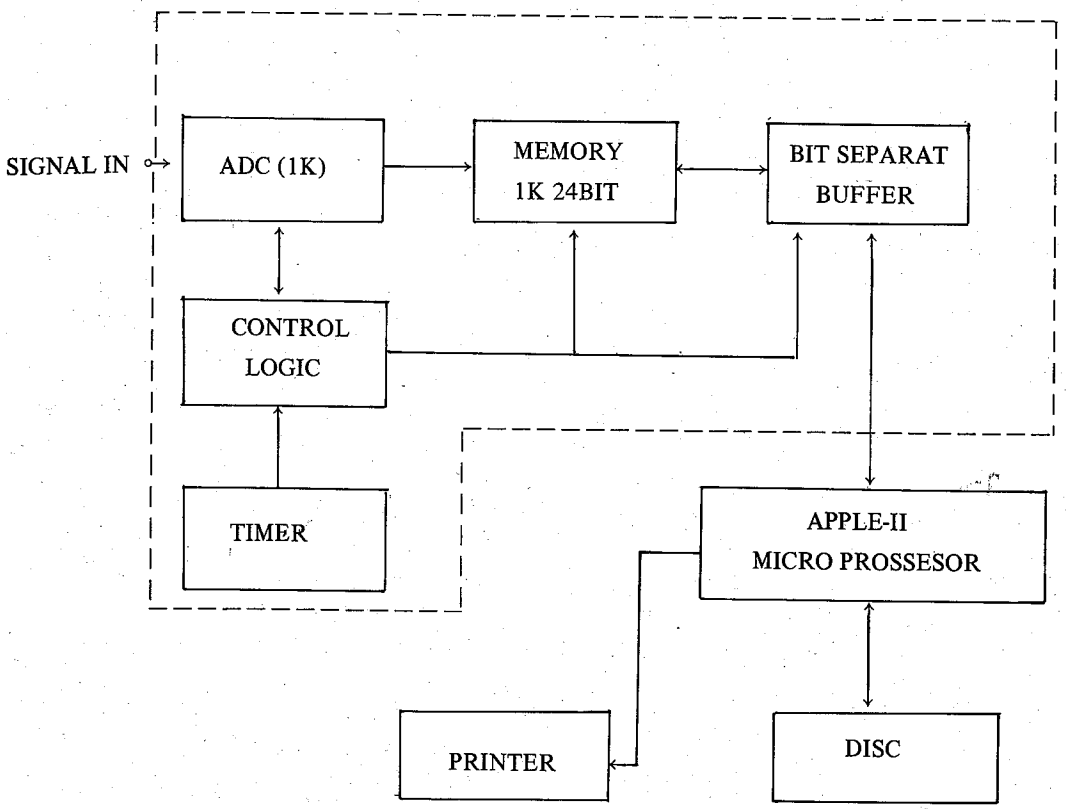

圖 1　微型ＤＡＳ之方塊系統圖

＊虛線框內本系統可同時使用 6 個相同之組合

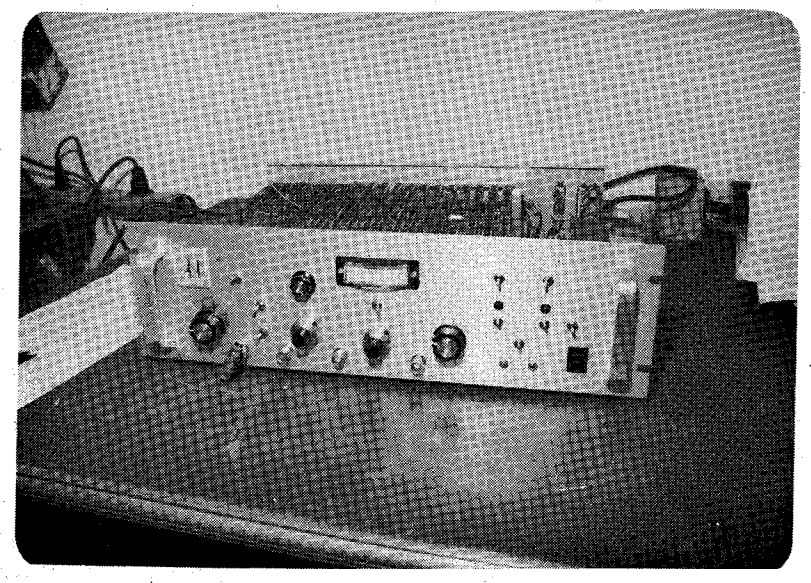

圖 2　ADC MIU 之外觀圖

The O^+, $T = 0 \rightarrow 1^+$, $T = 1$ Gamow-Teller Transitions via $^{24}Mg(p, n)^{24}Al$ Reaction at $E_p = 35$ MeV*

G.C. Kiang (江紀成), *L.L. Kiang*† (李　琳), *G.C. Jon* (仲國慶)

and

E.K. Lin (林爾康)

Institute of Physics, Academia Sinica

Nankang, Taipei

Republic of China

ABSTRACT

Three O^+, $T = 0 \rightarrow 1^+$, $T = 1$ Gamow-Teller transitions are observed in the $^{24}Mg(p, n)^{24}Al$ reaction at $E_p = 35$ MeV. The three 1^+, $T = 1$ states are 0.44, 1.12 and 3.06 MeV in A . DWBA analyses with Brown and Wildenthal wave function and M3YE+TN (odd) effective nucleon-nucleon interaction give satisfactory results. Resonable comparison between the low-energy (p, n) cross-section and the β–decay rates has been obtained for the GT transitions leading to the 1^+ states.

The magnetic excitation of nuclei is an area of high interest recently[1, 2], A π meson carries a unit of $\Delta\sigma$ and $\Delta\tau$, where σ and τ are the nucleonic spin and isospin variables. Hence pionic excitations are unnatural-parity excitation have $\Delta T = 1$. Such a spin-isospin mode of excitation can be directly related to charge-exchange reactions, such as (π^+, π^0), (p, n) and (^{3}He, t), etc. Charge-exchange reactions can excite states carrying a singnificant fraction of the Gamow-Teller (GT) strength, expecially those which are inaccessible in β-decays, and are thus hoped to supplement other experiments with independent information. In recent (p, n) studies a close relationship has been established between the GT β-decay strength and (p, n) data which are subject to the choise of the effective interaction and the other assumptions involved.

In the $^{24}Mg(p, n)^{24}Al$ reaction at $E_p = 35$ MeV, three 1^+ states were observed in the neutron TOF spectra. The experiment was performed with use of a 35 MeV proton beam from the AVF cyclotron and the time-of-flight facilities at the Cyclotron and

* Work supported by National Science Council, R.O.C. NSC-73-0208-M001-07.

† Dept. of Phys. National Tsing Hua University, Hsinchu, Taiwan, R.O.C.

Radioisotope Center, Tohoku University, Japan. With a beam swinger system, we measured angular distributions of emitted neutrons from 0° to 140° , except the addition 3°, in 10°step. The target was prepared by vacuum evaporation for the enriched ^{24}MgO powder (99.9%) on mica backing. The thinkness was 3.4 mg/cm^2 Overall time resolution was 1.2 ns. and the error in absolute cross-section is estimated to be∿15% while the relative error is∿7%. Further details of the experiment are given in Refs. 3, 4.

A typical neutron energy spectrum is shown in Fig. 1. Three 1^+ states are located at 0.440, 1.12 and 3.06 MeV respectively. The first and second 1^+ states of ^{24}Aℓ have been observed both in (p, n) and (^{3}He, t) reactions previously[5, 6, 7, 8]. The strong isovector excitation in the sd shell is the magnetic state which is well known by its large transition rate. In comparison with the backward angle electron scattering data of ^{24}Mg[23], the two 1^+ states in ^{24}Aℓ should correspond to $J^\pi = 1^+$, $T = 1$ ^{24}Mg states at E_x = 9.96 and 10.73 MeV respectively.

Except the two 1^+, T = 1 states, another 1^+ state at E_x = 3.06±0.04 MeV was also observed in our TOF spectra. The IUCF data also have shown a 1^+ state excited at E_x = 3.1 MeV in ^{24}Mg(p, n)^{24}Aℓ at E_p = 65 MeV[9]. C.D. Goodman[9] interpreted that as the state found due to the spin-isospin strength split from E_x=1.12MeV, 1^+ state in ^{24}Aℓ. In fact, the measured cross-section of the 3.06 MeV state is much smaller than that of the 1.12 MeV state. Fig. 2 shows the angular distribution for the three 0^+, $T = 0 \rightarrow 1^+$, $T = 1$ transitions. Solid curves in Fig. 3 are the DWBA calculations calculated by the code DWBA70 which includes knock-on exchange contributions[11]. For the p-n interactions, a set of effective interactions M3Y derived by Bertsch et al.[12] by fitting a superposition of Yukawa potentials with different ranges to the G-matrix generated from the nucleon-nucleon potential. The M3Y effective interactions have been extensively used in the DWBA analyses of low-energy (p, n) work[13]. However, it has shown that M3Y tends to understimate the cross-sections for isobaric analog state (IAS) and overestimate those for 1^+ state[13]. Petrovich[14] found that the S = 1, T = 1 part of M3Y was too strong by 40%. He suggested to reduce the strength $V_{\sigma\tau}$ of the M3Y by 40% (which is called as M3YP) for the DWBA calculations. Smith and Amos[15] used the Gaussian forms of central, tensor and spin-orbit forces, and compared them with Yukawa-type forces similiar to the M3Y. Central odd-state forces are ignored in their analysis. H. Ohnuma and H. Orihara[13] found that the very good fits both in

shape and magnitude have been obtained in the DWBA aralysis for the angular distribution measure in^{54,56} Fe (p,nn) reaction at E_p =28∿35MeV, if the odd forces were switched off. Orihara et al.[16] also reported recently that using the the M3Y + TN (odd) interactions gave very nice fitting for the angular distributtions leading to 0^-, 1^-, 2^- and 3^- states in ^{16}F via ^{16}O(p, n)^{16}F reaction at E_p = 35 MeV. M3YE + TN (odd) means that only the even terms of the effective interaction are taken to account for the central and L-S forces, while all channels for the tensor are included[16]. In the DWBA calculation, the optical potential parameters of Fabrci et al.[17] are used for protons. Those for neutrons are self-consistent potential parameters derived by Carlson et al.[18]. Pure configuration ($\pi d_{5/2}{}^4 \nu d_{5/2}{}^4$) is assumed for the ground state of ^{24}Mg. The DWBA curves for the E_x = 0.44, 1.12 and 3.06 MeV, 1^+ states are calculated based the one-body transition density matrix elements for the transition from the lowest T= 0 state of $J^\pi = 0^+$ to the lowest three states of T = 1, $J^\pi = 1^+$ states in A = 24 nucleus respectively[19]. The corresponding strengths of transition between $J^\pi = 0^+$, T = 0 and $J^\pi = 1^+$, T = 1 states were claculated from shell-model wave function constructed in from eight-particles $0d_{5/2}$-$1s_{1/2}$-$0d_{3/2}$ configuration space by Brown and Wildenthal[19], recnetly, these transition density matrix elements

$$(2\Delta J+1)^{-\frac{1}{2}} (2\Delta T+1)^{-\frac{1}{2}} < 1^+, T_f = 1^+ | a_j^+ \otimes a_{j'} | 0^+, T_i = 0 >$$

are shown in Table 1. The solid curves in Fig. 3 are the said three (J^π, T) = (1^+, 1) states in ^{24}Aℓ. Which give very nice fittings to the experimental data. Furthermore, in Fig. 3 we find that the magnitude ratios of these DWBA calculated cross-section at their peak values are very in match with those of the measured. The $[\sigma_{1.12\ \mathrm{MeV}} : \sigma_{3.06\ \mathrm{MeV}} : \sigma_{0.44\ \mathrm{MeV}}]^{\mathrm{exp}}_{\mathrm{peak}}$ = 10 : 4.3 : 1.6. The differential cross-section magnitude calculated for the 1^+ states with Brown and Wildenthal wave functions is found $(\sigma_{exp}/\sigma_{cal})_{0.44\ \mathrm{MeV}} = (\sigma_{exp}/\sigma_{cal})_{1.12\ \mathrm{MeV}} = (\sigma_{exp}/\sigma_{cal})_{3.06\ \mathrm{MeV}} = 0.98$. These results not only support the E_x = 3.06 state in ^{24}Aℓ to be 1^+, T = 1 state also support Brown and Wildenthal's shell-model calculation. By the way, Wildenthal and Chung[20] also presented the shell-model calculation employed a complete s-d basis and an effective Hamiltonian derived from adjustments of Kuo A = 18 s-d shell Hamiltonian to obtain a best fit to energy levels of the A = 18-24 nuclei. We also

claculated the differential cross-sections for the lowest three 1^+, T = 1 states with Wildenthal and Chung's one-body transition density matrix elements. The results are presented in Fig. 4. Comparing with the Fig. 3, the experimental data strongly suppor Brown and Wildenthal's calculation.

It is possible to extract the Gamow-Teller matrix element B(GT) of the 1^+ states from the DWBA calculations and the measured differential cross-section at low momentu transfer. We present the peak locations and the experimental value of $B(GT)_{exp}$ for th observed 1^+ excitations compared to theoretical predications obtained from the shell-model calculation of Brown and Wildenthal (see Table 1). The theoretical values of B(GT) were calculated by summing the product of each $j \rightarrow j'$ transition density with the corresponding reduced single particle matrix elements $< j' \,||\hat{O}_{GT}||\, j >$ which have the relationship with the conventional or "free-nucleon" values of the single-particle matrix element of the GT operator $\hat{O}_{GT}$.

$$< j' \,||\hat{O}_{GT}||\, j > = |g_A/g_V| < j' ||\, \sigma\tau \,||\, j > ,$$

where $g_A/g_V = 1.25 + 0.009$, as determined from the beta decay of the free neutron[21].

On the basis of the relationship from Wilson et al.[22], between Fermi (F) and G matrix elements and the ft values

$$|\, M_F \,| + 1.56 |\, M_{GT} \,|^2 = \frac{6163.4}{ft}$$

and, $B(GT) = |M_{GT}|^2$.

It is possible to extract the ft values from the GT decays ($M_F \doteq 0$). In this wa we obtain the $B(GT)_{TH}$ and compare with the $B(GT)_{exp}$ together with the logft values of the three 1^+ states in ^{24}Al for β^+-decay to the ^{24}Mg ground state (0^+) as shown in Table 3.

In conclusion, we observed three GT transitions leading to 1^+, T = 1 states at E_x = 0.44, 1.12 and 3.06 MeV in ^{24}Al via $^{24}Mg(p, n)^{24}Al$ reaction at E_p = 35 MeV. The effective nucleon-nucleon interaction of M3YE+TN(odd) was found to give very good corss-section estimation for the three angular distributions by the DWBA calculation. The obtained $\sigma_{exp}/\sigma_{cal}$ values together with the good agreement with the shape support the one-body density matrix elements for the three lowest $J^\pi = 1^+$, T = 1 states in A = 24 nuclei claculated by Brown and Wildenthal[19]. In comparison with the β -decay rates, the logft values for the β^+-decay from the 0.44, 1.12 and 3.06 $J = 1^+$, T = 1 states in ^{24}Al to the g.s. of ^{24}Mg are 4.97, 3.34 and 3.74 respectively.

REFERENCES

(1) For example, D.C. Goodman, C.A. Goulding, M.B. Creenfield, J. Rapapart, D.E. Bainum, C.C. Foster, W.G. Love, and F. Petrovich, Phys. Rev. Lett. 44, (1980) 1755.

(2) B.D. Anderson, R.J. McCarthy, M. Ahmad, A.M. Kalenda, J.N. Knudson, J.W. Watson R. Madey, and C.C. Foster, Phys. Rev. C26, (1982) 8.

(3) H. Orihara, T. Murakami, S. Nishihara, T. Nagakawa, K. Maeda, K. Miura and H. Ohnuma, Phys. Rev. Lett. 47, (1981) 301.

(4) H. Orihara and T. Murakami, Nucl. Instr. Meth. 188, (1981) 15.

(5) F. Ajzenberg-Selove, Nucl. Phys. A166, (1971) 1, P.M. Endt and C. Van der Leun, Nucl. Phys. A105, (1967) 1.

(6) C.E. Moss and A.B. Counter, Nucl. Phys. A178, (1971) 241.

(7) R.E. Tribble and A.V. Nero, Phys. Rev. C15, (1977) 2233.

(8) T. Shibata, J. Imazats, T. Yamazaki and B.A. Brown J. of the Phys. Soc. of Japan 47, (1979) 33.

(9) C.D. Goodman in 'The (p, n) Reaction and Nucleon-Nucleon-Force' ed. by C.D. Goodman et al., Plenum, (1980) 145.

(10) U.E.P. Beng, same as ref. 9, p. 387.

(11) R. Schaeffer and J. Raynal, Saclay Rept. No. CEA-R 4000, 1970.

(12) G. Bertsch, J. Bonysowize, H. McManus and W.G. Love, Nucl. Phys. A284, (1977) 378.

(13) H. Ohnuma and H. Orihara, Prog. Theor. Phys. 67, (1982) 353.

(14) F. Petrovich, same as ref. 9, p. 115.

(15) R. Smith and K. Amos, Aust. J. of Phys. 32, (1979) 155.

(16) H. Orihara, C.D. Zafiratos, S. Nishihara, K. Furukawa, M. Kabasawa, T. Nagakawa, K. Miura, G.C. Kiang and H. Ohnuma in Proceedings of 1983 RCNP International Symposium on Light Ion Reaction Mechanism, Osaka, Japan, May 16-20, 1983.

(17) E. Fabric, S. Micheletti, M. Pignanelli, F.G. Resmini, R. Delco, G. D'Eraimo and A. Pandabo, Phys. Rev. C21, (1980) 844.

(18) J.C. Calson, C.D. Zafiratos and D.A. Fund, Nucl. Phys. A249, (1975) 29.

(19) B.A. Brown and B.H. Wildenthal, Phys. Rev. C27, (1983) 1296.

(20) B.H. Wildenthal and W. Chung, same as ref. 9, p. 89.

(21) B.H. Wildenthal, Nucl. Phys. A209, (1973) 470. B.A. Brown, W. Chung and B.H. Wildenthal, Phys. Rev. Lett. 40, (1978) 1631.

(22) B.H. Wilson, Nucl. Phys. A209, (1973) 470.

Table 1. One-body transition density matrix elements for the transition from the lowe T = 0 J^+ = 0 states to the lowest three states of J = 1^+ T = 1 in A = 24.

$(2\,J+1)^{-\frac{1}{2}}\,(2\,T+1)^{-\frac{1}{2}} < 1^+, T_f = 1 \,|||\, a_j^+ \otimes a_{j'} \,|||\, 0^+, T_i = 0 >$

jj'	$1^{(a)}$	$1^{(b)}$	$2^{(a)}$	$2^{(b)}$	$3^{(a)}$	$3^{(b)}$
$1d_{5/2}1d_{5/2}$	-0.24035	-0.1964	-0.16280	-0.1960	-0.11784	0.1302
$1d_{5/2}1d_{5/2}$	-0.18750	-0.1862	-0.08589	-0.1135	0.06006	-0.0410
$2S_{1/2}1d_{3/2}$	-0.04746	-0.0612	-0.15993	-0.1437	0.12446	-0.1204
$2S_{3/2}1d_{3/2}$	-0.04746	-0.0612	-0.15993	-0.1437	0.12446	-0.1204
$1d_{3/2}1d_{5/2}$	-0.01057	-0.0137	-0.22470	-0.2273	0.32796	-0.3310
$1d_{3/2}2S_{1/2}$	-0.04787	-0.0419	-0.01227	-0.0030	0.06961	-0.0419
$1d_{3/2}1d_{3/2}$	-0.02131	-0.0147	0.02039	-0.0107	-0.07015	0.0785

(a) : From Ref. 19

(b) : From Ref. 20

Table 2. The Effective Nucleon-Nucleon Interaction Strength (M3YE + TM(odd)) of Different Ranges

	0.25 fm	0.4 fm	1.414 fm	0.7 fm
V_0(MeV)	6315	-1961	-3.924	0
V_σ	-1008	305	1.308	0
V_τ	-3202	1002	1.308	0
$V_{\sigma\tau}$	-2105	654	1.308	0
V_{LS}	0	- 203	0	
V_{LS}	0	203	0	
V_T	0	- 103	0	3.113
$V_{T\tau}$	0	386	0	10.508

Table 3. Comparison between the theorical and experimental values of the GT transitions strength.

E_x(MeV)	J, T	$\sigma(0^\circ)$ (mb/sr)	$B(GT)_{TH}$	$B(GT)_{ex}$	log ft_{exp}
0.440	1^+; 1,	0.176	0.059	0.042	4.97
1.12	1^+; 1,	0.624	0.967	1.792	3.34
3.06	1^+; 1	0.0828	0.525	9.722	3.74

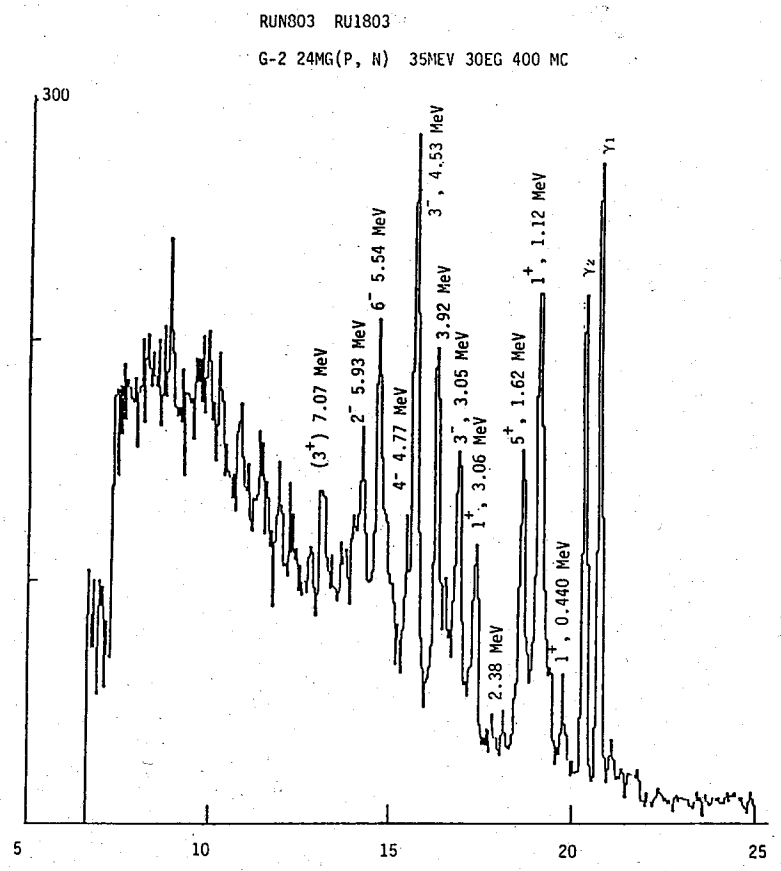

Fig. 1. The neutron spectrum obtained by $^{24}Mg(p, n)^{24}Al$ reaction at E_p=35MeV measured at 3° lab.

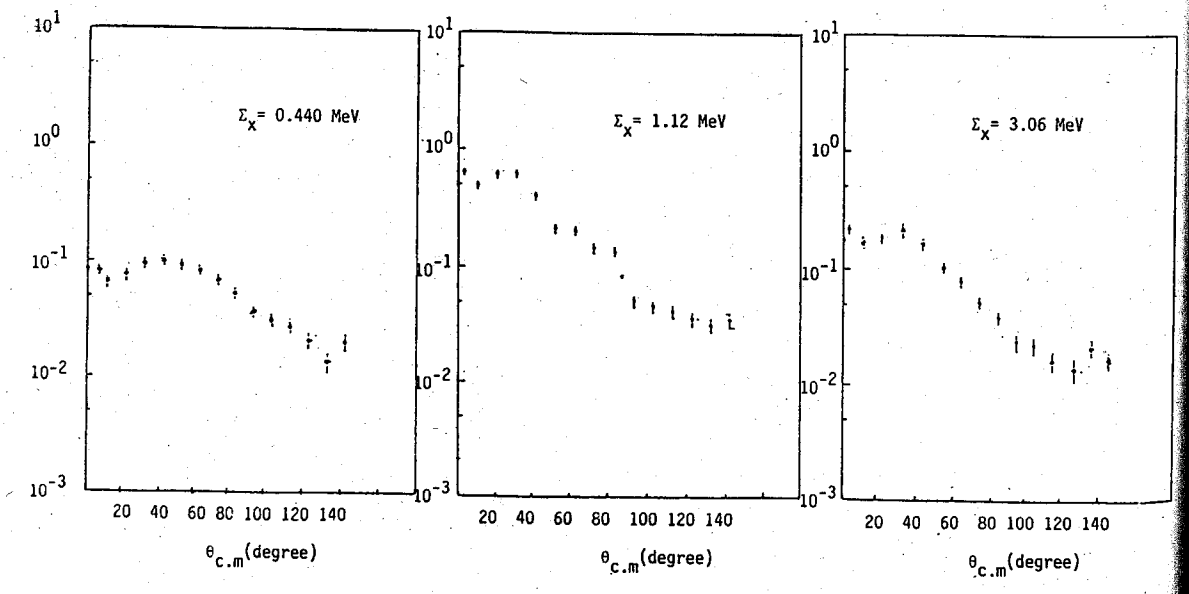

Fig. 2.

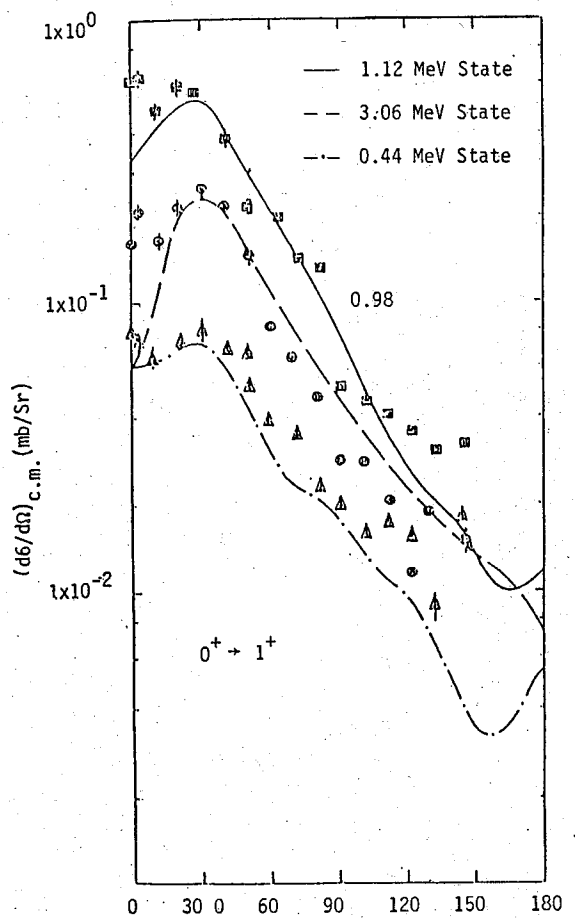

Fig. 3. The DWBA calculated angular dis ribution for 0.44 MeV (dash dotted) 1.12 MeV (solid) and 3.06 MeV (dashed) 1^+ states in ^{24}Al. Under brown and Wildenthal $0^+ \rightarrow 1^+$ one-body transition. (ref. 19). Note the ratio of $(\sigma_{exp}/\sigma_{cal})$ = 0.98 for three of them.

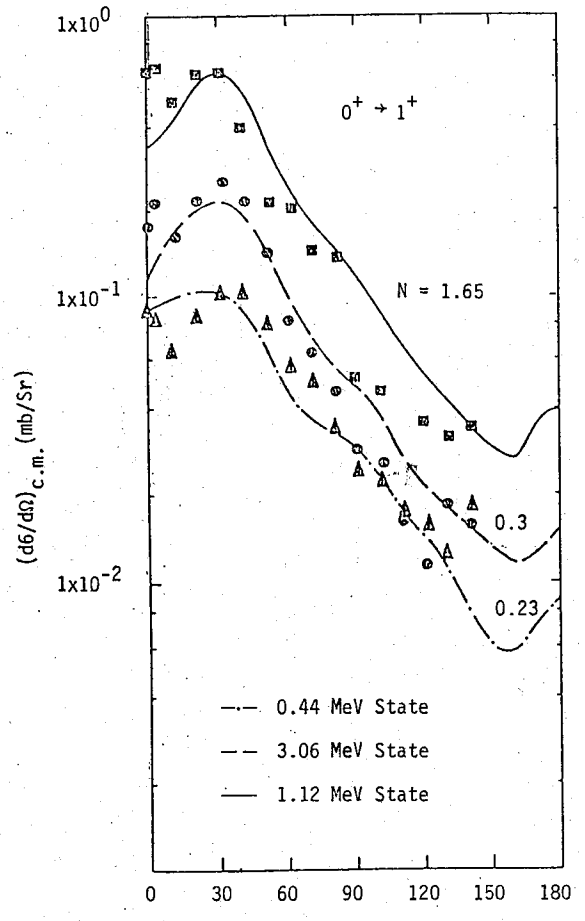

Fig. 4. The DWBA calculated angular distribution for 0.44 MeV (dash-dotted) 1.12 MeV (solid) and 3.06 MeV (dashed) 1^+ state in ^{24}Al under Wildenthal and Chung $0^+ \rightarrow 1^+$ one body transition density matrix element (ref. 20). The ratio of $(\sigma_{exp}/\sigma_{cal})_{1.12MeV}$ = 1.65, $(\sigma_{exp}/\sigma_{cal})_{0.44MeV}$ = 0.23 and $(\sigma_{exp}/\sigma_{cal})_{3.06}$ =0.3.

GAP DEFECT STATES IN AMORPHOUS THIN FILMS

Chun Chiang
Institute of Physics, Academia Sinica
Nankang, Taipei, Taiwan
Republic of China

ABSTRACT

It is proposed that the amorphous film is an inhomogeneous film with many clusters of different lattice strain quenched during the formation stage. Depending on the extent of the strain, some lattice ($E > E_F$) may transform to other configuration ($C_1^\circ \rightarrow C_3^\circ$, $C_2^\circ \rightarrow C_3^\circ$) so as to release the stress, and forms the Valence Alternation Pair. The present model emphisizes the combination of chemical energy of the species of VAP and lattice strain as the origin of defect states and the paring of electrons. Concept of negative effective correlation energy need not be introduced. Origin of formation of tail states in conduction band and valence band is suggested.

In recent decade, there are some important developments in elucidating the amorphous systems. To explain the pecular lacking of EPR signals in chalcogenide films, Anderson[1] has postulated that the effective interaction between a pair of electrons in the same site can be attractive because of coupling to atomic motion, namely the second electron prefers to pair with the first electron. This attraction is the effective negative correlation energy resulting from the polaron energy gained by the contraction of a bond more than compensates for the electron repultion. The postulation of this negative effective correlation energy accounts for the non-observation of EPR signals in chalcogenide films. Street and Mott[2] furthur apply this idea to the defect sites and assuming that the dangling bonds (D°) may act both as donors (becomming D^+) or acceptors (becomming D^-), and local lattice distortion is sufficiently strong when the electron occupation of the dangling bond changes such that the reaction

$$2D^\circ \rightarrow + \; D^+ \; + \; D^- \qquad (1)$$

is exothermic. All defect centers are either positively charged or negatively

charged and D° only occurs by excitation. The preference of pairing of electrons due to local lattice distortion is the negative effective correlation energy. Toyozawa[3] postulates that the double occupancy of electrons will distort the lattice twice more in amplitude and will gain in energy four times more, thus double occupancy is more faborable than single occupancy. Literally applying this idea of negative correlation energy for quantitative calculation, Adler and Yoffa[4] get some pecular result that the Fermi level lies below the highest filled level even at absolute zero temperature. Kastner[5] regards that the dangling bond model of Street and Mott[2], Anderson's hypothesis[1] of a negative effective energy and CFO[6] model are ad hoc, and Kastner and Fritzsche[7] regard that the negative effective correlation energy is a result of special chemistry of these materials not a result of disorder. Kastner et al[8] . further postulate the valence alternation pairs (VAP) and specialize that the reaction

$$2C_3^\circ \rightarrow C_3^+ + C_1^- \qquad (2)$$

is exothermic, so that VAP is formed. The first electron removed from C_1^- costs the first ionization energy; the resulting C_1° moves toward a neighboring C_2° to form C_3° a the second electron removed from C_3° cost less energy than the first electron. This plains the negative effective correlation energy. While it is very nice to be able identify the negative effective correlation energy as originating from chemistry, ho ever, they take the position that chemical species determined the environment (the environment changes to accomodate the postulate species), rather than the environmen constraint determines the chemical species. Their postulation of the timeing of the existance of C_1° or the timeing of its movement toward C_2° to form C_3° is also ad hoc. The purpose of this letter is to explain that the environmental constraints in most case determine decesively the chemical species, rather than the other way around; furthermore, the lattice energy combined with VAP determine the pairing of electrons and the concept of effective negative correlation energy is not required, thus the pecular concequence that the Fermi level lies below the highest filled level at absolute zero temperature can be avoided.

We first ultilize the Ovshinsky's idea[9] that the lone pair electrons in chalco-

genide amorphous films can interact to each other, we further assume that different lone pairs at different location have different lattice distortion and different extent of interaction (The irregular atomic arrangement in X-ray data may be regarded as a proof), thus two neighbors C_2° with the lone pairs too near may interact to form $2C_3^\circ$ as follows:

$$2C_2^\circ(\ell) \rightarrow 2C_3^\circ \rightarrow 2C_3^+ + 2e^-(*), \ \ell \text{ (lattice energy) is large,} \qquad (3)$$

the extent of the reaction is determined by the lattice energy ℓ and the star indicates the excited state. Also, the amorphous films are not perfect and there are dangling bonds in the films. Depending on the environmental constrains and distance between the lone pair electrons and the near by dangling bond, the following reaction may occur:

$$C_1^\circ(\ell) + C_2^\circ(\ell) \rightarrow C_2^\circ + C_3^\circ \rightarrow C_2^\circ + C_3^+ + e^-(*), \ \ell \text{ is large} \qquad (4)$$

the extent of this reaction also depends on the lattice energy ℓ. In order to maintain the equality of Fermi level within the film, the electrons at the excited anti-bonding state will flow to the low energy site and release the energy there; the low energy sites avalable are those $C_1^\circ(\ell)$ where the lattice energy ℓ is not too high:

$$C_1^\circ(\ell) + e^- \rightarrow C_1^-(\ell) + \text{energy}, \ \ell \text{ is small} \qquad (5)$$

At the energy higher than Fermi level, all the $C_2^\circ(\ell)$ and $C_1^\circ(\ell)$ will react according to equation (3) and (4), the total charged species produced are:

$$e^- = C_3^+ = \int_{E_F}^{E_c} [\, C_1^\circ(\ell) + C_2^\circ(\ell)\,]\, dE \qquad (6)$$

the charges produced in (6) are absorbed by C_1° with ℓ smaller than E_F and concequently the number of $C_1^-(\ell)$ produced according to equation (5) are

$$e^- = C_1^-(\ell) = \int_{E_V}^{E_F} C_1^\circ(\ell)\, dE \qquad (7)$$

To sumarize the above idea, Fig. 1(a) indicates that two dangling bonds (E = 0) may at normal bonding distance combine to form one bonding level and one anti-bonding level. Fig. 1(b) shows that two lone pairs locate too close to each other therefore their lattice energy is higher (E > 0); they may however also combine to form one

bonding level and one anti-bonding level. However, even though they are too close for lone pairs, they speration is still larger than normal bonding distance and orbital overlap is less, thus the bonding level and anti-bonding level are seperated to a lessen extent and located in the gap state. Fig. 1(c) indicates the spatial location of the defect states for the entile amorphous system. Negative C_1^- is ocupi up to Fermi level in the gap, some C_3^+ bonding states (from Fig. 2(b)) are located between bonding band and valence band, some anti-bonding un-occupied states (from Fig. 2(b)) indicated by the Δ symbol are located between E_F and conduction band. Some neutral C_2^o with strain less than E_F, which has not transformed to C_3^+, are indicated by the circle sign. This model shows the origin of formation of tail states in conduction band and valence band.

If we know the distribution of $C_1^o(\ell)$ and $C_2^o(\ell)$, equations (6) and (7) may be use to calculate E_F. However, the distribution of $C_1^o(\ell)$ and $C_2^o(\ell)$ depends on the preparation of films and annealing process. During the stage of film formation, the atoms are piled up one after another and side by side. Some electrons are located just right to form a normal covalent bond; some electrons are located not right, thus forming a dangling bond; some forms the lone pair. During the annealing proces some dangling bonds and lone pairs having high lattice energy will react according to equation (6) and (7). However, unlike the fluid state the movement and reactivi of atoms in solid state are relativily limited, the atoms can only move a small dis tance and preserve approximately the global from-work and no homogeneous film is expected. Thus even though the annealing process can remove the lattice strain somewhat, the finnal result is an inhomogeneous film with many clusters of differen lattice energy. Since the film is not in thermodynamic equalibrium, there is no a priori reason to predict what the distribution of $C_1^o(\ell)$ and $C_2^o(\ell)$ are, and we can only rely on experimental methods, such as the photo-transient-spectroscopy or the experimentally determined E_F, to probe the distribution.

For a very rough and simplified estimation, we may assume that the distributio is linear, and $C_1^o(\ell) = k(E_C-E)$, $C_2^o(\ell) = 2k(E_C-E)$, where k is a constant. With thes assumptions and equations (6) and (7), E_F can be calculated to be mid-way between and E_V.

This model emphasizes that the electron at high energy site will flow to the l

energy site to maintain the Fermi level, this lead naturally to the paring of electrons; also, there are many electrons at Fermi level and the energy required to excite the first electron or the second electron is the same, and the concept of negative effective correlation energy need not be introduced, thus avoiding the pecular result that the Fermi level is below the highest filled level at absolute zero temperature. This model also explain the $e^{-E/KT}$ type of conductivity and is consistant with the view from the transient photospectroscopy[10] that the defect states are distributed in a continuous and exponential way.

In conclusion, we emphisize that the VAP is determined by the interplay of the lattice distortion, the chemical energy of the species and the highest electronic energy of the occupied state, rather by the chemical energy of the species alone. Unlike the original VAP model, which maintains that the negative effective correlation energy is a result of the special chemistry of the materials not a result of disorder; the present model emphysizes the importance of the lattice distortion and global structure in determining the chemical species and its subcequent properties, rather than the chemical species determine the local relaxed structure. It proposes that charcogenide thin films consist of many clusters with different lattice energy, (the irregular arrangement of atoms as revealed by X-ray data in amorphous thin films supports this idea), this lattice energy determines the chemical species, and the electrons at highest occupied sites adjust and flow to low energy site so as to maintain the Fermi level all over the film. A continuous distribution of defect forming the tail states in the gap is expected from the model and is supported by the transient photospectroscopy.

REFERENCT

1. P.W. Anderson, Phys. Rev. Lett. 34, 953 (1975).
2. R.A. Street and N.F. Mott, Phys. Rev. Lett. 35, 1293 (1975).
3. Y. Toyozawa, Tech. Rept. ISSP, Tokyo, Ser. A. No. 1112 (1981).
4. D. Adler and E.J. Yoffa, Phys. Rev. Lett. 36, 1197 (1976).
5. M. Kastner, J. Non-cryst. Sol. 31, 223 (1978).
6. M.H. Cohen, H. Fritzshe and S. R. Ovshinsky, Phys. Rev. Lett. 22, 1065 (1969).
7. M. Kastner and H. Fritzsche, Philosophical Magazine 13 37, 199 (1978).

8. M. Kastner, D. Adler and H. Fritzshe, Phys. Rev. Lett. 37, 1504 (1976).

9. S. Ovshinsky, Phys. Rev. Lett. 36, 1469 (1976).

10. J. Orenstein and M. Kastner, Phys. Rev. Lett. 46, 1421 (1981).

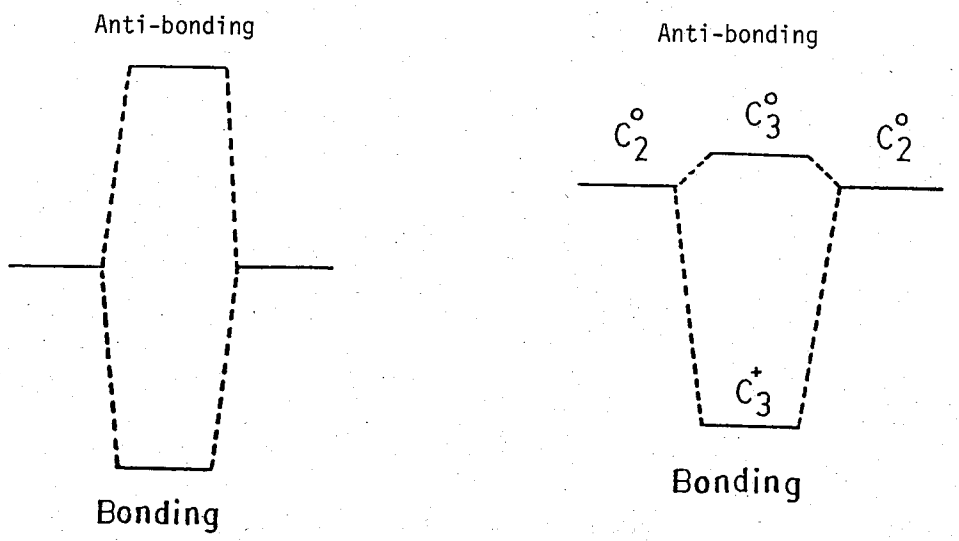

(a) Two-p-orbitals of chalcogenide atoms with energy at E=0 (valence band) may at normal bonding distance combine to form one bonding orbital and one anti-bonding orbital (conduction band).

(b) Two lone pair orbitals from near atom are too close (but still larger than normal bonding distance), thus their energy is higher and located in the gap. However, these two orbitals may also combine to form one bonding orbi and one anti-bonding orbital, but wit less seperation between the energy le

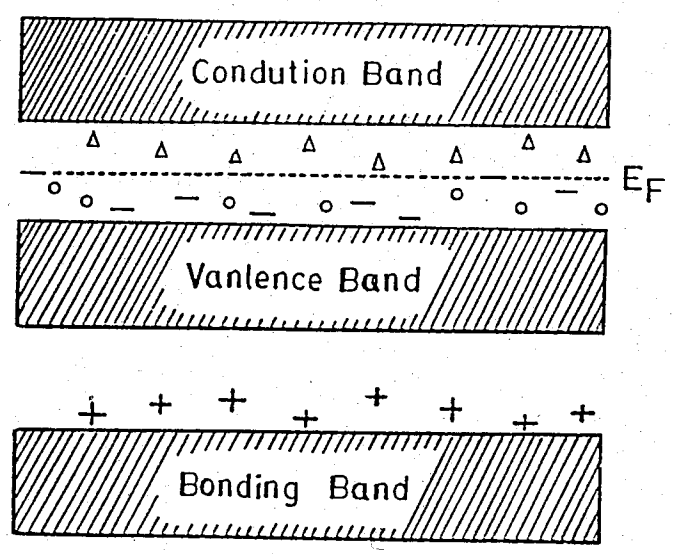

(c) Spatial location of species and its highest occupied energy level. - indicates the C_1^- defect states in the gap, + indicates the C_3^+ defect states in the gap, o indicates the neutral defect states (C_2^o with strain) in the gap, and Δ indicates un-occupied anti-bonding states.

SPECIFIC HEAT STUDY OF Ni-Cu ALLOYS NEAR THE CURIE TEMPERATURE

Shang-Kai Lee
Physics Department, Fu Jen University
Taipei, Taiwan, R.O.C.

Yeong Der Yao and Chun Chiang
Institute of Physics, Academia Sinica
Taipei, Taiwan, R.O.C.

ABSTRACT

The specific heat of nickel-copper alloys containing 0.0, 4.6, 9.3, 14.0 and 18.8 at.% Cu has been studied near the Curie temperature. The effective critical exponents of specific heat were analyzed using a simple power law; our results show that the value of the effective critical exponents depends on the concentration of impurities. Higher-order correction techniques are definitely necessary for analyzing the universality and symmetry of the critical exponents of specific heat.

1. INTRODUCTION

Recently the studies of transport properties near critical points are considerably increased[1-2]. The singularities in various thermodynamic quantities near the critical point are described by the critical exponents. Critical exponents have usually served as the common meeting ground between experiments and theories; the power-law analysis of the critical behavior has been widely studied both experimentally and theoretically[3-5]. However, different analyzing technique always produces different results. Up to now, much attention has been drawn to the universality of these critical exponents and some other parameters. Theretically, systems with the same number of degrees of freedom of the order parameter and with the same dimensionality should belong to the same universal class.[6] Experimentally, the thermal, electronic and other background terms besides the singularities are quite difficult to treat accurately.

The critical exponent "β"[7] and the electrical resistivity[8] of nickel-copper

alloy system have been studied near the Curie temperature before. The specific heat of nickel copper alloys has been measured by Pawel and Stansbury,[9] however, their experimental data does not allow to do the critical exponent analysis. For pure nickel, the specific heat near the Curie temperature has been reported by Handler et al[10], they found that $\alpha = 0.0 \pm 0.1$ and $\alpha' = 0.3 \pm 0.1$ for $-3.2 \leq \log|\varepsilon| \leq -1.5$; Connelly et al[11] reported that $\alpha=\alpha'=-0.10\pm0.03$ for pure single-crystalline Ni; recently, the specific heat of Ni-Cu alloys with the Cu concentration less than 9.6 wt% has been studied by Papp[12]. He concluded that if the experimental data is analyzed with higher-order correction terms in the Ni-Cu system, the impurity (Cu) does not alter the critical behavior of the universal parameters. In this study, we report further research works on the critical exponent behavior for the Ni-Cu system with the Cu concentration up to 20 wt%; and only the results of the effective specific heat critical exponents analyzed by means of the simple power law are discussed. The studies of using the correction to scaling etc. will be not included in this report.

2. EXPERIMENTAL CONSIDERATIONS

Specific heat were measured in the neighborhood of the corresponding magnetic transitions on Ni-Cu alloys containing 0.0, 4.6, 9.3, 14.0 and 18.8 at% Cu. The samples of these meterials were prepared from the original arc-melted ingots used in the electrical resistivity work described elsewhere[8]. Specific heat data mere obtained using a Perkin-Elmer differential scanning calorimeter, DSC-4. A system 4 microcomputer controller was used to program the DSC-4 from an initial temperature to a final temperature. The heating rate used was 6K per minute. The specific heat data of Ni-Cu samples were calibrated by the standard specific heat of sapphire (Fig. 1). This procedure is desired for the maximum achievable accuracy in specific heat determinations.

Our specific heat data were analyzed with the following simple power-law equations:

$$C(T) = A\varepsilon^{-\alpha} + B \qquad T < T_c \qquad (1)$$

$$C(T) = A'\varepsilon^{-\alpha'} + B' \qquad T > T_c \qquad (2)$$

where $\varepsilon = |T/T_c - 1|$ is the reduced temperature, T_c is the Curie temperature. A, A', B, B', α and α' are constants.

3. RESULTS AND DISCUSSION

Fig. 2 shows the specific heat data of five Ni-Cu samples near their Curie temperature. However, owing to the rounding effect of the transition, our data near the maximum point were excluded. As a quantitative measure of this rounding, we chose the temperature interval about 1K in which our data were excluded from the fitting analysis. Within this temperature range, the Curie temperature was chosen by the criterion of the best fitting. The values of T_c are 629.9K, 578.0K, 526.7K, 475.5K and 424.6K for Ni-Cu alloys containing 0.0, 4.6, 9.3, 14.0 and 18.8 at% Cu, respectively. This is not the same value of T_c determined by different method[7,8]; however, the difference is small. As shown in Fig. 3 and Table I, it is evident that T_c decreases linearly with a slope of 10.9K per at% of Cu.

By differentiating Eqs. (1) and (2) and taking logarithms, a series of linear fits were made by computer; and by varying the T_c as a parameter in the linear fitting, we obtained the best fitting of $\log \frac{\Delta C}{\Delta T}$ versus $\log \varepsilon$. Figs. 4 and 5 plot the $\log \frac{\Delta C}{\Delta T}$ versue $\log\varepsilon$ for all the Ni-Cu samples in the temperature range of $T<T_c$ and $T>T_c$, respectively. The slope of these curves determines the critical exponents α and α'. The values of α and α' as well as T_c are summarized in Table I. Our data shows that $\alpha \neq \alpha'$ for all the samples except Ni-4.6 at% Cu sample. The values of α and α' varies significantly with the concentration of Cu. This means that we did not excluded the effects besides the magnetic contribution. The specific heat, C, measured is exact the specific heat at constant pressure, C_p, which can be presented by:

$$C_p = C_m + C_L + C_e + V\beta^2 T/K \qquad (3)$$

where C_m is the magnetic contribution at constant volume, C_L is the lattice contribution, C_e is the normal electronic term and the last term is the lattice dilation term resulting from the lattice expansion (where V is the molar valume, β is the volume thermal expansivity, and K is the isothermal compressibility). After differentiating with the temperature, the temperature dependent terms besides the magnetic

contribution are not excluded.

Further analyses basing on the higher-order correction are definitely necessary for analyzing the universality and symmetry of the exact critical exponents. Those works will be reported elsewhere.

ACKNOWLEDGEMENTS

The authors are grateful to the National Science Council of Republic of China fo the financial support of this work.

Table I: The Curie temperatures and critical exponents determined experimentally fo Ni-Cu samples

Sample	T_c(K)	α	α'
Ni	629.9	-0.08	-0.16
Ni-4.6 at% Cu	578.0	-0.16	-0.16
Ni-9.3 at% Cu	526.7	-0.24	-0.17
Ni-14.0at% Cu	475.5	-0.38	-0.21
Ni-18.8at% Cu	424.6	-0.36	-0.27

REFERENCE

1. K.G. Wilson, Rev. Mod. Phys. 55, 583 (1983).
2. M.C. Chang and J.J. Rehr, J. Phys. A 16, 3899 (1983).
3. L.P. Kadanoff, W. Gotze, D. Hamblen, R. Hecht, E.A. S. Lewis, V.V. Palciauskas M. Rayl, J. Swift, D. Aspres and J. Kane, Rev. Mod. Phys. 39, 395 (1967).
4. M.E. Fisher, J. Appl. Phys. 38, 981 (1967).
5. S.K. Ma, Modern Theory of Critical Phenomena, W.A. Benjamin, Inc. (1976).
6. M.E. Fisher, Rev. Mod. Phys. 46, 597 (1974).
7. E.E. Anderson, S. Arajs, A.A. Stelmach, B.L. Teham and Y.D.Yao, Phys. Lett. 36 173 (1971).
8. Y.D. Yao and J.H. Tsai, Chinese J. Phys. 16, 189 (1978).
9. R.E. Pawel and E.E. Stansbury, J. Phys. Chem. Solids, 26, 607 & 757 (1965).
10. P. Handler, D.E. Mapother and M. Rayl, Phys. Rev. Lett. 19, 356 (1967).
11. D.L. Connelly, J.S. Loomis and D.E. Mapother, Phys. Rev. B3, 924 (1971).
12. E. Papp, Phase. Trans. 3, 177 & 197 (1983).

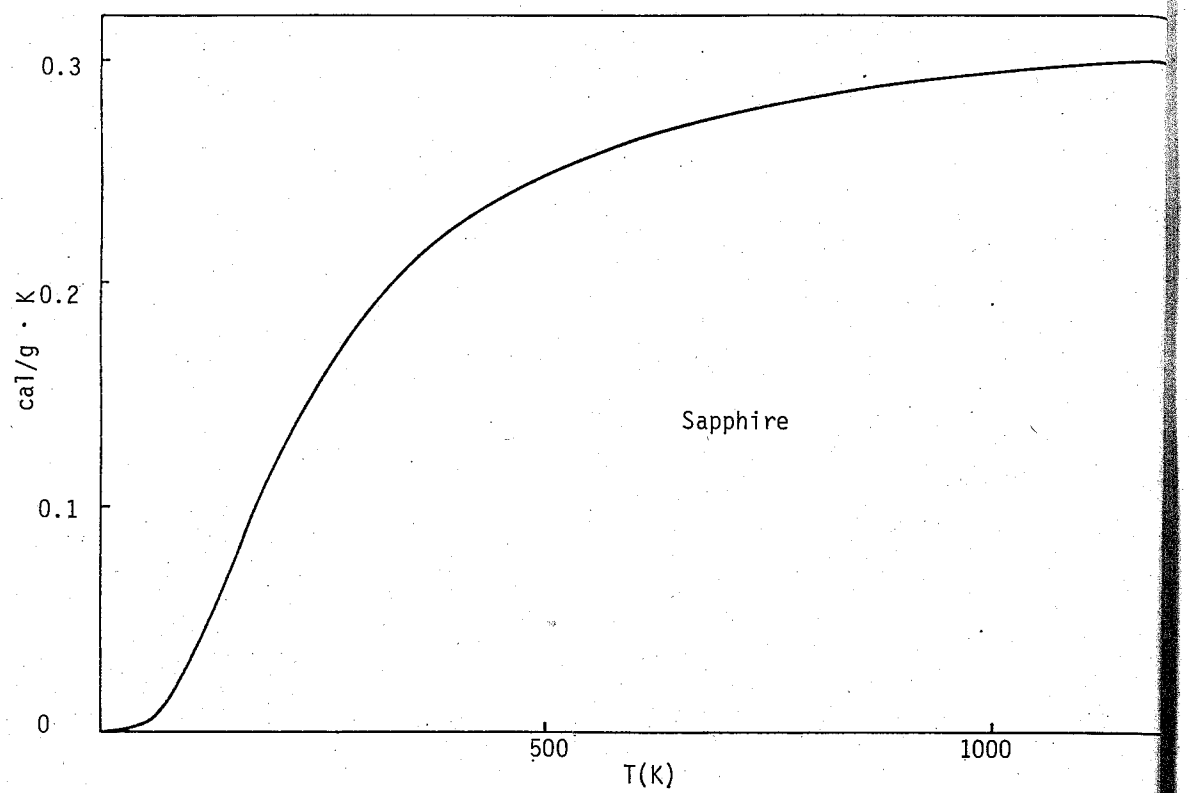

Fig. 1. The specific heat of sapphire used for standard.

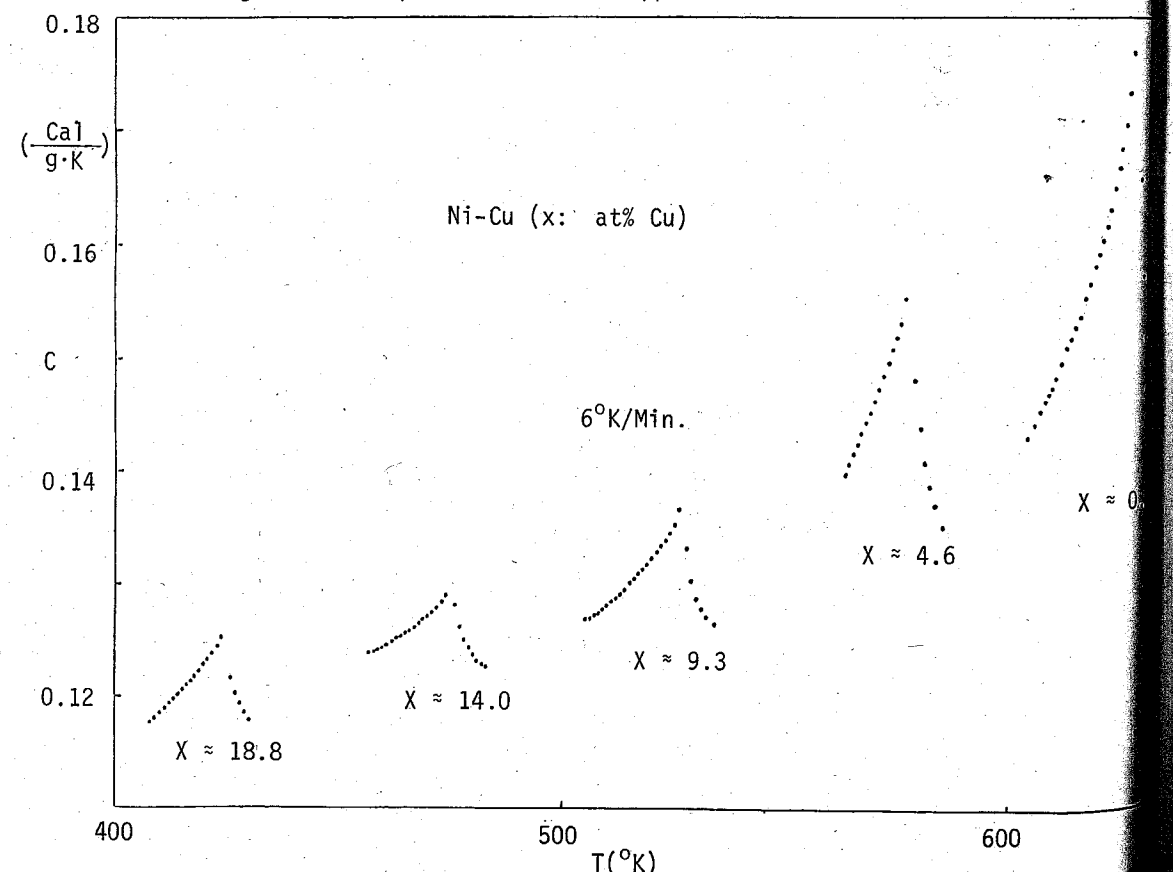

Fig. 2. The specific heat of Ni-Cu samples near the Curie temperature.

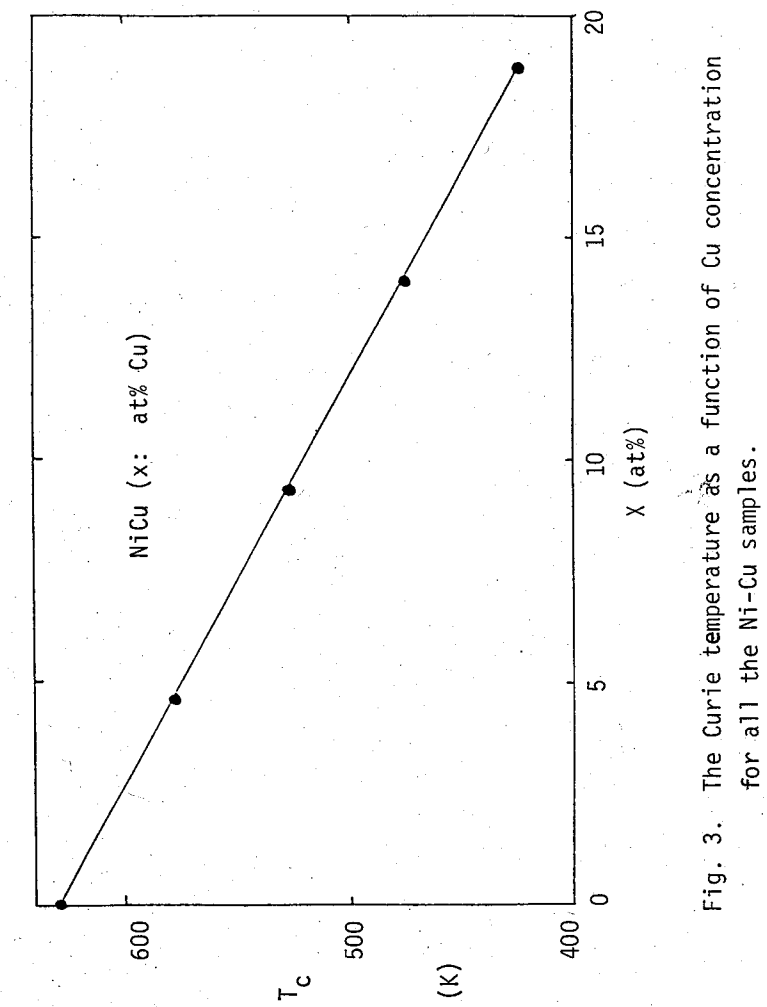

Fig. 3. The Curie temperature as a function of Cu concentration for all the Ni-Cu samples.

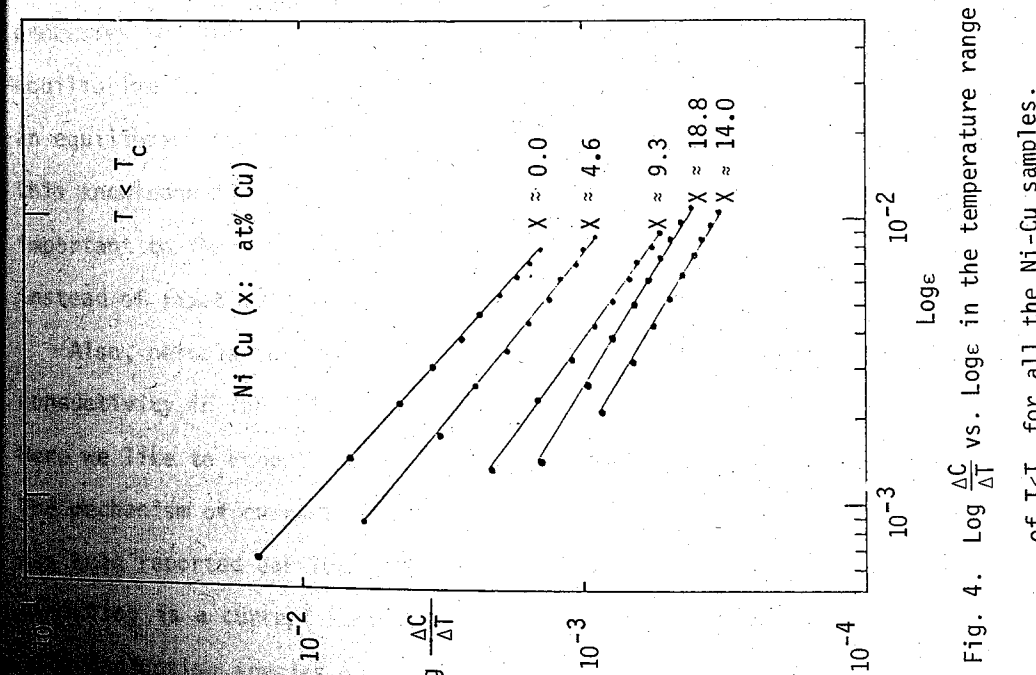

Fig. 4. Log $\frac{\Delta C}{\Delta T}$ vs. Logε in the temperature range of $T<T_c$ for all the Ni-Cu samples.

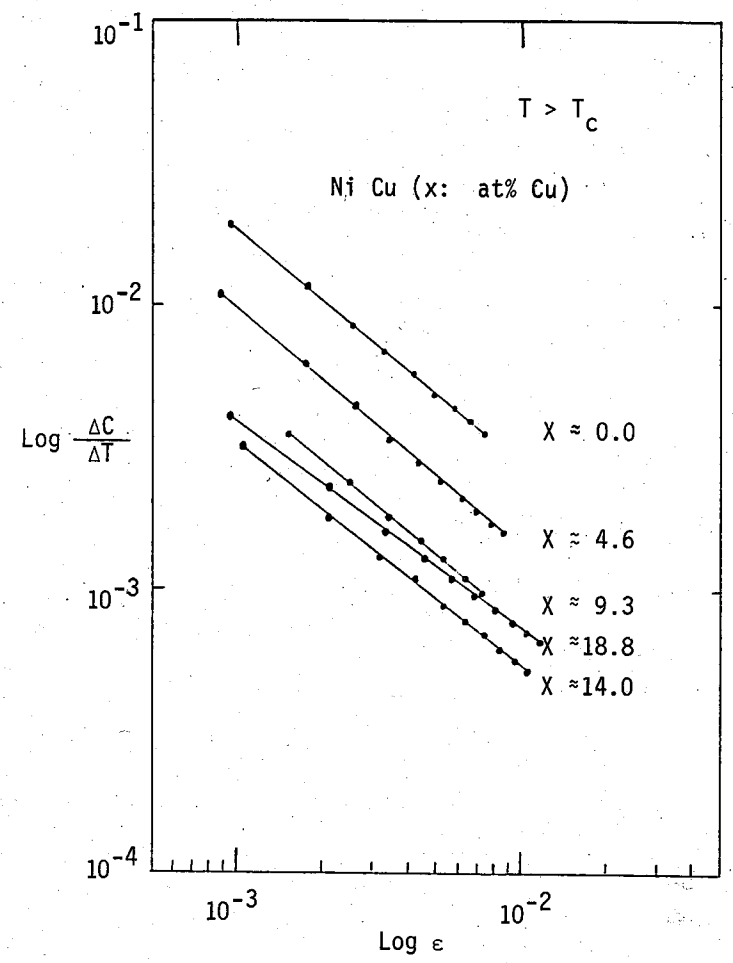

Fig. 5 Log $\frac{\Delta C}{\Delta T}$ vs. Logε in the temperature range of $T > T_c$ for all the Ni-Cu samples.

CURRENT CONTROLLED PERCOLLATION AND SWITCHING PROCESS IN AMORPHOUS THIN FILMS

Chun Chiang and Y. D. Yao
Institute of Physics, Academia Sinica
Nankang, Taipei, Taiwan 115
Republic of China

ABSTRACT

When performing in a constant current condition, amorphous films is observed to show a jump during switching for the first time. This is explained by suggesting that fragmental filaments of high conducting species are induced by the current. When these spikes in fregmental filaments make contact, conductivity drops sharply. Further growth in size of the filament will futher increase the conductivity and lower the voltage and make the differential resistance negative.

Switching[1] in amorphous thin films is a very interesting and important phenomenon. In recent years, intensive investigation has been directed to this phenomenon (for example, see Ref. 2-3); usually, the experimental design imposes a dynamical stimulus processes to the films such that the static switching process or switching process in equilibrium is masked. Specifically, the knowledge of the exact shape of I vs. V in an equilibrium condition is important for elucidation of the switching phenomenon and this knowledge is lost in the dynamical experimental design. For this purpose, it is important to find the exact resposes of the film under each constant current step, instead of fixed voltage step or voltage ramp condition.

Also, percolation process is an interesting and important phonomenon. Usually the conductivity in thin films is determined by the percolation of the back-lone bonds[4-8]. Here we like to report a percolation process of conductivity controlled by current. The mechanism of current controlled changing of conducting species in thin film matrix has been reported earlier[9, 10]. Evidence is given in this report that process of switching is a current controlled percolation process from low conducting species to high conducting species.

The sample we used came from Energy Conversion Devices, Inc. which has composition of $Si_{18}Ge_7As_{35}Te_{40}$. A large resistor ($10^3\Omega$) is in series with the sample, and a precision DC current source (Model CS-12, North Hills Electronics, Inc.) provides a stable current in discret steps. The I vs. V curve is shown in Fig. 1. There are several distinct regions which can be identified in the curve. (a) non-linear OFF region accessible by both increasing and decreasing the current. (b) non-linear OFF region accessible only by increasing the current. (c) Sudden change of voltage indicated by dotted lines. (d) Non-linear negative resistance region, current increasing. (e) Normal linear resistance. (f) Non-linear negative resistance region, current decreasing. (g) Sudden change of voltage. Regions (c) and (d) or (f) and (g) are what we normally mean to be the switching. This diagram may also be replotted with I/V vs. I as shown in Fig. 2. Corresponding regions are indicated in the figures. We interpreate the various regions of conductivity using percolation of conducting species (black area) in Fig. 3 as follows:

(a) This is the region where the current initiates some isolated spheres of higher conductivity and growth of number and size of these spheres to be fragmental filaments.

(b) Further growth and advancement of spikes of the filaments.

(c) The spikes or fragmental filaments start to make contact with the most advanced filament which may already reach the other end of the film. Render and Brooks[4], and Watson and Leath[5] have observed these jumps in analogue experiments, these jumps are more apparent if the matrix is a directed percolating system. In our amorphous films, no polarity effect should be expected; however, since the high conducting species are initiated by the unitary direction of flow of the current by electronic impact and chemical reactions[10], certain amount of directional preference is also expected.

(d) The region where the filaments will further growth in size with current and voltage is further dropped; the differential resistance is negative.

(e) This is the region where the filaments will not further grow with current and normal ohm low is observed.

(f) This is similar to region (b) except that it is exhibiting itself in the decreasing current case. A hysteresis phenomenon is apparent. The reason for this

s that it is not a perfectly equilibrium situation. In inducing the high conducting pecies, a higher than equilibrium current is required, whereas in reducing the high onducting species, a lower than equilibrium current is required to make the transiion.

(g) This is the region where the connected filaments are broken and the conducivity drops. This is similar to region (c) except that the required current is less.

Sometime in our experiments, the voltage not only shows one jump, instead, two umps may be observed. This is shown in Fig. 4. This can be explained by the fact hat in the high conductivity filament formation process, the spikes not only make ontact once, instead, two contacts are made. In the analogue and computer simulaion[4], indeed, more than one jump in conductivity is observed.

In conclusion, we show for the first time that switching in amorphous thin films as a discontinueous jump in voltage when the experiment is performed in a constant urrent condition. This jump is interpreted to be the current controlled percolaion process of high conductivity Species. Existing literatures suport this view.

ACKNOWLEDGEMENT

We are greatful to Prof. F. U. Wu and Prof. H. Henisch for helpful discussion nd to Energy Conversion Device, Inc. for the supply of switching devices through he curtesy of Prof. H. Henisch.

REFERENCE

1. S.R. Ovshinsky, Phys. Rev. Lett. 21, 1450 (1968).
2. D. Adler, H. Henisch and N. Mott, Rev. Mod. Phys. 50, 209 (1978).
3. A. Waren, IEEE, Trans. Electron Devices 20, 123 (1973).
4. S. Render, J.S. Brooks, J. Phys. A 15, L605 (1982).
5. B.P. Watson and P.L. Leath, Phys. Rev. B 9, 4893 (1974).
6. B.J. Last and D.J. Thouless, Phys. Rev. Lett. 27, 1719 (1971).
7. D. Adler, L.P. Flora and S.D. Senturia, Solid State Comm 12, 9 (1973).
8. S. Kirkpatrick, Phys. Rev. Lett. 27, 1722 (1971).
9. [illegible] Chrang, Phys. Lett. 99A, 453 (1983)
10. [illegible] Chrang, Phys. Lett. 101A, 106 (1984).

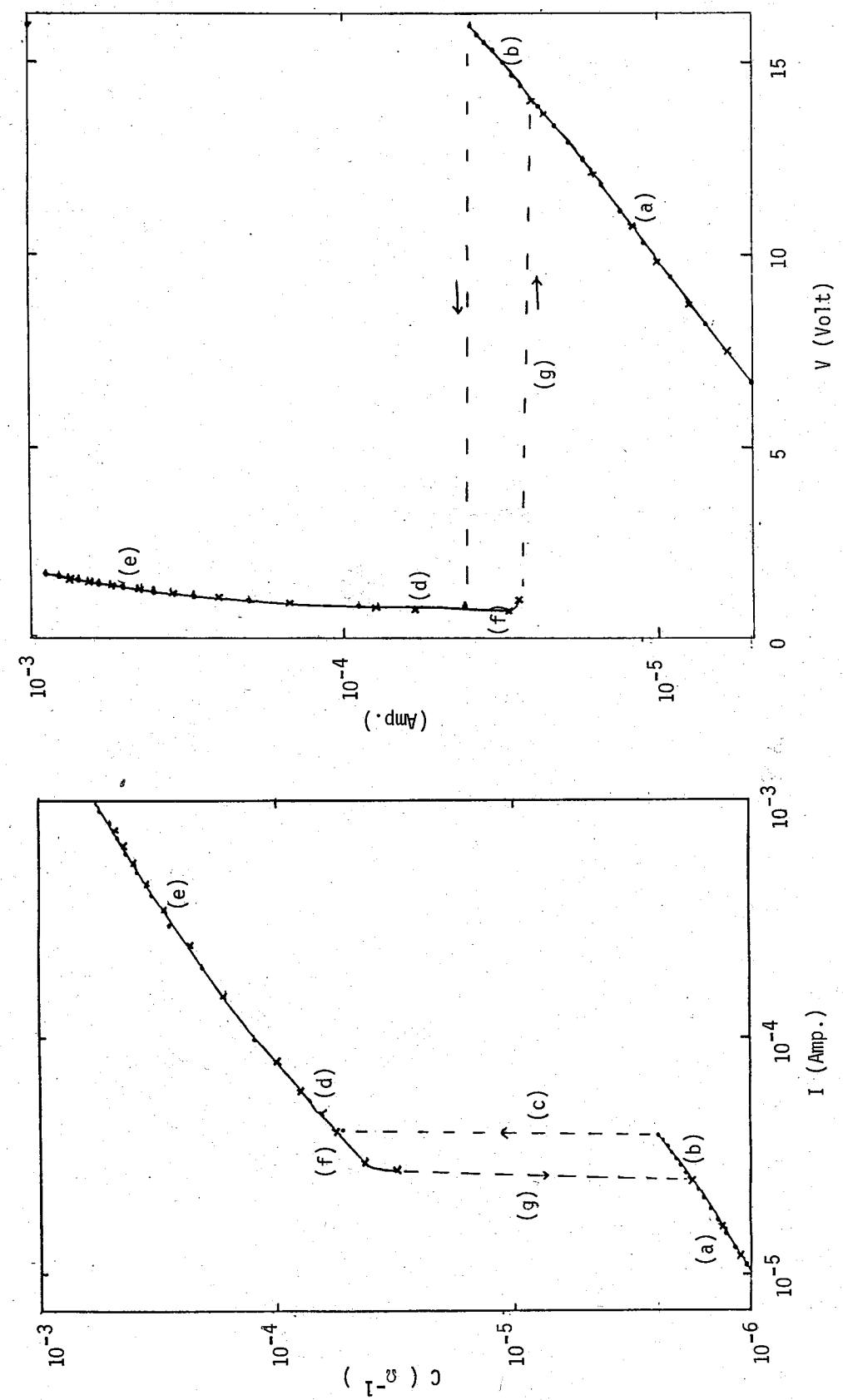

Fig. 1. Current vs voltage curve of amorphous thin films.
Regions (a) to (g) are discussed in text.

Fig. 2. Conductivity vs current curve of amorphous thin films.

Seperate islands of high conducting species.

Fragmental filaments make progress and spikes are formed. Conductivity increases.

Fragmental filaments make contact and conductivity jumps up.

Further growth of filament and the differential resistance is negative.

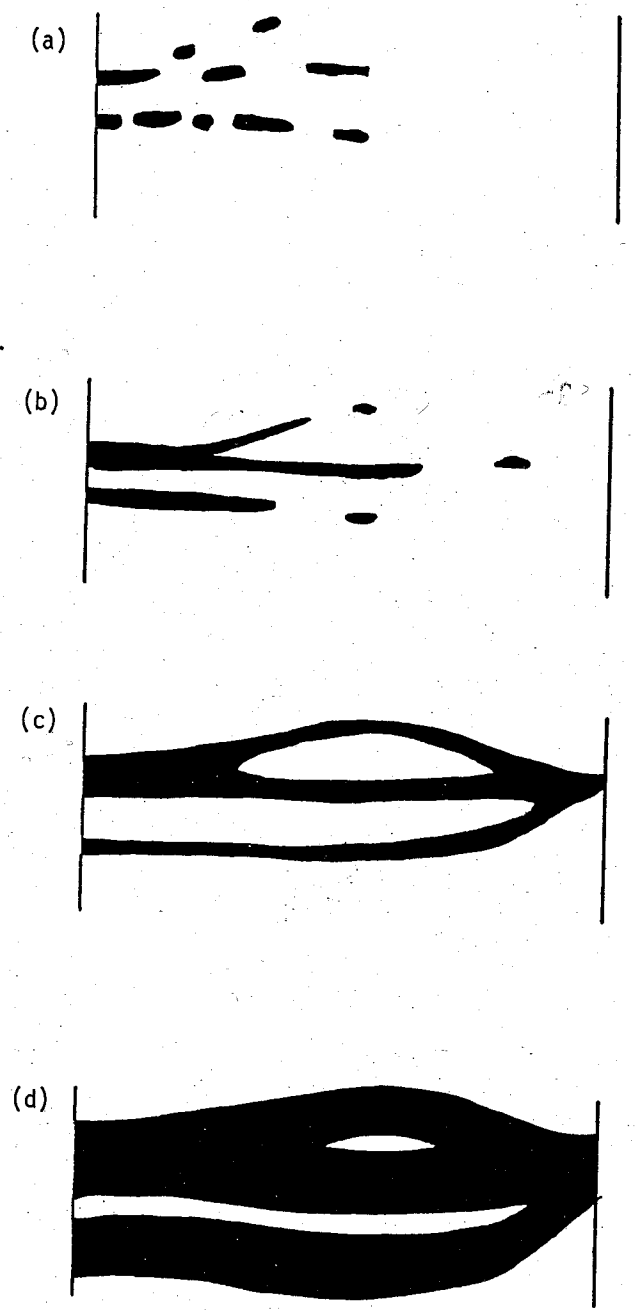

High conducting species (black area) formed in different stages corresponding to Fig. (1) and Fig. (2).

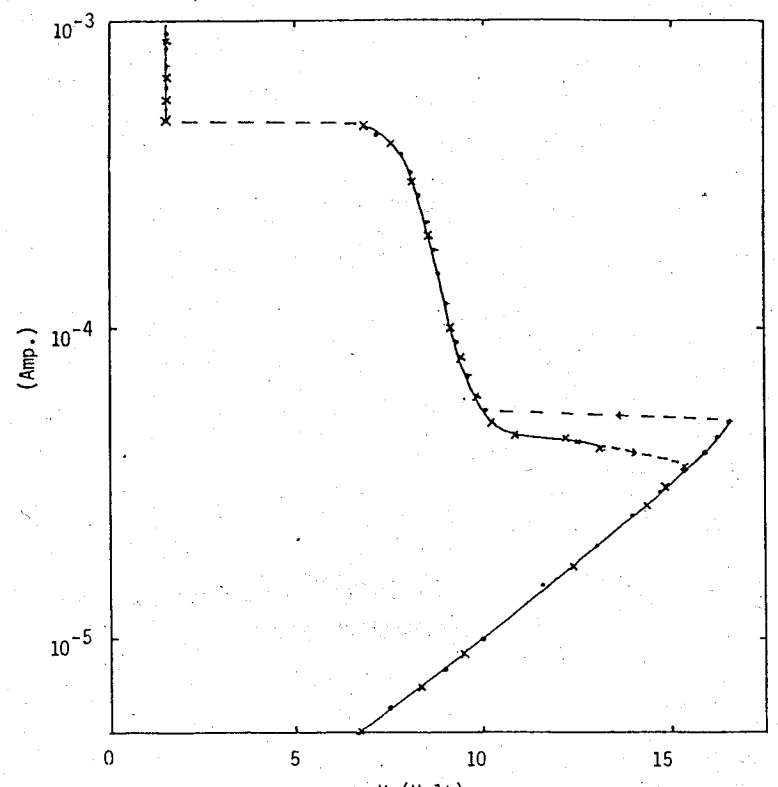

(a) I vs V curve.

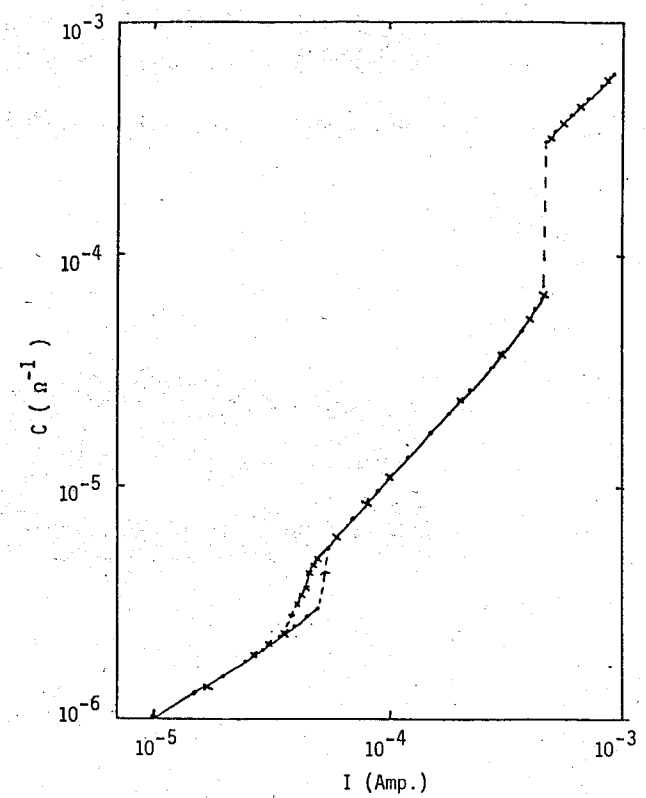

(b) C vs I curve.

Fig. 4. More than one Switching or jump is often observed.

EFFECTIVE SPECIFIC HEAT CRITICAL EXPONENT STUDY OF Cr-Fe ALLOYS

S. U. Jen, Y. D. Yao, and C. L. Liu[+]

Institute of Physics, Academia Sinica,

Taipei, Taiwan, R.O.C.

ABSTRACT

Simple power law is used to study the effective specific heat critical exponent "α" of Cr-Fe alloys containing 0, 2.3, and 4.9 at% Fe near the Neel temperatures. The fitting of data is reasonable only over a restricted temperature regions either above or below the temperature at which the specific heat exhibits its maximum value. By varying the Neel temperature T_N and from the least rms deviation fitting, we have determined the values of α and T_N etc. Our result shows that the transition temperatures of those alloys are 308.9 K, 256.9 K, and 231.5 K respectively. Also, our data show that $\alpha \neq \alpha'$ for a given concentration. This is not consistent with the universiality. The correction to scaling technique will be used for further studies.

1. INTRODUCTION

Recently, there has been much experimental and theoretical effort toward understanding of the critical phenomena.[1-9] In this paper, we present the result of the effective critical exponent of the specific heat studies of polycrystalline Cr and Cr-Fe alloys containing 2.3- and 4.9 at% Fe near the antiferromagnetic transition.

For the fit of the specific-heat data in the vincinity of the critical point, we first use the simple power low. The temperature dependence of the sepcific heat should be of the form,

$$C = A\varepsilon^{-\alpha} + B, \qquad T > T_N \qquad (1)$$

$$C = A'\varepsilon^{-\alpha'} + B', \qquad T < T_N \qquad (2)$$

where A, A', B, B', α and α' are constants, $\varepsilon = |1 - T/T_N|$, T_N is the Neel temperature. The critical region, over which Eqs. (1) and (2) should be valid, is typically small usually a value of $\sim 5\times10^{-2}$ was taken. Further, if we consider correction to scaling specific-heat data, the specific heat is of the form,

$$C = A\varepsilon^{-\alpha}(1 + D\varepsilon^{X}) + B, \qquad T > T_N \qquad (3)$$

$$C = A'\varepsilon^{-\alpha'}(1 + D'\varepsilon^{x'}) + B', \qquad T < T_N \qquad (4)$$

the term $D\varepsilon^x$ represents the lowest order correction to scaling. In fitting the dat we imposed the scaling constraints $\alpha = \alpha'$, $x = x'$, and $B = B'$, which follows from t renormalization-group theory.

2. EXPERIMENT AND ANALYSIS

The specific heat data of three Cr-Fe samples containing 0, 2.3, and 4.9 at% Fe were quoted from the drawings sent by Prof. Arajs; and those data have been publish already[10]. We checked these results by measuring the specific heat of pure Cr wi a differential scanning calorimeter, Perkin-Elmer DSC-4 model. It is clearly seen that there is a peak in each specific curve. This is an indication of antiferromag tic transition. The corresponding value of the temperature at the peak is consider as T_{max}. As noticed, T_{max} decreases as the concentration of Fe in the sample decr For the sake of better analysis, we drew a smooth curve through data points in the temperature regions both $T < T_{max}$ and $T > T_{max}$.

As a preliminary analysis of the data, we adopt a method using the derivative the specific heat. This method has an advantage of reducing the number of variabl in fitting the critical data[6]. From Eqs. (1) and (2), we have variables A, A', α', B, B', and T_N. By taking the temperature derivative of the asymptotic forms and (2) in temperature ranges $T > T_{max}$, $T < T_{max}$, and the values of ε being rough $3\times10^{-3} \leq |\varepsilon| \leq 10^{-2}$, we obtain,

$$\frac{dC}{dT} = \left|\frac{\alpha A}{T_N}\right| \varepsilon^{-(1+\alpha)} \qquad (5)$$

Therefore, variables B and B' have been eliminated.

From eq.(5), a log-log plot of $\frac{dC}{dT}$ vs ε will produce a limear curve with a slope of $-(1+\alpha)$. If the data are numerically differentiated, the best linear fit a log-log plot can be determined by varying only one variable T_N in the temperatu range near T_{max}. The critical exponents α and α' are determined from the slope o this best fit. Once we know α, α' and T_N, variables B and A can be determined fr substitution of the data points into equation (1), and B' and A' determined from equation (2).

For the detailed-analysis work, we have set up computer programs to complete the rocedures stated above. During this analysis, since there are two groups of data, e., those for $T > T_N$ and those for $T < T_N$, we obtain the total deviation by adding the deviation of the $T > T_N$ data and the deviation of the $T < T_N$ data for each T_N. hen, we find out as we change the value of T_N, there exists a minimum value for the otal deviation. Our results are shown in Fig. 1 to Fig. 3. We chose that T_N, which orresponds to the minimum total deviation, as the Neel temperature of the system. t the same time, the effective critical indices α and α' could also be determined rom the slope specified for that T_N.

3. RESULTS AND DISCUSSION

In our preliminary analysis, the Neel temperature, T_N, is chosen by the criterion the minimum value of the total least rms deviation, $\sigma_T = \sigma_{T<T_N} + \sigma_{T>T_N}$. The values f T_N for these alloys are 308.9K, 256.9K and 231.5K, respectively; it is not exactly he same value of T_{max}, which was chosen to be the Neel temperature by Kemeny et al[10] he values of the effective critical exponents α and α' determined from the above nalysis are listed in Table 1. As an example, we plot $-\ln\frac{dC}{dT}$ vs $-\ln\varepsilon$ in the tem- erature range of $T < T_N$ for the Cr-2.3 at% Fe sample in Fig. 4. The constants, A, A', and B' in Eqs. (1) and (2) were determined from a best fit after finding the values f T_N, α and α'. All these values are summarized in Table 1.

The above results show that $\alpha \neq \alpha'$ for each sample; also, the ratio of the critical mplitudes, $\frac{A}{A'}$, varies in an unexpected way. Therefore, the results for the critical arameters are very unsatisfactory from the theoretical point of view. Here we must otice that there exist quite large electrical resistivity and specific heat anomalies hich have been observed[10, 11] in these alloy system near the magnetic transitions. he avalanche effect for Cr-Fe alloys containing 3 to 4 at% Fe was interpreted by emeny et al[10] as the attribution of a nucleation controlled phase transition from etastable magnetic state. These large anomalous behaviors may imply that the ef- ective critical exponents may include some other physical terms except the term for antiferromagnetic system. However, as far as we know, this is the first time effective critical exponents of the specific heat near the Neel temperature system is analyzed. There is no other value of α can be compared with for

the Cr-Fe system.

Our results show that the critical exponents are not consistent with the unive sality which was expected by theoretical point of view and also has been observed some other systems[3]. Therefore, further analysis for the specific heat of the C Fe system with the correction terms D and D' in equations (3) and (4) is required; more accurate experimental data are definitely needed. At present, we have tried only the first step to analyze the data with Eqs.(3) and (4) and with the scaling constraints. It determines the values of α, B, and T_N. The next step is to deter A, A', D, D', and X by fitting the data. Once we know all the values of the param ters, we can compare the results with the theoretical prediction. For the complet ness of analysis, we shall show the result from the correction to scaling method i the forthcoming publication.

Table 1. The Neel temperatures and the critical specific-heat parameters obtaine using the simple power law.

	Cr	Cr-2.3 at% Fe	Cr-4.9 at% F
T_N(K)	308.9	256.9	231.5
α	0.34	-0.21	0.021
α'	0.024	-0.084	0.015
A ($\frac{Cal}{g.k}$)	4.65×10^{-4}	-0.068	0.35
A'($\frac{Cal}{g.k}$)	0.021	-0.093	0.38
B ($\frac{Cal}{g.k}$)	0.11	0.13	-0.28
B'($\frac{Cal}{g.k}$)	0.087	0.17	-0.30

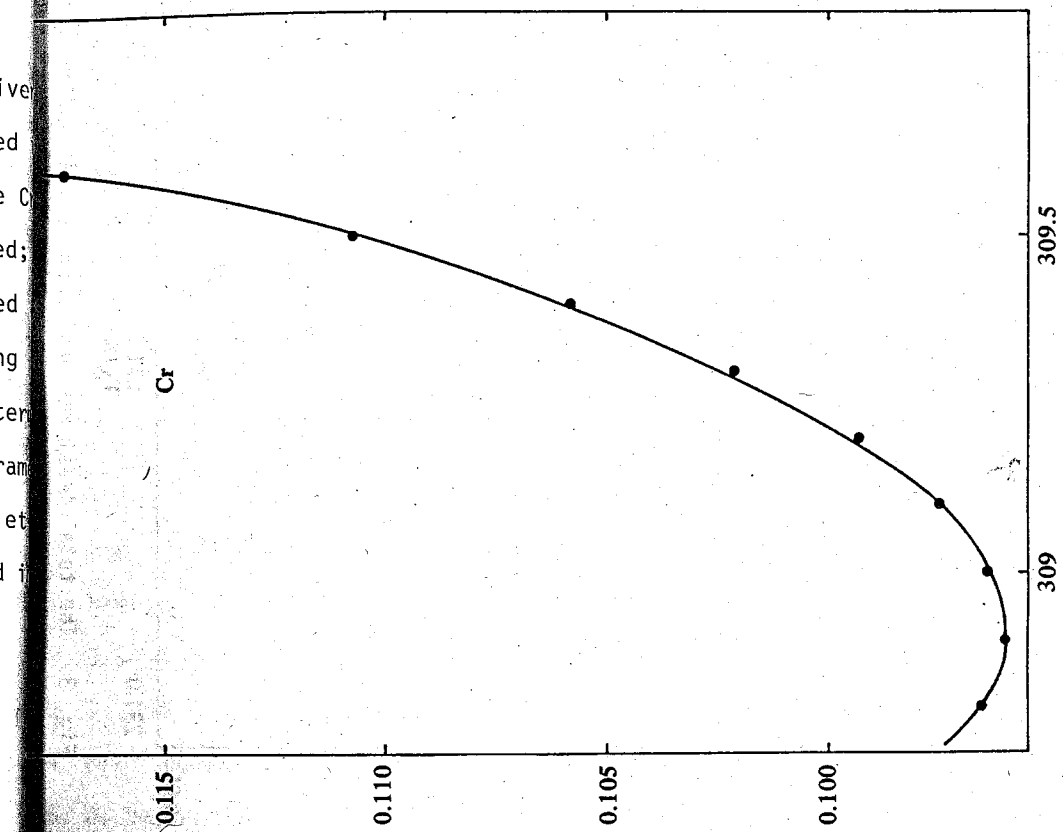

Fig. 1. The total least rms deviation, α , as a function of T_N for pure C_r.

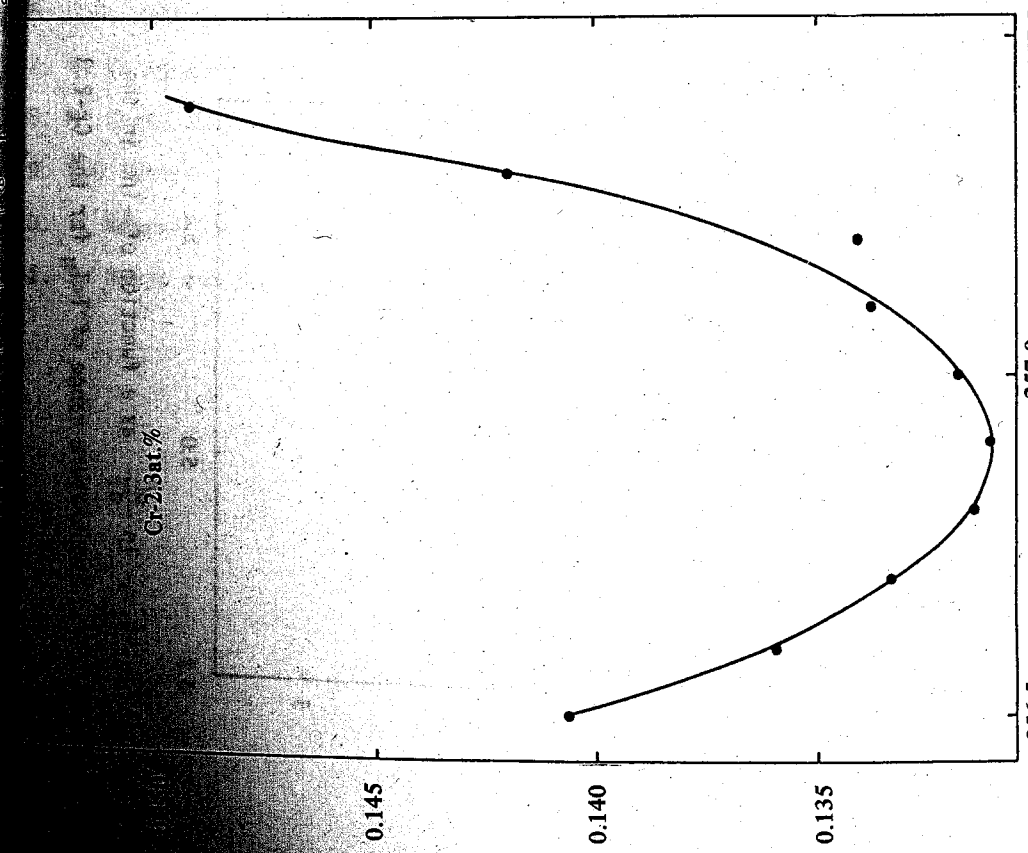

Fig. 2. The total least rms deviation, α_T, as a function of T_N for Cr-2.3 at% Fe.

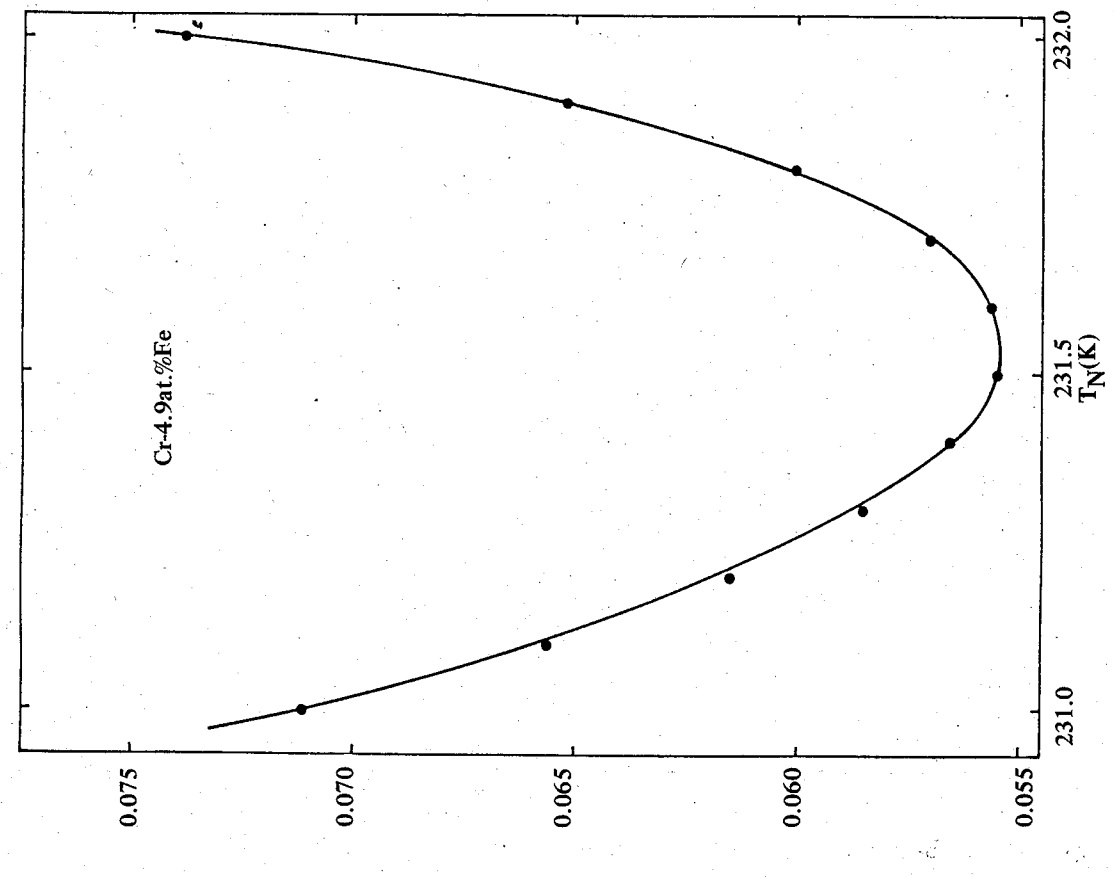

Fig. 3. The total least rms deviation, σ_p, as a function of T_N for the Cr-4.9at.% Fe alloy.

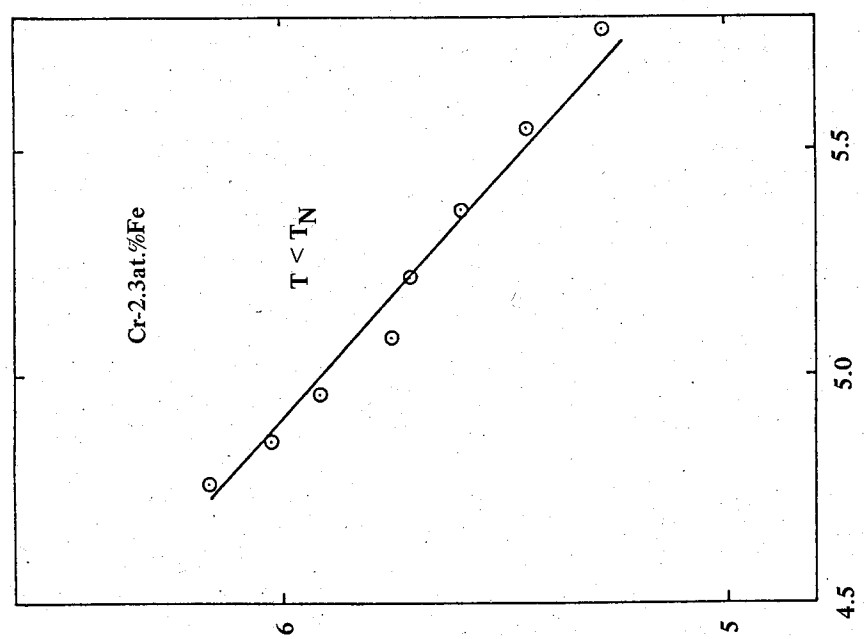

Fig. 4. - ln $\frac{dC}{dT}$ as a function of -lnε in the temperature range of $T<T_N$ for the Cr-2.3

ACKNOWLEGEMENT

The authors are grateful to the National Science Council of Republic of China for the financial support of this work.

Comment: + Mr. Liu is a undergraduate student of Physics Department, Center University, Chung-Li, Taiwan, R.O.C. Mr. Liu helped us to do the computer analysis work during his summer vacation in 1984.

REFERENCE

1. L.P. Kadanoff, W. Fotje, D. Homblen, R. Hecht, E.A.S. Lewis, V.V. Palciauskas, M. Rayl, J. Swift, D. Aspres and J. Kane, Rev. Mod. Phys. 39, 395 (1967).
2. G.S. Dixon and J.E. Rives, Phys. Rev. 177, 871 (1969).
3. J.E. Rives and D.P. Landau, Phys. Rev. B17, 4426 (1978).
4. D.T. Teaney, Phys. Rev. Lett. 14, 898 (1965).
5. J. Skalyo, Jr. and S.A. Friedberg, Phys. Rev. Lett. 13, 133 (1964).
6. J.J. White and J.E. Rives, Phys. Rev. B6, 4352 (1972).
7. M. Chang and A. Houghton, Phys. Rev. Lett. 44, 785 (1980).
8. M. Chang and J.J. Rehr, J. Phys. A: Math. Gen. 16, 3899 (1983).
9. K.G. Wilson, Rev. Mod. Phys. 55, 583 (1983).
10. T. Kemeny, B. Fogarassy, S. Arajs and C.A. Moyer, Phys. Rev. B 19, 2975 (1979).
11. S. Arajs and G.R. Dunmyre, J. Appl. Phys. 37, 1017 (1966).

A THERMAL INVESTIGATION OF THE PHASE TRANSITIONS IN SOLID CARBON TETRABROMIDE

*W. S. Tse, Y. D. Yao and W. W. Lin**
Institute of Physics, Academia Sinica,
Taipei, Taiwan 115 R.O.C.

ABSTRACT

The heat capacity at constant pressure of CBr_4 has been measured as a function of temperature T between 298 K and 343 K. A first-order phase transition is observed. The transition temperatures determined from both endotherm and exotherm curves are about 320 K and 308 K, respectively. The enthalpy of this phase transition is about 1,398 cal/mole.

1. INTRODUCTION

Carbon tetrabromide is an interesting molecular crystal for the study of libra-
tional dynamics in the four phases which are characterized by a varying degree of
orientational order /1-3. Below its freezing point (365K), CBr_4 forms the disordered
"plastic" crystal (CBr_4 I) in which the centre of mass of the tetrahedral molecules
occupy the sites of a face-centred cubic lattice /4/, but their orientations remain
largely disordered. A first order transition occurs near 320K and the crystal trans-
forms to an orientational-ordered monoclinic structure (CBr_4 II) with space group
$C2/c$ and 32 molecules per unit cell /5/ which is stable at room temperatures.
Another monoclinic phase (CBr_4 III) exists at higher densities, that is, at lower
temperatures and elevated pressures /2, 3/. Two studies /6, 7/ had been made of the
thermodynamic properties of CBr_4 but their values reported for the enthalpies of the
transition (I-II) and heat capacity values disagreed significantly. It thus seemed
worthwhile to re-examine the behaviour of the phase transitions of CBr_4 from plastic
to ordered monoclinic phase II carefully with a precision Differential
calorimeter in the temperature range 298-343K.

Physics, Tamkang University, Tamsui, Taipei Hsien, Taiwan (251), R.O.C.

2. EXPERIMENTAL CONSIDERATION

A commercial Differential Scanning Calorimeter, Perkin-Elmer DSC-4 model, was used to carry out the measurements under a flow of dry nitrogen. It was calibrated frequently with indium metal. Aluminum sample containers loaded with 10-20mg of the sample was used for measuring the heat capacity and the enthalpy of the transition from CBr_4 I to CBr_4 II. Each scan in this work was limited to a span of 45K so that the uncertainty of interpolating the base line from isothermal conditions from both ends of the measurement were minimized. The heating rate used was 5 K/min. and the absolute accuracy in Cp was about 5%. The specific heat was calibrated by the standard heat capacity of ultra pure copper /8/ of different masses.

3. RESULTS AND DISCUSSION

Typical results of endotherm and exotherm of CBr_4 are shown in Figure 1. A single first-order phase transition is observed and the extrapolated onset phase transition temperature from many independent measurements is 320 K. Several determination of the enthalpy associated with the phase transition are made and the mean value is 1398.2 cal/mol. This heat of transition has been determined by Marshall et al /6/ with 1594.5 cal/mol and also by Frederick and Hildebrand /7/ with a value of, 1420 cal/mol by adiabatic calorimeter. The results of measurements of enthalpies of transition in this work and previous results are summarized in Table. The agreement between our result and Frederick and Hildebrand is reasonable considering that different physical methods have been used. The transition also shows a hysteresis between heating and cooling which indicated a first order component to the phase transition. Besides, from the endotherm curve, where the transition region is narrow and a large ΔH value obtained, indicates also a first-order phase transition.

The heat capacity from 298K to 343K are also listed in Table 1 and are plotted in Figure 2. These measurements show a rapid and sharp transition typical of usual first-order phase transitions. The heat capacity before and after the transition may be represented by a simple proportionality to the temperature as

$$Cp = (0.354)\ T$$

where Cp and T are in units of J/K/mol and K respectively. From Table 1, it shows that the high value of Cp at 320K is due to a "pretransition" effect instead of 317.6K as reported by Marshall et al /6/. The average values obtained by Marshall et al for Cp below the transition are about 27 J/mol/K larger than our results. However, their average values of Cp above the transition are mere or less the same as our results. It seems that the Cp values recorded by Frederick and Hildebrand /7/ could possibly to be too large.

It should be noted that Marshall's measurements on Cp were carried out in an adiabatic calorimeter and was calibrated by Cp values of water. Frederick and Hildebrand employed the differential measurements on Cp and the heat capacity of the calorimeter was determined by means of a copper rod. In this work a commerical made precision differential scanning calorimeter was used and high accurated standard calibration materials were used, so that a more precise results should be obtained.

This research was supported by a grant from the National Science Council of the Republic of China.

REFERENCES

/1/ Y. Ebisuzaki, Intern. Conf. on Lattice Dynamics, Paris (1977).

/2/ J. Timmermans, J. Phys. Chem. Solids. 18, 1 (1961).

/3/ P. W. Bridgman, Collected Experimental Papers, Harvard University Press, Cambridge, Ma., (1964).

/4/ M. More, J. Lefebvre and R. Fouret, Acta Crystallog. B, 33, 3862 (1977).

/5/ M. More, F. Baert and J. Lefebvre, Acta Crystallog. B, 33, 3681 (1977).

/6/ J. G. Marshall, L. A. K. Staveley and K. R. Hart, Trans. Faraday Soc., 52, 19 (1956).

/7/ Frederick and Hildebrand, J. Amer. Chem. Soc., 61, 1555 (1939).

/8/ CRC Handbook of Chemistry and Physics, 61ST ed. (1981).

Table 1.

Molar heat capacity (in J/mol. K) and Enthalpy of transition (in Cal/mole) or CB

(1) Cp (J/mole K)

T(C)	Cp	T	Cp	T	Cp	T	Cp	T	
27.5	97.271	45	109.936	51.88	567.527	56.25	121.905	61.5	125
30.0	98.023	45.5	110.315	52.5	321.807	56.88	121.933	62.5	126
32.5	100.368	46	113.313	53.13	186.849	57.5	121.906	63.5	127
35.0	102.102	46.5	139.776	53.75	130.582	58.13	122.390	65	128
37.5	10 .006	47	322.757	54.38	122.835	58.75	122.714	67.5	130
40.0	105.497	47.5	600.465	55.0	121.854	59.38	123.521	70	134
42.5	106.579	50	1095.527	55.63	121.881	60.0	123.849		

(2) ΔH (cal/gm)

4.096	4.074	4.347	.156	4.225	4.399

mean value: 4.216 cal/gm = 1398.18 cal/mole

Marshall et al (1955) ΔH = 1594.5 cal/mole

Frederick and Hildebrand (1939) ΔH = 1420 cal/mole

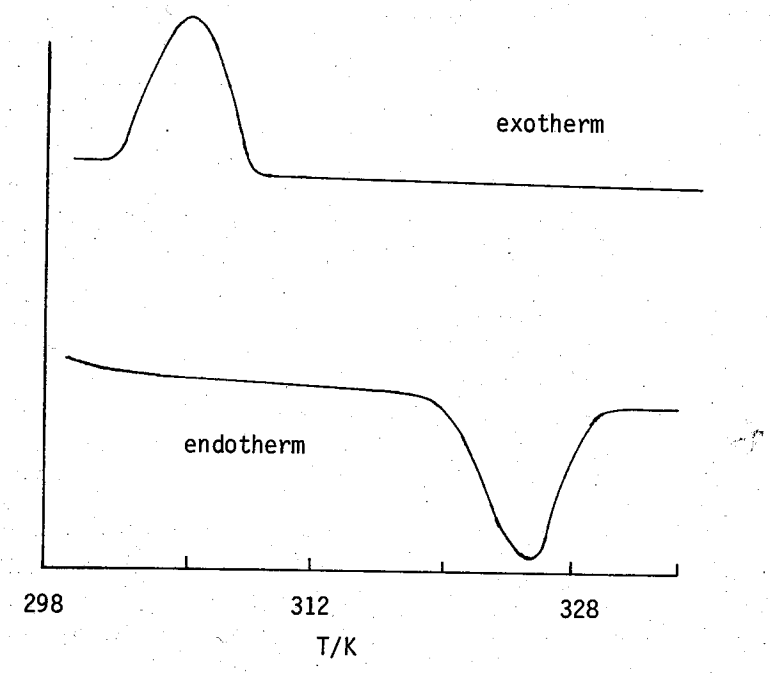

Figure 1. Endotherm and Exotherm of CBr_4

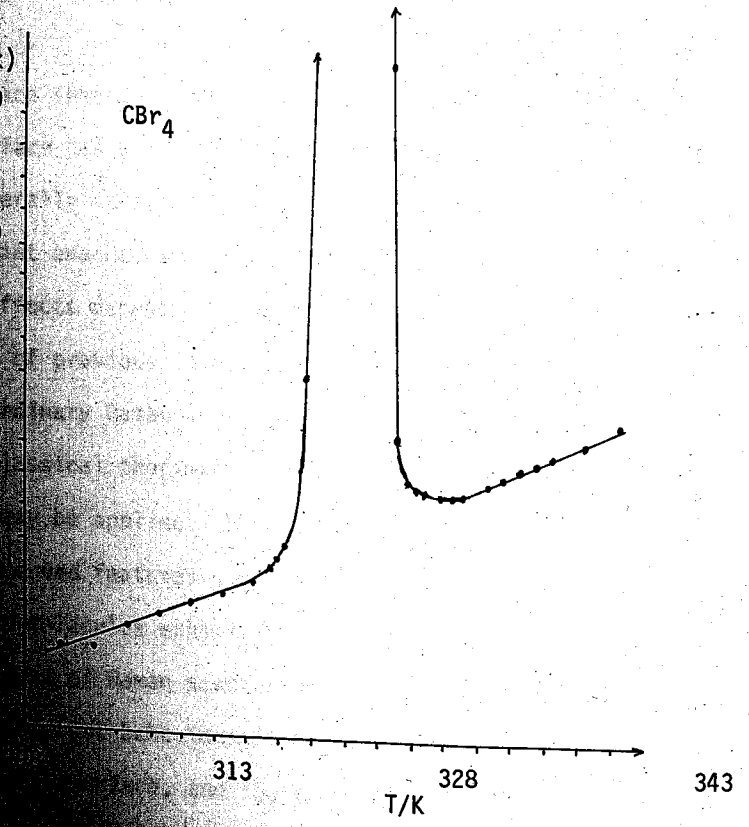

Molar heat capacity Cp of solid Carbon Tetrabromide

RESONANCE RAMAN SCATTERING FROM CRYSTAL VIOLET DEPOSITED ON ROUGH Ag FILMS

Y. C. Chou
Department of Physics, National Tsing Hua University
Hsinchu, Taiwan 300, Republic of China

N. T. Liang
Institute of Physics, Academia Sinica
Nankang, Taipei, Republic of China

ABSTRACT

The observed thickness dependence and excitation profiles of the surface enhanced resonance Raman scattering (SERRS) from crystal violet (CV) on Ag films demonstrated the importance of surface roughness and chemical effects. A tentative argument based on the overlap between the molecular resonance and the excitable surface resonances could reasonably explain the observed excitation profiles.

1. INTRODUCTION

Surface enhanced Raman scattering (SERS) of molecules adsorbed on rough noble-metal surface has been extensively studied both experimentally and theoretically[1]. It is generally accepted that both electromagnetic (EM) and chemical effects contribute to the gaint enhancement ($X10^6$) in Raman cross section. The relative contribution of the two effects depends on the particular adsorbate-adsorbant system.

Most of previous investigations were focused on SERS from molecules, which show ordinary Raman scattering, adsorbed on rough metal surfaces. In this case the semi-classical treatment[2], regarding the adsorbed molecules as fluctuating dipoles, may be applied. Hence, the classical EM model successfully explained most of the observed features such as the large enhancement and the excitation profiles of the molecules exhibiting resonance Raman scattering, were the intermediate state of Raman scattering is a real electronic state, one might expect completely different behaviors from the ordinary SERS when molecules were adsorbed on the metal surface, and the quantum mechanical effects should be considered[1, 3]. Here we report dye molecules, which exhibit resonance Raman scattering, adsorbed

on rough Ag electrode has been reported by Jeanmaire and Van Duyne[4]. Recently Watanabe and Pettinger[5] and Burstein, Burns and Decol[6] reported SERS from crys violet (CV) adsorbed on the Ag surface. Both of their results showed that the influence of chemical effects on SERS due to strong interaction between CV and metal surfaces is substantial. We had studied the resonance Raman scattering from the crystalline phonon modes of Sb deposited on rough Ag films, where there were small or no chemical effects[7]. Continuing the interest in the enhancing effects of rough Ag filmes on the resonance Raman scattering, we carefully investigated the Raman spectra of CV adsorbed on island Ag films.

The main findings of our experiments were (a) the enhancement factor of a 60A film was at least 2 x 10^4, (b) the enhancing effect of a 60A Ag film was 5000 ti stronger than that of a continuous (200 Å) film, (c) the excitation profiles were different for various Raman modes (see Fig. 3), which could not be explained by t classical EM model, (d) the Raman intensities of CV deposited on the rough Ag fi were resonantly enhanced when the molecular resonance and surface electronic reso were overlapped, and (e) the vibronic coupling between excited states of CV for various Raman bands might be altered, as evidence in Fig. 3, when CV was chemical adsorbed on the rough Ag film.

2. EXPERIMENTS

The optical arrangement and film preparation were described in Ref. 7. The cident intensity was kept below 2 mW to reduce photodecomposition, however, a 10 decrease in Raman intensity was found for two subsequent runs with laser beam in cident on the same spot. CV was deposited on Ag films by putting a drop of 0.01 aqueous solution on the film, then the solution was spinned off after 2 minutes. Raman intensity was observed to be the same within the area covered by the drop. With this technique, the coverage was estimated to be roughly one monolayer. The Raman spectra of 1 mM CV solution in a very thin cell of thickness ~200 μm were as reference standard. The solution was renewed for every spectrum to avoid the change of concentration by photochemical effects. As a check of our experimenta apparatus, the excitation profiles of the resonance Raman scattering of the 1 m ageous solution normalized by the Raman spectra of $LiNbO_3$ was measured, and fo

o be the same as previously published data[8].

3. RESULTS AND DISCUSSION

Fig. 1 shows examples of Raman spectra for CV molecules adsorbed on the rough Ag m (Fig. 1(a)) and CV in aqueous solution (Fig. 1(b)). The spectra are the same as se observed in other laboratories. Small shifts in peak positions, such as 225 cm^{-1}, cm^{-1} and 1340 cm^{-1} were observed for CV deposited on Ag film, which was believed to influenced by the bonding between CV molecules and Ag films. Also more weak peaks e distinguishable in the spectrum of CV deposited Ag film than that of the CV solu-on, due to the enormous enhancement on the rough Ag film. For incident light of velength longer than 5682Å, the Raman spectra of CV solution superpose with lumi-scence. For CV deposited on rough Ag films (CV/Ag) the luminescence spectra were latively weak compared with the Raman spectra. However, the luminescence spectrum of /Ag was resonantly enhanced for the incident wavelength λ_{in} close to 6328Å, and was ch stronger than the Raman spectrum. This observation is contridict to that of tanabe and Pettinger[5], who claimed that the chemisorbed CV molecules was non-orescent.

The enhancement in the Raman cross section of 1620 cm^{-1} band of each molecule was least 2 x 10^4 at λ_{in} = 5145Å for CV deposited on rough Ag film. It is noted that hancement for different Raman modes were different, which was a fact that could not ccounted for by the classical EM model.

ness dependence:

The larger resonance Raman cross section of CV molecules and the enhancement due e presence of the Ag film make the measurements of thickness dependence possible e whole thickness spectrum. In this part of experiment, the films of various s were evaporated onto the same microscope slide and CV was deposited under process as described above, so that the thickness dependence could be studied mparison. The observed thickness dependence is shown in Fig. 2. Please ertical axis is in logrithmic scale. Such a sharp dependence on Ag not been reported. For example, Bergman et al[9] observed a 10X decrease for a increase in the film thickness from 60Å ato 128Å. As for our

observation, Raman intensity decreases by a factor of 1000 in the range between 60Å and 120Å. These results clearly demonstrate the importance of roughness in SERS. The strong thickness dependence might not be a characteristics of the surface enha resonance Raman scattering, since benzoic acid deposited on the same films gave th similar thickness dependence in the thickness range that SERS was observable.

Excitation profile:

Excitation profile gives important information to understand various mechanis which might contribute to the enormous enhancement in SERS[10]. To illustrated th effects of the rough Ag surface, we eliminated the resonant contribution from CV molecules by normalizing the Raman intensities of various peaks of CV deposited o the rough Ag surface with those of the corresponding peaks of 1 mM CV aqueous sol The results are shown in Fig. 3(a) and 3(b). The data were corrected for the abs tion of the CV aqueous solution. If the classical EM model could be applied to o system then the excitation profile would follow the expectation of the local plasm resonance of the rough Ag film[10]. Figs. 3(a) and 3(b) clearly did not reveal t expected EM effects of the rough Ag films. Hence, the interaction between the me surface and the adsorbed molecules must be considered. The common feature for al the Raman modes in Figs. 3(a) and 3(b) was that, in the long wavelength side, the was a strong peak close to 5682Å. For λ_{in} > 6328Å, the Raman spectra of CV solut were masked by fluorescence, so that the enhancement could only be measured for t Raman mode at 225 cm^{-1} and λ_{in} = 6471Å. However, in the short wavelength side, t Raman modes in Fig. 3(a) and Fig. 3(b) showed different wavelength dependence. B of the rising in Fig. 3(a) and the flatness in Fig. 3(b) in the short wavelengthi could not be accounted for by the classical EM model.

Before proceeding to analyze the observed excitation profiles, we first brie reviewed the work of Angeloni[8] et al., who studied the resonance Raman scatte of the CV solution in CH_3OH. They found that the dependence of Raman intensity o λ_{in} could be decribed by the vibronic coupling of the two energy states around 25 and 5400Å or by a Franck-Condon overlap allowed transition. For example, the Ra bands at 1180 cm^{-1}, 1590 cm^{-1} and 1620 cm^{-1} were caused by vibronic coupling bet the energy states at 2500Å and 5400Å, whereas the bands at 210 cm^{-1}, 1380 cm^{-1} a

14 cm^{-1} were a Frank-Condon overlap transition.

The adsorbed dye molecules were known to interact strongly with the rough metal substrate[11], hence, the electronic resonance of the rough films would couple strongly o the electronic and vibrational resonance of the molecules. This coupling would nhance the intermolecular electronic excitation of the adsorbate-adsorbant system, ence, as suggested by Burstein et. al.[6], would contribute to the Raman cross ection of the adsorbate-adsorbant system. Also, Nitzan and Brus[12] argued that he resonant excitation of molecules would be enhanced if the molecular resonance nd the excitable surface resonance overlapped. Thus, a tentative argument, that he overlap between the energy band (5400Å-5900Å) of the excited state of CV molecules nd the broad local surface plasmon resonance[13] of the rough metal film greatly increases the Raman cross section, might explain the broad peak arround λ_{in} = 5682Å in the excitation profiles in Figs. 3(a) and 3(b). The difference in the heights of he broad peaks among various Raman modes might be due to the difference in vibronic coupling of energy states of CV to which those modes belong.

According to the above argument, the rising of the Raman intensities of 1590cm^{-1} and 1180 cm^{-1} in the short wavelength region shown in Fig. 3(a) might be explained by the molecular energy state at 2500Å of CV overlapped with some kind of electronic esonance in the rough Ag film[12]. The argument could also explain the independence f the Raman cross section of the band at 920 cm^{-1}, because, from the analysis of ngelonl et. al., this band has nothing to do with the high energy state at 2500Å. owever, the argument could not, explain the behaviors of the Raman bands at 225 cm^{-1}, cm^{-1} and 1620 cm^{-1} these peaks showed trends in the short λ_{in} region different hose expected from the argument. The difference between the bands at 1590 cm^{-1} cm^{-1} was clearly demonstrated in the changes in the intensity ratio of the for various λ_{in}. This difference was puzzling because the two bands be- ordingly in solution.[8] Similar split in the dependence on λ_{in} was also for 420 cm^{-1} and 446 cm^{-1} Raman bands. One plausible possibility might be characteristics of chemisorption, the interaction between CV molecules surface changed the coupling between the energy states of CV molecules routes for the coupling[14]. Thus, the argument that the enhancement increased by the overlap of the molecular resonance and the electronic

resonance in the rough Ag film may not be rejected just because the above mentioned inconsistancy. Further studies on other adsorbate-adsorbant systems are in progress.

ACKNOWLEDGEMENT

We have profited from discussions with C. C. Chen, T. T. Chen, S. Y. Wang, and especially H. Chang, most of our experiments were finished in his laboratory. This research is supported by the National Science Council of the Republic of China.

REFERENCE

(1) R.K. Chang and T.E., Furtak, Surface Enhanced Raman Scattering (Plenum Press, New York) 1982.

(2) J. Gersten and A. Nitzan, J. Chem. Phys. 73 (1980) 3023.

(3) W.L. Peticolas, L.A. Nafie, P. Stein, and B. Fanconi, J. Chem. Phys. 52 (1970) 1576.

(4) R.P. van Duyne, in: Chemical and Biochemical Applications of Lasers, Vol. 4, ed. C.B. Moore (Academic Press, New York, 1979).

(5) T. Watanabe and B. Pettinger, Chem. Phys. Lett., 89, (1982) 501.

(6) E. Burstein, G. Burns and F.H. Dacol. Solid State Commun. 46 (1983) 595.

(7) N.T. Liang, T. T. Chen, H. Chang, Y.C. Chou, and S. Wang, Optics Lett. 8 (1983) 374.

(8) L. Angeloni, G. Smulevich and M. P. Marzocchi, J. Raman Spectry. 8 (1979) 305.

(9) J.G. Bergman, D.S. Chemla, P.F. Liao, A.M. Glass, A. Pinczuk, R.M. Hart, and D.H. Olson, Optics Lett. 6 (1981) 33.

(10) D.A. Weitz, S. Garoff, and T.J. Gramila, Optics Lett. 7 (1982) 168.

(11) S. Garoff, R.B. Stephens, C.D. Hanson, and G.K. Sorensen, J. Limin. 24/25 (1981) 773.

(12) A. Nitzan and L.E. Brus, J. Chem. Phys. 75 (1981) 2205.

(13) S. Yamguchi, J. of Phys. Soc. Japan, 15 (1960) 1577.

(14) R. Kotz and E. Yeager, J. Electroanal. Chem. 113 (1980) 113.

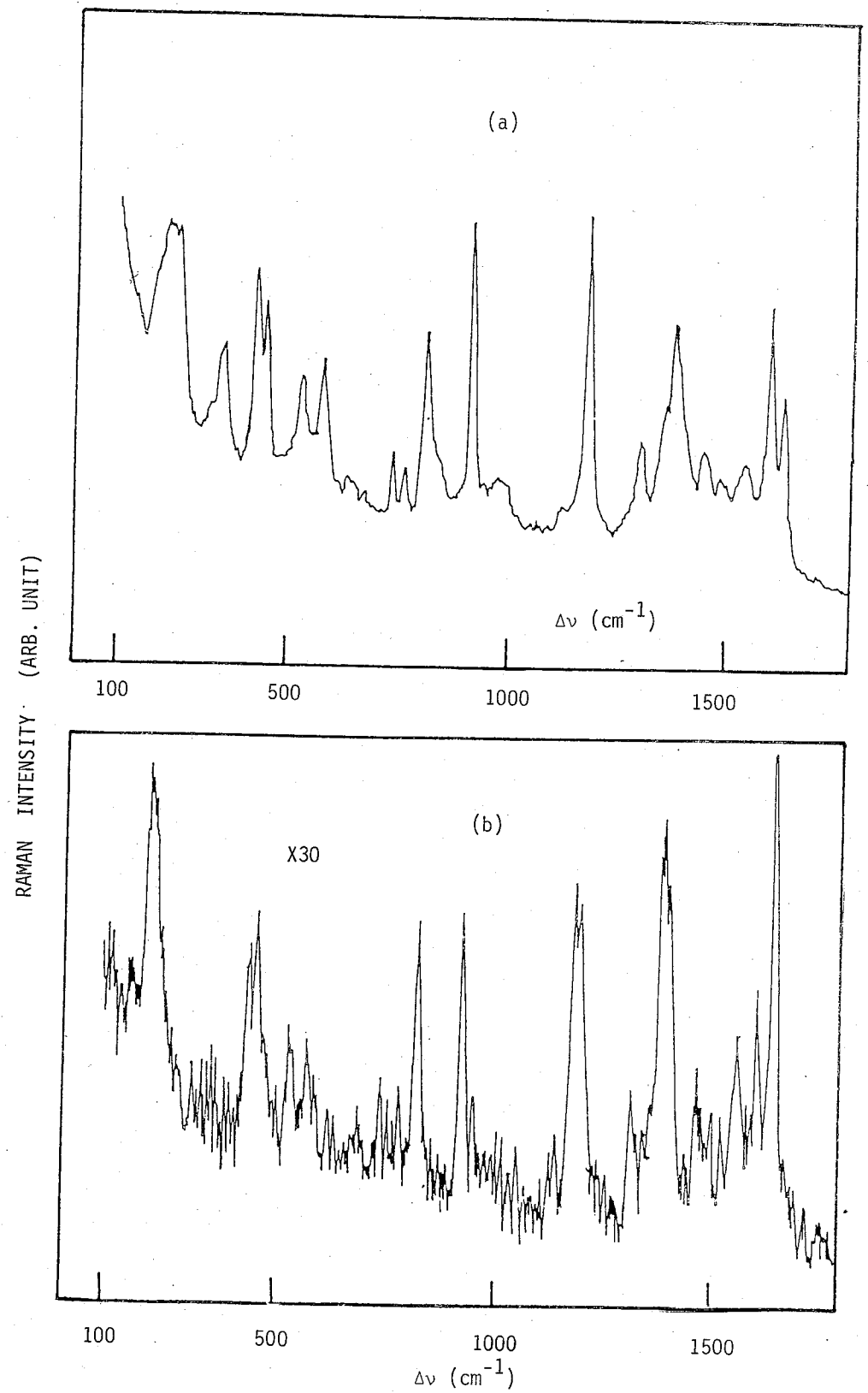

Fig. 1. Raman spectra of (a) CV molecules adsorbed on the rough Ag(60Å) film, and (b) 1 mM CV in the aqueous solution of ∿200 μm thickness, λ_{in} = 5145Å.

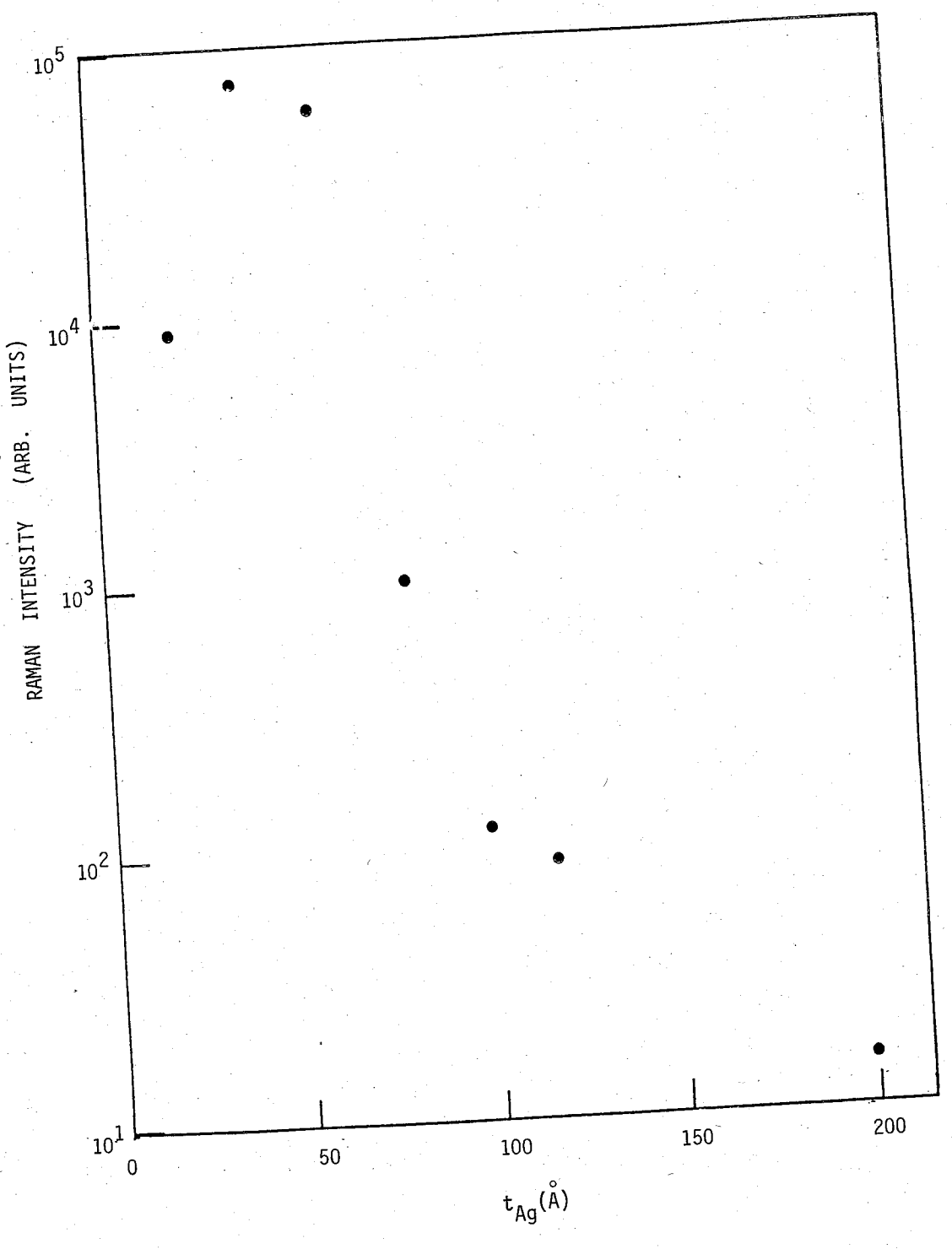

Fig. 2. Ag-film-thickness dependence of the Raman intensities at 1620 cm^{-1} of CV/Ag (60Å), λ_{in} = 5145Å.

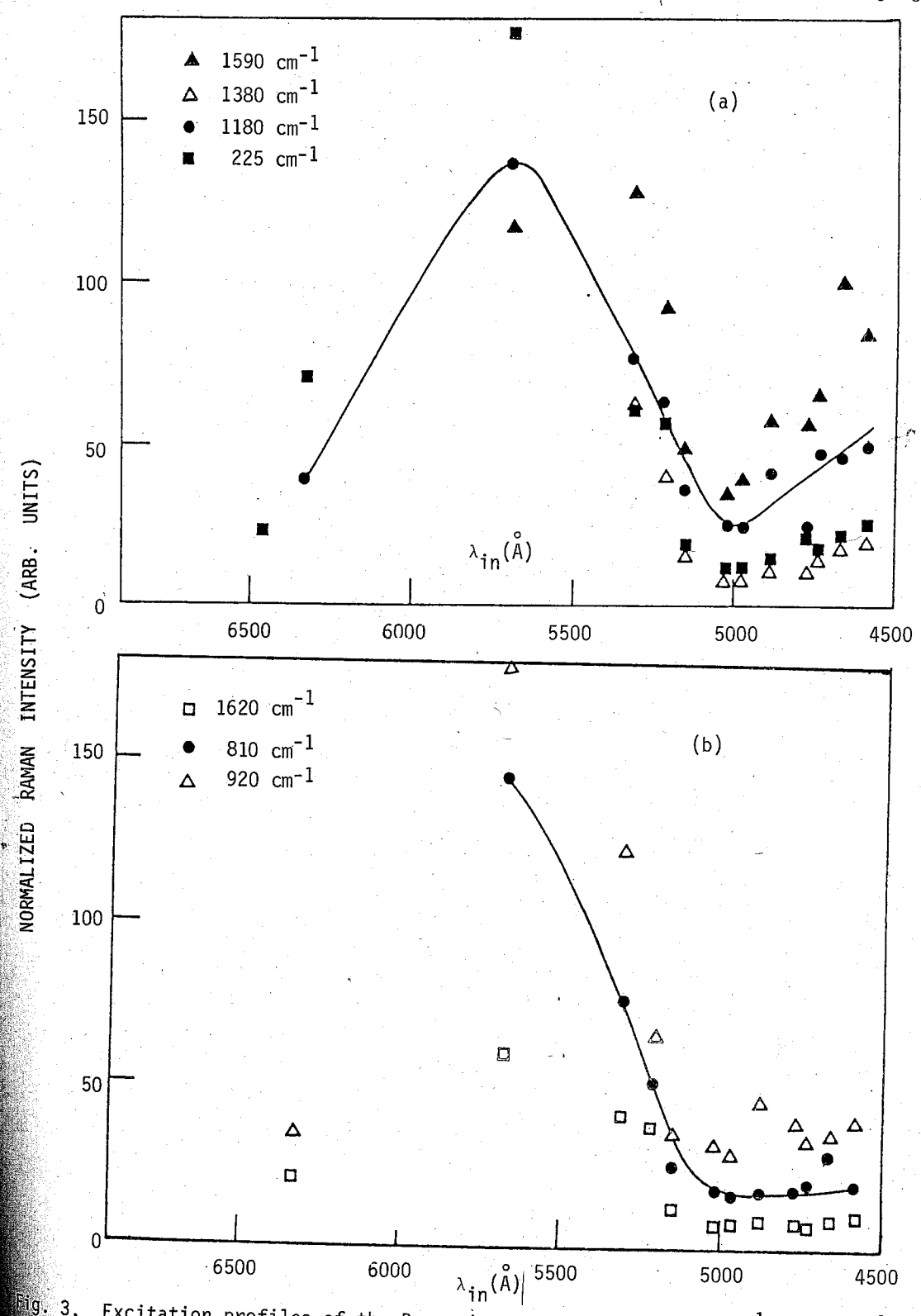

Fig. 3. Excitation profiles of the Raman intensities of (a) 225 cm^{-1}, 1180 cm^{-1}, 1380 cm^{-1} and 1590 cm^{-1} of CV/Ag(60Å), and (b) 810 cm^{-1}, 920 cm^{-1}, 1620 cm^{-1}. The data were normalized by the Raman intensities of the corresponding Raman bands of 1 mM CV aqueous solution. The lines in (a) and (b) are for easy visualization of the trend only.

EFFECT OF BROMOCRIPTINE AND HALOPERIDOL ON THE DOPAMINE AUTO-REGULATION

W.K. Wang, T.L. Hsu and Y. Chiang
Biophysics Laoratory, Institure of Physics, Academia Sinica,
Taipei, Taiwan, 115, Rep. of China

Biochemical, histochemical and behavioural studies indicate that the bromocriptine act as a postsynaptic dopamine receptor agonist (Corrodi et al 1973, Fuxe et al 1974, Johnson et al 1976, Loew, et al 1976). In the lower dose range it might preferentially activate dopamine presynaptic receptors (Di Chiara et al 1978, Fuxe et al 1974, 1978, Silbergeld and Pfeiffer 1978, Snider et al 1976). From our study, we found that bromocriptine (BCP) did activate the dopamine (DA) presynaptic autoreceptors in low doses. However, this effect was diminished when the doses were increased.

In contrast to bromocriptine, haloperidol (HD) (Anden et al 1964, Bochaert et al 1977, Carlsson and Lindqvist 1963, Clement-Cormier et al 1974, Miller et al 1974) has long been identified as an antagonist to DA postsynaptically. Some studies (Christiansen and Squires 1974, Iversen et al 1976) on synaptosomal preparation also showed that it antagonized the inhibitory effect of apomorphine (APO) which had been characterized as a DA agonist that preferentially bound presynaptic DA receptor, (Nagy et al 1978, Raiteria et al 1978). Nevertheless, we found that the HD would not antagonize DA auto-regulation. Its inhibitory effect and DA auto-inhibition were additive.

These evidences suggest that we might need to refine our terminology and separate the presynaptic and postsynatpic effect of drugs.

Sprague-Dawley rats (180-230g) were killed by decapitaiton. The corpus striatum was dissected on ice and homogenized in 10 vols 0.32 M sucrose using a Teflon pestle tissue homogenizer. After cnetrifugation at 1000g for 15 min. 50 μℓ aliquots of the synaptosome-containing supernatant were incubated with 150 μℓ physiological medium as

described before (Wang et al 1982), only some NaH_2PO_4 were replaced by $NaHCO_3$ to give final pH of 7.4 after equilibration with 95% O_2 - 5% CO_2 at 37°C. Bromocriptine Mesylate (2-bromo-alpha-ergocriptine) was first dissolved in alcohol then 10 μℓ solutions were added in the vials; dried at room temperature before the incubation medium was added, dopamine (DA), and haloperidol (HD) were added to the incubation medium with 10 μℓ 0.1 M phosphorous buffer pH 7.4 as carrier. DA formation was calculated from the $^{14}CO_2$ output from 1 - ^{14}C tyrosine, averaged over 60 minutes of incubation to 140 minutes of incubation. The rate of dopamine synthesis was about 60% of that at pH = 6.6. We shifted to this pH because it is a more physiological pH.

The concentration effect of BCP and HD on $^{14}CO_2$ release were summerized in table 1. BCP 10^{-8} M added to the incubation mixture had no significant effect.

BCP at 10^{-7} M reduced the $^{14}CO_2$ release to 83.8±2.5% (mean±S.D. from 4 preparations) of its normal rate.

Compares to the control, BCP at 1 x 10^{-5} M reduced the $^{14}CO_2$ release at the first 90 min. of incubation then increased the $^{14}CO_2$ release from the 100 minutes of incubation. The average amount of $^{14}CO_2$ release from 60 minutes to 140 minutes of incubation is 101.6±2.0%. The relative amounts of $^{25}CO_2$ released from the added tyrosine were shown in Fig. 1.

HD at 10^{-5} M reduced the $^{14}CO_2$ release to 76.2±2.9%. The effect was decreased when the concentration of HD was decreased. HD at 10^{-7} M had no significant effect. The data in table 2 showed that $^{14}CO_2$ released from the preparation with HD and DA compared to the one with HD along. The presence of HD did not change the auto-inhibition effect of DA (Only at HD (10^{-5}M) and DA (10^{-6} M) seemed to have slight blocking effect). Fig. 2 showed some of these data.

Our results show that the high dose of BCP had lower agonist activity at DA presynaptic receptors. Actually, BCP even showed some antagonist activity at DA presynaptic receptors with concentration up to 10^{-5} M.

Goldstein et al (1978) carried out experiments about the effect of bromocriptine on synaptosomal tyrosine hydroxylase activity by measuring the ^3H_2O amount which was produced by ^3H 3-5 tyrosine added. In their experiments the TH activity was inhibited 8.0±2.0% and 12.5±2.0% for bromocriptine concentration at 10^{-7} M and 10^{-6}M respectively. These results are not contradiction to our data. We also showed the

inhibition effect of bromocriptine at 10^{-7} M and 10^{-6} M, however the inhibition effect was decreased when the dose was increased, and we got no significant effect with 10^{-5} M. The slight but critical difference between our results and those of Goldstein et al may be due to the incubation conditions, ours seemed more physiologically and they did not show the effect of bromocriptine at 10^{-5} M either.

For haloperidol, it alone behaved like a DA agonist presynaptically. It did not antagonize DA auto-inhibition either. Christiansen and Squires (1974) had measured the effects of haloperidol on synaptosomal tyrosine hydroxylase. They found little effect on TH activity when the concentrations of haloperidol was ranging from 0.1 to 0.5 μM. They got inhibitory effect when the concentration was much above 1 μM. Their results fit well with our data. They also found that haloperidol would reverse the apomorphine elicited inhibition of DA synthesis. Although, it did reverse APO elicited inhibition in our system also, however, we found the haloperidol would not antagonize DA autoinhibition presynaptically, it's effect and DA effect were additive (see table 2). The possible different binding sites of apomorphine and DA on DA pre-synaptic receptor may explain this phenomena.

Most importantly, our results may also offer a possible explaination why bromocriptine and haloperidol are so clinically efficient. At suitable concentration, bromocriptine acted like DA agonist which activated the DA postsynaptic receptors, but it did not inhibite the DA synthesis presynaptically. For haloperidol it blocked DA effects post-synaptically as well as inhibited DA synthesis presynaptically. We also see that the tranditional way to define agonist and antagonist should be refined to separate the presynaptic and postsynaptic effect. The most effective stimulating agent will be the one like bromocriptine, it worked as agonist postsynaptically, but it won't inhibite (it might even stimulate) the dopamine synthesis via presynaptic auto-receptors. While the most effective blocking agent will be the one like haloperidol, it worked as antagonist postsynaptically and as agonist presynaptically.

We thank Janssen Pharmaceutics for sending pure haloperidol.

Table I. $\frac{^{14}CO_2 \text{ release (Drug)}}{^{14}CO_2 \text{ release (Control)}}$

Drug / Concentration	BCP	HD
10^{-5} M	101.6±2.0 (5)	76.2±2.9 (5)
10^{-6} M	90.6±3.0 (6)	89.8±0.9 (5)
10^{-7} M	83.8±2.5 (4)	100.5±2.2 (5)
10^{-8} M	97.4±3.6 (5)	

BCP : Bromocriptine HD : Haloperidol

the data present as Mean±S.D. (No. of experiments)

Table II. $\frac{^{14}CO_2 \text{ release (DA+HD)}}{^{14}CO_2 \text{ release HD}}$

Concentration of DA / Concentration of HD	10^{-5} M	10^{-6} M
10^{-5} M	38.6±6.5 (4)	95.0±2.3 (4)
10^{-6} M	42.6±6.4 (6)	89.3±3.7 (5)
10^{-7} M	37.9±2.8 (5)	91.5±1.7 (5)
0	40.1±7.9 (4)	89.7±3.5 (8)

DA : Dopamine HD : Haloperidol,

the data present as Mean±S.D. (No. of experiments)

REFERENCES

1. Anden, N.E.; Roos, B.E.; and Werdinius, B. (1963) Life Science 3: 149-158.
2. Bochaert, J.; Tassin, J.P.; Thierry, A.M.; Glowinsky, J.; and Premont, J. (1977) Brain Res. 232: 391-400.
3. Carlsson, A.; and Lindqvist, M. (1963) Acta Pharmacol. et Toxicol. 20: 140-144.
4. Christiansen, J. and Squires, R.J. (1974) J. Pharm. Pharmac. 26: 267-369.
5. Christiansen, J. and Squires, R.J. (1974) J. Pharm. Pharmac. 26: 742-743.
6. Clement-Cormier, Y.C.; Kebabian, J.W.; Petzold, G.L. and Greengard, P. (1974) Proc. Nat. Acad. Sci. USA 71(4): 1113-1117.
7. Corrodi, H.; Fuxe, K.; Hokfelt, T.; Lidbrink, P.; Ungerstedt, U. (1973) J. Pharm. Pharmac. 25: 409-411.
8. Di Chiara, G.; Pordeddu, M.L.; Vargiu, L.; Gessa, G.L. (1978) Pharmacology 16 (Suppl. 1): 135-142.
9. Fuxe, K.; Corrodi, H.; Hökfelt, T.; Lidbrink, P.; Ungerstedt, U. (1974) Med. Biol. 52: 121-132.
10. Fuxe, K.; Fredholm, B.B.; Ögren, S.O.; Agnati, L.F.; Hökfelt, T. and Gustafsson, J.A. (1978) Acta Endocrinologica Suppl. 216, 88: 27-56.
11. Goldstein, M.; Lew, J.Y.; Nakamura, S.; Battista, A.F.; Lieberman, A. and Fuxe, K. (1978) Fed. Proc. 37(8): 2202-2206.
12. Iversen, L.L.; Rogawski, M.A.; Miller, R.J. (1976) Molec. Pharmac. 12: 251-262.
13. Johnson, A.M.; Loew, D.M.; Vigouret, J.M. (1976) Br. J. Pharmac. 56: 59-68.
14. Loew, D.M.; Vigouret, J.M.; Jaton, A.L. (1976) Postgrad. Med. J. 52 (Suppl. 1): 40-46.
15. Miller, R.J.; Horn, A.S. and Iversen, L.L. (1974) Molec. Pharmac. 10: 759-766.
16. Nagy, J.I.; Lee, T.; Seeman, P. and Fibiger, H.C. (1978) Nature 274: 278-781.
17. Raiteri, M.; Cervoni, A.M.; Carmine, R.O.; Levi, G. (1978) Nature 274: 706-708.
18. Silbergeld, E.K. and Pfeiffer, R.F. (1977) J. Neurochemistry 28: 1323-1326.
19. Snider, S.R.; Hutt, C.; Stein, B.; Prasad, A.L.N. and Fahn, S. (1976) J. Pharm. Pharmac. 28: 563-566.
20. Wang, W.K.; Jeng, L.S.; Chiang, Y.; Chen, N.K. (1982) Nature 296: 354.

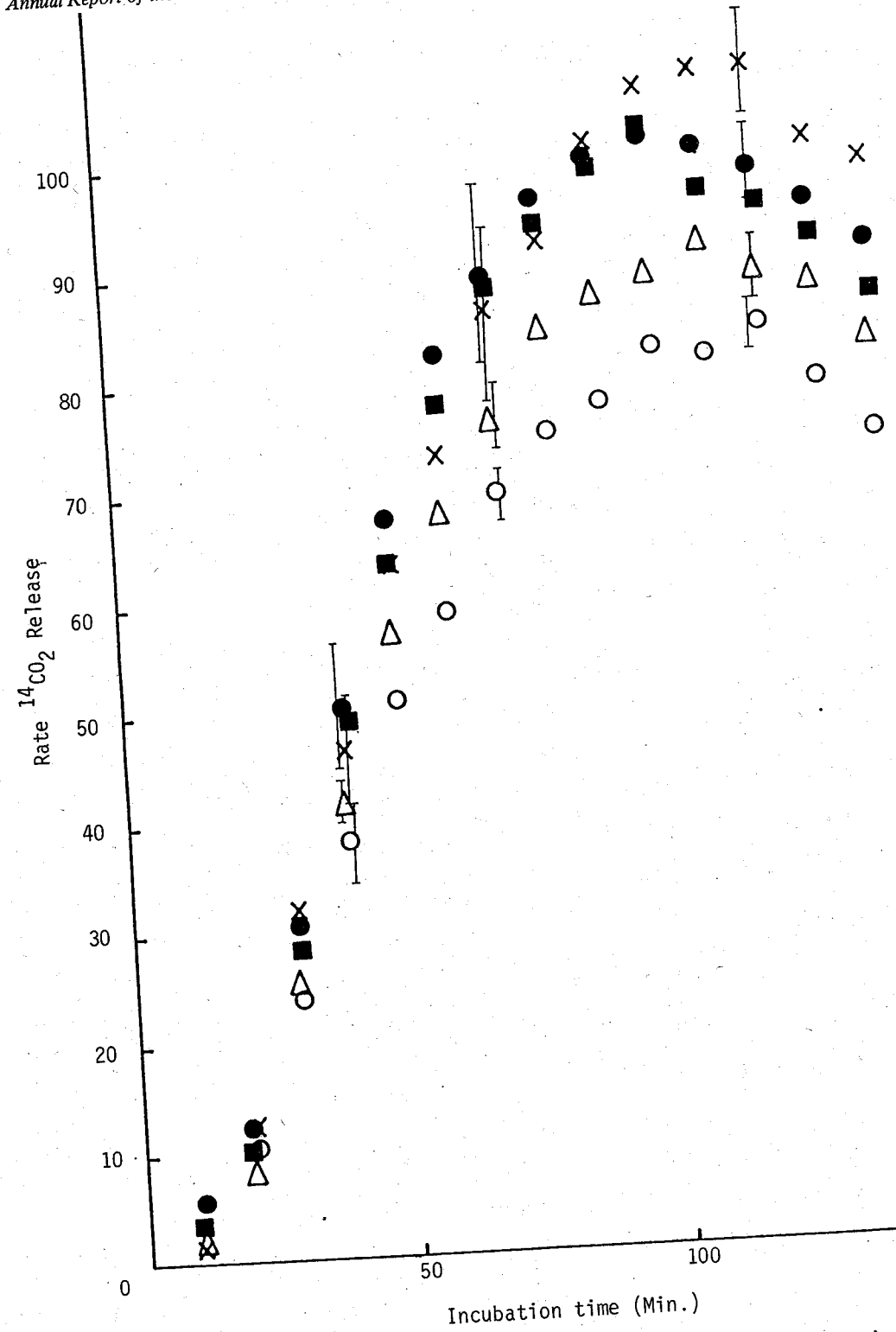

Fig. 1. Rate of $^{14}CO_2$ release from labelled tyrosine plotted against incubation tim
Error bar shown are standard deviation (mean±S.D. for five preparations).
Bromocriptine added to the preparation at 1 x 10^{-5} M(x), 1 x 10^{-6} M(Δ),
1 x 10^{-7} M(o). The higher the dose inhibited dopamine synthesis the less
Bromocriptine at 1 x 10^{-8}M(▪) had no significant difference with control

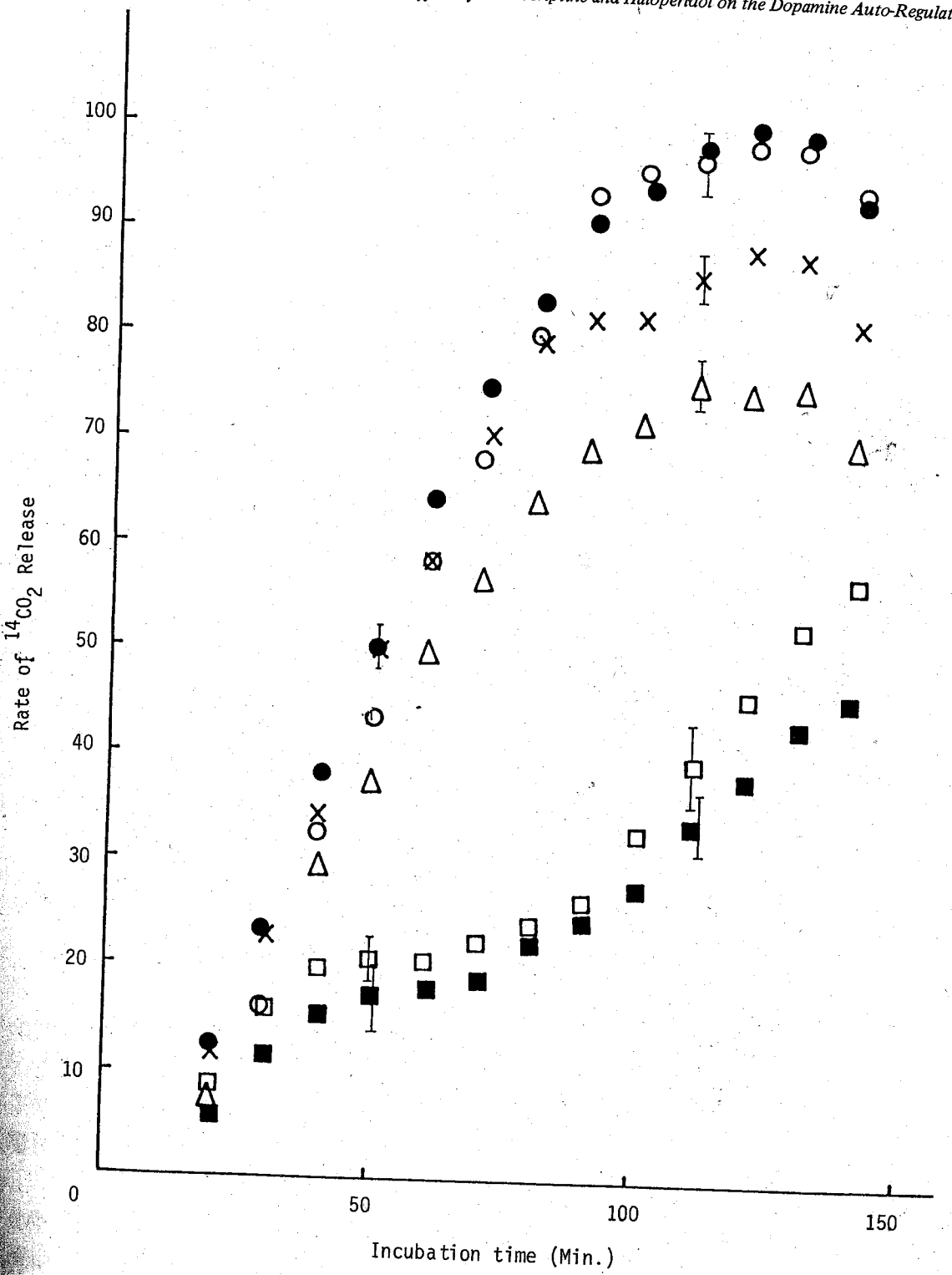

Fig. 2. Rate of $^{14}CO_2$ release from labelled tyrosine plotted against incubation time, error bar show are standard deviation (mean±S.D. for five preparations). Haloperidol at 1 x 10^{-5} M(Δ), 1 x 10^{-6} M(x), 1 x 10^{-7} M(o) added to the preparation inhibited dopamine synthesis. Dopamine at 1 x 10^{-5} M(□) strongly inhibited dopamine synthesis. Haloperidol at 1 x 10^{-6} M together with dopamine at 1x10^{-5} M(▪) further inhibited dopamine biosynthesis. Control (∘).

多點污染源光化學空氣污染擴散模式之理論與應用

梁　文　傑
中央研究院物理研究所
國立臺灣大學機械工程學系

華　梅　英
中央研究院物理研究所

摘　要

本研究的目的在建立一個普遍性光化學擴散模式（Photochemical Dispersion Model），此模式是應用由高斯擴散方程式推演而來的大氣擴散模式，將擴散空間分割成許多含有等量污染物質的巢（cell）空間，由於污染物的擴散，此巢空間也隨之變大，並依風向往下風處傳送，在傳送過程中，巢內產生光化學作用，使污染物濃度改變。本研究將模式的理論由污染物的擴散至化學反應的參與過程以及推演方法做一敍述，並參考國內外相關的研究，選擇發生機率較多且較重要的反應方程動力機制，將不同排放污染物濃度、氣象狀況所造成各污染物彼此間的相互影響加以模擬分析，並於高雄地區較大污染源排放情況做個案的探討。

壹、引　言

所謂光化學作用（Photochemical Reaction）是因陽光的照射，使污染物間產生化學反應，而形成第二次污染物的作用。由於大氣流場的複雜與化學污染物含量的繁多，將擴散系統中任何化學反應數學化，會導出一系列非線性、偏微分聯立方程式組，爲了簡化這些方程式，乃將化學反應和擴散分開考慮，也就是流動所造成的濃度改變將影響反應速率，但由化學反應所造成的濃度變化，將不會影響擴散。

本研究中仍以高斯煙柱模式做爲擴散的基本模式，但是高斯煙柱模式無法說明各種化學反應存在時，各種污染物間的交互作用，因而有箱模式的假設，根據 Smith〔1〕所提出的非穩定（unsteady）污染物在都市中的累積效應。基本上，它是假設污染物在箱中迅速且均質（homogeneous）的混合。箱的體積是由都市的表面積和混合層高度來決定，然後將箱空間中的均勻（uniform）污染物，以一常微分方程式來表示濃度的變化情形，這時濃度會受平流、化學反應和降雨的影響而改變。此均質混合的假設，有效解決了箱中紊流混合的問題，但是無法顧及垂直方向濃度分佈的實際情形，如此將會造成較大誤差。針對這項缺點，Reiquam〔2〕、Seinfeld 和 Mac Cracken et al. 等人

士提出了更進一步的箱模式，那就是把空間劃分成許許多多的小箱子，來解決不同濃度的分佈問題。其基本假設爲：①污染物一旦進入箱中，能迅速且均勻的混合。②箱中污染物濃度爲排放進入、平流和化學反應間的變數。③忽略壁間的擴散作用。

箱模式的發展，彌補了高斯煙柱模式的不足，但是必須選擇合理的箱體積才能確實表示出擴散和化學反應的作用。

環理論是由點源的煙柱擴散發展出來的，將排放煙柱的橫截面上，劃分成許多的同心圓或橢圓，每二條分隔線間所圍成的區域，即爲每一環的面積，環的厚度爲無限小。環面積大小分隔的決定，是將此橫截面的污染質作等量的分配，換句話說，於每一環中的污染質，其量相當於其他各環的污染量（見圖一）。因爲排放濃度在每一橫截面上，並不呈均勻狀態，而是以高斯分佈爲主，濃度的擴散以主軸最高，因此所區分出每環的面積並不相同。面積的大小，和所欲區分的環數N有關，與離排放源x軸的距離和y、z方向的擴散係數也有關。假設在任一環中的污染物濃度是均勻的，並且同一環中任一處的反應速率相同，這項將煙流區分成同心環的作法是將連續常態分配等似於不連續常態分配，環的數目，相當於不連續常態分配的區間，當間隔增加，不連續的常態分配和原有連續常態分配愈爲趨近。因此這項假設將依環數增加而愈眞。這種將會造成計算量的增加（依Freiberg 的研究，最佳環數爲100）〔3〕，在任一環中污染物的反應與其他環相互獨立，每一環的表面和寬度依煙流擴散的分佈而異。由環理論及箱模式的結合即成爲可以考慮化學反應的巢模式。

貳、基本理論

在三度空間座標系統中，污染物濃度公式爲：

$$C_i(x,y,z;h)=\frac{Q_i}{2\pi\sigma_y\sigma_z U}\exp\left(-\frac{y^2}{2\sigma_y^2}\right)\left[\exp\left(-\frac{(z+h)^2}{2\sigma_z^2}\right)+\exp\left(-\frac{(z-h)^2}{2\sigma_z^2}\right)\right] \quad (1)$$

式中C_i爲第i種污染物的濃度，是空間座標的函數（單位爲$\mu g/m^3$），Q_i爲第i種污染物的排放程度（$\mu g/sec$），（x，y，z）爲三度空間中欲測濃度點的座標位置。x爲下風向距離，y爲與下風向垂直的水平向距離，z爲測點的高度（單位皆爲m）。h爲煙囪高度（m），σ_y，σ_z爲高斯濃度分佈y，z方向的濃度標準偏差（m）其計算方式見表十及表十一，U爲風速（m／sec）。U爲高度z的函數，因此必須採用平均數值。適當的數值爲煙柱整體的平均值〔12〕。通常採用煙囪高度的時間平均風速。但有時甚至無法得知，此時必須加以估計，估計的方法可採用流速剖面指數定律（Power law velocity profile）即$U=U_{10}(h/10)^p$，其中U_{10}爲地面10公尺的風速，p爲無因次常數隨穩定度不同而異，見表一。上式中（z－h）與（z＋h）是基於地面爲完全反射的假設，當煙柱擴散到達地面時，地面對污染物不造成任何沉降或吸收作用，因此可以視爲有一假想污染源，位於眞正污染源的對稱位置（以地面而言見圖二），做

同污染量的排放。

一、模式的推演

若測站的位置在地面（即h＝0），根據高斯擴散模式，式(1)可寫成

$$C_i=\frac{Q_i}{\pi\sigma_y\sigma_z U}\exp\left[-\frac{1}{2}\left(\frac{y^2}{\sigma_y^2}+\frac{z^2}{\sigma_z^2}\right)\right] \quad (2)$$

當下風距離x爲定值時$\frac{y^2}{\sigma_y^2}+\frac{z^2}{\sigma_z^2}$爲定值，可以視爲在yz平面上的一組橢圓，

$$\gamma^2=\frac{y^2}{\sigma_y^2}+\frac{z^2}{\sigma_z^2} \quad (3)$$

代入(3)式中可得

$$C_i=\frac{Q_i}{\pi\sigma_y\sigma_z U}\exp\left(-\frac{1}{2}\gamma^2\right) \quad (4)$$

由於h＝0且地面爲全反射，因此應爲半橢圓區域。於是當煙流繼續往下風向進行，每環內有不同的反應速率，它將由中心至周邊逐漸減少。由於化學反應物和產物是均質分佈（homogeneously distribution），並且在每一環中爲獨立，所以在連接二環由化學反應造成的結果並不影響擴散，這假設的準確性建立於反應與擴散在濃度和時間上的相對大小。

當h≠0時，因爲測站的濃度測定以地面爲主，可以視爲z＝0。

同理

$$\gamma^2_{z=0}=\frac{y^2}{\sigma_y^2}+\frac{h^2}{\sigma_z^2} \quad (5)$$

測站位置在任一環上，都可測得地面污染源排放二倍的濃度，理論上和地面污染源有些許出入，但實際計算上則無差異。

本研究所用的巢理論是根據箱模式把擴散空間分格成許多環區域，每個環面積依x軸距離的增長而加大，再將上節所計算環的面積，給予下風x向一段適當距離，做爲環體的厚度，於是由不同環體構成的各個巢格子便在空間中建立起來。同一巢號的巢體積依下風向逐漸增大，增大的程度，依風速、穩定度等氣象因素而異，所以巢理論能充分表示擴散的特性。

由於在每一半橢圓環體中含有等量污染質，因此在濃度C_i和排放量Q_i間存在一關係：

$$\int_0^{\pi}\int_{\gamma_{ns-1}}^{\gamma_{ns}} u C_i\sigma_y\sigma_z\gamma\,d\gamma\,d\theta=\frac{Q_i}{N},\quad ns=1,2,\cdots\cdots,N \quad (6)$$

其中ns爲所計算的環號，N爲所選用環區的總數（即yz平面上巢區的總數）。將(5)式代入(6)式可推演出：

$$\int_0^{\pi}\int_{\gamma_{ns-1}}^{\gamma_{ns}}\exp\left(-\frac{1}{2}\gamma^2\right)\gamma\,d\gamma\,d\theta=\frac{\pi}{N},$$

或

$$\left[-\exp\left(-\frac{1}{2}r^2\right)\right]_{r_{ns-1}}^{r_{ns}}=\frac{1}{N},$$

令 $r_0=0$，則可推知

$$r_{ns}=\sqrt{2\,\ell n\left(\frac{N}{N-ns}\right)} \tag{7}$$

第 ns 環的側面積 A_{ns} 可表爲：

$$A_{ns}=\int_0^{\pi}\int_{r_{ns-1}}^{r_{ns}}\sigma_y\sigma_z r\,dr\,d\theta,$$

$$=\pi\sigma_y\sigma_z\ell n\left(\frac{N-ns+1}{N-ns}\right), \tag{8}$$

假設巢體厚度爲單位時間風速所走的距離，則巢體體積 V_{ns} 爲

$$V_{ns}=\left[\int u\,dA\right]_{ns}=u\left[\int dA\right]=u\,A_{ns} \tag{9}$$

至此，由擴散所造成的影響，已被體積的變化所描述。並且大氣中已存在的污染物，也可以和煙柱混合後，加入其中反應〔 4 〕〔 5 〕。

今假設大氣中本身污染物能均勻分佈，並且能和煙柱中的污染物接觸，而以相同的速率進行化學反應，且凡是參與化學反應的污染物，不論是否爲排放源所排放的，皆列入考慮，則背景污染物儘管能與煙柱污染物紊亂混合，而進行化學反應，但却沒有擴散因素的介入，因此這二種不同來源的污染質，在觀念上，仍然需要加以區分。也就是說，各個巢格子內部的化學反應，由背景和煙柱的污染物同時參與，但是因爲背景污染物並不擴散，故在巢與巢的交界處，應不斷地有大氣污染物補充。

對於固定的第 ns 區，$D^j_{i,ns}(X)$ 表示第 j 巢在 x 軸位置（ $X_{j-1}\le X\le X_j$）所含有第 i 種污染物的總量，$C_{i,ns,b}$ 表示在X處 i 種污染物的濃度，則在 $j-1$ 巢與 j 巢交界處（ $X=X_{j-1}$），$D^{j-1}_{i,ns}(t_{j-1})$ 與 $D^j_{i,ns}(t_{j-1})$ 的關係爲（參看圖三）：

$$D^j_{i,ns}(t_{j-1})=D^{j-1}_{i,ns}(t_{j-1})+WC_{i,ns,b,x_{j-1}}(V_{ns,j}-V_{ns,j-1}), \tag{10}$$

而 $D^j_{i,ns}(X)$ 的起始值爲：

$$D^j_{i,ns}(t_0)=(C_{i,ns,0}+WC_{i,ns,b,0})V_{ns,1}, \tag{11}$$

其中W表示排放源與大氣混合程度的參數（ $0\le W\le 1$ ）。$V_{ns,j}$ 表第 j 巢的體積，$C_{i,ns,j}$ 表示在 X_j 處的濃度值。則 $D^j_{i,ns}(X)$ 在 j 盒內因化學反應所引起的變化，可以由下式求得：

$$\frac{dD^j_{i,ns}(X)}{dt}=V_{ns,j}R_i,$$

$$C_{i,ns,t,j}=\frac{D^j_{i,ns}(X)}{V_{ns,j}}+(1-W)C_{i,ns,b,j}, \tag{12}$$

式中 $C_{i,ns,t,j}$ 爲 ns 區域中，大氣與煙柱的污染總濃度。

在模式的建立過程中，巢體積的計算，和光化學反應作用，被視爲二種完全獨立的過程。擴散所造成濃度減少的特性可用相對的體積增大來表示。

二、光化學反應機制

光化學煙霧的產生，在汽車排入大氣方面，大多由於 NO 和未燃燒完成的 H.C. 之間的作用，其煙霧形成在於 NO 氧化成 NO_2 的過程，能將未飽和芳香族碳氫化物氧化成醇類和酮類，並產生 O_3 和 PAN（ Peroxyacyl Nitrates ）。在模擬大氣過程時欲將化學反應與擴散模式相結合，必須先得知各種污染物排放量，以及化學反應的機構，對工廠污染排放方面，通常得考慮 SO_2 的氧化和所造成的系列反應。

光化學反應過程十分複雜，即使在極爲精良的實驗室中，亦完全無法確知其反應情形，所以想了解空氣中化學作用混合的情形是非常艱難的，再加上對均質紊流與化學反應間的關係，並沒有更爲深入的了解，假使用極多連鎖反應，來推測光化學反應模式，又無法量測污染物的濃度，其結果也是罔然，因此，爲了簡化極大數量可能反應，僅在複雜項目中選取速率較快或較具代表性的反應。反應速率常數，曾經多位專家在實驗室中研究並發表。

對於光化學反應方程式的選取，最基本的光解循環爲〔 6 〕：

$$\begin{aligned}&NO_2+NO\xrightarrow{1}NO+O\\&O+O_2+M\xrightarrow{2}O_3+M\\&O_3+NO\xrightarrow{3}NO_2+O_2\end{aligned} \tag{13}$$

式(13)的三項反應，其中M爲第三種介質用以吸收反應的能量，在空氣中M物質可能爲 O_2 或 N_2。根據實驗這三項反應作用非常迅速。若是所有光化學反應都能包括在式(13)中此項假設正確的話，則可推知NO 、NO_2 、O_3的濃度將爲定值，反應所產生穩定狀態的 O_3，濃度爲初始 NO_2 的函數。因此由 NO_2 濃度可算出 O_3 的濃度，再因燃燒過程排入大氣中以 NO 爲主，NO_2 量極微，臭氧濃度應該維持在一定限度之內。然而，事實上 O_3 濃度遠大於此限度，因此可以斷定除式(13)之反應外還有其他反應存在使 NO 氧化成 NO_2 時不消耗 O_3，造成 O_3 累積成高濃度，而氮氧化物濃度則逐漸降低，正如大氣中所發生的情形一般。這一點由於碳氫化合物的存在而獲得解決。已存在有相當反應性的氧原子，能打擊碳氫化合物，尤其是穩定性較弱的烯屬烴（ olefin ），使雙鍵處斷裂爲二，產生自由基（ free radical ），此自由基具有高度反應性，能繼續參與其他的反應。這些有機性自由基與 O_2 形成過氧基（ Reroxy radicals ）能釋出一氧原子而使NO氧化爲 NO_2，因而干擾了上述所提及的NO 、NO_2 、O_3 循環。在烯屬烴參與反應時形成另一種基，可能是醛類，因爲醛類爲氧原子與烯系烴反應所產生生成物的一種。過氧基的旁支反應，可能形成硝基過氧乙醯（ PAN ），這是一種非常强烈的眼睛刺激劑，對植物會造成傷害。

本模式中光化學反應，是根據A.Q. Eschenroeder et al.〔 7 〕所做的研究，也就是取上面所述最基本又具代表性的反應爲主。因烯屬烴中以直鏈一二丁烯的活性較其他碳氫化合物爲多，因此以 C_4H_8 爲碳氫化合物的代表。其反應方程組式見表二。表三中

除碳氫化合物與氮氧化物的作用外還包括SO_2的作用，一旦空氣中含有碳氫化合物與氮氧化物時，SO_2的氧化速率比在清潔空氣中有極爲顯著的增加。相對的，在工業區的煙囪排放物若含有金屬離子時，其催化機構又異於此，此處對金屬離子催化的反應並不加以討論。實驗上Wilson 等人〔 8 〕曾發現當SO_2 與碳氫化物、氮氧化物同作用的系統中，會產生較低NO_3峰頂，並且也能使 O_3形成量減少，因爲烷屬烴和烯屬烴系統中加入SO_2作用，SO_2將NO_x移除而降低NO_2濃度，因而引起 O_3濃度降低。假使空氣中，SO_2已以緩慢的速度氧化成SO_3，當存在水時，則SO_3快速變成H_2SO_4。事實上輻射波長小於 2,900 Å的光不會達到地表，而SO_2作用形成 SO 和O的波長只限於波長小於 2,180 Å以下（鍵能 135kcal ），因此低層大氣中基本上由SO_2吸收而形成的光化學作用仍是以活性SO_2分子作用。

綜合上述，光化學作用物種類與吸收特性歸納如下：

O_2 ：由基態欲達解離狀態，其波長將在 3000 Å以下，否則會因能量太弱而不能反應。

O_3 ：能强烈吸收 2000 ～ 3200 Å之間的光波，對 4500 ～ 7000 Å間波長的吸收較弱，其反應能以$O_3 + h\nu \rightarrow O_2 + O$表示。

NO_2：NO_2是大氣中最重要的吸收性分子，它吸收低層大氣中所有可見光與紫外光範圍內的陽光光波。低於 4200 Å時，NO_2以下形式分解：$NO_2 + h\nu \rightarrow NO + O$。但最佳吸收光波範圍爲 3000 ～ 3700 Å間，約有 90 %會分解。鍵能約爲 73kcal／mole ，此約 4000 Å之光波能量，故在 4200 Å 以上之光波，無法提供足夠能量。

SO_2：SO_2 的吸收以 2850 Å左右的波長最多，超過 3400 Å時吸收極微。$SO_2 \rightarrow SO + O$反應之鍵能約 135 kcal ／mole ，相當於波長在 2180 Å之能量。因此波長在大氣中幾乎沒有，因此SO_2吸收光線後，只能分解成 $^1SO_2$與 $^3SO_2$兩種型態。

三、光化學反應的計算

表二與表三爲二組光化反應系列，各污染濃度隨時間而變化，因此可以將各污染物的濃度變化寫成系列聯立常微分方程式。以第一組光化學反應爲例，各污染物之濃度變化情形如下：

$$\frac{dC_{NO_2}}{dt} = -P_1 + P_3 + P_6 - P_8 ,$$

$$\frac{dC_{NO}}{dt} = P_1 - P_3 - P_6 ,$$

$$\frac{dC_{O_3}}{dt} = P_2 - P_3 - P_5 + 0.5\,P_7 ,$$

$$\frac{dC_{O_2}}{dt} = -P_2 + P_3 - P_7 ,$$

$$\frac{dC_{C_4H_8}}{dt} = -P_4 - P_5 ,$$

$$\frac{dC_{RCO_X}}{dt} = 2.5\,P_4 + 2.5\,P_5 - P_6 - P_7 - P_8 ,$$

$$\frac{dC_{ALD}}{dt} = 0.12\,P_4 + 0.12\,P_5 ,$$

$$\frac{dC_{PAN}}{dt} = 0.67\,P_8 , \qquad (14)$$

其中

$$P_1 = \alpha_1 C_{NO_2} , \quad P_2 = \alpha_2 C_O C_{O_2} C_M , \quad P_3 = \alpha_3 C_{O_3} C_{NO} ,$$
$$P_4 = \alpha_4 C_O C_{C_4H_8} , \quad P_5 = \alpha_5 C_{O_3} C_{C_4H_8} , \quad P_6 = \alpha_6 C_{RCO_X} C_{NO} ,$$
$$P_7 = \alpha_7 C_{RCO_X} C_{O_2} , \quad P_8 = \alpha_8 C_{RCO_X} C_{NO_2} , \qquad (15)$$

而 α爲化學反應速率。

根據式(13)中的光化學反應循環中，可得：

$$\frac{dC_O}{dt} = K_1 C_{NO} - K_2 C_O C_{O_2} C_M ,$$

若將上式的等號右方做數值上的估計，其值將非常趨近於 0 ，在物理意義上，反應 1 中氧原子的產生和反應 2 中氧原子的消耗量幾乎相等，因此習慣上將氧原子的濃度視爲定值，不隨時間而變，此稱爲穩定近似（ Steady-State Approximation ）。同樣的在此處的光化學反應模式中，也採用穩定近似的假設

$$\frac{dC_O}{dt} = P_1 - P_2 - P_4 = 0 ,$$

即

$$C_O = \frac{\alpha_1 C_{NO_2}}{\alpha_2 C_{O_2} C_M + \alpha_4 C_{C_4H_8}} \qquad (16)$$

在每一巢體積中氧原子的濃度不隨時間而變化。但巢與巢的比較，氧原子濃度則未必相同。

參、模式的程式原理及處理步驟

模式的程式其流程圖見圖十至圖十四，以下將分別介紹其中各變數的計算。

一、穩定度

目前被廣泛承認求取穩定度的方法有四種〔 9 〕：① Turnen 法：係依照Pasquill對日照、雲量及地面風速三種因素之觀測，加以推算而成的六分法（即按大氣不穩定程度由大至小，分成A～F六級，見表四所示）。此法因需要較爲齊全的氣象資料，因此在使用上可能會因資料不足而無法應用。②水平風向之標準偏差（σ_θ）與垂直方向氣溫直減率（$\partial T / \partial Z$，Temperature lapse Rate Method），如（表五）所示。③純以水平風向標準偏差計算者，如（表六）所示。④考慮夜間情況之改良法，如（表七）所示，此法乃是修正六分法，增加一極穩定的G級。本模式中所採用的爲第④種方法，其

求取方式如下。

由（表四）知，在白天時，日射量之强弱爲穩定度等級判定的重要因素，其值可由太陽天頂角（Solar Altitude，α）與雲量之多寡決定。太陽天頂角角度又與當時之月份、日期及時間有關，可由下列公式求得。而雲量、日射量與太陽天頂角之關係，可參考表八所示。

$$\sin\alpha = \sin(\pi\phi/180)\sin\delta + \cos(\pi\phi/180) \cdot \cos\delta \cdot \cos\left[\frac{\pi}{12}(h-12)\right], \tag{17}$$

其中

$$\delta = 23.5\left(\frac{\pi}{180}\right) \cdot \sin\left\{\frac{\pi}{180}\left[30(m-1)+d-81\right]\right\},$$

上二式中，δ爲太陽傾斜角（Solar Declination），m爲月份，d爲日，h爲時（當地標準時間），ϕ爲緯度。

二、濃度分佈的水平垂直標準偏差

污染物擴散的水平、垂直標準偏差與下風方向距離 x 有關，經 Pasquill 研究〔10〕與 Gifford 改良〔11〕，由 Turner 〔12〕繪出了各種穩定度情況下 σ_y、σ_z 與距離間的關係圖，本模式中即根據此圖而求得 σ_y、σ_z。

三、風速的歸類

當模式應用在短期的計算上時，可直接輸入小時風速值，所使用的單位是公尺／秒，假使原輸入值是以 knots 爲單位則應將其值乘以 0.51444 做爲轉換方可使用。當模式應用在長期的計算上時，風速的區分，一般分爲六級，各級的風速範圍內以平均值，亦即中間風速（central wind speed）來代表。因爲風速計受到儀器本身的限制，對於較小風速的量測，極不準確，可能存在過大誤差，所以爲避免此，乃將第一級（即最小風速）之中間風速值定爲 1.5 公尺／秒。且凡風速小於 1 公尺／秒者，皆令爲 1 公尺／秒。表九爲各級風速區間與中間風速值。

四、有效煙囪高度的求取

本模式中之有效煙囪高度（H_e），依下法求得：

$$H_e = H_o + \Delta h \tag{18}$$

式中 H_e 爲煙囪高度，Δh 爲煙流上升高度。Δh 求法依 Briggs〔13〕之三分之二定律求之。當穩定度爲A至D級時（穩定與不穩定之間時）：

$$\Delta h = 1.6\,F^{1/3}U^{-1}S^{2/3} \quad , S \le 3.5X^* \ ,$$
$$\Delta h = 1.6\,F^{1/3}U^{-1}(3.5X^*)^{1/3} \quad , S > 3.5X^* \ , \tag{19}$$

其中

$$X^* = 14\,F^{5/8} \quad , \quad F \le 55 \text{ 時},$$
$$X^* = 34\,F^{2/5} \quad , \quad F > 55 \text{ 時},$$
$$F = gV_sR_s^2[(T_s - T_a)/T_s],$$

式中 g 表示重力加速度，單位爲（m／sec²）；V_s表示煙流排放速率，單位爲（m/sec

）；R_s 表煙囪內徑，單位爲（m）；T_a 表周圍環境空氣溫度，單位爲（°K）；T_s表平均煙流溫度，單位爲（°K）；U表煙囪頂端風速，單位爲（m／sec），其值依冪次律求得（Power Law Velocily Profile）：

$$U_{He} = U_{10}(Z_{He}/Z_{10})^p \tag{20}$$

U_{He} 與 Z_{He} 分別爲有效煙囪高度處的風速（m／sec）與高度（m），U_{10} 與 Z_{10} 爲離地面 10 公尺上方之風速（m／sec）與高度（m）。p 值參看表一，爲無因次常數隨穩定度等級而變。當穩定度爲E、F、G時（即爲穩定狀況下）：

$$\Delta h = \begin{cases} 2.4[F/(US)]^{1/3} & \text{，風速大時} \\ 5\,F^{1/4}S^{-3/8} & \text{，風速小時} \end{cases} \tag{21}$$

其中S爲穩定度參數，是大氣中絕熱運動的每單位垂直位移的回復加速度（restoring acceleration, sec^{-2}），其值定義爲：

$$S = g\frac{\partial\theta}{\partial z}T_a^{-1}$$

式中，g 爲重力加速度，$\partial\theta/\partial z$爲煙囪口至煙囪上緣之垂直方向的位溫（Potential temperature, $(°\,km^{-1})$），T_a爲周圍環境空氣溫度。

五、不連續巢空間誤差的控制

模式中將空間剖分成許多小格，由於將連續空間改爲不連續空間，其中可能會引起相當的誤差。對於 j－1 巢，當 $x = x_{j-1}$，(12)式成爲：

$$C_{j,ns,t}^{j-1} = \frac{D_{i,ns}^{j-1}(x_{j-1})}{\overline{V}_{ns,j-1}} + (1-W) \times C_{i,ns,b}^{j-1} \tag{22}$$

對於 j 巢，當 x_{j-1}時，(12)式成爲：

$$C_{i,ns,t}^{j} = \frac{D_{i,ns}^{j}(x_{j-1})}{\overline{V}_{ns,j}} + (1-W) \times C_{i,ns,b}^{j-1} \tag{23}$$

理論上，同樣在 $x = x_{j-1}$ 處，(22)應等於(23)，但實際上將二式相減得

$$\Delta C_{i,t,ns}^{j} = \frac{D_{i,ns}^{j}(x_{j-1})}{\overline{V}_{ns,j}} - \frac{D_{i,ns}^{j-1}(x_{j-1})}{\overline{V}_{ns,j-1}} \ , \tag{24}$$

則$\Delta C_{i,t,ns}^{j}$表示二者的誤差。將(10)代入上式，則：

$$\Delta C_{i,t,ns}^{j} = \left[\frac{D_{i,ns}^{j-1}(x_{j-1})}{\overline{V}_{ns,j}} + WC_{i,ns,b}^{j-1}\left(1 - \frac{V_{ns,j-1}}{\overline{V}_{ns,j}}\right)\right] - \frac{D_{i,ns}^{j-1}(x_{j-1})}{\overline{V}_{ns,j-1}} \ ,$$
$$= \left[WC_{i,ns,b}^{j-1} - \frac{D_{i,ns}^{j-1}(x_{j-1})}{\overline{V}_{ns,j-1}}\right]\left(1 - \frac{\overline{V}_{ns,j-1}}{\overline{V}_{ns,j}}\right),$$
$$= C_{i,ns}^{j-1}\left(\frac{\overline{V}_{ns,j-1}}{\overline{V}_{ns,j}} - 1\right) \tag{25}$$

由(25)可知，$\Delta C_{i,ns,t}^{j}$ 直接與$\overline{V}_{ns,j-1}/\overline{V}_{ns,j}$有關，當$\overline{V}_{ns,j-1} = \overline{V}_{ns,j}$時，$\Delta C_{j,ns,t}^{j} = 0$。因此對相鄰兩巢的體積比，應控制在一定的程度下，以減少誤差。

六、巢體積的求取

每一巢體積，是由環面積與巢體在 x 方向上長度的乘積而得，環面積的求法已在式

(7)中獲得，長度求法則以下式估算 (26)

$$x_j - x_{j-1} = a'U \times (j)^{cs} ,$$

其中 a 與 cs 皆爲控制巢體在 x 方向上長度的係數，其值可根據上節誤差的估計，在某誤差忍受值內，使體積隨距離增加將 x 方向尺度擴大，以減少部份計算機使用時間。

七、求解化學反應

體積計算之後，由於擴散是以同一層區爲假設，因此將所欲計算的層區體積由近而遠輸入第二部分計算光化學反應部分中，使擴散與反應溶合，巢體中的化學反應，污染物間相互影響，使化學反應的計算成爲數個至數十個常微分方程式的聯解，在一個巢中的反應時間是以污染物在此巢中的停留時間爲準，濃度以時間的變率計算。基於上述 x 方向巢尺度隨距離增加而增大的設計，在每巢中的作用時間爲

$$t = (x_j - x_{j-1}) / U ,$$

得到 t 後，再代入計算化學反應的副程式中。

對於各組化學反應聯立常微分方程式的求解，是利用四階蘭吉固達法計算（Fourth-order Runge-Kutta Method）每一步驟需要計算函數值四次，本模式選用蘭吉固達法的原因有：①步驟簡單，計算時只要知道前一點即可。②它的誤差與泰勒級數相較爲四階準確。③過程中不必計算函數的導數值，僅須重複計算函數值即可。

八、單位轉換

化學變化時以 ppm 爲濃度單位作用。但是巢體積變化已取代擴散效應，污染物傳送應以量代替濃度，故得將單位轉換。對於氣體 ppm 和 $\mu g/m^3$ 間的轉換係數，依溫度和污染物種類而異。

九、格子座標系統的建立

由前面所討論到的擴散體積與光化反應合成後，可以求出同一環號的巢內污染物，由近而遠彼此間相互作用，產生濃度的變化情形，但是對於受污染排放的地區而言，應該是一整個面，而不是一單線，因此，本模式中同時考慮格子座標系統，使排放源下風向的區域，能夠經由等濃度線的繪製，而明白受污染的程度。格子座標，系統由相同大小的正方格子構成。格子點位置除非在三倍 σ_y, σ_z 長度內，不予計算。這樣不但能消除濃度不合理的增高現象，並能節省許多計算機計算時間。而所以要以三倍 σ_y, σ_z 範圍，則是基於統計上三倍標準偏差範圍內，污染物總量已達百分之 99.7 。

十、污染源資料處理

所輸入的污染源資料，除了最基本的排放速率（$\mu g/$ sec ），煙囪高度（ m ）外，因爲要求有效煙囪高度，因此還得輸入煙囪直徑（ m ），氣體出口（ m / sec ），排氣溫度（°K）等。如果是長期資料，則應求取平均排放速率。

十一、氣象資料的處理

㈠風向——本模式中只考慮污染排放對下風方向區域的影響，因此此處並不需要做任何預先處理。

㈡風速——在計算短期間時，可直接代入小時平均等短期值，如果計算長期間，則可將風速分類，或將相同風方與穩定度集中後，求其平均風速亦可。輸入值以（公尺/

秒）爲單位。

㈢穩定度——假使在已有的氣象資料中，沒有穩定度的分類，則應就所有已知條件，選擇最佳穩定度求取法，求其等級。

㈣溫度——由於溫度擴散與光化反應過程，如有效煙囪高度的求取、光化反應速率，以及單位 $\mu g/m^3$ 與 ppm 的轉換，因此溫度值必須獲知。短期計算可直接代入溫度值，長期則需求其平均值，輸入值以°K 表示。

十二、其他資料的處理

㈠光化學反應速率常數——程式在計算過程中，可以根據所欲模擬的光化反應方程組，而輸入代號選擇不同副理程式來計算，因此在輸入代號前，對程式中數據檔的建立，應配合相同的反應速率常數，以免發生錯誤。反應速率常數值以 sec^{-1}, $ppm^{-1}sec^{-1}$ 及 $ppm^{-2}sec^{-1}$ 爲單位。根據表二至表三記錄，受溫度影響較大的速率常數，應將溫度代入計算。

㈡各污染物分子量——在單位轉換過程中，會運用到各污染物的分子量，因此分子量值必須記錄於數據檔案中輸入。

㈢模式係數值——在模式的推導過程中，有一些無因次的係數值，如控制巢長度 a 與 cs （ 見式㉖ ），控制解聯立常微分方程蘭吉固達法區間的 HH，以及計算有效煙囪高度處風速的 P 值，都在輸入數據檔或程式開端予以界定。

㈣程式執行的輸入資料——計算格子作標系統中污染影響區域的濃度分佈情形時，首先必須將所欲研究的區域予以界定，如格子座標中每一正方小格的邊長 SL，在 x 和 y 方向計算的格子點數 NI，NJ 等。就擴散上，將整個空間分成的環數 NN 亦應給予。因此對這幾項必須且變動的大值的控制，其輸入方式，在程式執行中才就問題出現時，直接由終端機打入。

肆、研究結果與討論

一、個案研究與討論

PDM 程式的使用，在資料的輸入上分成二大類，第一類是在程式未執行前，先建立輸入數據檔。內容包括氣象資料、煙囪高度（ m ）、排放污染量（ $\mu g/Nm^3$ ）、背景污染濃度（ ppm ）、光化學反應常數值以及各污染物的分子量等。第二類是程式正在執行中由終端機打入，此類資料爲變動性較大者，如輸入輸出數據檔的名稱，所區分的環數，選用第幾組光化學反應式，以及污染物的種類數等，假使在格子座標系統中，則需輸入 x , y 方向的分格數以及每一格子的邊長等資料。

此處所做的個案研究，在氣象資料方面，是採用中央氣象局 1983 年於高雄所設的測站全年記錄值，見表十三及十四。輸入模式中時將全年逐時記錄先行轉換分類爲六種風速，六種穩定度及十六種風向。污染源以高雄地區興達火力發電廠、中油公司高雄煉油總廠及大林火力發電廠爲模擬（ 見表十二 ），先行計算各個污染源排放對附近的影響濃度再將結果予以累加。三污染源所在位置並依格子座標系統點繪出相對關係，由於三

污染源彼此間相距皆有 10 公里以上，因此座標系統函蓋範圍東西方向長 25 公里，南北方向長 66 公里，若以 1 公里爲各格子點的間距，總計格子數共 26 × 67 點。圖四～圖十一爲依第二組光化學反應計算結果，因全年累計第十六及十五風向次數最多，所以濃度的分佈較偏於南方及東南方向，以三污染源爲中心向外遞減。在污染源之間地區，因濃度累加作用，故等濃度線的變化並不規律，甚或有增高的趨勢，但畢竟離污染源較遠，原來濃度已降低，影響範圍有限。

二、污染物濃度間非線性影響的研究與討論

根據表二及式(14)、(15)所示，各污染物濃度之間的變化爲非線性，因此以具有影響力的各因素，如輸入的三種污染物 NO_2，NO，C_4H_8 濃度、風速、穩定度及溫度等做爲變數，當某種情況改變，其他種情況不變時對各污染物的影響。表十五爲各變數的輸入值分類，穩定度與風速各分爲六類，NO_2 與 NO 各分爲五類，C_4H_8 分爲二類。以下將分別討論各變數的改變造成污染物濃度在 1,000 公尺以內的濃度變化情形，爲便於比較乃以單位排放量計算。

由圖十二所示，當輸入 NO 值增加時，NO_2 濃度所受的影響極小，至下風距離較遠時有略微增加的趨勢。比較圖十二及十三，可知當穩定度增加時，污染物濃度很明顯的上升。比較圖十二及十四，可知當風速增加時，污染物濃度降低，且 NO 所造成的影響更爲減少。由圖十二及十五，可知 NO_2 不受 C_4H_8 輸入濃度影響。由圖十六及十七，可知氣溫愈高，NO_2 濃度較大，但增加量少。同理由圖十八至圖二十三可知當 NO_2 的排放濃度增加時，NO 至下風距離愈遠有略微增加的趨勢，但增加量極小。穩定度增加，NO 濃度增加。風速增加，NO 濃度降低。不受 C_4H_8 濃度影響。溫度降低，NO 濃度略低。圖二十四至圖二十九，可知 O_3 之變化，至下風向一段距離濃度受化學作用影響，有顯著的增加趨勢，且依 NO 排放量變大而加大，O_3 濃度變大。風速增加，O_3 濃度減小。C_4H_8 濃度增加對 O_3 影響極微，有略微減少的趨勢。當溫度增加時，O_3 濃度略爲加大。由圖三十至圖三十五可知 C_4H_8 濃度不受 NO_2、NO 排放量影響。穩定度增大，C_4H_8 濃度增加。風速增加，C_4H_8 濃度減少。溫度減少，C_4H_8 濃度略減。圖三十六至圖四十一可知 RCO_x 濃度隨 NO 增大而減少，隨 NO_2 增大而略增，隨穩定度增加而增加，隨風速增大而減少，隨 C_4H_8 排放量增大而增加，隨溫度增加而有極微量的增加。圖四十二至圖四十七爲 ALD 濃度的變化，其濃度隨 NO_2 排放量增加而增加，隨 NO 增大而減少，隨穩定度增加而增加，隨風速增加而減少，隨 C_4H_8 排放量增大而增加，隨溫度升高而略增。圖四十八至圖五十三爲 PAN 濃度的變化，其濃度隨 NO_2 排放量增加而增加，隨 NO 增大而減少，隨穩定度增加而增加，隨風速增加而減少，隨 C_4H_8 排放量增大而增加，隨溫度升高而增加。

綜合上述可知當穩定度及溫度增加時，污染物濃度加大但溫度影響的增值極小，當風速增加時，污染物濃度減少，O_3、NO_2 及 NO 受 C_4H_8 排放量影響小，而 ALD、PAN、RCO_x 則依 C_4H_8 排放增加而增加。

伍、結論及建議

根據本研究中發展出來的光化學巢式模式，可以做爲長期各種污染物濃度的估算，也可以下風向做爲縱剖面繪出濃度變化曲線圖。但是由於光化學反應十分複雜，在計算上爲一連串微分方程組的解，所以將耗費較多的計算機時間，並且由於其非線性的變化，污染物間無一定的增減關係，任何地區的污染值必需由排放口處開始推算，更增加許多計算機時間。在化學反應方面的探討，仍有待深入，國內外至今尚未有光化學反應機制的研究。從事擴散模式模擬時，擴散標準偏差值依各地地形、建築物等而有變化，應做正確的修正。

參考文獻

1. Smith, M., "The Concentrations and Residence Times of Pollutions in the Atmosphere", Intercience, New York, 155-166., (1961).
2. Reiquam, H., "Sulfur: Simulated Long-Range Transport in the Atmosphere", Science, 170, 318-320, (1976).
3. Freiberg, J., "The Iron Catalyzed Oxidation of SO_2 to Acid Sulphate Mist in Dispersing Plumes, Atmos. Environ. 10, 121-130, (1976).
4. O'Brein, E.E., "Turbulent Mixing of Two Rapidly Reacting Chemical Species", Phys. Fluids, 14, 1326-1331, (1971).
5. Donaldson, C. du P., and Hilst, G.R., "Effect of Inhomogeneous Mixing on Atmospheric Photochemical Reactions", Envir. Sci. Tech., 6, 812-816, (1972).
6. Seinfeld, J.H., Air Pollution: Physical and Chemical Fundamentals, McGraw-Hill, Inc., (1975).
7. Eschenroeder, A.Q., and Martinzs, J.R., "A Modeling Study to Characterize Photochemical Atmospheric Reactions to the Los Angeles Basin Area', General Research Corporation, CPA-22-69-127, (1969).
8. Wilson, W.E., Jr., Levy, A. "A Study of Sulfur Dioxide in Photochemical Smog, I. Effect of SO_2 and Water Vapor Concentration in the 1-Butene/NO_x/SO_2 System", J.A.P.C.A., 20, 385, (1970).
9. Dabberdt, W.F., Brodzinsky, R., Cantrell, B.C., Ruff, R.E., Dietz, R., Sethu-Raman, S., Atmospheric Dispersion Over Water and in the Shoreline Transition Zone, SRI Project 3450, Vol. I, (1982).

10. Pasquill, F. "Atmospheric Diffusion", 2nd edi, John Wiley & Sons., 204-328, (1974).

11. Gifford, F.A., "Use of Routine Meteorological Observations for Estimating Atmospheric Dispersion", Nuclear Safety, 2, No. 4, 47-51, (1962).

12. Turner, D.B., "Workbook of Atmospheric Dispersion Estimates", Public Health Service Publication No. 999-Ap-26, (1970).

13. Briggs, G.A., "Plume Rise", USAEC Critical Review Series TID-25075, NTIS, Springfield, VA., (1969).

表一　垂直方向風速剖面係數

Pasquill　穩定度級數	風速剖面指數，P (S)
A	0.10
B	0.15
C	0.20
D	0.25
E	0.30
F	0.30

表二　第一組光化學反應（PC-1），此爲最基本的光化學反應式，H.C.是以C_4H_6的狀態排出

編號	反應	反應速率常數
1	$NO_2 + h\nu \rightarrow NO + O$	0.072～0.05 min^{-1}
2	$O + O_2 + M \rightarrow O_3 + M$	1.32×10^{-5} $ppm^{-2}min^{-1}$
3	$O_3 + NO \rightarrow NO_2 + O_2$	21.8 $ppm^{-1}min^{-1}$
4	$O + C_4H_8 \rightarrow 2.5RCO_x + 0.12$ ALD	$1.11 \times 10^{+5}$ $ppm^{-1}min^{-1}$
5	$O_3 + C_4H_8 \rightarrow 2.5\,RCO_x + 0.12$ ALD	6×10^{-1} $ppm^{-1}min^{-1}$
6	$RCO_x + NO \rightarrow NO_2$	50 $ppm^{-1}min^{-1}$
7	$RCO_x + O_2 \rightarrow 0.5\ O_3$	5×10^{-6} $ppm^{-1}min^{-1}$
8	$RCO_x + NO_2 \rightarrow 0.67$ PAN	6 $ppm^{-1}min^{-1}$

表三　第二組光化學反應（PC-2），本組光化學反應同時考慮SO_2與H.C.的參與

編號	反應	反應速率常數
1	$NO_2 + h\nu \rightarrow NO + O$	0.072～0.05 min^{-1}
2	$O + O_2 + M \rightarrow O_3 + M$	1.32×10^{-5} $ppm^{-2}min^{-1}$
3	$O_3 + NO \rightarrow NO_2 + O_2$	21.8 $ppm^{-1}min^{-1}$
4	$O + C_4H_8 \rightarrow 2.5RCO_x + 0.12$ ALD	$1.11 \times 10^{+5}$ $ppm^{-1}min^{-1}$
5	$O_3 + C_4H_8 \rightarrow 2.5RCO_x + 0.12$ ALD	6×10^{-1} $ppm^{-1}min^{-1}$
6	$RCO_x + NO \rightarrow NO_2$	50 $ppm^{-1}min^{-1}$
7	$RCO_x + O_2 \rightarrow 0.5\ O_3$	5×10^{-6} $ppm^{-1}min^{-1}$
8	$RCO_x + NO_2 \rightarrow 0.67$ PAN	6 $ppm^{-1}min^{-1}$
9	$SO_2 + NO_2 \rightarrow SO_3 + NO$	1.3×10^{-14} $ppm^{-1}min^{-1}$
10	$SO_2 + CH_3 \rightarrow CH_3\,SO_2$	441 $ppm^{-1}min^{-1}$

表四　Pasquill大氣穩定度分類

地面風速（m/s）（10公尺高）	白天日射量			夜晚	
	強	中	弱	雲量≥4/8	雲量≤3/8
2	A	A～B	B	—	—
2～3	A～B	B	C	E	F
3～5	B	B～C	C	D	E
5～6	C	C～D	D	D	D
＞6	C	D	D	D	D

註：(1)不論白天或夜晚，當至天空雲量爲8/8時，穩定度級爲D。

(2)對於A～B級，乃是各別以A、B所對應之值再平均者。

表五　以水平風向標準偏差和溫度遞減率爲指標之大氣穩定度分類

穩定度	變化範圍
A	$22.5° \leq \sigma_\theta$
B	$17.5° \leq \sigma_\theta < 22.5°$
C	$12.5° \leq \sigma_\theta < 17.5°$
D	$-1.5° \leq \partial T/\partial Z < -0.5°$
E	$-0.5° \leq \partial T/\partial Z < 1.5°$
F	$1.5° < \partial T/\partial Z$

表六　以水平風向標準偏差爲指標之大氣穩定度分類

穩定度	變化範圍
A	$\sigma_\theta \geq 22.5$
B	$22.5 > \sigma_\theta \geq 17.5$
C	$17.5 > \sigma_\theta \geq 12.5$
D	$12.5 > \sigma_\theta \geq 7.5$
E	$7.5 > \sigma_\theta \geq 3.8$
F	$3.8 > \sigma_\theta$

表七　以水平風向偏差爲指標之大氣穩定度分類在夜間之修正

σ_θ（°）	白天之穩定度	風速（m／sec）	夜間穩定度
$\sigma_\theta \geq 22.5$	A	$u < 2.4$	G
		$2.4 \leq u < 2.9$	F
		$2.9 \leq u < 3.6$	B
		$3.6 \leq u$	D
$22.5 > \sigma_\theta \geq 17.5$	B	$u < 2.4$	F
		$2.4 \leq u < 3.0$	E
		$3.0 \leq u$	D
$17.5 > \sigma_\theta \geq 12.5$	C	$u < 2.4$	E
		$2.4 \leq u$	D
$12.5 > \sigma_\theta \geq 7.5$	D	所有風速	D
$7.5 > \sigma_\theta \geq 3.8$	E	所有風速	B
$3.8 > \sigma_\theta \geq 2.1$	F	所有風速	F
$2.1 > \sigma_\theta$	G	所有風速	G

註：所謂「夜間」，乃指日落前一小時至日出後一小時之時間。

表八　日射量、太陽天頂角、α及雲量之關係

日射量 ＼ 雲量 / α	≥4／8	＜4／8
0°～35°	弱	弱
35°～60°	弱	中
60°～90°	中	強

表九　風速歸類表

風速等級	風速區間 Knots	風速區間 m／s	各級中間風速（m／s）
1	0 — 3	0.0 — 2.0	1.50
2	4 — 6	2.0 — 3.5	2.46
3	7 — 10	3.5 — 5.7	4.47
4	11 — 16	5.7 — 8.3	6.93
5	17 — 21	8.3 — 11.0	9.61
6	＞21	＞11.0	12.52

表四　Pasquill大氣穩定度分類

地面風速（m/s）（10公尺高）	白天日射量			夜晚	
	强	中	弱	雲量≥ 4/8	雲量≤ 3/8
2	A	A～B	B	—	—
2～3	A～B	B	C	E	F
3～5	B	B～C	C	D	E
5～6	C	C～D	D	D	D
＞6	C	D	D	D	D

註：(1)不論白天或夜晚，當至天空雲量爲8/8時，穩定度級爲D。

(2)對於A～B級，乃是各別以A、B所對應之值再平均者。

表五　以水平風向標準偏差和溫度遞減率爲指標之大氣穩定度分類

穩定度	變化範圍
A	$22.5° \leq \sigma_\theta$
B	$17.5° \leq \sigma_\theta < 22.5°$
C	$12.5° \leq \sigma_\theta < 17.5°$
D	$-1.5° \leq \partial T/\partial Z < -0.5°$
E	$-0.5° \leq \partial T/\partial Z < 1.5°$
F	$1.5° < \partial T/\partial Z$

表六　以水平風向標準偏差爲指標之大氣穩定度分類

穩定度	變化範圍
A	$\sigma_\theta \geq 22.5$
B	$22.5 > \sigma_\theta \geq 17.5$
C	$17.5 > \sigma_\theta \geq 12.5$
D	$12.5 > \sigma_\theta \geq 7.5$
E	$7.5 > \sigma_\theta \geq 3.8$
F	$3.8 > \sigma_\theta$

表七　以水平風向偏差爲指標之大氣穩定度分類在夜間之修正

σ_θ（°）	白天之穩定度	風速（m／sec）	夜間穩定度
$\sigma_\theta \geq 22.5$	A	$u < 2.4$	G
		$2.4 \leq u < 2.9$	F
		$2.9 \leq u < 3.6$	B
		$3.6 \leq u$	D
$22.5 > \sigma_\theta \geq 17.5$	B	$u < 2.4$	F
		$2.4 \leq u < 3.0$	E
		$3.0 \leq u$	D
$17.5 > \sigma_\theta \geq 12.5$	C	$u < 2.4$	E
		$2.4 \leq u$	D
$12.5 > \sigma_\theta \geq 7.5$	D	所有風速	D
$7.5 > \sigma_\theta \geq 3.8$	E	所有風速	B
$3.8 > \sigma_\theta \geq 2.1$	F	所有風速	F
$2.1 > \sigma_\theta$	G	所有風速	G

註：所謂「夜間」，乃指日落前一小時至日出後一小時之時間。

表八　日射量、太陽天頂角、α及雲量之關係

日射量 ＼ 雲量 ／ α	≥4／8	＜4／8
0°～35°	弱	弱
35°～60°	弱	中
60°～90°	中	强

表九　風速歸類表

風速等級	風速區間 Knots	風速區間 m／s	各級中間風速（m／s）
1	0 — 3	0.0 — 2.0	1.50
2	4 — 6	2.0 — 3.5	2.46
3	7 — 10	3.5 — 5.7	4.47
4	11 — 16	5.7 — 8.3	6.93
5	17 — 21	8.3 — 11.0	9.61
6	＞21	＞11.0	12.52

表十　z 方向污染物濃度擴散標準偏差 σ_z 與 x 之關係

穩定度等級	$\sigma_z = a x^b$ a	b	下風距離範圍
A	158.08	1.0542	$x \leq$ 150
	170.22	1.0932	$150 < x \leq$ 200
	179.52	1.1262	$200 < x \leq$ 250
	217.41	1.2644	$250 < x \leq$ 300
	258.89	1.4094	$300 < x \leq$ 400
	346.75	1.7283	$400 < x \leq$ 500
	453.85	2.1166	$500 < x \leq$ 3,110
	$\sigma_z = 5000$		$3,110 < x$
B	90.673	0.93198	$x \leq$ 200
	98.483	0.98332	$200 < x \leq$ 400
	109.30	1.0971	$400 < x$
C	61.141	0.91465	
D & G	34.459	0.86974	$x \leq$ 300
	32.093	0.81066	$300 < x \leq$ 1,000
	32.093	0.64403	$1,000 < x \leq$ 3,000
	33.504	0.60486	$3,000 < x \leq$ 10,000
	36.650	0.56589	$10,000 < x \leq$ 30,000
	44.053	0.51179	$30,000 < x$
E	23.331	0.81956	$x \leq$ 300
	21.628	0.75660	$300 < x \leq$ 1,000
	21.628	0.63077	$1,000 < x \leq$ 2,000
	22.534	0.57154	$2,000 < x \leq$ 4,000
	24.703	0.50527	$4,000 < x \leq$ 10,000
	26.970	0.46713	$10,000 < x \leq$ 20,000
	35.420	0.37615	$20,000 < x \leq$ 40,000
	47.618	0.29592	$40,000 < x$
F	15.209	0.81558	$x \leq$ 200
	14.457	0.78407	$200 < x \leq$ 700
	13.953	0.68465	$700 < x \leq$ 1,000
	13.953	0.63227	$1,000 < x \leq$ 2,000
	14.823	0.54503	$2,000 < x \leq$ 3,000
	16.187	0.46490	$3,000 < x \leq$ 7,000
	17.836	0.41507	$7,000 < x \leq$ 15,000
	22.651	0.32681	$15,000 < x \leq$ 30,000
	27.074	0.27436	$30,000 < x \leq$ 60,000
	34.219	0.21716	$60,000 < x$

表十一　y 方向（與風向正交的水平方向）污染物濃度擴散標準偏差，σ_y

穩定度級數	$\sigma_y = 1000 \times y \times \sin\theta / (2.15 \times \cos\theta)$ θ 值計算式
A	$\theta = (24.167 - 2.5334\ \ell n(y)) / 57.2958$
B	$\theta = (18.333 - 1.8096\ \ell n(y)) / 57.2958$
C	$\theta = (12.5 - 1.0587\ \ell n(y)) / 57.2958$
D 與 G	$\theta = (8.3333 - 0.72382\ \ell n(y)) / 57.2958$
E	$\theta = (6.25 - 0.54287\ \ell n(y)) / 57.2958$
F	$\theta = (4.1667 - 0.36191\ \ell n(y)) / 57.2958$

表十二　污染源及其排放條件

高雄煉油廠資料乃採鍋爐集合煙囪的排放資料。各污染源的污染物排放量係假設值。

污染源 \ 排放條件	煙囪彎度 (m)	排放速度 (m/s)	煙囪直徑 (m)	排放溫度 (℃)	NO_x (g/s)	C_4H_8 (g/s)	SO_2 (g/s)
興達火力發電廠	250	13.4	6.9	150	400	0.28	1400.0
大林火力發電廠	132	18.48	6.09	147	700	0.3	2800.0
高雄煉油廠	70	10.0	7.8	161	420	0.3	1150.0

表十三　全年各種溫度發生機率

穩定度	A	B	C	D	E	F
發生機率累計	0.03920	0.16212	0.14308	0.32703	0.15232	0.17640

表十四　全年各種風向發生機率

風向	1	2	3	4	5	6	7	8
發生機率	0.08988	0.09184	0.08344	0.03584	0.01372	0.03192	0.03528	0.03388
風向	9	10	11	12	13	14	15	16
發生機率	0.03360	0.02660	0.03948	0.06020	0.10276	0.05740	0.12179	0.14252

表十五　計算各污染物濃度間非線性變化時不同輸入因素的分類

影響因素	分類					
穩定度	A	B	C	D	E	F
風速（m/s）	1.50	2.46	4.47	6.93	9.61	12.52
NO_2（ppm）	100	300	500	700	900	
NO（ppm）	900	700	500	300	100	
C_4H_8（ppm）	2			50		
	15			25		

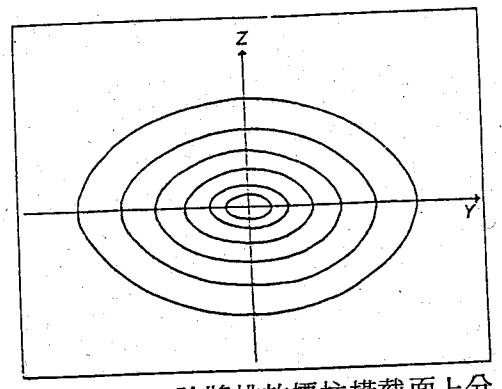

圖一　環理論將排放煙柱橫截面上分成許多同心圓或橢圓。每二環線間的面積中含有和其他環等量的污染物質，由於擴散，環面積逐漸擴大。x 軸向環面也逐漸增大。

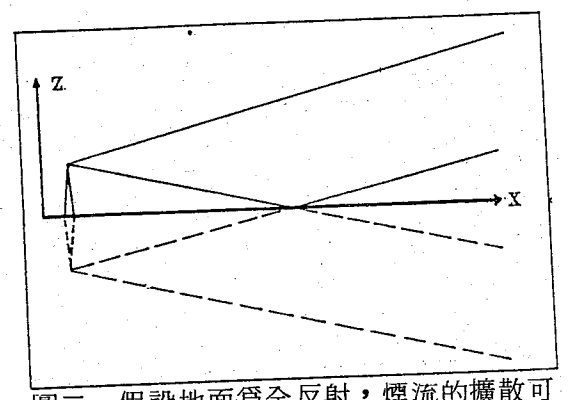

圖二　假設地面爲全反射，煙流的擴散可視爲位於眞正污染源的對稱位置上（以地面而言），存在一假想污染源做等量的排放。

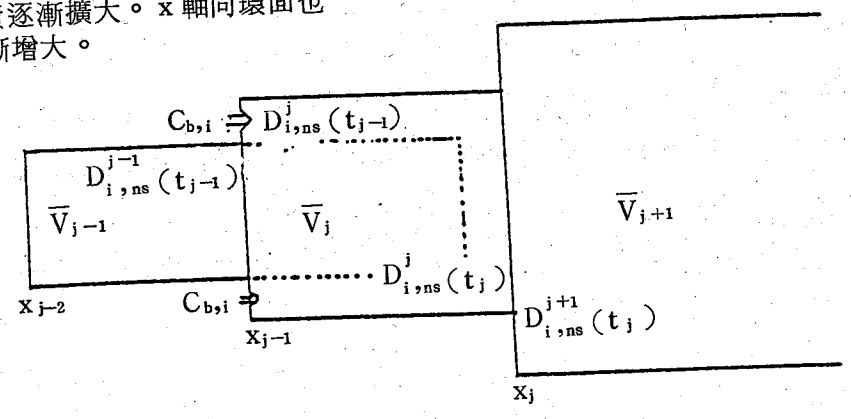

圖三　巢與巢的交界處二端，理論上污染物量會相同，但因背景濃度的加入，使結果並不相同。V_j 表示在 t 時之巢體積。$C_{b,i}$ 爲第 i 種污染物之背景濃度。x_j 爲 t_j 時之 x 軸向位置點。$D_{i,ns}(t_j)$ 和 $D^{j+1}_{i,ns}(t_j)$ 分別表示在 x_j 點區分成的左右二巢中接近 x_j 處，第 i 種污染物在第 ns 層區中的污染物總量。

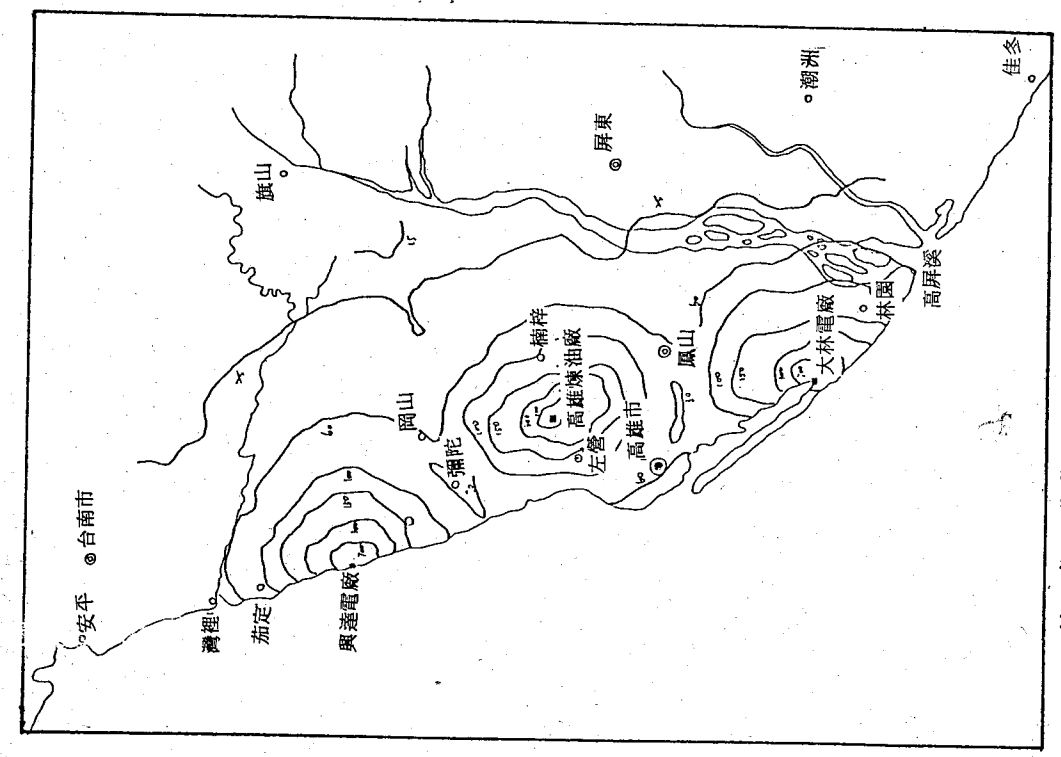

圖四　第二組光化學反應所計算 NO_2 的濃度分佈圖（$\times 10^{-6}$ ppm）

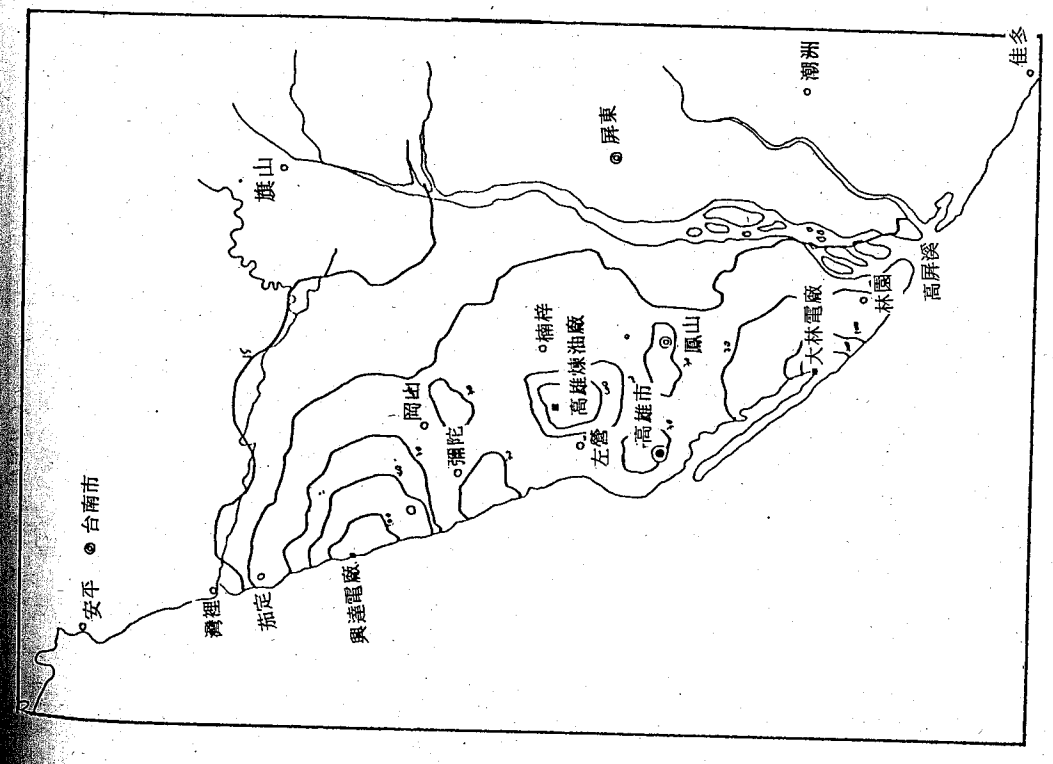

圖五　第二組光化學反應所計算 NO 的濃度分佈圖（$\times 10^{-6}$ ppm）

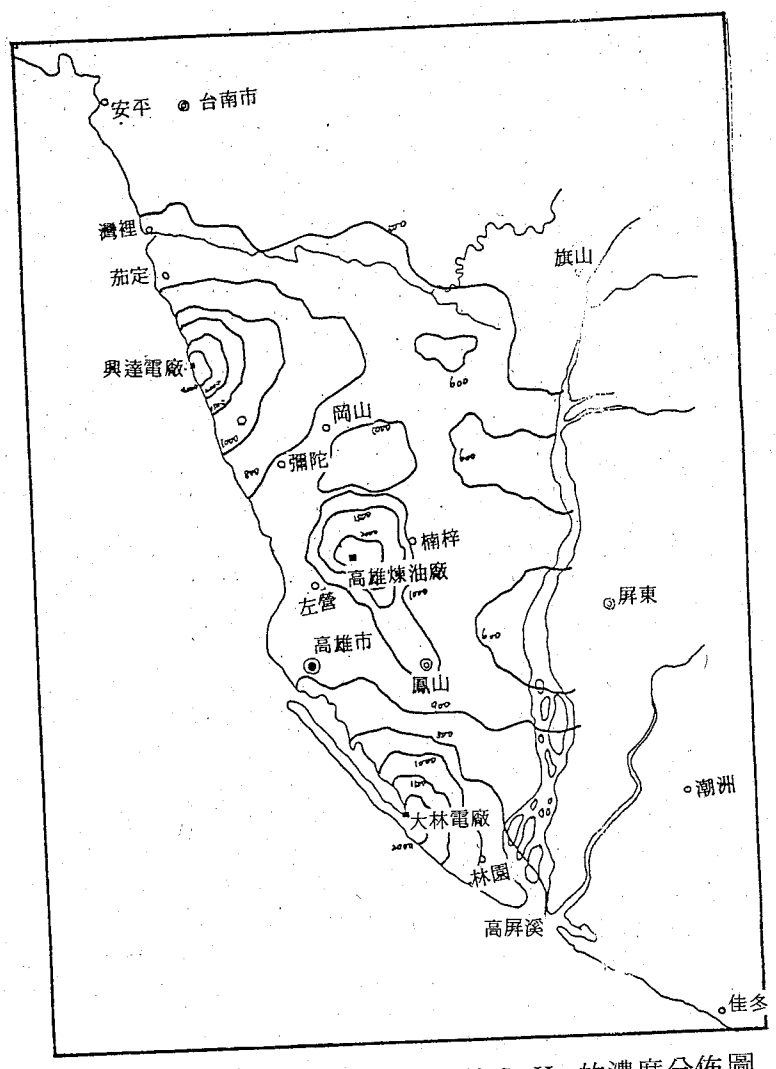

圖七　第二組光化學反應所計算C_4H_8的濃度分佈圖
（$\times 10^{-9}$ ppm）

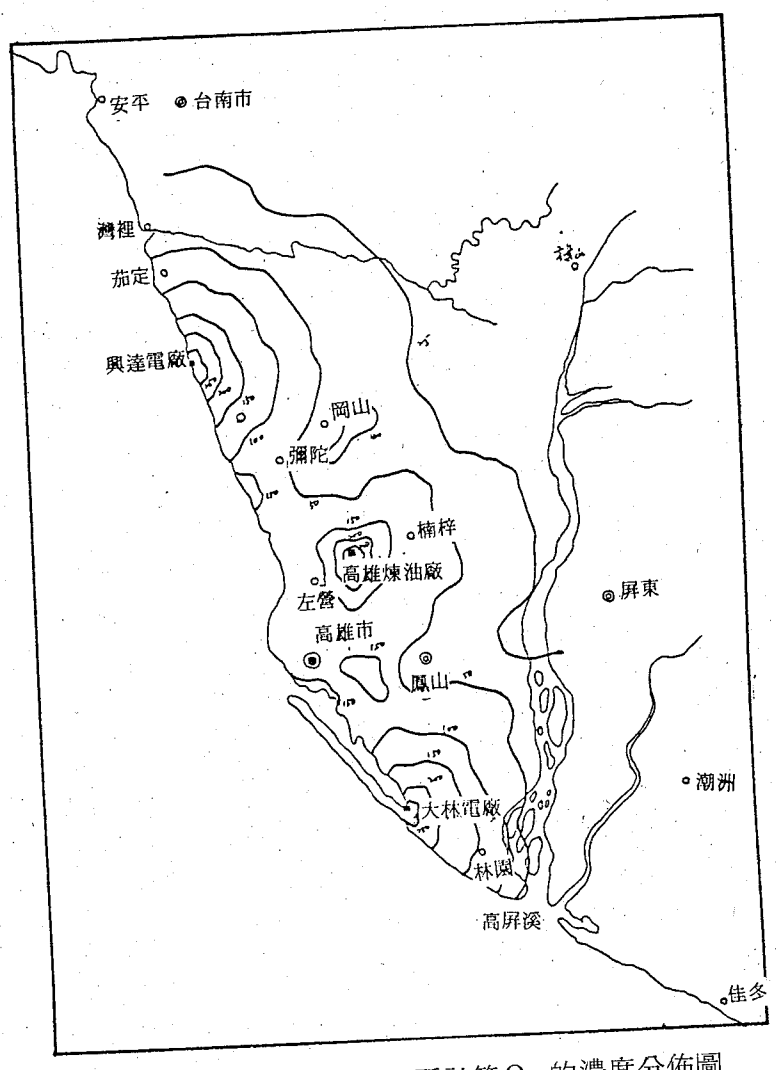

圖六　第二組光化學反應所計算O_3的濃度分佈圖
（$\times 10^{-6}$ ppm）

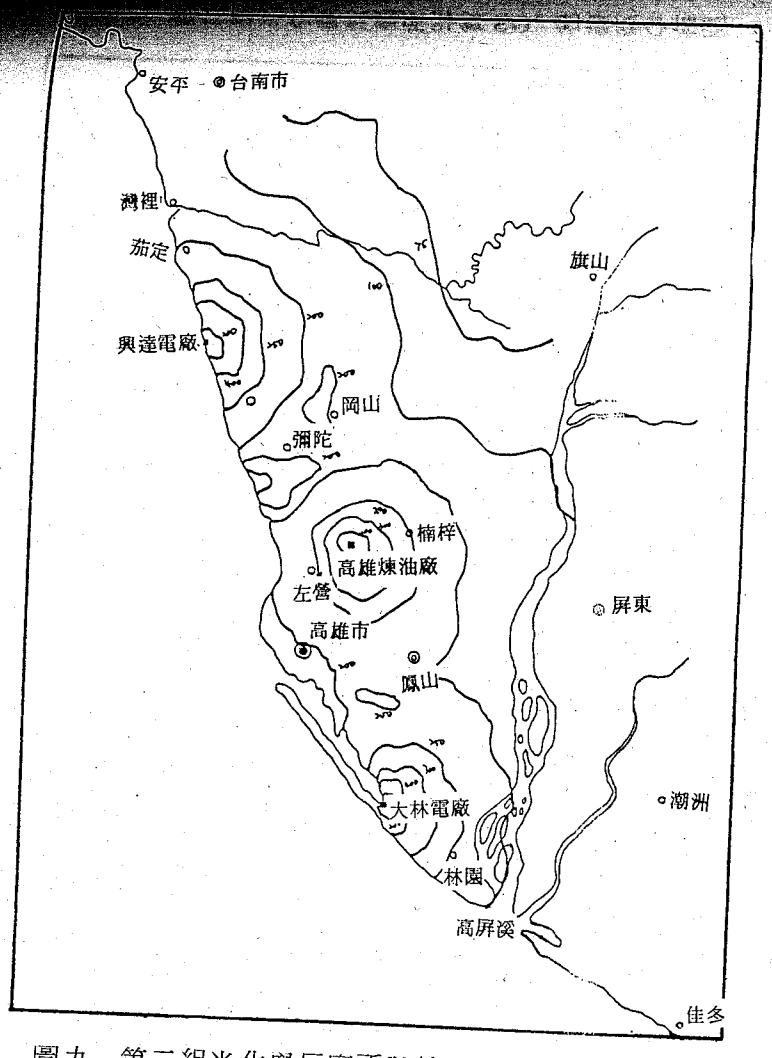

圖九　第二組光化學反應所計算ALD的濃度分佈圖
（$\times 10^{-12}$ ppm）

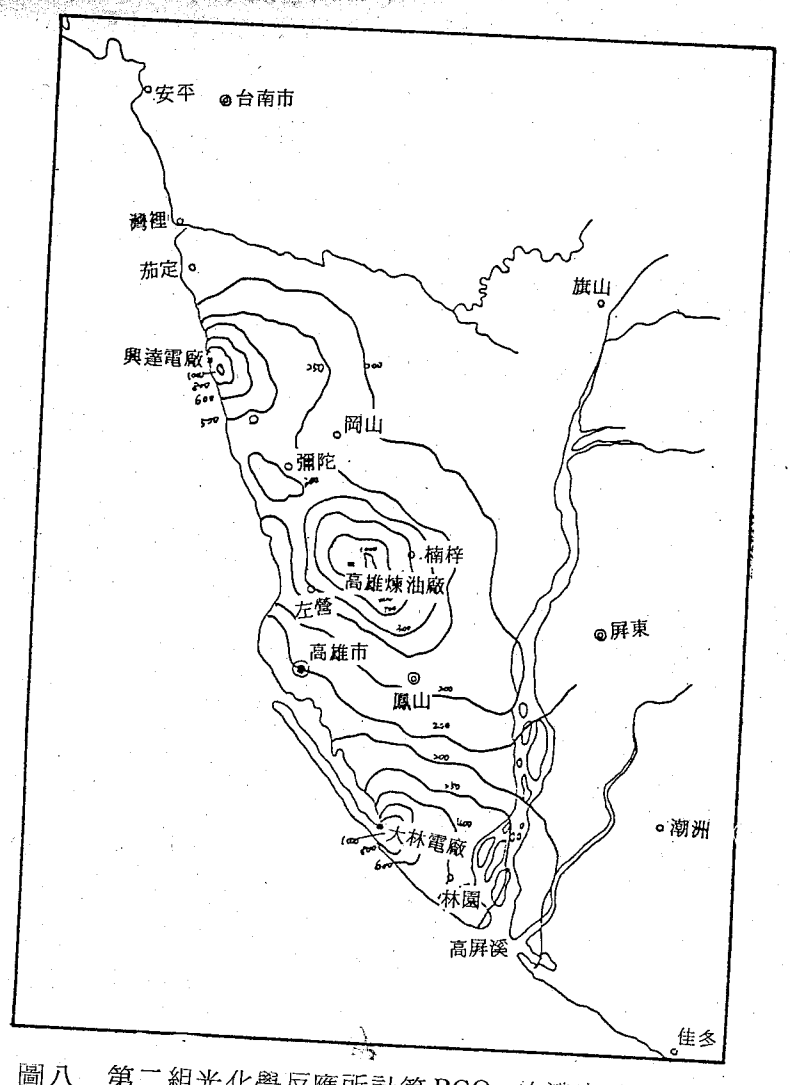

圖八　第二組光化學反應所計算RCO_x的濃度分佈圖
（$\times 10^{-6}$ ppm）

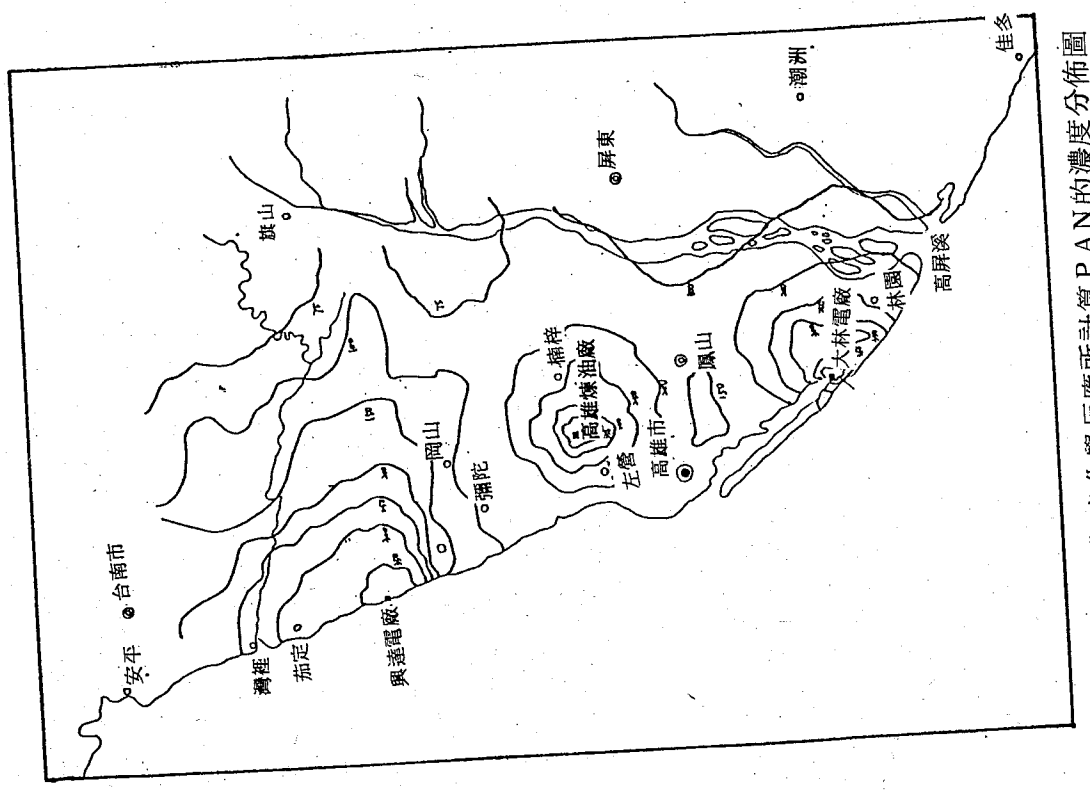

圖十　第二組光化學反應所計算 PAN 的濃度分佈圖（$\times 10^{-9}$ ppm）

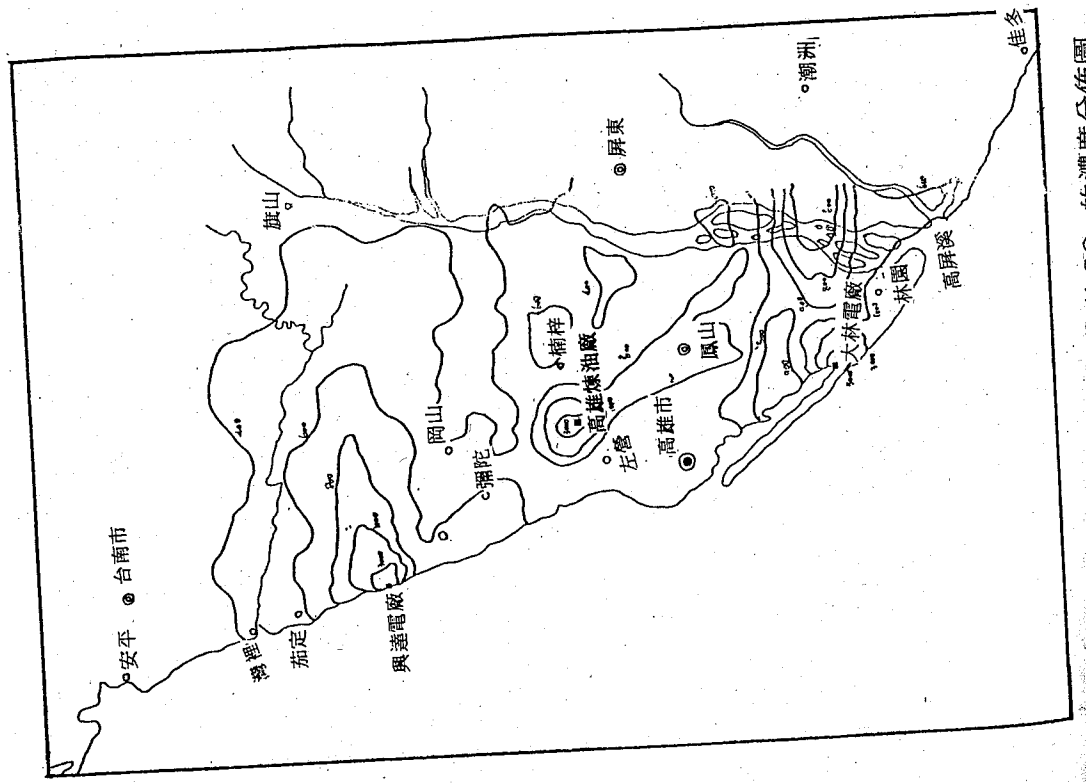

圖十一　第三組光化學反應所計算 SO_2 的濃度分佈圖

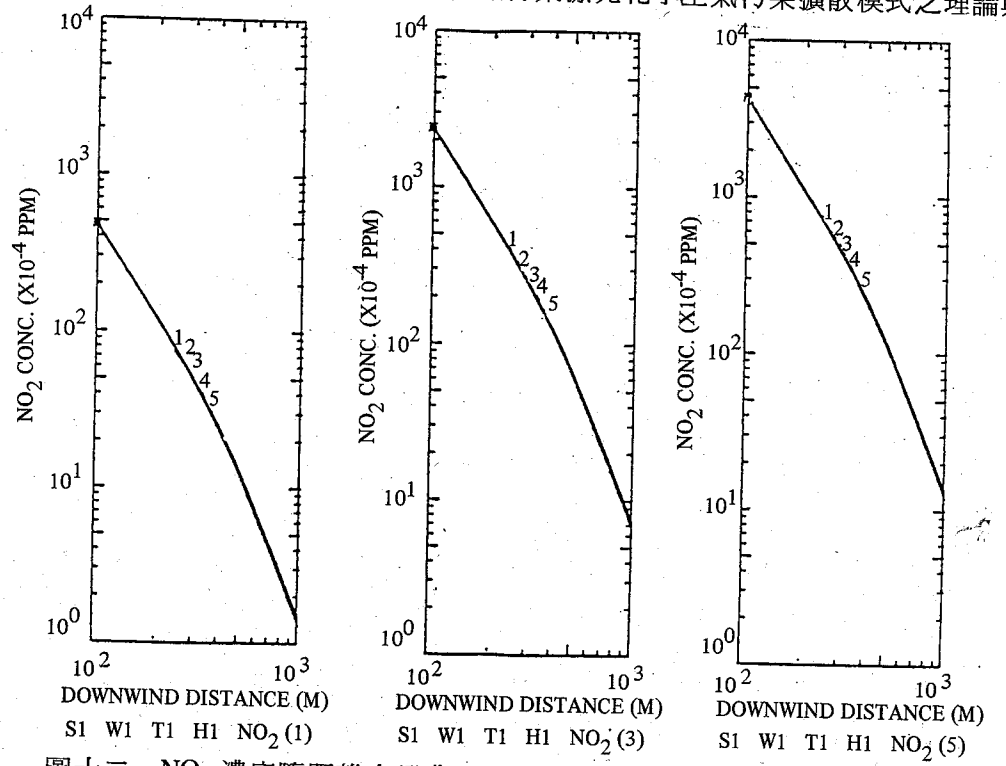

圖十二　NO_2 濃度隨距離之變化圖。圖中線 1 ～ 5 表 NO 排放濃度爲 100 、 300 、 500 、 700 、 900 ppm。NO_2(1) 、(3) 、(5)分別表 NO_2 排放濃度爲 100 、 500 、 700 ppm。本圖在穩定度 A 風速 1.5 m / s，溫度 25 ℃，C_4H_8 濃度爲 2 ppm 情況。

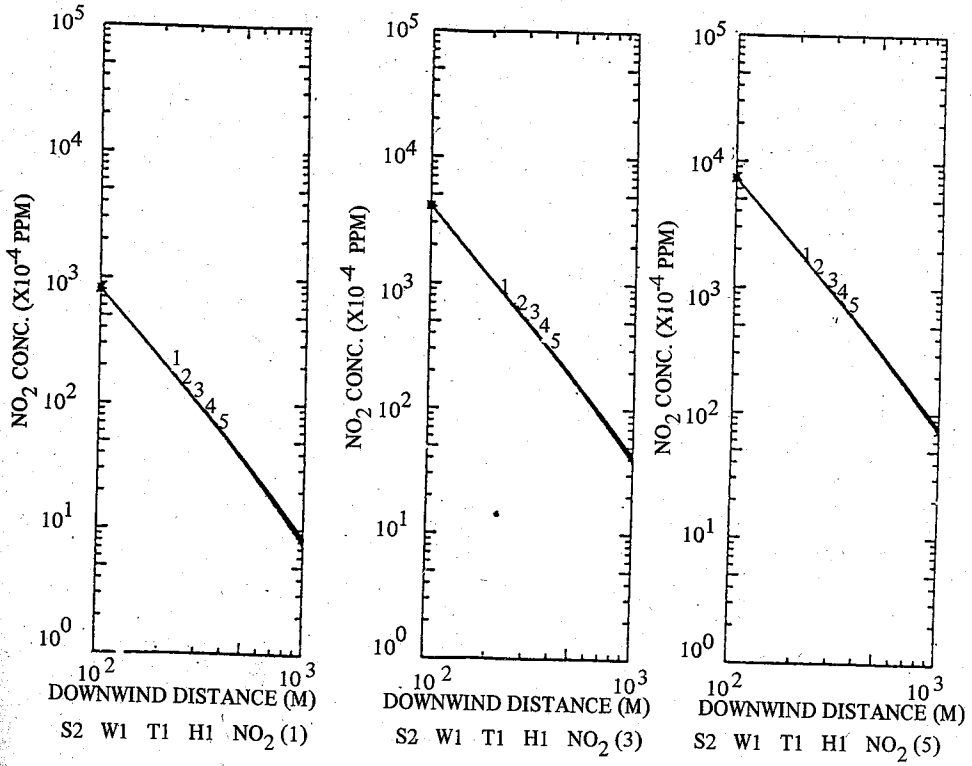

圖十三　同圖十二，但爲穩定度 B 情況。

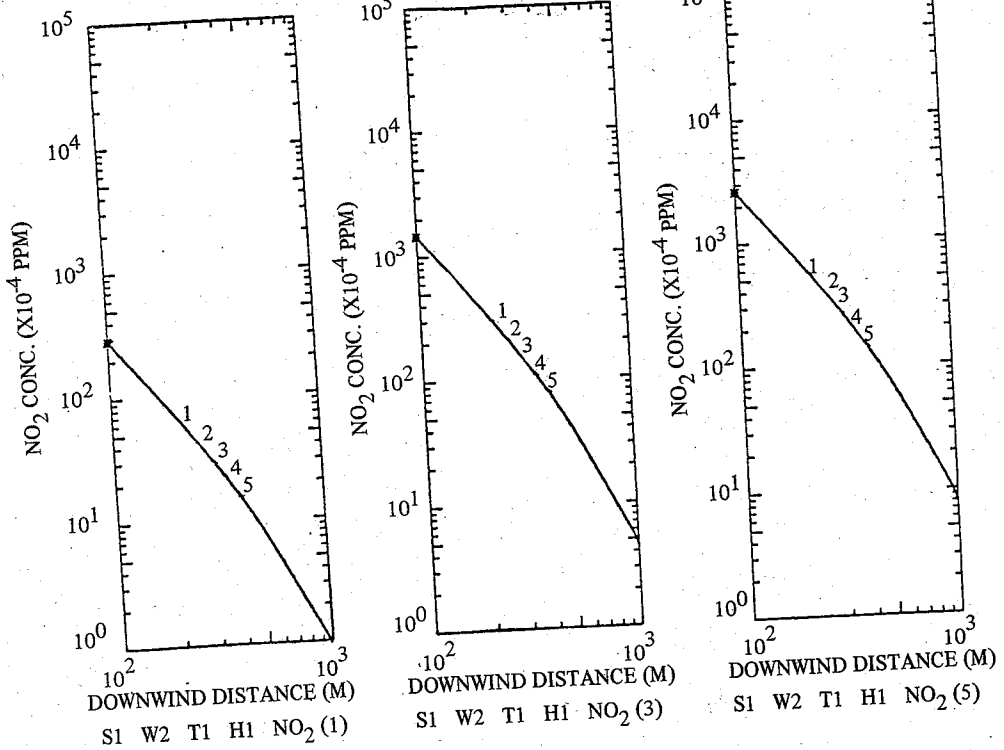

圖十四　同圖十二，但爲風速＝2.46 m/s。

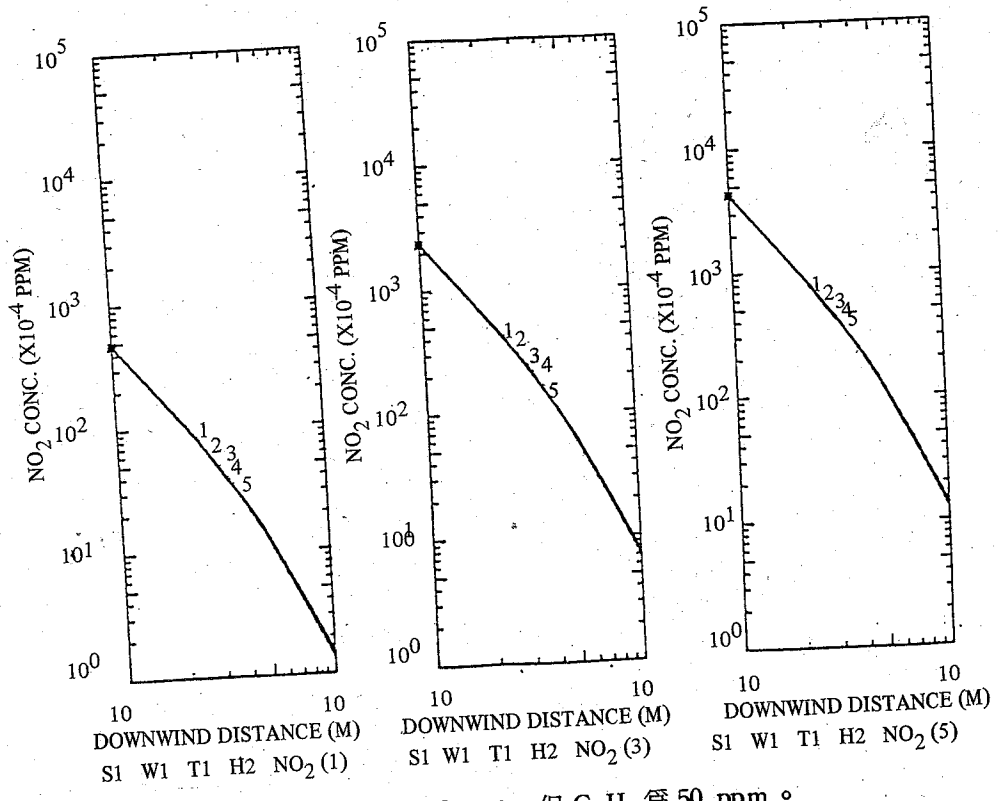

圖十五　同圖十二，但 C_4H_8 爲 50 ppm。

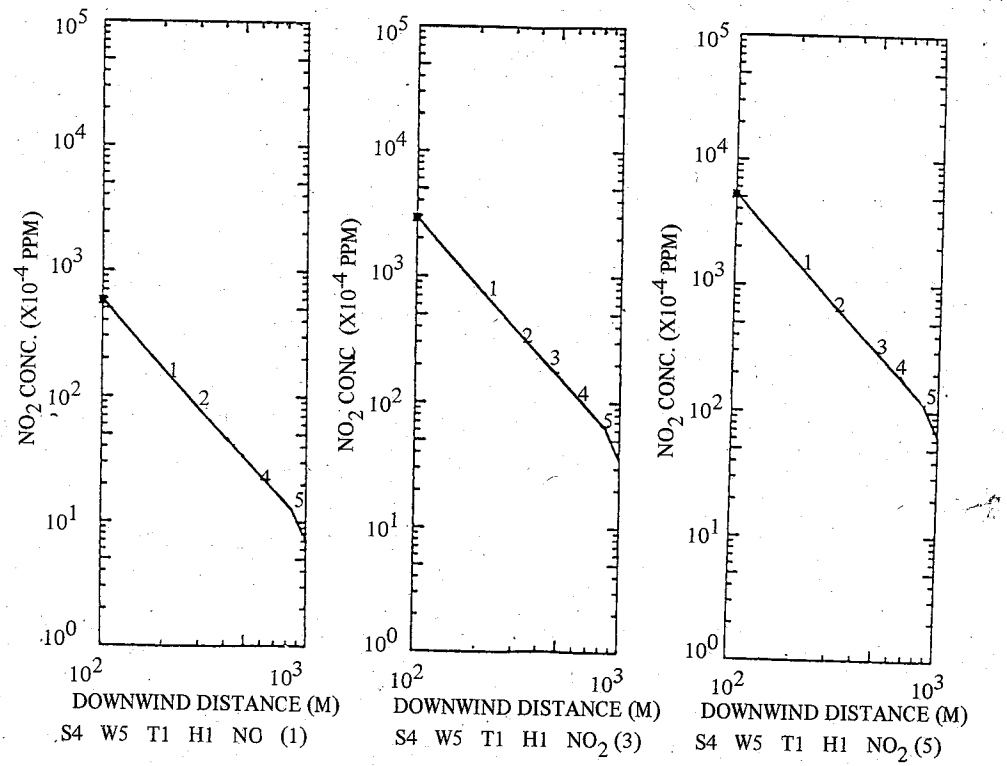

圖十六　同圖十二，但爲穩定度 D，風速 9.61 m/s 情況。

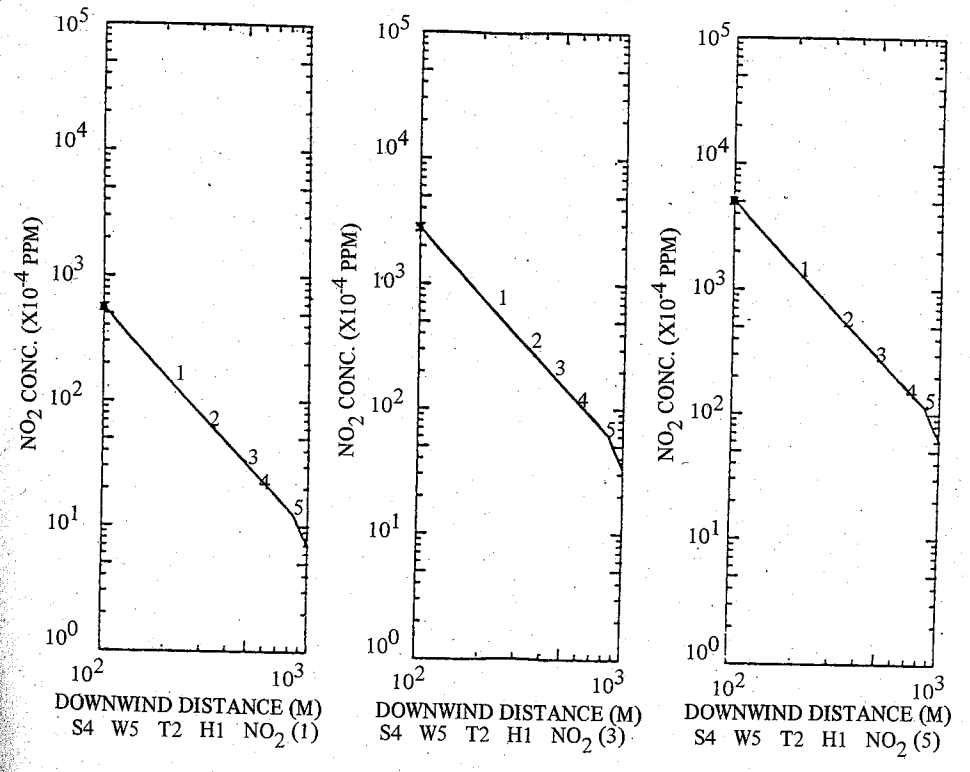

圖十七　同圖十二，但爲穩定度 D，風速 9.61 m/s，溫度 15 ℃情況。

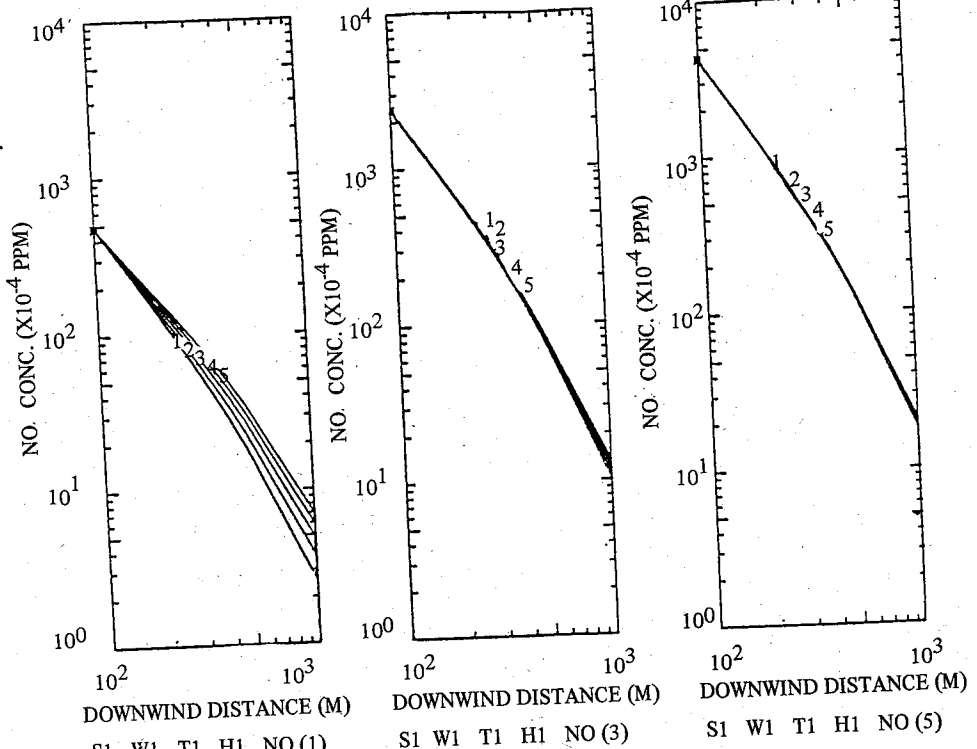

圖十八　NO 濃度隨距離之變化圖。圖中線 1 ～ 5 表 NO_2 排放濃度爲 100 、300 、500 、700 、900 ppm 。NO (1)、(3)、(5)分別表 NO 排放濃度爲 100 、500 、700 ppm 。本圖在穩定度 A，風速 1.5 m/s ，溫度 25 ℃，C_4H_8 濃度爲 2 ppm 情況。

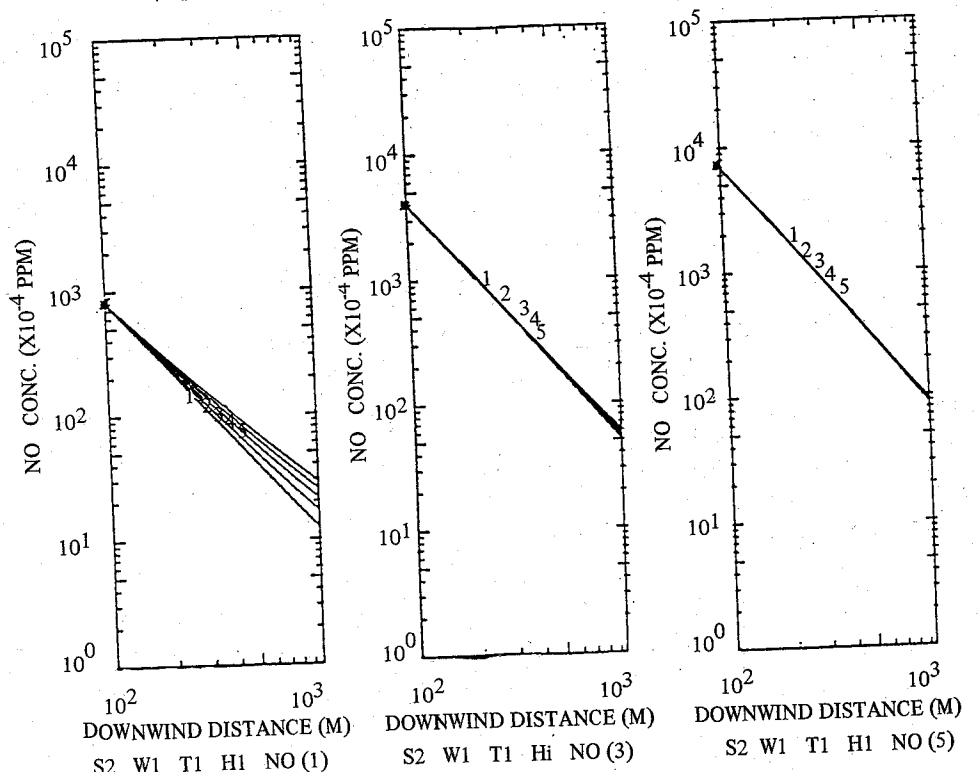

圖十九　同圖十八，但爲穩定度 B 情況

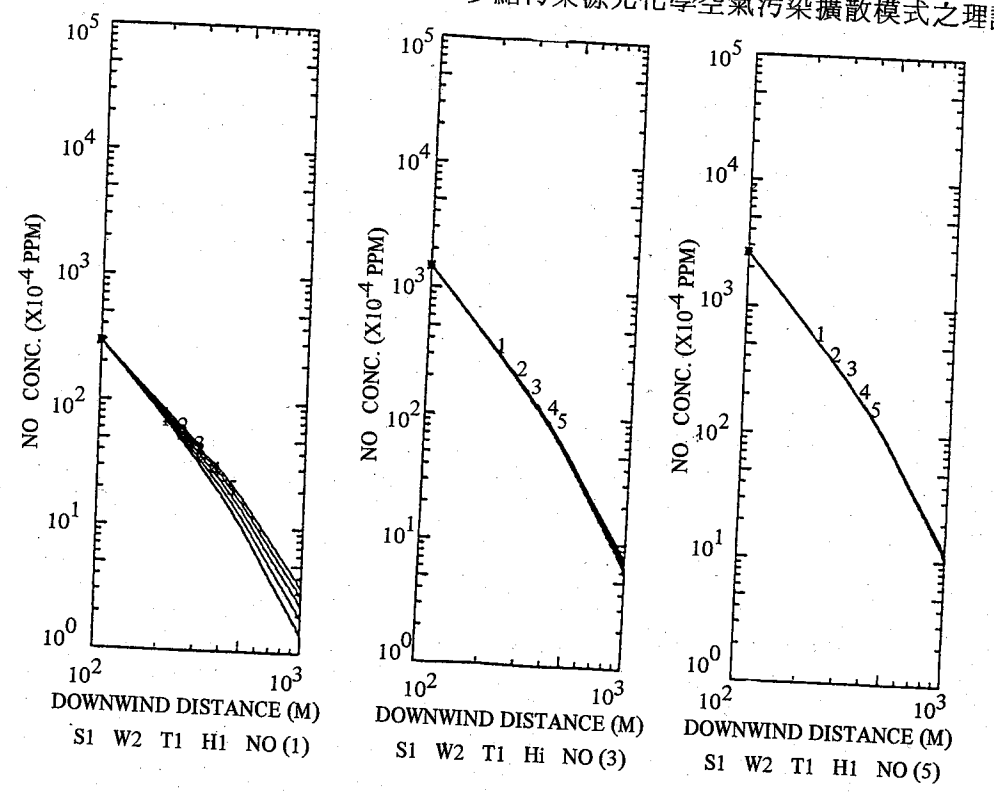

圖二十　同圖十八，但爲風速 2.46 m/s 情況

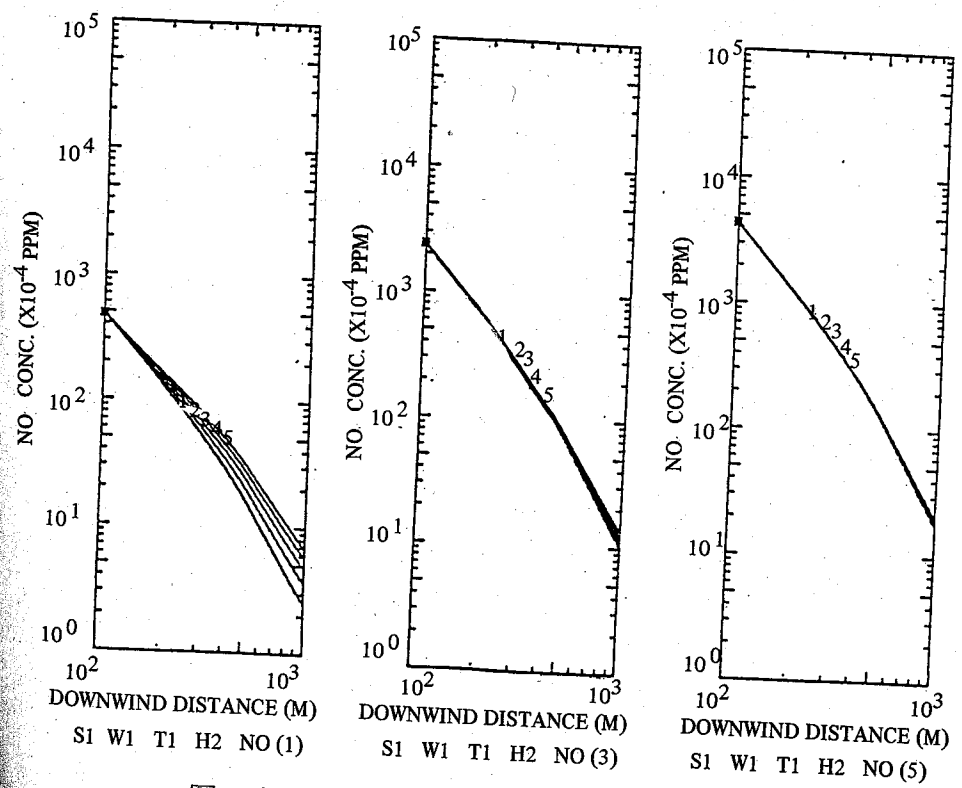

圖二十一　同圖十八，但 C_4H_8 爲 50 ppm 情況

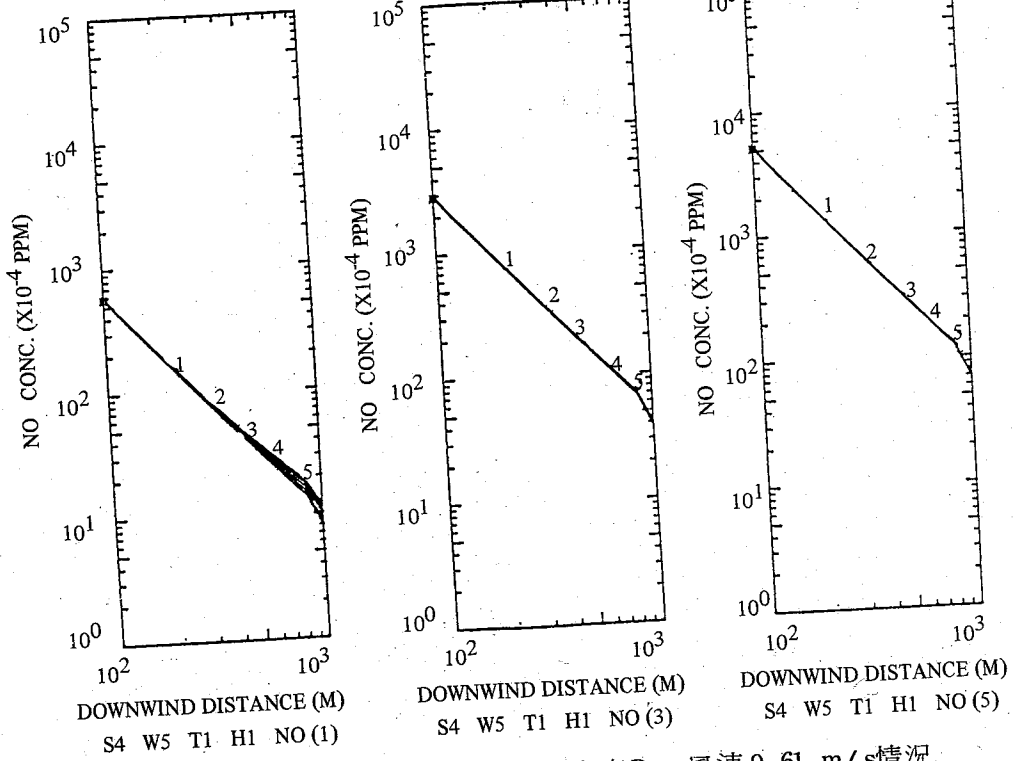

圖二十二　同圖十八，但爲穩定度D，風速 9.61 m/s情況

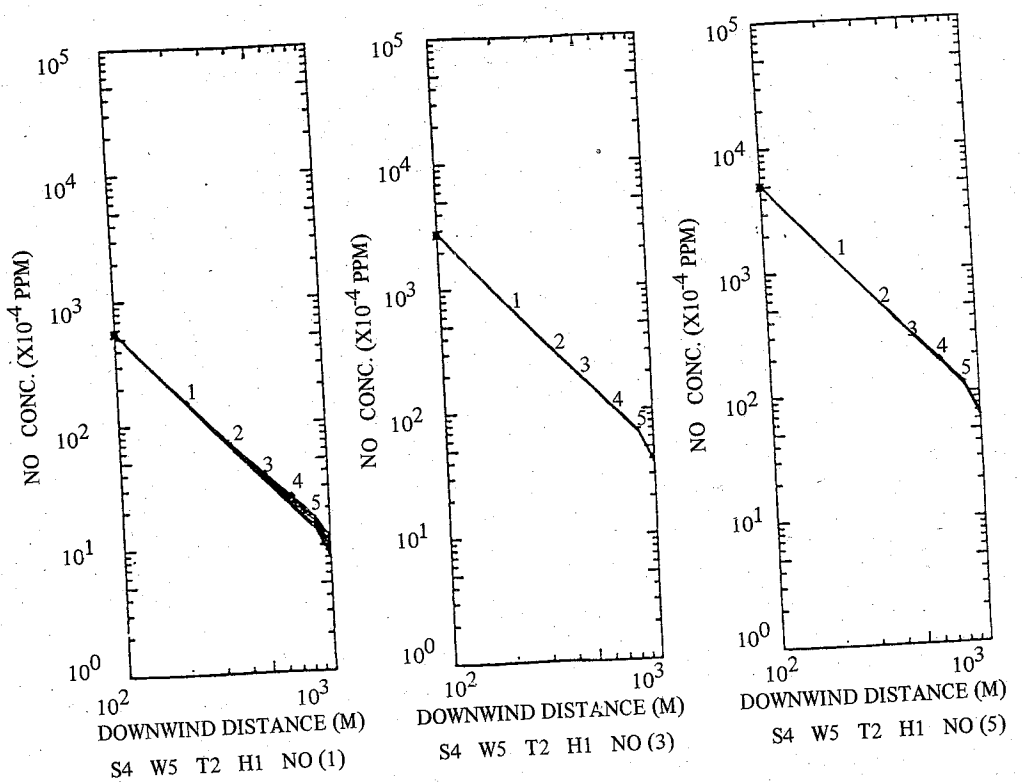

圖二十三　同圖十八，但爲穩定度D，風速 9.61 m/s，溫度 15 ℃情況

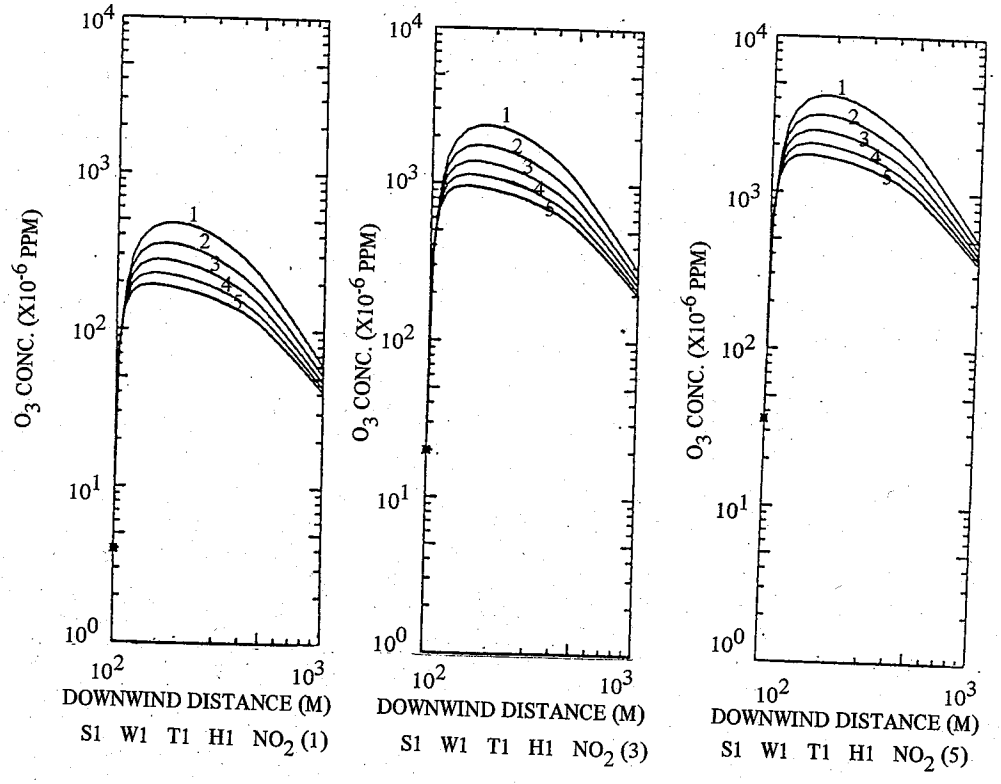

圖二十四　O_3 濃度隨距離之變化圖，其餘情況同圖十二。

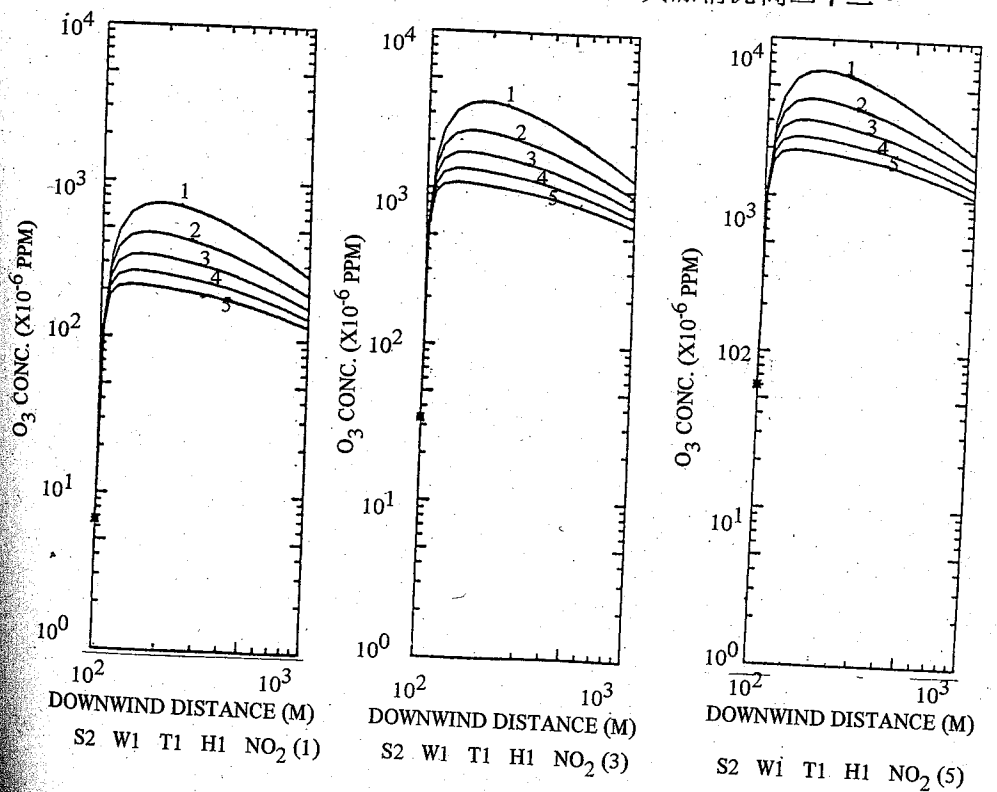

圖二十五　O_3 濃度隨距離之變化圖，其餘情況同圖十三。

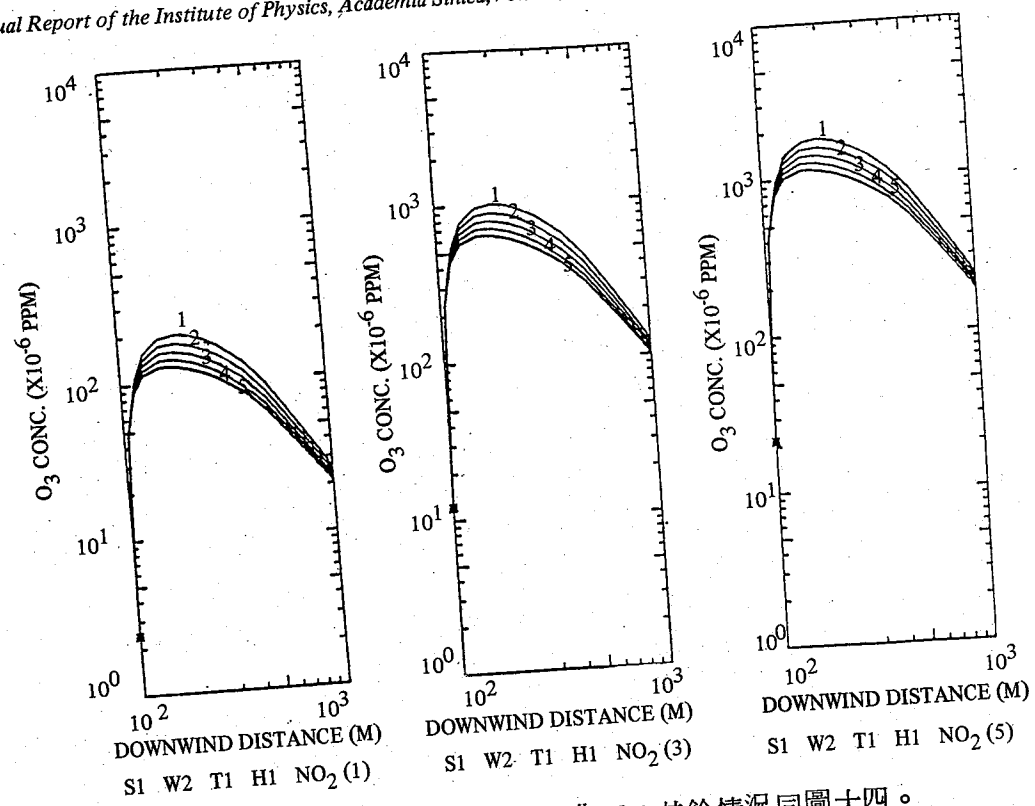

圖二十六　O_3 濃度隨距離之變化圖，其餘情況同圖十四。

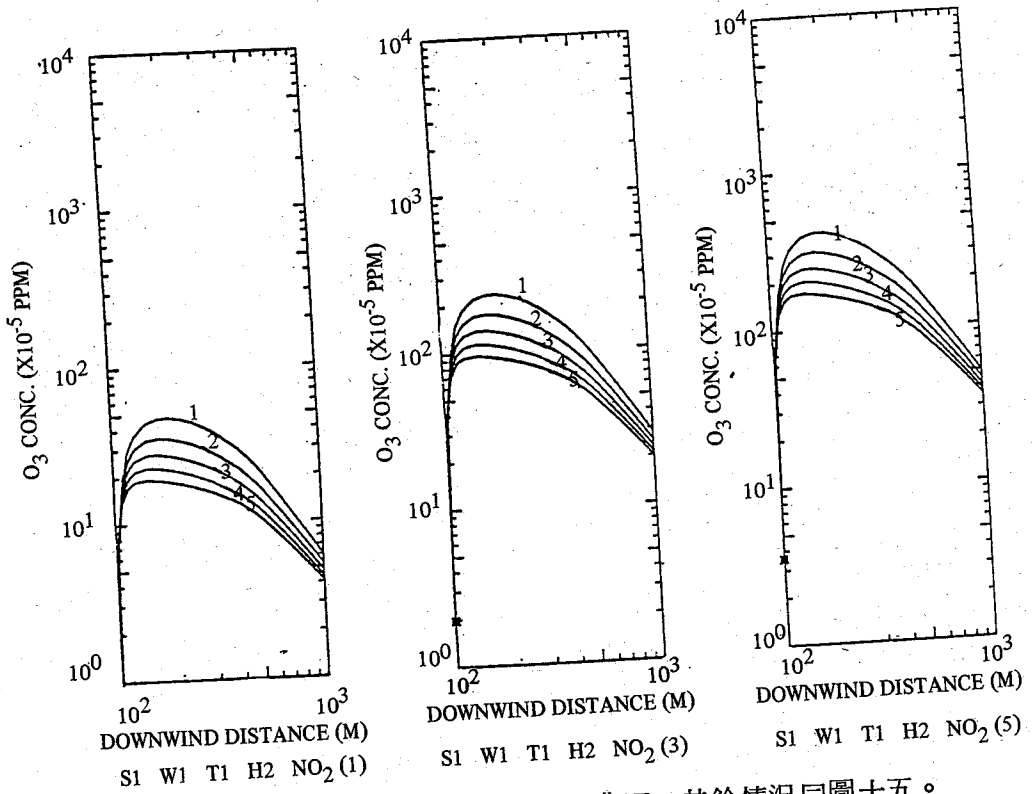

圖二十七　O_3 濃度隨距離之變化圖，其餘情況同圖十五。

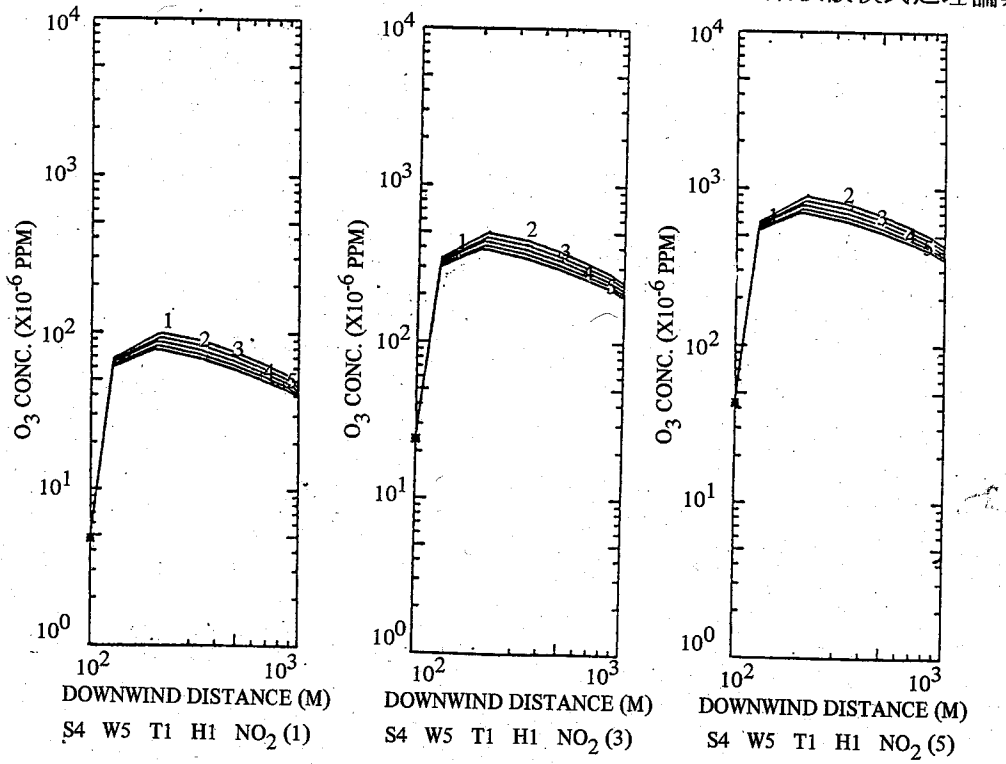

圖二十八　O_3 濃度隨距離之變化圖，其餘情況同圖十六。

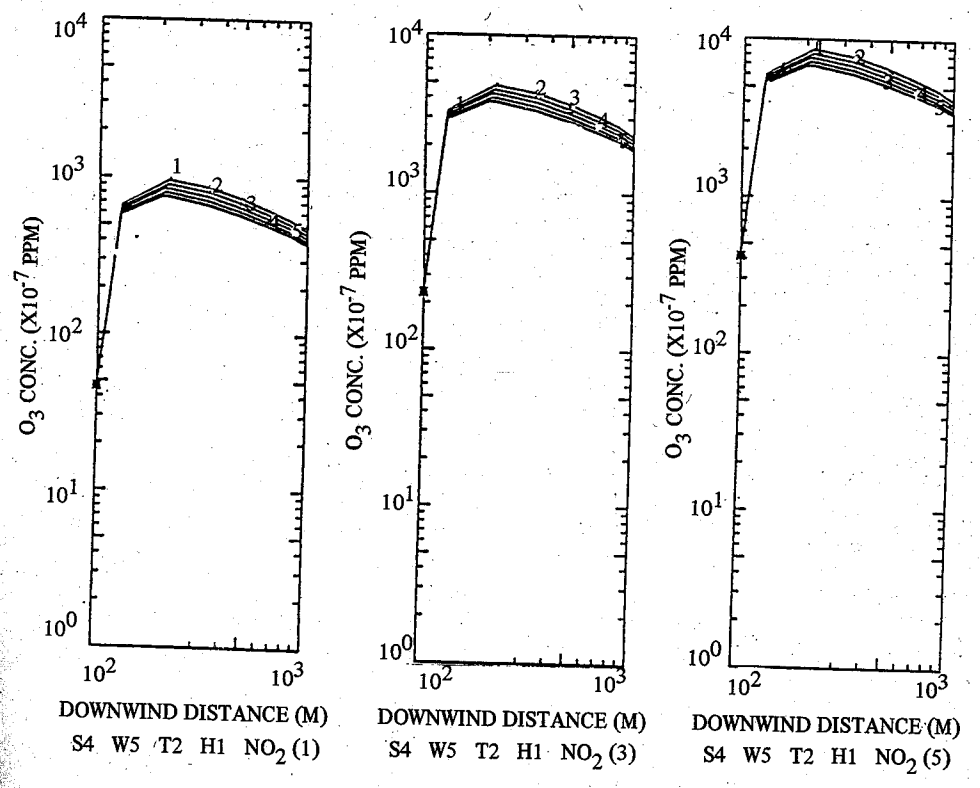

圖二十九　O_3 濃度隨距離之變化圖，其餘情況同圖十七。

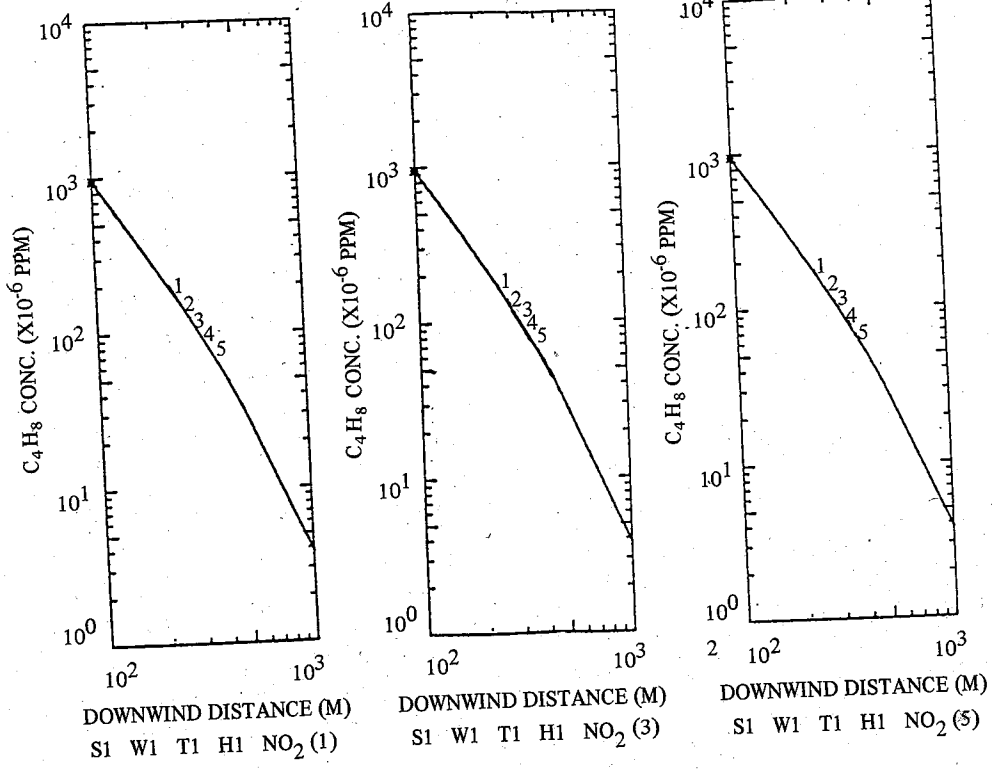

圖三十　C_4H_8 濃度隨距離之變化圖，其餘情況同圖十二。

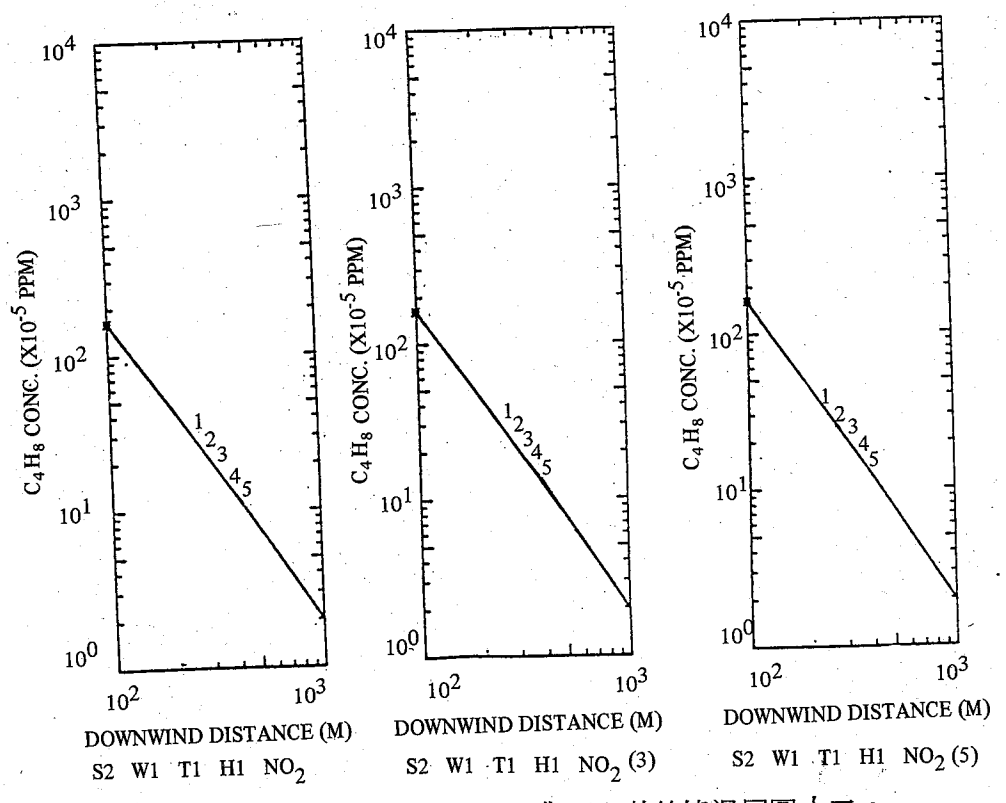

圖三十一　C_4H_8 濃度隨距離之變化圖，其餘情況同圖十三。

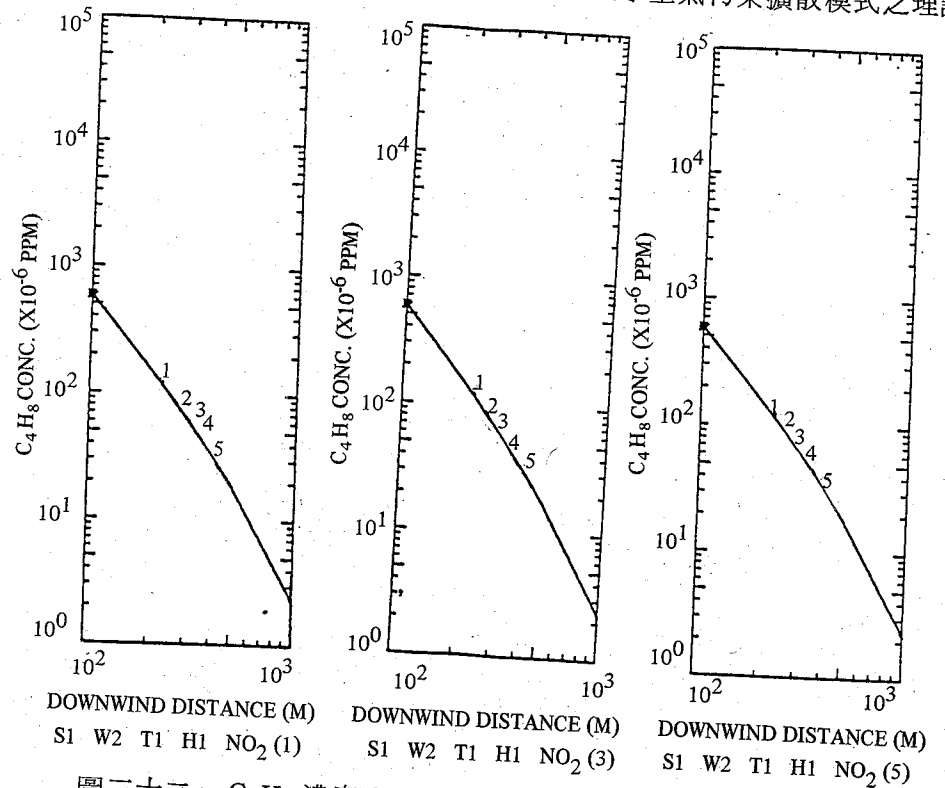

圖三十二　C_4H_8 濃度隨距離之變化圖，其餘情況同圖十四。

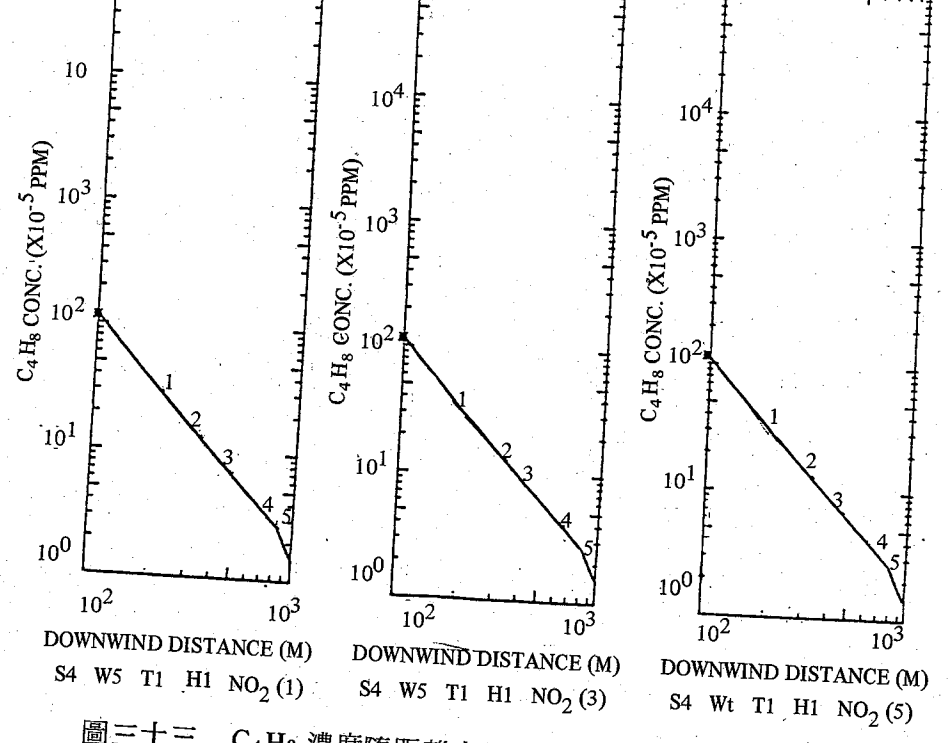

圖三十三　C_4H_8 濃度隨距離之變化圖，其餘情況同圖十六。

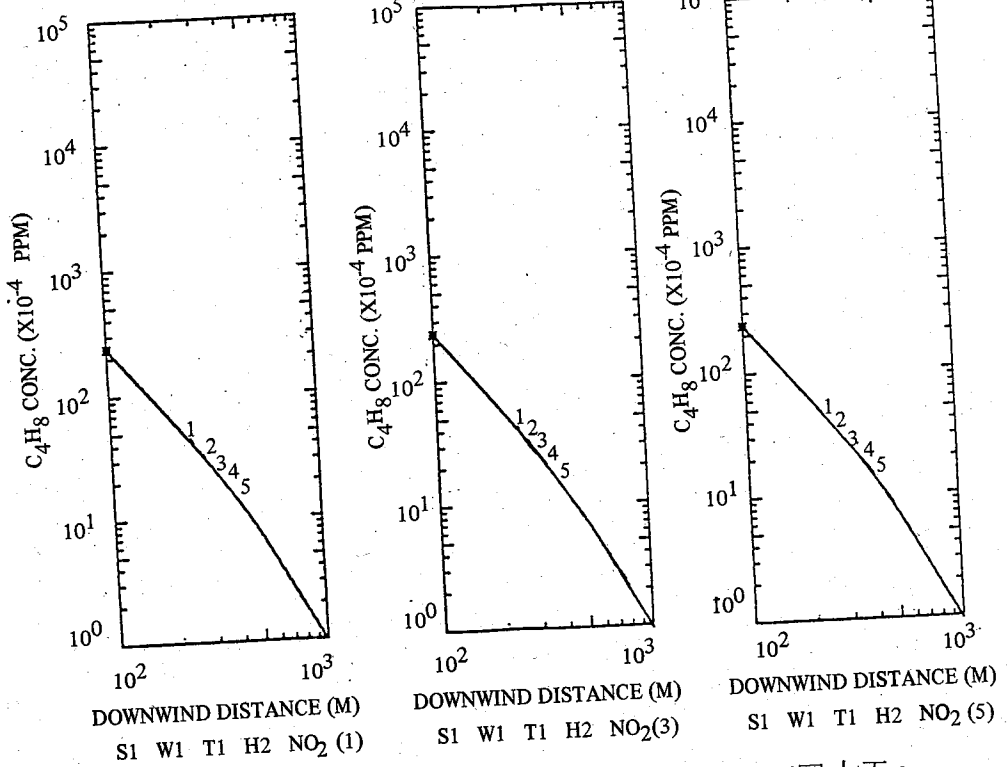

圖三十四　C_4H_8 濃度隨距離之變化圖，其餘情況同圖十五。

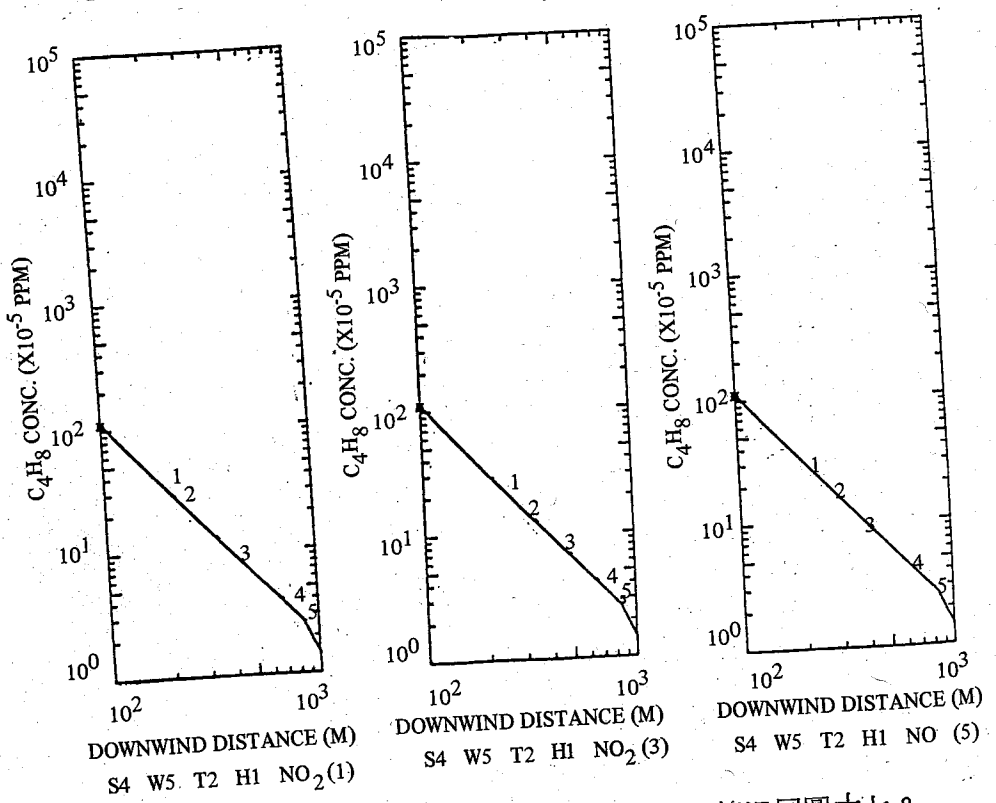

圖三十五　C_4H_8 濃度隨距離之變化圖，其餘情況同圖十七。

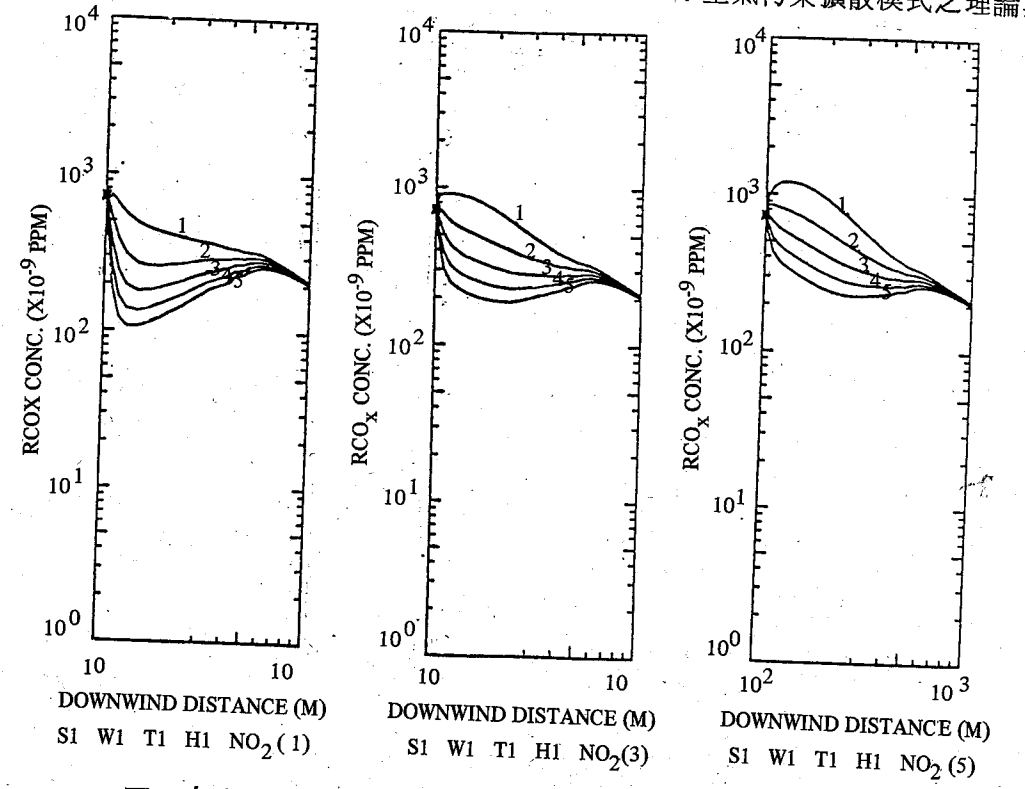

圖三十六　RCO_x濃度隨距離之變化圖，其餘情況同圖十二。

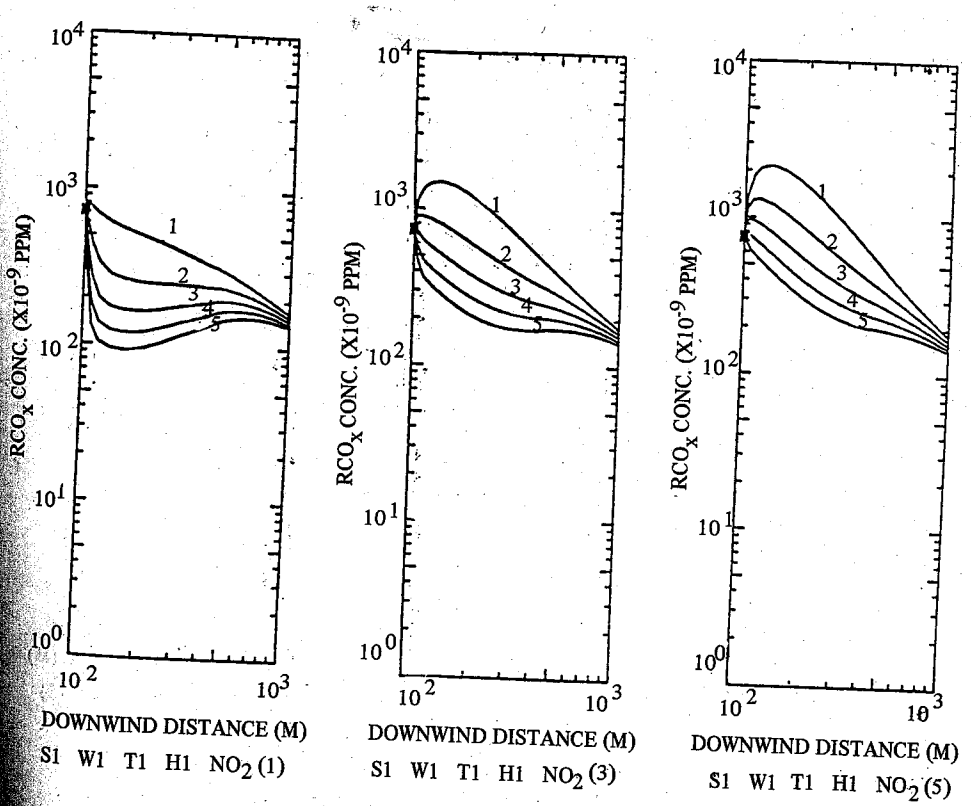

圖三十七　RCO_x濃度隨距離之變化圖，其餘情況同圖十三。

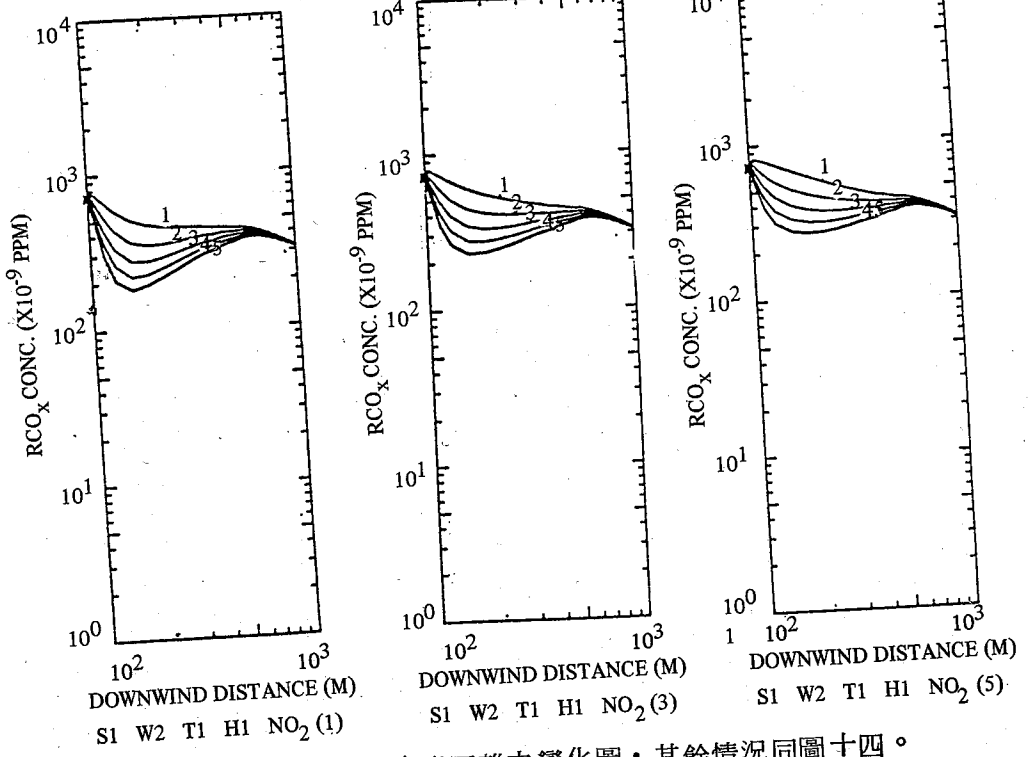

圖三十八　RCO$_x$濃度隨距離之變化圖，其餘情況同圖十四。

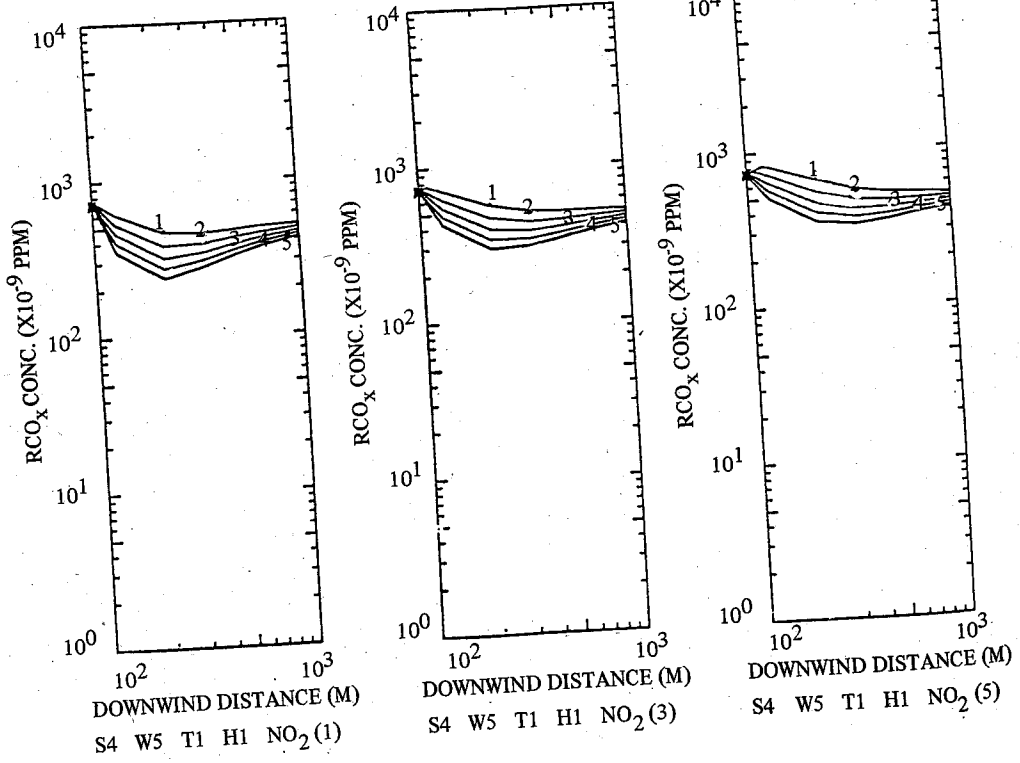

圖三十九　RCO$_x$濃度隨距離之變化圖，其餘情況同圖十六。

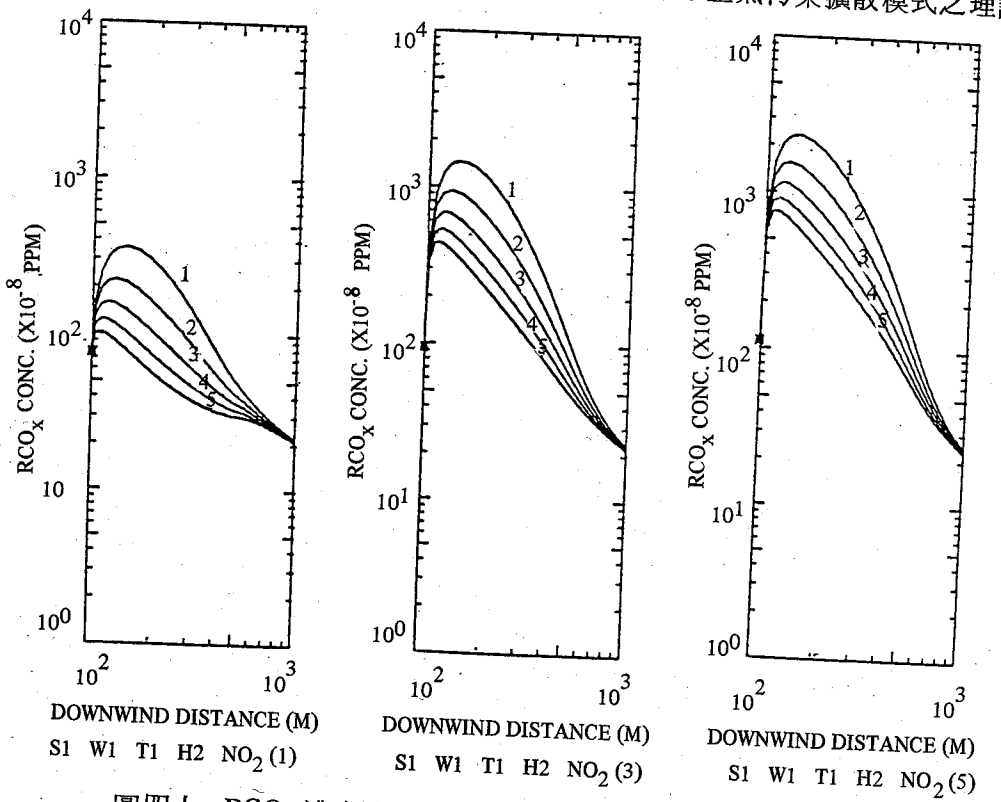

圖四十　RCO$_x$濃度隨距離之變化圖，其餘情況同圖十五。

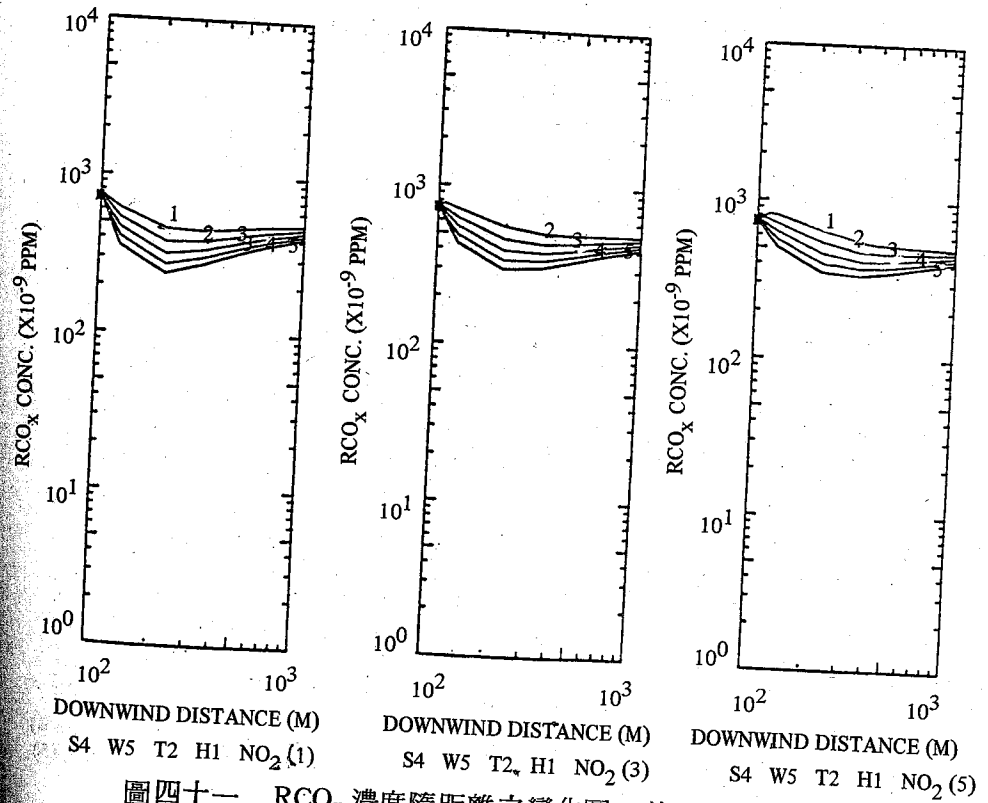

圖四十一　RCO$_x$濃度隨距離之變化圖，其餘情況同圖十七。

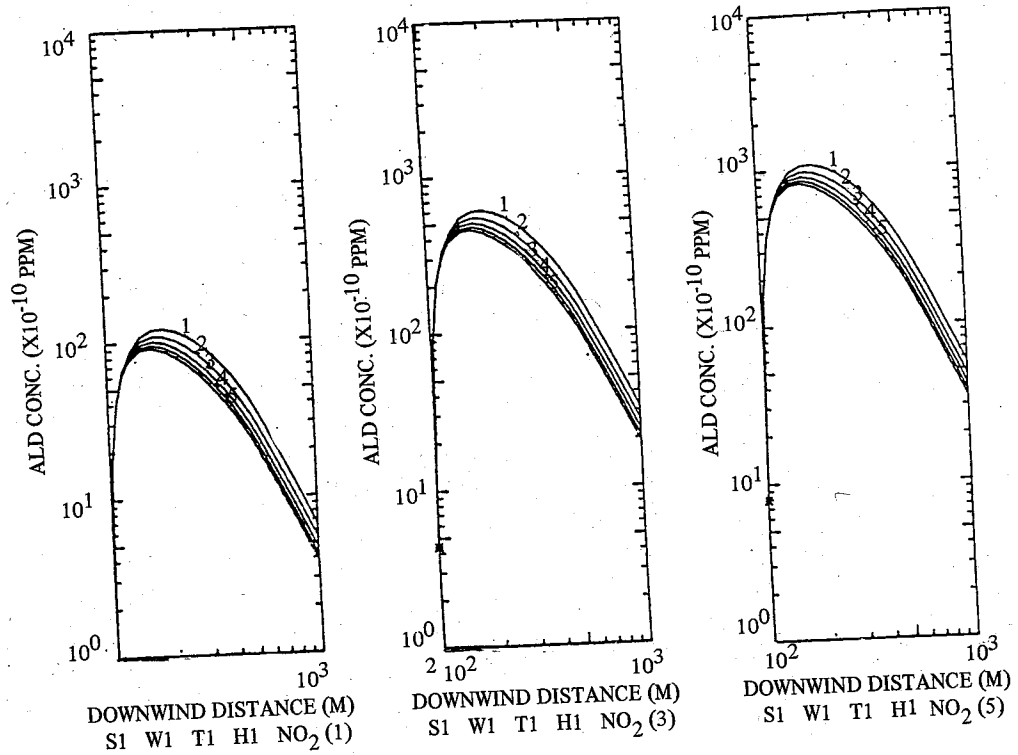

圖四十二　ALD 濃度隨距離之變化圖，其餘情況同圖十二。

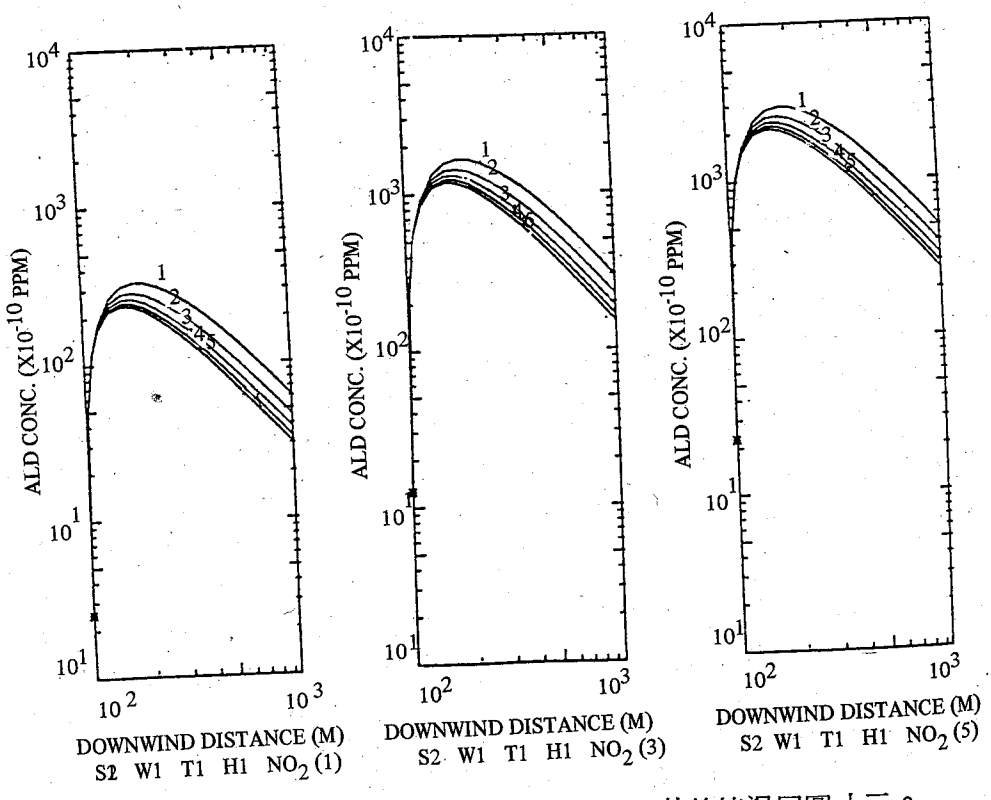

圖四十三　ALD 濃度隨距離之變化圖，其餘情況同圖十三。

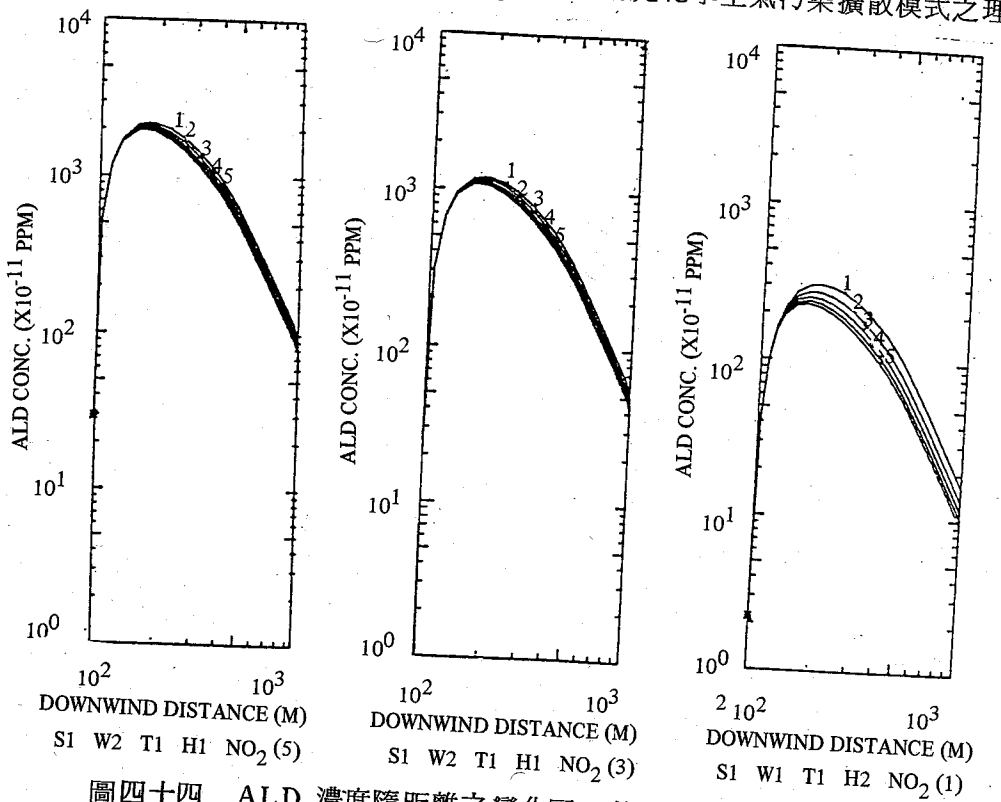

圖四十四　ALD 濃度隨距離之變化圖，其餘情況同圖十四。

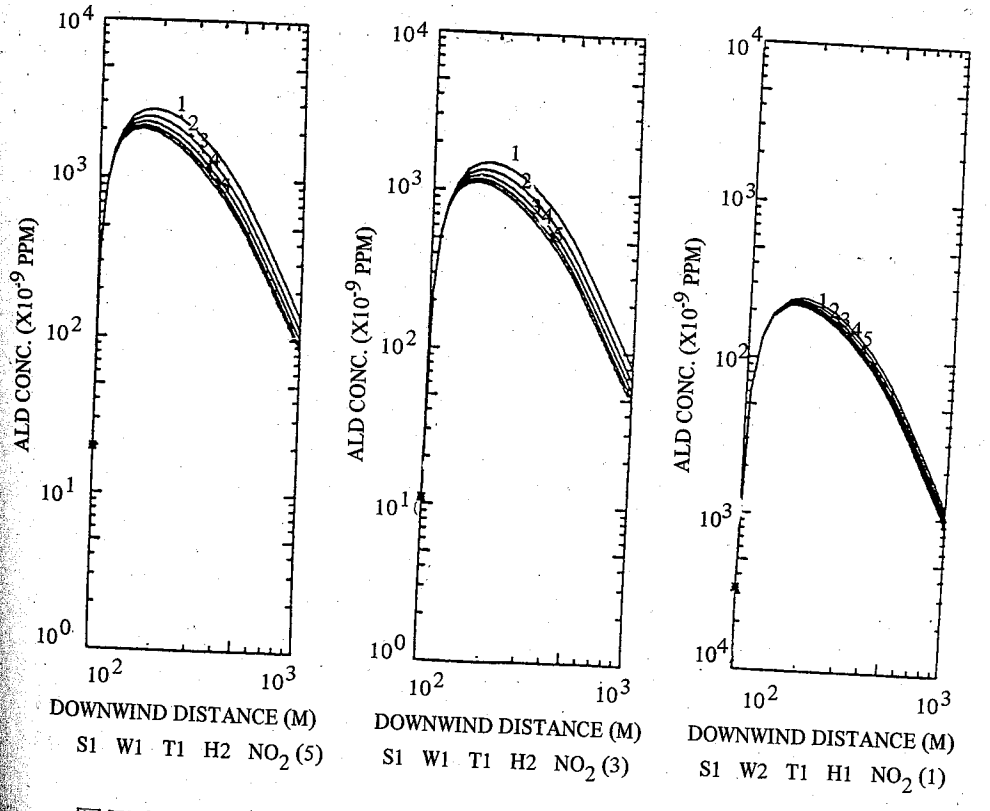

圖四十五　ALD 濃度隨距離之變化圖，其餘情況同圖十五。

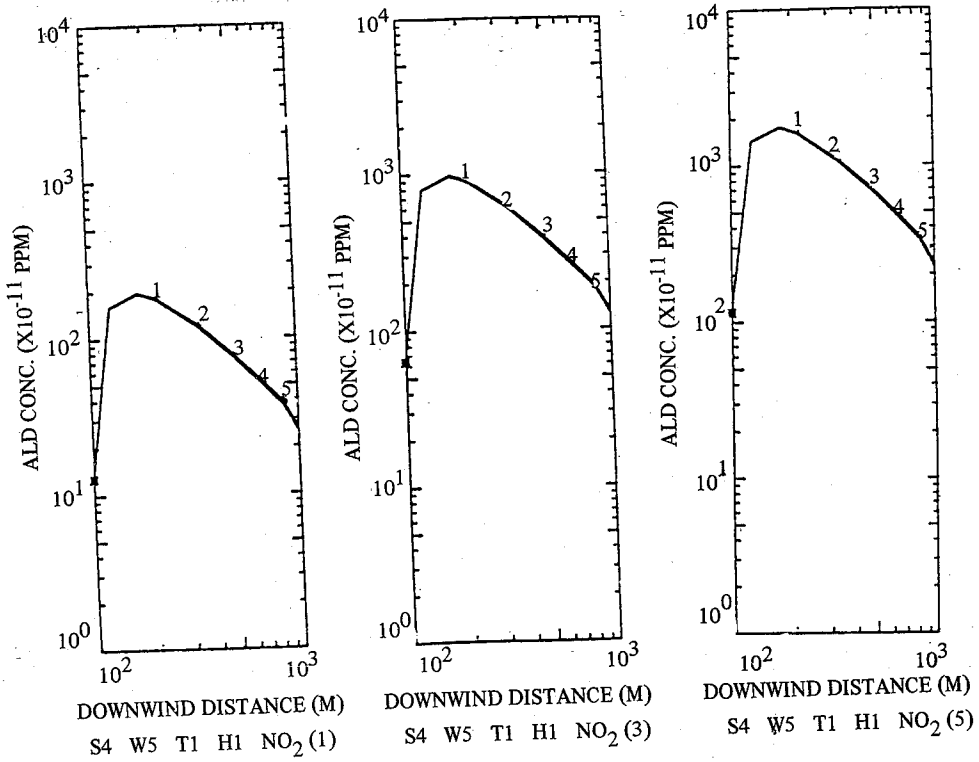

圖四十六　ALD 濃度隨距離之變化圖，其餘情況同圖十六。

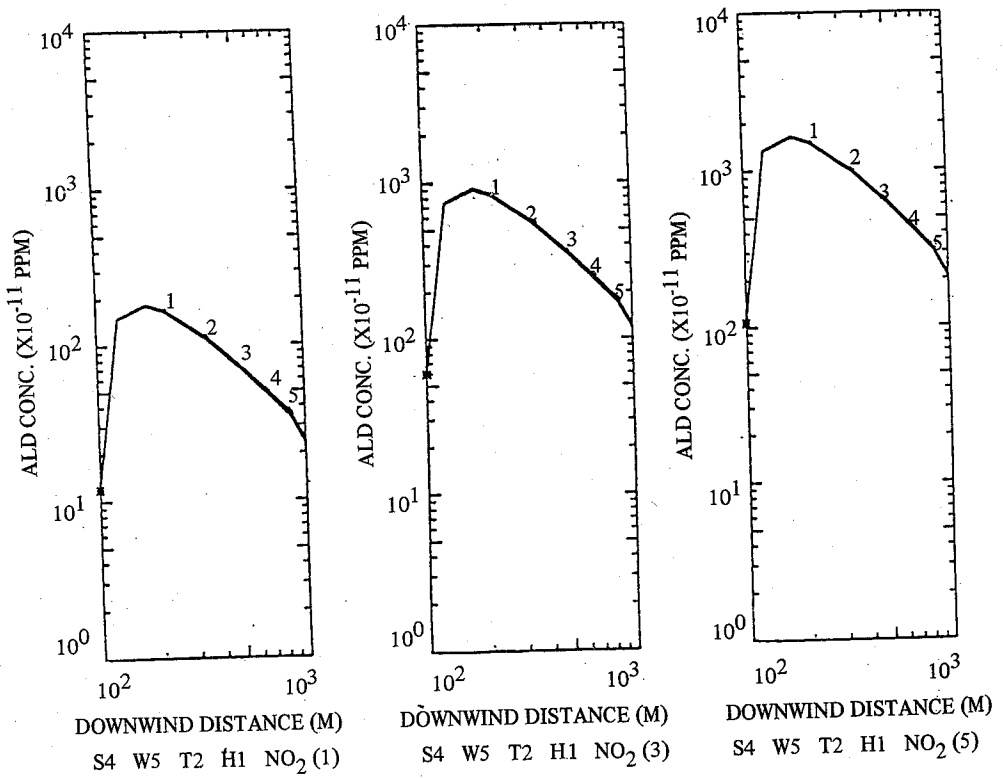

圖四十七　ALD 濃度隨距離之變化圖，其餘情況同圖十七。

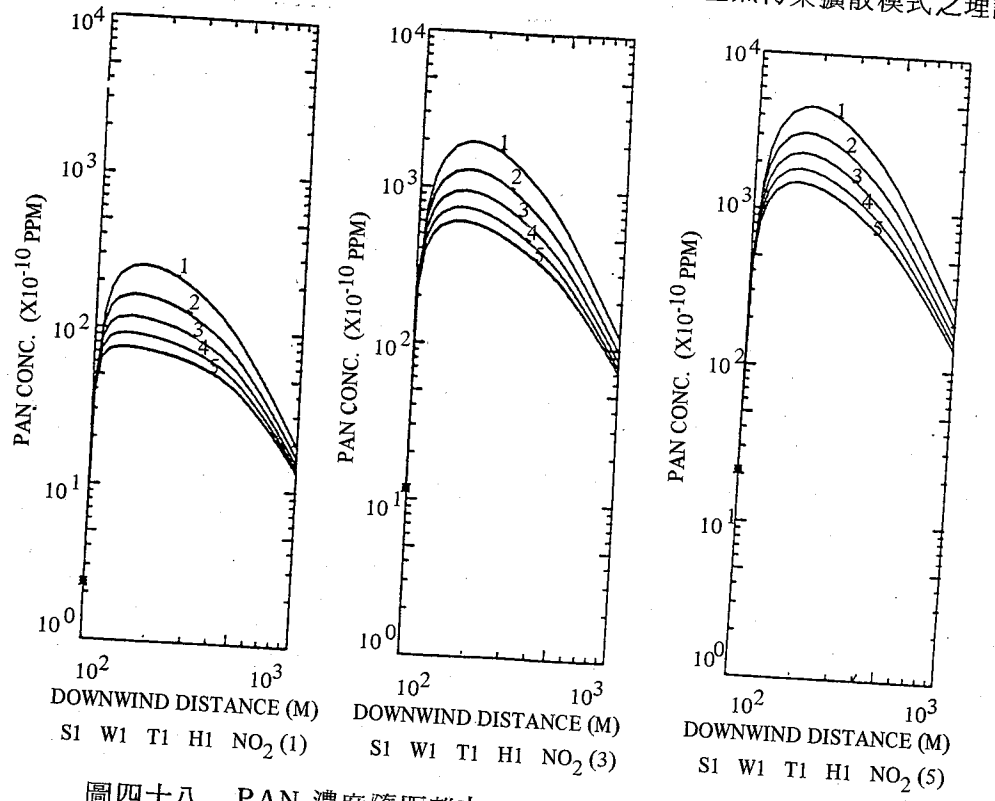

圖四十八　PAN 濃度隨距離之變化圖，其餘情況同圖十二。

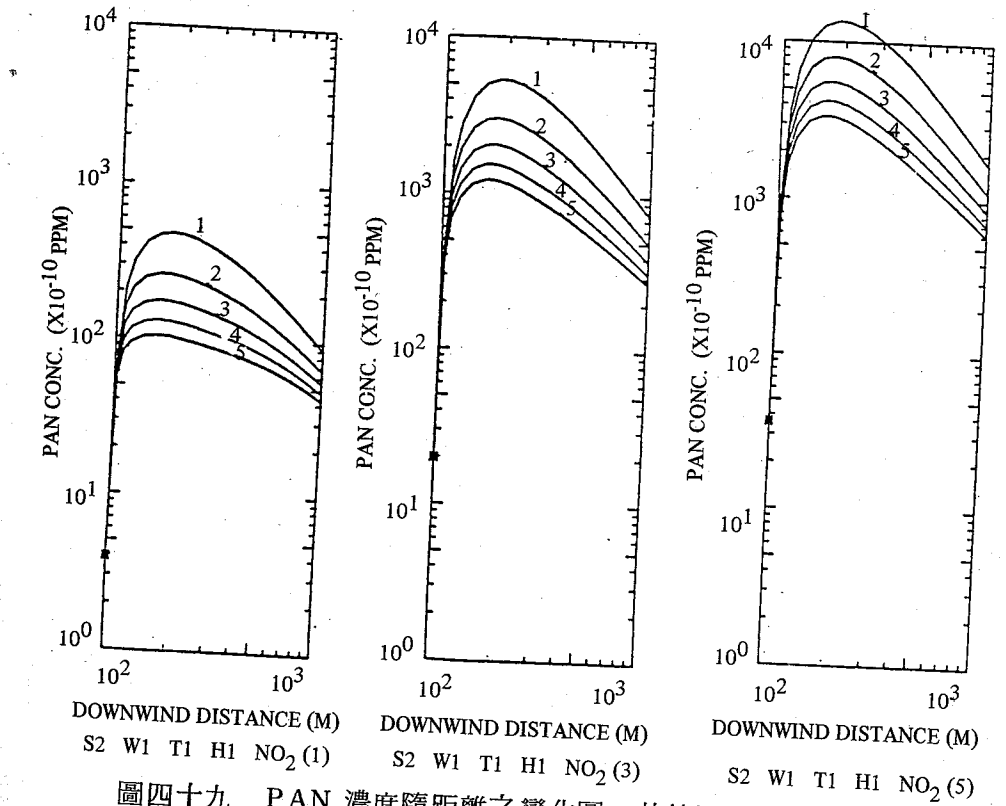

圖四十九　PAN 濃度隨距離之變化圖，其餘情況同圖十三。

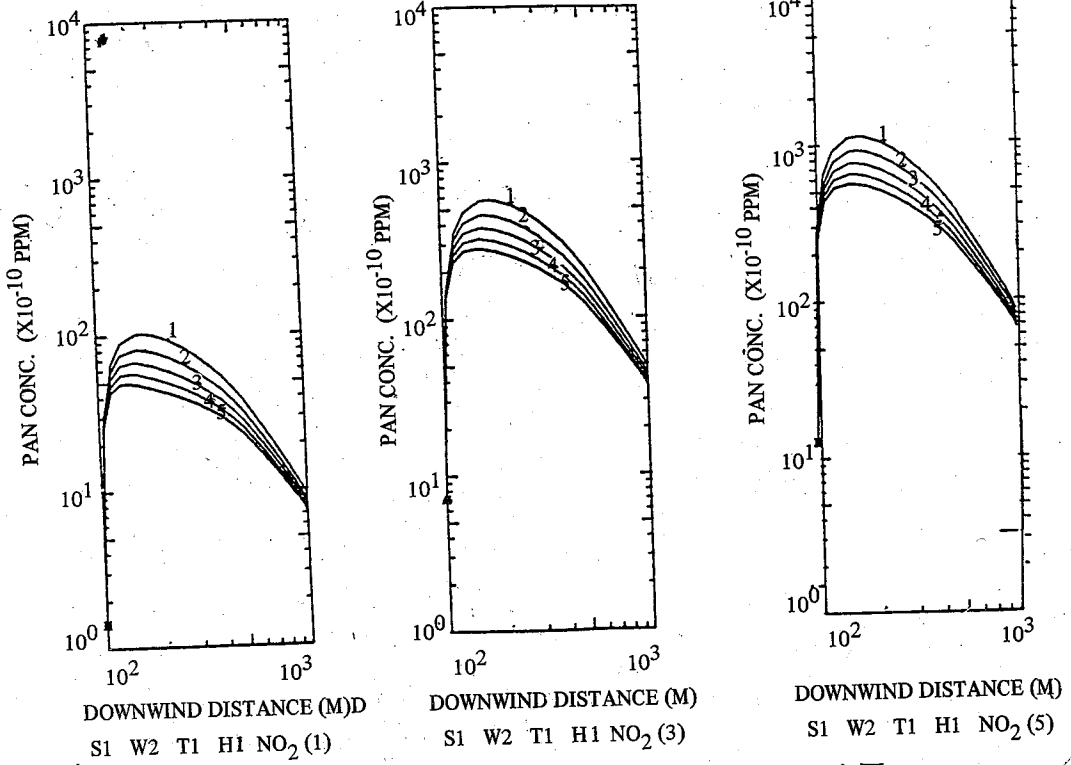

圖五十　PAN 濃度隨距離之變化圖，其餘情況同圖十四。

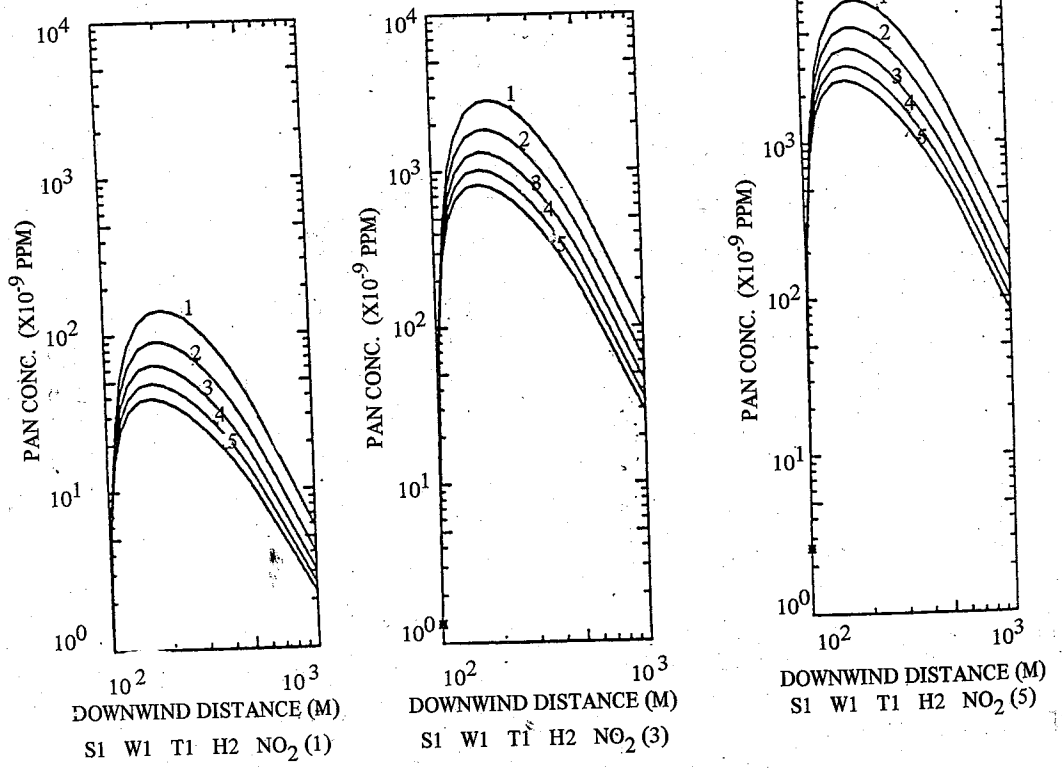

圖五十一　PAN 濃度隨距離之變化圖，其餘情況同圖十五。

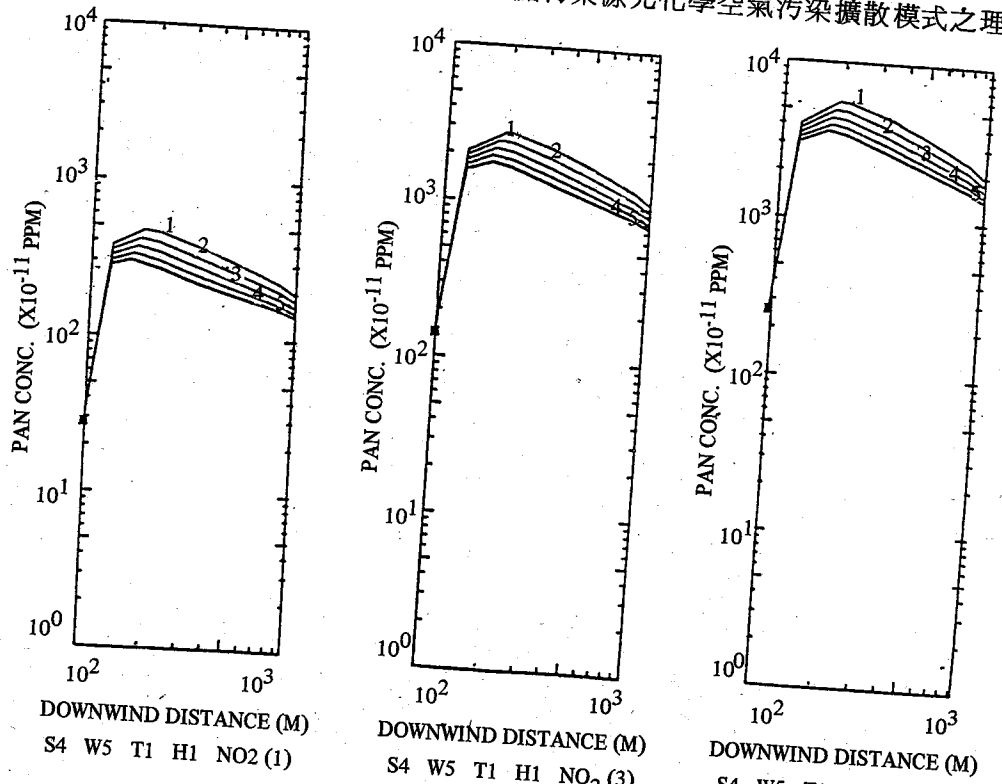

圖五十二　PAN 濃度隨距離之變化圖，其餘情況同圖十六。

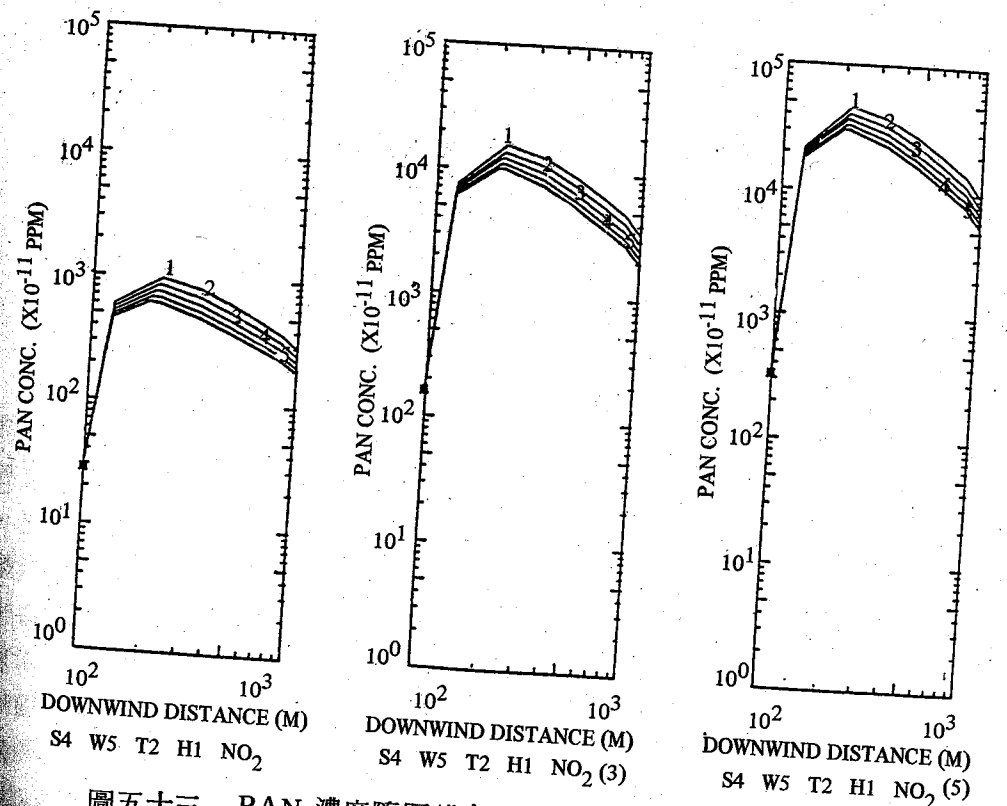

圖五十三　PAN 濃度隨距離之變化圖，其餘情況同圖十七。

經驗正交函數之風能評估理論與應用

梁　文　傑
中央研究院物理研究所
國立台灣大學機械工程學系

王　垂　森
國立台灣大學機械工程學系

謝　全　生
中國文化大學地學研究所

李　秀　芳
中央研究院物理研究所

摘　要

本文以經驗正交函數從事風能評估，此理論適用於處理大量重複使用數學模式。由於經驗正交函數僅適用於模式之輸入與輸出成線性關係情況，故需先從事數學模式輸入輸出線性化。本文使用胡氏的地面流場數學模式，模式線性化後，利用經驗正交函數，求取全部觀測資料的地面流場，以分析風力特性，進行風能評估。

文中分析線性數學模式與非線性模式之間的差異，以證明線性模式的可用性。同時比較隨機取樣分析與經驗正交函數分析法，以探討經驗正交函數的效益。結果顯示本文所發展的經驗正交函數風能評估理論確能兼顧經濟與準確，協助風能系統尋找正確的風能廠址，供風能規劃之用。

壹、引　言

在工程研究或科學分析的領域裡，建立理論模式以模擬實際系統的操作狀況，不失爲經濟有效的方法。一組特定的變數可以描述一個特定系統的狀態，即系統的狀態隨著控制變數的變化而改變，這種變化有其規律性，根據此一規律性，可建立一個理論模式。針對特定的控制變數，理論模式可求出相對的系統狀態。在某些情形下，這些控制變數隨著時間呈現隨機性變化，因而系統的狀態亦呈現隨機變化。如果要瞭解一個操作系統在某段期間內的狀態變化，勢必針對該期間內每一瞬間的各隨機變數，利用理論模式求出相對的系統狀態。實際應用時，需將該期間分割成有限時段，每一時段對應一組控制變數值。理論上愈多組的控制變數值愈能顯示出系統在該期間的實際狀態，即選取控制變數值的時間間隔愈短愈好。面對如此多組的控制變數值，如果每一組變數值都要用理論模式求出相對的系統狀態，不但耗時，且不經濟。

經驗正交函數（Empirical Orthogonal Function）可以分析這些控制變數值的相關性（Corelation），並求出有限組的特徵控制變數值（Characteristic Control Variables），然後利用理論模式計算相對的特徵系統狀態（Characteristic System States），根據這些特徵系統狀態，可獲得相對於任何控制變數值的系統狀態。然而這種方法只適用於控制變數與系統狀態成線性關係。對於非線性關係數學模式，使關係線性化是應用經驗正交函數的先決課題。經驗正交函數的觀念曾應用於心理學與氣象學，是一種預測工具。本文結合經驗正交函數與線性數學模式，使得數學模式能以有限的使用次數，求出全部取樣時間的系統狀態。

風能評估爲風能轉換系統具有良好經濟效益的基礎。風能評估除能提供最佳風能廠址外，對全國能源的整體規劃亦有助益。本文利用台灣北部地區現有的風力資料與風場分佈的數學模式，發展經驗正交函數風能評估理論，使相對於任一組風力資料的風場分佈能在有限的電腦計算時間內求得，並分析風力特性，從事風能評估，研究結果可提供風能轉換系統設置的參考。一般風能評估的方法都是先求各取樣時間觀測資料的平均值，再用數學模式求平均風場。因爲風能與風速成三次方關係，平均風速約爲3 m/s，標準偏差約爲1.8 m/s，所以平均風場求出的風能分佈含有非常大的誤差。經驗正交函數風能評估理論，求出各取樣時間的風場後，再分析風能分佈，不會有上述誤差。

貳、經驗正交函數

空間的點可以表示爲三個不共面向量的線性組合。根據相同的觀念，一個函數可以表示爲許多獨立函數的線性組合，這些獨立函數的個數必須等於函數的自由度，才能完全定義函數。一般而言，函數的自由度等於函數包含的獨立變數個數。

設觀測函數有N個控制變數，P_r爲這些變數的函數值（$r=1,2,\cdots\cdots,N$），利用n個獨立函數X_{ir}的線性組合（$i=1,2,\cdots\cdots,n$）（$n\leq N$），可以求出P_r的近似值$\hat{P}_r$，爲

$$\hat{P}_r=\sum_{i=1}^{n} a_i X_{ir} \qquad 〔1〕$$

〔1〕式中的係數$\{a_i\}$可由最小均方誤差法決定。

若獨立函數X_{ir}彼此正交，且爲準正交函數，即

$$\sum_{r=1}^{N} X_{ir} X_{jr}=0\ ,\quad (i\neq j) \qquad 〔2〕$$

$$\sum_{r=1}^{N} X_{jr}^2=1\ , \qquad 〔3〕$$

則
$$a_i=\sum_{r=1}^{N} X_{ir}\hat{P}_r\ ,\quad (i=1,2,\cdots\cdots,n) \qquad 〔4〕$$

若取樣次數爲M，共有M組控制變數組，每一組變數皆可以〔1〕式表之，則全部N個控制變數經M次採樣之近似值$P_{\tau r}$可表爲

$$\hat{P}_{\tau r}=\sum_{i=1}^{n} a_{ri} X_{i\tau}\ ,\qquad \begin{matrix} r=1,2,\cdots\cdots N \\ \tau=1,2,\cdots\cdots M\end{matrix} \qquad 〔5〕$$

〔5〕式中，r爲變數指標，τ爲不同取樣時間，i則區分各獨立正交函數。寫成矩陣形式爲

$$〔P〕_{M\times N}=〔A〕_{M\times n}〔X〕_{n\times N}\ , \qquad 〔6〕$$

令

$$〔C〕=〔A〕^T〔A〕\ , \qquad 〔7〕$$

則〔C〕爲n階對稱矩陣，具有n個標準正交特徵向量。

令〔R〕爲以這些特徵向量爲行所組成的特徵矩陣，則有下列結果：

$$〔R〕^T〔C〕〔R〕=〔R〕^T(〔A〕^T〔A〕)〔R〕=〔D〕\ , \qquad 〔8〕$$

及

$$〔R〕^T〔R〕=〔R〕〔R〕^T=〔I〕\ , \qquad 〔9〕$$

其中

〔D〕爲對角矩陣，〔I〕爲單位矩陣。

若定義一個M×n的矩陣，〔Q〕爲

$$〔Q〕=〔A〕〔R〕\ ,$$

則

$$〔\hat{P}〕=〔A〕〔X〕=〔Q〕〔R〕^T〔X〕 \qquad 〔11〕$$

若再定義一個n×N的矩陣，〔Y〕爲

$$〔Y〕=〔R〕^T〔X〕\ ,$$

則

$$〔\hat{P}〕=〔Q〕〔Y〕 \qquad 〔12〕$$

由以上的討論，可知時間取樣的M組變數的矩陣〔P〕可分解爲兩個矩陣〔Q〕及〔Y〕的乘積。其中〔Y〕爲標準正交函數矩陣，而係數矩陣〔Q〕爲正交矩陣。如果正交函數的個數等於變數個數，即n=N，則N個正交函數的線性組合可以完全定義N個控制變數，故

$$〔P〕=〔\hat{P}〕=〔Q〕〔Y〕 \qquad 〔13〕$$

由〔7〕式可知矩陣〔Y〕的列爲矩陣〔P〕的N個特徵向量，即

$$〔Y〕=\begin{bmatrix}\vec{y}_{(1)}\\ \vec{y}_{(2)}\\ \vdots\\ \vdots\\ \vec{y}_{(N)}\end{bmatrix} \qquad 〔14〕$$

則

$$〔Y〕〔Y〕^T=〔I〕. \qquad 〔15〕$$

若令

$$〔H〕=〔P〕^T〔P〕\ , \qquad 〔16〕$$

則

$$〔Y〕〔H〕〔Y〕^T=〔D〕 \qquad 〔17〕$$

其中對角矩陣〔D〕的對角線元素爲相對於特徵向量 $\vec{y}_{(1)}$, $\vec{y}_{(2)}$, …… , $\vec{y}_{(N)}$ 的特徵值 λ_1 , λ_2 , …… , λ_N 。

這些特徵函數向量稱爲經驗正交函數，因爲它隱含實驗取樣的時間系列變數之間的相關性。爲了將時間取樣的各組變數表示爲此N個經驗正交函數的線性組合，必須求得係數矩陣〔Q〕，且因爲經驗正交函數爲標準正交函數，故係數矩陣的計算變得極爲容易。總之，

因

$$〔P〕=〔Q〕〔Y〕 ,$$

且

$$〔Y〕〔Y〕^T=〔I〕 ,$$

故

$$〔P〕〔Y〕^T=〔Q〕〔Y〕〔Y^T〕 , \qquad 〔18〕$$

即

$$〔Q〕=〔P〕〔Y〕^T \qquad 〔19〕$$

參、地面風場模式

在複雜的地形表面，估計大氣流場之實際分佈狀況，是各種資源規制工作從業者無可避免的工作。探討地面流場時，必然會面臨缺少觀測資料的嚴重問題。譬如台灣北部地區，只有台北、宜蘭、淡水、竹子湖、鞍部、基隆、新竹等少數地區可以取得長期的氣象觀測資料。限於有限的觀測資料，我們必須尋找模擬大氣邊界層流場的數學模式，以替代昂貴的資料觀測網。本研究係根據胡氏（Fosberg）的數學模式加以修正[1]，以模擬台灣北部地區地面風場。胡氏模式考慮三種效應對地面流場的影響，此三種效應爲地形效應、熱效應及摩擦效應。將這三種效應所引起之風場變化量分別修正地轉風以求取實際風場分佈。

因爲觀測資料有限，無法由完整的流體力學方程式及熱力學方程式解出大氣流場，鑑於此，統御方程式必須簡化。統御方程式包括連續方程式、動量方程式、能量方程式及氣體狀態方程式。此數學模式利用參數取代一些氣象的現象，所以此模式能夠適用於不同的地形，而且不需要複雜的資料觀測網。

此數值模式的統御方程式包括連續方程式、動量方程式、氣體狀態方程式[4]，即

連續方程式，

$$\frac{\partial \rho}{\partial t}+\nabla\cdot(\rho\vec{v})=0 , \qquad 〔20〕$$

動量方程式，

$$\frac{\partial \vec{v}}{\partial t}+(v\cdot\nabla)\vec{v}+f\vec{k}\times\vec{v}=-\frac{1}{\rho}\nabla P+K\nabla^2\vec{v} , \qquad 〔21〕$$

氣體狀態方程式，

$$P=\rho R T .$$

1 地形效應 〔22〕

對整個探討的區域而言，氣流必須滿足質量守恒定律，氣流下面，完全受地形支配。假設整個流場爲穩定狀態（Steady state），即

$$\nabla\cdot(\rho\vec{v})=-\frac{\partial(\rho w)}{\partial z} , \qquad 〔23〕$$

$\vec{v}$ 爲水平速度。在非彈性近似的假設下，上式可以改寫爲

$$\vec{\rho}(\nabla\cdot\vec{v})=-\frac{\partial(\rho w)}{\partial z} , \qquad 〔24〕$$

上式 $\bar{\rho}$ 表示由地面高度h至邊界層高度H空氣密度的平均值。則

$$\bar{\rho}\int_h^H \nabla\cdot\vec{v}\,dz=-\int_h^H\frac{\partial(\rho w)}{\partial z}\,dz , \qquad 〔25〕$$

令 δ 爲水平輻散度（Divergence）$\nabla\cdot\vec{v}$ ，由均值定理，$\bar{\delta}$ 爲水平輻散度之邊界層平均值，則

$$\bar{\rho}\bar{\delta}(H-h)=-\rho w(H)+\rho w(h) , \qquad 〔26〕$$

邊界層高度H爲風場擾動影響的上限，即不受地形影響，故w在該處爲零。在地面h處，垂直速度由地形效應產生，因此

$$w(h)=\vec{v}\cdot\nabla h ,$$

於是地形引起的水平輻散度可以表示爲 〔27〕

$$\bar{\delta}=\frac{\rho\vec{v}\cdot\nabla h}{\bar{\rho}(H-h)} \qquad 〔28〕$$

2 熱效應與摩擦效應

欲研究熱效應與摩擦效應對風場之作用，可以由動量方程式着手，

$$\frac{\partial \vec{v}}{\partial t}+(\vec{v}\cdot\nabla)\vec{v}+f\vec{k}\times\vec{v}=-\frac{1}{\rho}\nabla P+K\nabla^2\vec{v} , \qquad 〔29〕$$

式中 $f\vec{k}\times\vec{v}$ 爲科氏加速度（Coriolis acceleration），f爲科氏參數（Coriolis parameter），若Ω爲地球轉速，ϕ 爲緯度，則f爲 $2\Omega\sin\phi$ ，Ω約爲 7.29×10^{-5} sec^{-1} ，K爲紊流黏性係數。

將動量方程式取輻散運算，並忽略對流效應可得輻散度方程式

$$\frac{\partial\delta}{\partial t}=\nabla\cdot(-c_p\theta\nabla P_*)+\nabla\cdot(K\nabla^2\vec{v}) , \qquad 〔30〕$$

式中

$$P_*=\left(\frac{P}{P_0}\right)^{R/c_p} , \qquad 〔31〕$$

$$\theta = T / P_* \ ,$$

$$P_0 = 1000\,\text{mb} \ .$$

因水平摩擦遠小於垂直摩擦，即

$$\left|\frac{\partial^2 \vec{v}}{\partial x^2}\right| << \left|\frac{\partial^2 \vec{v}}{\partial z^2}\right| \ ,$$

$$\left|\frac{\partial^2 \vec{v}}{\partial y^2}\right| << \left|\frac{\partial^2 \vec{v}}{\partial z^2}\right| \ ,$$

故摩擦項可以進一步化簡，

$$\nabla \cdot (K \nabla^2 \vec{V}) \doteq \nabla \cdot K \left(\frac{\partial^2 \vec{v}}{\partial z^2}\right) = K \left(\frac{\partial^3 u}{\partial x \partial z^2} + \frac{\partial^3 v}{\partial y \partial z^2}\right) \qquad 〔33〕$$

接近地面，風速的垂直分佈爲對數函數（Logarithmic wind profile），即

$$\frac{u}{u_*} = \frac{1}{k} \ln \frac{z}{z_0} \ , \qquad 〔34〕$$

而

$$\frac{\partial u}{\partial z} = \frac{u_*}{kz} \ , \qquad 〔35〕$$

$$\frac{\partial v}{\partial z} = \frac{u_*}{kz} \ , \qquad 〔36〕$$

式中 u_* 及 v_* 爲摩擦速度之分量，k 爲 Von Karman 常數。摩擦速度可以由風速及地面粗糙度求得，

$$u_* = \frac{|\bar{u}|k}{\ln\left(\frac{z}{z_0}\right)} \qquad 〔37〕$$

$$v_* = \frac{|\bar{v}|k}{\ln\left(\frac{z}{z_0}\right)} \qquad 〔38〕$$

z_0 爲地面的粗糙度，z 爲離開地面的高度，$|\bar{u}|$及$|\bar{v}|$爲高度 z 的風速分量絕對值。如果用 $z + z_0$ 取代 z，則

$$u_* = \frac{|\bar{u}|k}{\ln\left(\frac{z+z_0}{z_0}\right)} \qquad 〔39〕$$

$$v_* = \frac{|\bar{v}|k}{\ln\left(\frac{z+z_0}{z_0}\right)} \qquad 〔40〕$$

經由以上之討論，及進一步運算得到

$$\frac{\partial^2 u}{\partial z^2} = -\frac{u_*}{kz^2} \ , \qquad 〔41〕$$

$$\frac{\partial^2 v}{\partial z^2} = -\frac{v_*}{kz^2} \ , \qquad 〔42〕$$

於是輻散方程式可以改寫爲

$$\frac{\partial \delta}{\partial t} = -c_p \theta \nabla^2 P_* - c_p \nabla\theta \cdot \nabla P_* - \frac{K}{kz^2}\left(\frac{\partial u_*}{\partial x} + \frac{\partial v_*}{\partial y}\right) . \qquad 〔43〕$$

上式右側，前兩項代表熱效應，第三項代表摩擦效應。如果把熱效應與摩擦效應視爲脈衝波動，然後再考慮此波動引起的擾動流場，則問題可大爲化簡。因輻散度的相速度（Phase velocity）約爲聲速，上式對時間積分可得

$$\delta = \frac{1}{2}\Delta t_\delta \left[-c_p \theta \nabla^2 P_* - c_p \nabla\theta \cdot \nabla P_* - \frac{K}{kz^2}\left(\frac{\partial u_*}{\partial x} + \frac{\partial v_*}{\partial y}\right)\right] + \bar{\delta} \qquad 〔44〕$$

式中 ∇t_δ 爲計算格點距離除以聲速。

對動量方程式取旋度運算，可得渦旋度方程式，再依上述化簡輻散度方程式的程序，可得

$$\frac{\partial \zeta}{\partial t} = -c_p \frac{\partial(\theta, P_*)}{\partial(x, y)} - (\zeta + f)\delta - \frac{K}{kz^2}\left(\frac{\partial v_*}{\partial x} - \frac{\partial u_*}{\partial y}\right) \qquad 〔45〕$$

若輻散度已經求得，則上式可視爲一階的常微分方程式

$$\frac{\partial \zeta}{\partial t} + \delta\zeta = -c_p \frac{\partial(\theta, P_*)}{\partial(x, y)} - f\delta - \frac{K}{kz^2}\left(\frac{\partial v_*}{\partial x} - \frac{\partial u_*}{\partial y}\right) \qquad 〔46〕$$

仍將上式右側視爲脈衝波動；因渦旋度的相速度約爲風速，上述常微分方程式可得之解爲

$$\begin{aligned}\zeta &= e^{-\int \delta dt} \int \left[-c_p \frac{\partial(\theta, P_*)}{\partial(x, y)} - f\delta - \frac{K}{kz^2}\left(\frac{\partial v_*}{\partial x} - \frac{\partial u_*}{\partial y}\right)\right] e^{\int \delta dt}\, dt \\ &= \exp\left(-\frac{1}{2}\delta\Delta t_\zeta\right) \frac{1}{2}\Delta t_\zeta \left[-c_p \frac{\partial(\theta, P_*)}{\partial(x, y)} - f\delta - \frac{K}{kz^2}\left(\frac{\partial v_*}{\partial x}\right.\right. \\ &\quad \left.\left. - \frac{\partial u_*}{\partial x} - \frac{\partial u_*}{\partial y}\right)\right] \exp\left(\frac{1}{2}\delta\Delta t_\zeta\right)\end{aligned} \qquad 〔47〕$$

式中 Δt_ζ 爲計算格點距離除以風速。

格點的距離一般爲 1 公里至 10 公里，風速約爲 1 m/sec 至 10 m/sec，故 Δt_ζ 的數量級約爲 1,000，而輻散度之數量級約爲 10^{-5} 至 10^{-3}，因此 $\exp(-1/2\delta\Delta t_\zeta)$ 約爲 1，於是

$$\zeta \doteq \frac{1}{2}\Delta t_\zeta \left[-c_p \frac{\partial(\theta, P_*)}{\partial(x, y)} - f\delta - \frac{K}{kz^2}\left(\frac{\partial v_*}{\partial x} - \frac{\partial u_*}{\partial y}\right)\right] \qquad 〔48〕$$

3.座標轉換

因爲模式是建立在平面上（二維模式），但觀測資料都從離地面一定高度取得，必須把觀測資料轉換成相當於平面上的資料。此座標轉換的目的是要將隨著地形變化的觀

測值轉換爲水平方向變化量。沿地形表面，故

$$S=S(x,h(x))$$

$$\left.\frac{\partial S}{\partial x}\right)_T=\left.\frac{\partial S}{\partial x}\right)_E+\left.\frac{\partial S\partial h}{\partial z\partial x}\right)_T \quad , \qquad 〔49〕$$

足碼T表示沿地形表面的變化量，E表示沿水平面的變化量，於是

$$\left.\frac{\partial S}{\partial x}\right)_E=\left.\frac{\partial S}{\partial x}\right)_T-\left.\frac{\partial S\partial h}{\partial z\partial x}\right)_T \quad , \qquad 〔50〕$$

$$\left.\frac{\partial^2 S}{\partial x^2}\right)_E=\left.\frac{\partial^2 S}{\partial x^2}\right)_T-2\left.\frac{\partial^2 S}{\partial x\partial z}\frac{\partial h}{\partial x}\right)_T \quad , \qquad 〔51〕$$

上面的第〔51〕式中，地形h(x) 的高次微分項已經忽略。如果，變數S的垂直變化率爲已知，則此二式子可以將沿地形的變化量轉換爲沿水平方向的變化量。

假設大氣沿垂直方向爲液壓靜力平衡，則其靜安定度（Static Stability）σ爲

$$\sigma=\frac{1}{\theta}\frac{\partial\theta}{\partial z} \quad , \qquad 〔52〕$$

故位溫之垂直變化率爲

$$\frac{\partial\theta}{\partial z}=\sigma\theta \quad ,$$

其轉換方程式爲

$$\left.\frac{\partial\theta}{\partial x}\right)_E=\left.\frac{\partial\theta}{\partial x}\right)_T-\theta\sigma\left.\frac{\partial h}{\partial x}\right)_T \quad , \qquad 〔53〕$$

$$\left.\frac{\partial\theta}{\partial y}\right)_E=\left.\frac{\partial\theta}{\partial y}\right)_T-\theta\sigma\left.\frac{\partial h}{\partial y}\right)_T \quad , \qquad 〔54〕$$

在液壓靜力平衡之條件下，壓力之垂直變化率爲

$$\frac{\partial P}{\partial z}=-\rho g \quad , \qquad 〔55〕$$

故無因次壓力的垂直變化率爲

$$\frac{\partial P_*}{\partial z}=-\frac{g}{c_p\theta} \quad , \qquad 〔56〕$$

其轉換方程式如下

$$\left.\frac{\partial P_*}{\partial x}\right)_E=\left.\frac{\partial P_*}{\partial x}\right)_T+\left.\frac{g}{c_p\theta}\frac{\partial h}{\partial x}\right)_T \quad , \qquad 〔57〕$$

$$\left.\frac{\partial P_*}{\partial y}\right)_E=\left.\frac{\partial P_*}{\partial y}\right)_T+\left.\frac{g}{c_p\theta}\frac{\partial h}{\partial y}\right)_T \quad , \qquad 〔58〕$$

$$\left.\frac{\partial^2 P_*}{\partial x^2}\right)_E=\left.\frac{\partial^2 P_*}{\partial x^2}\right)_T-2\left.\frac{g}{c_p\theta^2}\frac{\partial h\partial\theta}{\partial x\partial x}\right)_T \quad , \qquad 〔59〕$$

$$\left.\frac{\partial^2 P_*}{\partial y^2}\right)_E=\left.\frac{\partial^2 P_*}{\partial y^2}\right)_T-2\left.\frac{g}{c_p\theta^2}\frac{\partial h\partial\theta}{\partial y\partial y}\right)_T \quad , \qquad 〔60〕$$

因爲我們所考慮的邊界層很薄，所以摩擦速度在垂直方向可以視爲不變，其轉換方程式爲

$$\left.\frac{\partial u_*}{\partial x}\right)_E=\left.\frac{\partial u_*}{\partial x}\right)_T \quad , \qquad 〔61〕$$

$$\left.\frac{\partial u_*}{\partial y}\right)_E=\left.\frac{\partial u_*}{\partial y}\right)_T \quad , \qquad 〔62〕$$

$$\left.\frac{\partial v_*}{\partial x}\right)_E=\left.\frac{\partial v_*}{\partial x}\right)_T \quad , \qquad 〔63〕$$

$$\left.\frac{\partial v_*}{\partial y}\right)_E=\left.\frac{\partial v_*}{\partial y}\right)_T \quad 。 \qquad 〔64〕$$

4. 風場的計算

把地形效應、熱效應與摩擦效應所引起之擾動流場依次修正地轉風。擾動流場可以分爲兩部份：一部份爲無旋轉的輻散量（irrotational divergent component），另一部份爲無輻散的旋轉量（nondivergent rotational component），即

$$\vec{V}=\vec{k}\times\nabla\psi+\nabla\phi \qquad 〔65〕$$

式中ϕ爲速度勢函數（Velocity potential），ψ爲流線函數（Stream function），而$\vec{V}$爲擾動流場。因此可得下式

$$\zeta=\vec{k}\cdot(\nabla\times\vec{V})=\nabla^2\psi \quad , \qquad 〔66〕$$

$$\delta=\nabla\cdot\vec{V}=\nabla^2\phi \quad . \qquad 〔67〕$$

輻散度與渦旋度求得後，代入上面二個式子，可求出速度勢函數與流線函數，然後修正背景風場（Background wind），可得修正風場，即

$$u=u_0+\frac{\partial\phi}{\partial x}-\frac{\partial\psi}{\partial y} \qquad 〔68〕$$

$$v=v_0+\frac{\partial\phi}{\partial y}+\frac{\partial\psi}{\partial x} \qquad 〔69〕$$

式中u_0與v_0爲背景風（Background wind）。

本數值模式的特色爲不需要費時且昂貴的氣象觀測網，基本上這是一種探討地面風場特性的模式，而不能作爲與時間有關的預測模式。換句話說，此數值模式求得之風場乃是一種時間與空間的平均風場。故作爲風力潛能之評估模式，它是可以信賴的。

使用本數值模式需要的輸入變數爲地形高度、地形梯度、觀測溫度、觀測壓力、觀測風速、觀測風向。地形高度及梯度可由地圖上讀取。溫度、壓力、風速與風向則從現有的氣象觀測站取得。

經座標轉換後的輻散度方程式爲

$$\delta=\frac{1}{2}\Delta t_\delta\{-C_p[\theta\frac{\partial^2 P_*}{\partial x^2}+\theta\frac{\partial^2 P_*}{\partial y^2}+\frac{\partial\theta}{\partial x}\frac{\partial P_*}{\partial x}+\frac{\partial\theta}{\partial y}\frac{\partial P_*}{\partial y}$$

$$-\sigma\frac{\partial h}{\partial x}\theta\frac{\partial P_*}{\partial x}-\sigma\frac{\partial h}{\partial y}\theta\frac{\partial P_*}{\partial y}-\frac{g}{C_p}\frac{\partial h}{\partial x}\frac{1}{\theta}\frac{\partial\theta}{\partial x}-\frac{g}{C_p}\frac{\partial h}{\partial y}\frac{1}{\theta}\frac{\partial\theta}{\partial y}$$

$$-\sigma\frac{g}{C_p}\left(\frac{\partial h}{\partial x}\right)^2-\sigma\frac{g}{C_p}\left(\frac{\partial h}{\partial y}\right)^2\Big]-\frac{K}{kz^2}\left(\frac{\partial u_*}{\partial x}+\frac{\partial v_*}{\partial y}\right)\Big\}$$

渦旋方程式爲

$$\zeta\doteqdot\frac{1}{2}\Delta t_\zeta\Big\{-C_p\Big[\frac{\partial\theta}{\partial x}\frac{\partial P_*}{\partial y}-\frac{\partial\theta}{\partial y}\frac{\partial P_*}{\partial x}-\sigma\frac{\partial h}{\partial x}\theta\frac{\partial P_*}{\partial y}+\sigma\frac{\partial h}{\partial y}\theta\frac{\partial P_*}{\partial x}$$
$$+\frac{g}{C_p}\Big(\frac{\partial h}{\partial y}\frac{1}{\theta}\frac{\partial\theta}{\partial x}-\frac{\partial h}{\partial x}\frac{1}{\theta}\frac{\partial\theta}{\partial y}\Big)\Big]-f\delta-\frac{K}{kz^2}\Big(\frac{\partial v_*}{\partial x}-\frac{\partial u_*}{\partial y}\Big)\Big\}$$

肆、經驗正交函數之風能評估理論

假設某一數學模式需要N個系統變數P_r，且P_r可以表示爲n個獨立正交函數X_{ir}的線性組合，

$$P_r=\sum_{i=1}^{n}a_i X_{ir}\quad,\quad r=1,2,\cdots\cdots,N \qquad〔70〕$$

針對一組系統變數值（$P_1,P_2,\cdots\cdots,P_N$），數學模式可解出一組系統結果（$V_1,V_2,\cdots\cdots,V_{Ns}$），若以L代表數學模式的運算，則如下式

$$L(P_r)=V_s,\quad r=1,2,\cdots\cdots,N;\quad s=1,2,\cdots\cdots,N_s \qquad〔71〕$$

如果數學模式爲線性模式，則

$$L(P_r)=L\Big(\sum_{i=1}^{n}a_i X_{ir}\Big)=\sum_{i=1}^{n}a_i L(X_{ir})=\sum_{i=1}^{n}a_i W_{is} \qquad〔72〕$$

$$r=1,2,\cdots\cdots,N$$
$$s=1,2,\cdots\cdots,N_s \qquad〔73〕$$

故 $V_s=\sum_{i=1}^{n}a_i W_{is}$

其中W_{is}爲以獨立正交函數X_{ir}爲系統變數所求得的系統結果。

前一章所提出的地面風場模式，利用輻散度δ及渦旋度ζ以描述地形效應，熱效應及摩擦效應。一旦輻散度δ與渦旋度ζ求出，則可以利用下列四個線性方程式求出修正流場

$$\zeta=\nabla^2\phi$$
$$\delta=\nabla^2\phi$$
$$u=u_0+\frac{\partial\phi}{\partial x}-\frac{\partial\psi}{\partial y}$$
$$v=v_0+\frac{\partial\phi}{\partial y}+\frac{\partial\psi}{\partial x}$$

可以發現地面風場模式的非線性部份爲輻散度方程式與渦旋度方程式。首先考慮地形效應求出的輻散度方程式

$$\overline{\delta}=\frac{\overline{\rho}\ \overrightarrow{v}\cdot\nabla h}{\overline{\rho}\ \ H-h}$$

式中地形高度h，地形梯度∇h與邊界層厚度H皆爲常數。由於邊界層厚度甚小，平均密度$\overline{\rho}$非常接近地面密度ρ，即$\frac{\rho}{\overline{\rho}}$的值約爲1，若$\frac{\rho}{\overline{\rho}}$採用長期平均值，則$\frac{\rho}{\overline{\rho}}$亦爲常數。於是地形效用所引起的輻散度方程式爲線性方程式。

其次考慮熱效應與摩擦效應所求得的輻散度方程式與渦旋度方程式

$$\delta=\frac{1}{2}\Delta t_\delta\Big[-C_p\theta\nabla^2P_*-C_p\nabla\theta\cdot\nabla P_*-\frac{K}{kZ^2}\Big(\frac{\partial u_*}{\partial x}+\frac{\partial v_*}{\partial y}\Big)\Big]$$

$$\zeta=\frac{1}{2}\Delta t_\zeta\Big[-C_p\frac{\partial(\theta,P_*)}{\partial(x,y)}-f\delta-\frac{K}{kZ^2}\Big(\frac{\partial v_*}{\partial x}-\frac{\partial u_*}{\partial y}\Big)\Big]$$

式中輻散度積分常數Δt_δ爲格點距離除以聲速，所以Δt_δ爲常數。而渦旋度積分常數爲格點距離除以風速，若風速採用長期平均值，則Δt_ζ亦爲常數。觀察輻散度方程式與渦旋度方程式的摩擦效應部份，可以發現K，k，Z_0皆爲常數，而

$$u_*=\frac{|\overline{u}|k}{\ln\left(\frac{z+z_0}{z}\right)}$$

$$v_*=\frac{|\overline{v}|k}{\ln\left(\frac{z+z_0}{z}\right)}$$

因爲z亦爲常數，所以輻散度方程式與渦旋度方程式的摩擦效應部份爲線性方程式。於是輻散度方程式與渦旋度方程式的非線性項僅餘熱效應部份

$$\theta\nabla^2P_*+\nabla\theta\cdot\nabla P_* \qquad〔74〕$$

$$\frac{\partial(\theta,P_*)}{\partial(x,y)} \qquad〔75〕$$

〔74〕式經座標轉換後爲

$$\big[\theta\nabla^2P_*+\nabla\theta\cdot\nabla P_*\big]_E=\theta\frac{\partial^2P_*}{\partial x^2}+\theta\frac{\partial^2P_*}{\partial y^2}+\frac{\partial\theta}{\partial x}\frac{\partial P_*}{\partial x}+\frac{\partial\theta}{\partial y}\frac{\partial P_*}{\partial y}$$
$$-\sigma\frac{\partial h}{\partial x}\theta\frac{\partial P_*}{\partial x}-\sigma\frac{\partial h}{\partial y}\theta\frac{\partial P_*}{\partial y}-\frac{g}{C_p}\frac{\partial h}{\partial x}\frac{1}{\theta}\frac{\partial\theta}{\partial x}$$
$$-\frac{g}{C_p}\frac{\partial h}{\partial y}\frac{1}{\theta}\frac{\partial\theta}{\partial y}-\sigma\frac{g}{C_p}\Big[\Big(\frac{\partial h}{\partial x}\Big)^2+\Big(\frac{\partial h}{\partial y}\Big)^2\Big] \qquad〔76〕$$

最後一項$-\sigma\frac{g}{C_p}\Big[\Big(\frac{\partial h}{\partial x}\Big)^2+\Big(\frac{\partial h}{\partial y}\Big)^2\Big]$爲空間變數，是與時間無關的常數。其對地面流場的影響，可以單獨計算。當不含此項的數值模式流場求出後，再把二者相加即爲總合流場。〔75〕式經座標轉換後爲

$$\left[\frac{\partial(\theta,P_*)}{\partial(x,y)}\right]_E=\frac{\partial\theta}{\partial x}\frac{\partial P_*}{\partial y}-\frac{\partial\theta}{\partial y}\frac{\partial P_*}{\partial x}-\sigma\{\frac{\partial h}{\partial x}\theta\frac{\partial P_*}{\partial y}-\frac{\partial h}{\partial y}\theta\frac{\partial P_*}{\partial x}\}$$
$$+\frac{g}{C_p}\{\frac{\partial h}{\partial y}\frac{1}{\theta}\frac{\partial\theta}{\partial x}-\frac{\partial h}{\partial x}\frac{1}{\theta}\frac{\partial\theta}{\partial y}\}\qquad〔77〕$$

爲了計算〔76〕及〔77〕，必須先求出θ與P_*的分佈。但是在本數學模式探討的區域裡，只有六個氣象觀測站可以取得長期的氣象觀測資料溫度、壓力、風速與風向。利用內差法可以由六個觀測值，求出每一點的值，即

$$\theta(x,y)=\sum_{s=1}^{6}W_s(x,y)\,\tilde{\theta}_s\qquad〔78〕$$

$$P_*(x,y)=\sum_{t=1}^{6}W_t(x,y)\,\tilde{P}_{*t}\qquad〔79〕$$

$W_s(x,y)$爲配重函數（Weighting Function），代表測站s的觀測值在(x,y)的配重。把上述兩個式子代入〔76〕及〔77〕則

$$\{\theta\nabla^2P_*+\nabla\theta\cdot\nabla P_*\}_E=\sum_{s=1}^{6}\sum_{t=1}^{6}(W_s\frac{\partial^2W_t}{\partial x^2}+W_s\frac{\partial^2W_t}{\partial y^2}+\frac{\partial W_s}{\partial x}\frac{\partial W_t}{\partial x}$$
$$+\frac{\partial W_s}{\partial y}\frac{\partial W_t}{\partial y}-\sigma\frac{\partial h}{\partial x}W_s\frac{\partial W_t}{\partial x}-\sigma\frac{\partial h}{\partial y}W_s\frac{\partial W_t}{\partial y})$$
$$\sim\sim\ \tilde{\theta}_s\tilde{P}_{*t}-\frac{g}{C_p}\frac{\partial h}{\partial x}\frac{1}{\theta_{av}}(\sum_{s=1}^{6}\frac{\partial W_s}{\partial x}\tilde{\theta}_s)$$
$$-\frac{g}{C_p}\frac{\partial h}{\partial y}\frac{1}{\theta_{av}}(\sum_{s=1}^{6}\frac{\partial W_s}{\partial y}\tilde{\theta}_s),\qquad〔80〕$$

$$\left[\frac{\partial(\theta,P_*)}{\partial(x,y)}\right]_E=\sum_{s=1}^{6}\sum_{t=1}^{6}(\frac{\partial W_s}{\partial x}\frac{\partial W_t}{\partial y}-\frac{\partial W_s}{\partial y}\frac{\partial W_t}{\partial x}-\sigma\frac{\partial h}{\partial x}W_s\frac{\partial W_t}{\partial y}$$
$$+\sigma\frac{\partial h}{\partial y}W_s\frac{\partial W_t}{\partial x})\tilde{\theta}_s\tilde{P}_{*t}+\frac{g}{C_p}\frac{\partial h}{\partial y}\frac{1}{\theta_{av}}\sum_{s=1}^{6}\frac{\partial W_s}{\partial x}\tilde{\theta}_s$$
$$-\frac{g}{C_p}\frac{\partial h}{\partial x}\frac{1}{\theta_{av}}\sum_{s=1}^{6}\frac{\partial W_s}{\partial y}\tilde{\theta}_s\qquad〔81〕$$

在〔80〕式的最後兩項，以及〔81〕式的最後兩項，非線性項$\frac{1}{\theta}$採用長期平均值$\frac{1}{\theta_{av}}$。由於配重函數爲與時間無關的空間函數，而且σ，g，C_p，h及θ_{av}皆爲常數，如果以$\tilde{\theta}_s\tilde{P}_t$爲輸入變數，則皆爲線性方程式。

經過上述線性化過程，已經獲得線性地面風場模式。這個線性數學模式需要54個輸入變數，且都是由六個測站的觀測資料求得，列舉如下：$\tilde{\theta}_1\tilde{P}_{*1}$，$\tilde{\theta}_1\tilde{P}_{*2}$，$\tilde{\theta}_1\tilde{P}_{*3}$，$\tilde{\theta}_1\tilde{P}_{*4}$，$\tilde{\theta}_1\tilde{P}_{*5}$，$\tilde{\theta}_1\tilde{P}_{*6}$，$\tilde{\theta}_2\tilde{P}_{*1}$，$\tilde{\theta}_2\tilde{P}_{*2}$，$\tilde{\theta}_2\tilde{P}_{*3}$，$\tilde{\theta}_2\tilde{P}_{*4}$，$\tilde{\theta}_2\tilde{P}_{*5}$，$\tilde{\theta}_2\tilde{P}_{*6}$，$\tilde{\theta}_3\tilde{P}_{*1}$，$\tilde{\theta}_3\tilde{P}_{*2}$，$\tilde{\theta}_3\tilde{P}_{*3}$，$\tilde{\theta}_3\tilde{P}_{*4}$，$\tilde{\theta}_3\tilde{P}_{*5}$，$\tilde{\theta}_3\tilde{P}_{*6}$，$\tilde{\theta}_4\tilde{P}_{*1}$，$\tilde{\theta}_4\tilde{P}_{*2}$，$\tilde{\theta}_4\tilde{P}_{*3}$，$\tilde{\theta}_4\tilde{P}_{*4}$，$\tilde{\theta}_4\tilde{P}_{*5}$，$\tilde{\theta}_4\tilde{P}_{*6}$，$\tilde{\theta}_5\tilde{P}_{*1}$，$\tilde{\theta}_5\tilde{P}_{*2}$，$\tilde{\theta}_5\tilde{P}_{*3}$，$\tilde{\theta}_5\tilde{P}_{*4}$，$\tilde{\theta}_5\tilde{P}_{*5}$，$\tilde{\theta}_5\tilde{P}_{*6}$，$\tilde{\theta}_6\tilde{P}_{*1}$，$\tilde{\theta}_6\tilde{P}_{*2}$，$\tilde{\theta}_6\tilde{P}_{*3}$，$\tilde{\theta}_6\tilde{P}_{*4}$，$\tilde{\theta}_6\tilde{P}_{*5}$，$\tilde{\theta}_6\tilde{P}_{*6}$，$\tilde{\theta}_1$，$\tilde{\theta}_2$，$\tilde{\theta}_3$，$\tilde{\theta}_4$，$\tilde{\theta}_5$，$\tilde{\theta}_6$，$V_1$，$V_2$，$V_3$，$V_4$，$V_5$，$V_6$，$U_1$，$U_2$，$U_3$，$U_4$，$U_5$，$U_6$。

有六個觀測值，需要六個重配函數，分別代表六個觀測值的配重分佈。

$$\theta(x,y)=\sum_{s=1}^{6}W_s(x,y)\,\tilde{\theta}_s$$

式中$W_s(x,y)$爲測站s的配重函數，θ_s爲測站s的觀測值，$\theta(x,y)$爲(x,y)處的內差函數值。

數值方法將研究的區域分爲若干網格點，然後研究各網格點的變數值。於是$\theta(x,y)$，$W_s(x,y)$都可以用數值方法描述，即由各網格點的函數值描述之。令$\vec{\theta}$爲$\theta(x,y)$在各網格點的函數值所組成的向量；$\vec{W}_s$爲$W_s(x,y)$在各網格的函數值所組成的向量；$\vec{\tilde{\theta}}$爲測站觀測值所組成的向量。假設有M個網格點及六個測站，則

$$\vec{\theta}=\begin{Bmatrix}\theta_1\\ \theta_2\\ \vdots\\ \theta_M\end{Bmatrix},\quad \vec{W}_s=\begin{Bmatrix}W_{1s}\\ W_{2s}\\ \vdots\\ W_{Ms}\end{Bmatrix},\quad \vec{\tilde{\theta}}=\begin{Bmatrix}\tilde{\theta}_1\\ \tilde{\theta}_2\\ \vdots\\ \tilde{\theta}_6\end{Bmatrix}\qquad〔82〕$$

若以W_s爲矩陣〔W〕的行（Column），

則 〔W〕$=\{\vec{W}_1,\vec{W}_2,\cdots\cdots,\vec{W}_6\}$

故 $\vec{\theta}=〔W〕\vec{\tilde{\theta}}$ 〔83〕

利用客觀分析可找出配重矩陣〔W〕，配重函數的微分可由數值方法求得。

伍、理論的應用

線性化的數學模式需要54個輸入變數已如前述，其輸出變數爲一組流場。本文針對71年3640組輸入變數，希望求出全年3640組地面流場。再根據這3640組地面流場分析風力特性，並計算風能分佈。如果每一組輸入變數都經數學模式計算，共需3640次，極其費時。經驗正交函數提供了一條簡便的途徑。

因爲有54個輸入變數，所以54組經驗正交函數的線性組合可以完全定義這3640組輸入變數。即

〔P〕$=$〔Q〕〔Y〕

式中〔P〕爲3640 × 54的輸入變數矩陣，每一列（row）爲一組輸入變數。〔Q〕爲3640×54的係數矩陣。〔Y〕爲54 × 54 的經驗正交函數矩陣，每一列爲一組經驗正交函數。

由於數學模式爲線性模式，根據上述討論，若以符號L代表本數學模式運算，則

$$L(〔P〕)=L(〔Q〕〔Y〕)=〔Q〕L(〔Y〕)\qquad〔84〕$$

以54組經驗正交函數爲輸入變數，本數學模式可以求出54組特徵流場，然後乘以係數矩陣〔Q〕，全年3640組流場皆可求得。最重要的是無論輸入變數有幾組，都只有54

組經驗正交函數，於是數學模式只需計算54次。在處理大量輸入變數時，經驗正交函數不失爲強而有力的工具。

根據許多學者的觀測分析與研究，風力的頻率分佈可以特定的概率密度函數來表示，一般常用者有對數常態概率密度函數（Log-normal probability density function）與魏伯概率密度函數（Weibull probability density function）。此種概率函數爲雙參數函數，亦即此二參數一旦被資料採樣（data sampling）所決定，則函數就被確定。

風力頻率之樣本概率函數（Sample probability function）之求取必須先對採樣期間作風力持續分析，由此作出風力持續曲線（Wind speed duration curve）根據此曲線作正常化（Normalization），便可求得風力頻率之樣本概率函數。風力頻率概率函數係指樣本概率函數的系集平均（ensemble average）。若以魏伯概率函數代表之，令P（V）爲出現風速V之概率，則

$$P(V)=\frac{S_h}{S_c}\left(\frac{V}{S_c}\right)^{S_h-1}\exp\left[-\left(\frac{V}{S_c}\right)^{S_h}\right] \qquad 〔85〕$$

式中參數S_h、S_c，分別由下兩式決定

$$V=S_c\Gamma\left(1+\frac{1}{S_h}\right) \qquad 〔86〕$$

$$\sigma^2=S_c^2\left[\Gamma\left(1+\frac{2}{S_h}\right)-\left(\Gamma\left(1+\frac{1}{S_h}\right)\right)^2\right] \qquad 〔87〕$$

式中Γ爲Gamma function。

理論上，風能與風速成三次方關係，亦即

$$W=\frac{1}{2}\rho v^3 \qquad 〔88〕$$

故

$$E<W>=\frac{1}{2}E<\rho v^3> \qquad 〔89〕$$

此處<>代表系集平均（ensemble average）一般假設風力與密度無相關性，則

$$E<W>=\frac{1}{2}E<\rho>\sigma^3\left[\sqrt{\beta}+3\frac{\overline{V}}{\sigma}+\left(\frac{\overline{V}}{\sigma}\right)^3\right] \qquad 〔90〕$$

式中V，σ，$\sqrt{\beta}$分別爲風速之平均、標準偏差與岐值（skewness）。今將魏伯函數代入，則

$$E<W>=\frac{S_c^3}{2}E<\rho>\Gamma\left(1+\frac{3}{S_h}\right) \qquad 〔91〕$$

可用風能（usable wind energy）可表示如下

$$W_a=\begin{cases}0 & ; \quad V\le V_0\\ A+BV+CV^2 & ; \quad V_0\le V\le V_1\\ W_r & ; \quad V_1\le V\le V_2\\ 0 & ; \quad V>V_2\end{cases} \qquad 〔92〕$$

式中V_0，V_1，V_2分別代表切入（cut in），額定（rated）與切離（cut off）風速，W_r爲額定功率（rated power），而A、B、C則因所採用之風能轉換系統而異。可用風能W_a與風速之關係如圖1。圖中$V_m=(V_0+V_1)/2$，若W_m爲風速V_m的可用風能，則$W_m=W_r(V_m^3/V_1^3)$。由下列聯立方程式，可求出A、B、C。

$$A+BV_0+CV_0^2=0 \qquad 〔93〕$$

$$A+BV_1+CV_1^2=W_r \qquad 〔94〕$$

$$A+BV_m+CV_m^2=W_r(V_m^3/V_1^3) \qquad 〔95〕$$

若風力頻率概率函數已知，則平均可用風能

$$\overline{W_a}=\int_0^\infty W_a(V)P(V)\,dV \qquad 〔96〕$$

容量因子F_c（Capacity factor）爲

$$F_c=\overline{W_a}/W_r \qquad 〔97〕$$

E<W>與$\overline{W_a}$或F_c即可用來評估風能場址的潛力。

陸、結果與討論

本文建立數值模式，並利用經驗正交函數評估台灣北部地區的風力潛能。研究的地區爲東經120°55.7′至121°46.6′，北緯24°43.6′至25°13.1′。東西距離84公里，南北52公里，而格點距離爲2公里。在這個區域範圍內，有台北、宜蘭、淡水、竹子湖、基隆、新竹等六個氣象觀測站。分別從這六個觀測站取得71年的溫度、壓力、風速、風向等全年觀測資料。這六個觀測站的每日觀測次數不同，最少爲10次。分別從六個觀測站中，每天選出10組同時間的觀測資料，由於12月31日的資料不全，故有3640組資料。然後利用地面風場數學模式及經驗正交函數，計算每一組資料的風場分佈，再利用風力分佈函數的曲線設定求取各網格點的風力特性作爲71年全年風力潛能評估的基礎。

地面風場模式利用地轉風逐步修正以求取實際風場分佈。在本文探討的台灣北部地區，地轉風可視爲常數。台灣沒有高空觀測資料，而且胡氏模式探討的流場爲地面風場，故本文不採用高空資料求取地轉風。求出六個測站的風速向量和後乘以一個常數，然後旋轉一個角度，則可作爲地轉風的近似值（6）。

至於地形影響的上限，隨不同地區的地形與地形變化情形而異。針對台灣北部地區，在計算平滑風場時，這個上限可以選擇3000公尺，這個變數必須隨地形特性而調整。用實際地形梯度修正平滑風場時，此變數值不容易決定。採取的方法是將實際地形與平滑地形的最大差值乘以一個倍數，以爲實際地形影響的上限。

綜合上述討論，有三個變數可以修正，以期獲得最佳的風場分佈。這三個變數爲平滑地形與實際地形最大差值的倍數a_h，六個測站平均風速的倍數a_v，以及平均風速旋轉角度a_θ。測站風速均被調整至離地面20公尺。首先求出全年的觀測資料平均值，然後分別針對這平均資料，進行數學模式最佳分析，求a_h，a_v及a_θ的最佳值。最佳分析法係

基於觀測風速及數學模式觀測站風速的最小標準偏差。

以全年的平均觀測資料作爲數學模式的輸入變數，然後作最佳分析。令 $a_\theta = 27$ 度，$a_v = 1.37$，然後針對不同的 a_h 值，求出風場分佈，並與六個觀測站的觀測風速比較，計算標準偏差

$$S.D. = \sqrt{\frac{\sum_{i=1}^{6} (V_c - V_o)^2}{5}}$$

式中 V_c 爲數值模式求得的測站風速，V_o 爲測站觀測風速，求出各 a_h 值後可得圖 2。最佳 a_h 值爲 4.4。令 a_h 爲 4.4，$a_\theta = 27°$，並針對不同的 a_v 值，求風場分佈，並計算標準偏差，可得最佳 a_v 值爲 1.18，如圖 3。令 $a_h = 4.4$，$a_v = 1.18$，針對不同 a_θ 求標準偏差，並作圖 4，可得最佳 a_θ 值爲 28°。再令 $a_v = 1.18$，$a_\theta = 28°$，針對不同 a_h 求標準偏差可得圖 5。最佳 a_h 值依然爲 4.4，根據以上討論，全年的最佳變數值爲 $a_h = 4.4$，$a_v \doteq 1.18$，$a_\theta = 28.0°$。

數學模式探討的風場必須離地面一定高度。若此高度爲20公尺，則觀測站的風速需校正至離地面 20 公尺，校正公式爲

$$\frac{V(Z)}{V_o} = \left(\frac{Z}{Z_o}\right)^{0.14}$$

各觀測站的測風高度：新竹爲 13.2 公尺，宜蘭爲 9.4 公尺，淡水爲 12.2 公尺，竹子湖爲 9 公尺，基隆爲 34.6 公尺，台北爲 23.4 公尺。上式中，V_o 爲觀測風速，Z_o 爲測風高度，Z 爲 20 公尺。

針對任一特定時間的一組觀測資料，數學模式能夠求得一組地面風場。全年有 3640 組資料，面對如此龐大的資料，勢必無法每一組資料都經數學模式計算一次地面風場。利用本文提出的經驗正交函數，數學模式只需計算固定次數，就能求出全部時間的地面風場。無論觀測資料的時間取樣次數如何增加，數學模式必須計算的次數不變。這是利用經驗正交函數的主要優點。此外，全部時間的地面流場可分爲兩個矩陣的乘積，一爲係數矩陣，另一爲經驗正交函數特徵流場。電腦只需記憶這兩個矩陣，而不需記憶全部時間的地面流場，因此大量節省記憶空間。在資料處理上，極爲方便。若想知道某一特定時間的地面流場，只需由係數矩陣中找出對應的係數，再乘以經驗正交函數特徵流場矩陣。

經驗正交函數雖有上述諸多優點，却只能應用於線性數學模式，或是用於資料處理。如何把非線性數學模式線性化，則爲應用上的一個重要課題。線性化數學模式與非線性數學模式之間必定存有誤差。基於維持數學模式的正確性，這個誤差必須限制在可容許的範圍內。本文由全年 3640 組觀測資料中，以隨機取樣方式選出 80 組觀測資料。然後利用非線性地面流場模式計算流場，再與經驗正交函數及線性化地面流場模式所求得的同時間流場相比較，以檢驗線性模式與非線性模式的差異。每個網格點的速度分爲 X 分量與 Y 分量。分別針對所有網格點的 X 速度分量與 Y 速度分量，求線性模式流場與非線性模式流場之間的標準偏差，據此分析模式線性化引起的誤差。表 1 爲全年 80 個

隨機取樣的標準偏差。由表 1，可以發現百分之九十以上 X 分量與 Y 分量標準偏差約爲 0.3 m／sec，極少數的特例高於 1 m／s。圖 6 爲線性模式 X 軸速度分量標準偏差分佈曲線。圖 7 爲線性模式 Y 軸速度分量標準偏差分佈曲線。分析這些特例發現其觀測風的風向差異非常大，於是向量和很小，亦即背景風非常小，而非線性模式的渦旋度積分常數大得不合理。在這些特殊情形下，如何求得合理的背景風，值得進一步探討。

利用經驗正交函數可輕而易舉求出全部時間的地面流場，然後分析風力特性，並作風能評估。如果不採用經驗正交函數，則只能以隨機取樣方式選取少數觀測資料，求出地面風場，然後分析風力特性，並作風能評估。本文在網格系統中隨機選取兩個網格點，在這 2 個網格點分別研究不同隨機取樣次數所求得的平均風速與風能密度，並繪圖表示如圖 8 至圖 11。X 軸爲隨機取樣次數，Y 軸爲平均風速與風能密度。平均風速單位爲 m／sec，風能密度單位爲 W/m^2。這些隨機取樣分析係根據全年 3640 組觀測資料。每個圖形的最後一點爲利用經驗正交函數所求得的平均風速與風能密度。圖中明顯指出低取樣次數的變動幅度非常大，隨著取樣次數增加，變動幅度漸趨平緩，逐漸接近於穩定值，此穩定值即爲利用經驗正交函數所求得的平均風速與風能密度。可見經驗正交函數提供了莫大的助益。圖 12 與 13 爲全年 3640 組流場中的最大風場等值線分佈圖與流線圖。圖 14 與 15 爲全年最小風場等值線分佈圖與流線圖。圖 16 與 17 爲全年風場向量平均的等值線分佈圖與流線圖。圖 18 爲全年風場絕對值平均分佈圖。圖 19爲全年風能密度分佈圖。圖 20 爲全年等容量因子分佈圖。圖 21 爲數學模式研究區域的地形分佈圖。本文係根據 NASA'S Plumbrook unit 風力機進行風能評估，其切入風速爲 3.6m／s，額定風速爲 8.0m／s，額定功率爲 100KW。冬半年比夏半年具有較高的等容量因子分佈，即冬半年具有較高的風能。

本文發展出來的地面流場數值模式執行一次約需 90 秒的 CPU時間。全年有 3640 組資料，若每一組資料都經數值模式計算其流場分佈，共需 327600 秒的 CPU 時間。引用經驗正交函數理論，可節省大量 CPU 時間。利用電腦分析全年的 3640 組資料，求出係數矩陣與經驗正交函數矩陣，約需 300秒的 CPU 時間。求出經驗正交函數後，數值模式必須計算 54 次，以求出 54 組特性流場，約需 4860 的 CPU 時間。係數矩陣與經驗正交函數矩陣相乘，可得到全部地面流場，每一組流場約需 3.7 秒的 CPU 時間，全年 3640 組流場需 13468 秒的 CPU時間。綜合上述討論，利用經驗正交函數求出 3640 組流場所費電腦時間約爲 18628 秒 CPU時間，比直接利用數值模式計算節省了 94.3％的 CPU時間。時間取樣資料愈多，此百分比愈高。

柒、結　論

本文提出經驗正交函數，並引用於線性數學模式。處理大量隨機性時間取樣資料時，經驗正交函數是爲經濟有效的方法。本文修正胡氏的地面流場數學模式，使之線性化，再引用經驗正交函數的觀念發展風能評估理論，並對台灣北部地區西海岸的風力潛能

做評估。本文提出的經驗正交函數可應用於任何線性模式。

本文利用全年，冬半年及夏半年的平均觀測值進行數學模式最佳分析。利用配重函數使非線性的胡氏地面流場數學模式線性化，並分析此線性模式與非線性模式的差異，發現百分之九十以上的線性模式標準偏差小於0.3m/s，正確性甚高。本文把經驗正交函數的觀念應用於此線性數學模式，求出全部取樣時間的流場。然後分析風力特性，進行風能評估。以全年3640組資料爲例，經驗正交函數分析法可節省94.3%的電腦時間。這個百分比隨取樣次數增加而提高。本文比較隨機取樣分析法與經驗正交函數分析法，發現低隨機取樣次數求得的結果具有頗大的變動幅度。經驗正交函數分析法沒有這種取樣誤差。風能評估的結果顯示冬半年有較多風能，而且風能有隨地形升高而增加的趨勢。

參考文獻

1. Franklin J. N., Matrix Theory (1968).
2. Hardy D.M., Empirical eigenvecter analysis of vector observations. Geephys. Res. Lett. 4, 319-320 (1977).
3. Fosberg M.A., Marlatt W.E., and Krupnak L., Estimating air-flow patterns over complex terrain. USDA Forest Research paper RM-162, Rocky Mountain, Forest and Range Experiment Station, Fort Collins, Colorado (1976).
4. Gerald C.F., Aplied Numerical method. 2nd edition, Addison-Wesley Publishing Company (1978).
5. Plate S.J., Aerodynamic characteristics of atmospheric boundary layer. N.T.I.S., Spring field, Virginia (1971).
6. 台灣北部西海岸地區風力潛能之評估，FM42，中央研究院物理研究所，民國七十三年四月。

表1　線性模式標準偏差（全年80隨機取樣）

取樣編號	U—SD	V—SD	取樣編號	U—SD	V—SD
1	0.136	0.184	41	0.313	0.287
2	0.128	0.186	42	0.329	0.255
3	0.137	0.175	43	0.310	0.330
4	0.305	0.274	44	0.272	0.273
5	0.379	0.403	45	0.220	0.260
6	0.163	0.257	46	0.157	0.280
7	0.137	0.208	47	0.399	0.331
8	1.658	1.723	48	0.544	0.597
9	0.145	0.180	49	0.435	0.512
10	0.138	0.176	50	0.251	0.261
11	0.134	0.244	51	0.132	0.282
12	0.486	0.476	52	0.826	0.924
13	0.232	0.284	53	0.145	0.205
14	0.757	0.760	54	0.979	1.066
15	0.465	0.527	55	0.647	0.632
16	0.123	0.189	56	0.140	0.231
17	0.509	0.588	57	0.155	0.190
18	0.243	0.308	58	0.153	0.221
19	0.281	0.263	59	0.181	0.200
20	0.519	0.711	60	0.140	0.277
21	1.427	1.115	61	0.141	0.219
22	0.342	0.237	62	0.144	0.222
23	0.182	0.290	63	0.114	0.221
24	0.127	0.179	64	0.154	0.279
25	0.144	0.190	65	0.149	0.257
26	0.154	0.191	66	0.212	0.307
27	0.328	0.343	67	0.182	0.301
28	0.213	0.238	68	0.250	0.266
29	0.124	0.231	69	0.136	0.203
30	0.920	1.011	70	0.192	0.226
31	0.217	0.306	71	0.174	0.237
32	0.131	0.240	72	0.115	0.235
33	0.141	0.271	73	0.213	0.213
34	0.325	0.390	74	0.232	0.237
35	0.208	0.312	75	0.149	0.194
36	0.272	0.286	76	0.172	0.198
37	0.789	1.028	77	0.168	0.202
38	0.283	0.342	78	0.126	0.183
39	0.186	0.199	79	0.254	0.322
40	2.058	2.170	80	2.433	2.210

U—SD：網格點速度的X軸分量標準偏差

V—SD：網格點速度的Y軸分量標準偏差

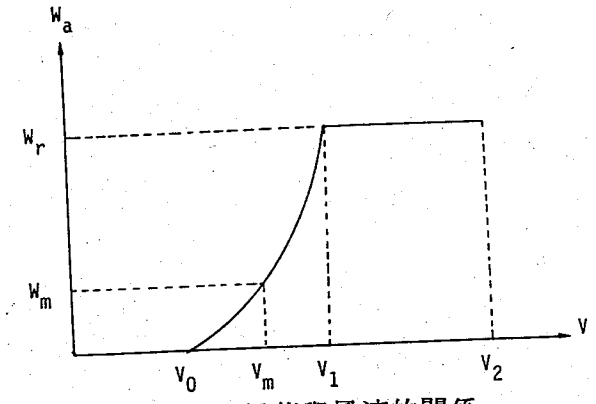

圖 1　可用風能與風速的關係

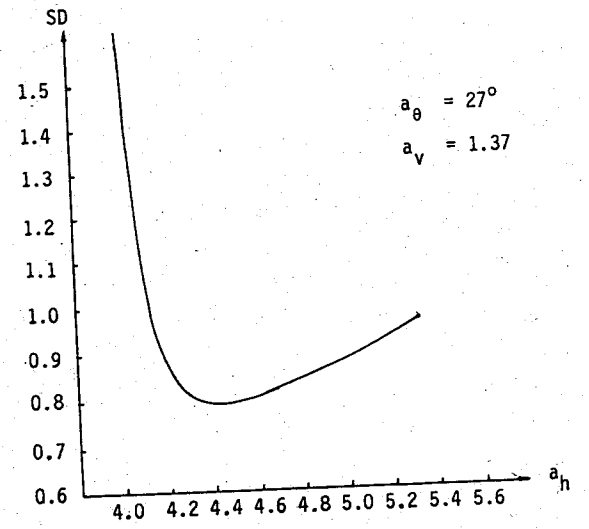

圖 2　不同 a_h 值的標準偏差（之 1）

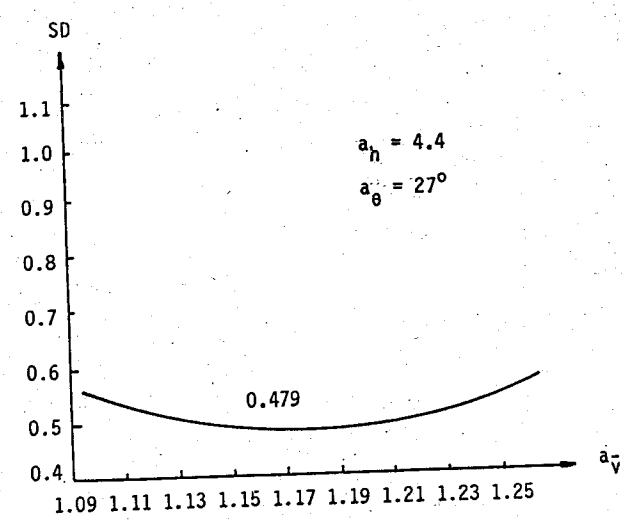

圖 3　不同 a_v 值的標準偏差

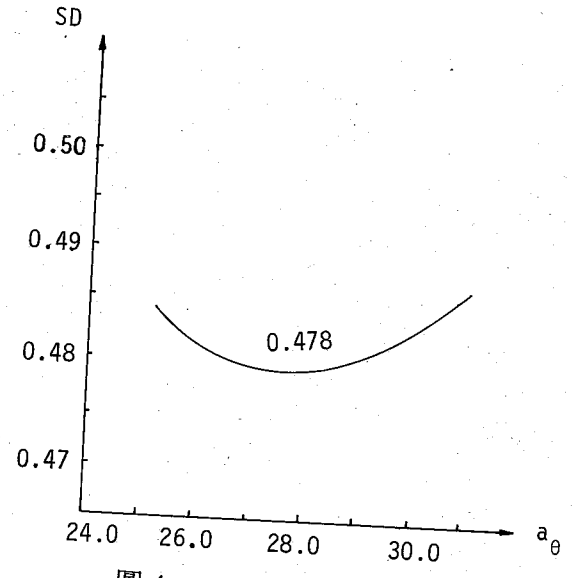

圖 4　不同 a_θ 值的標準偏差

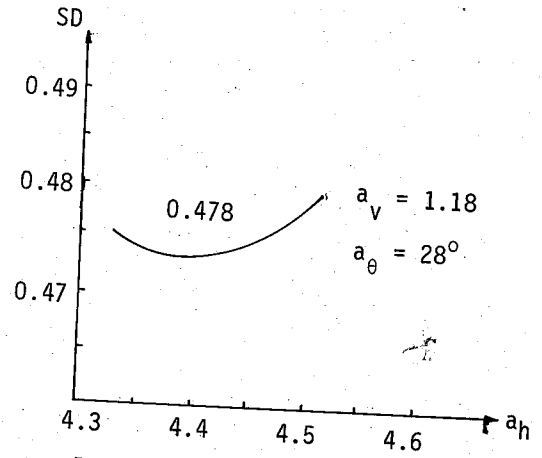

圖 5　不同 a_h 值的標準偏差（之 2）

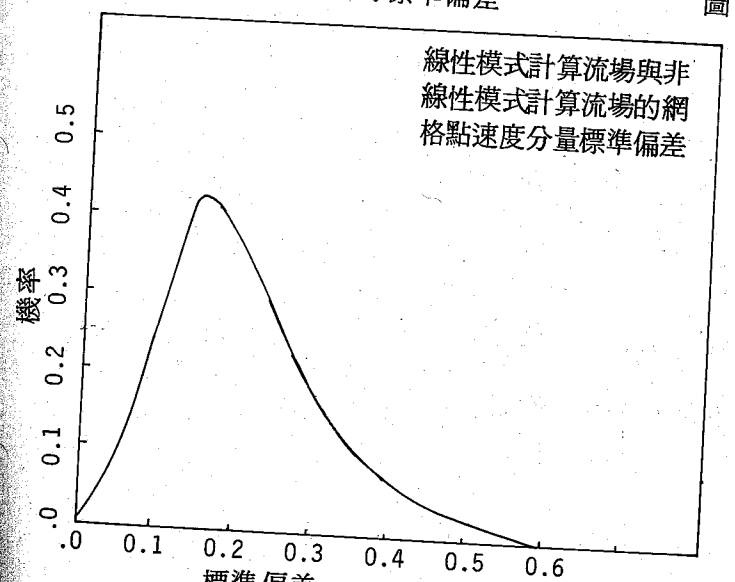

圖 6　線性模式 X 軸速度分量標準偏差分佈曲線

圖 7　線性模式 Y 軸速度分量標準偏差分佈曲線

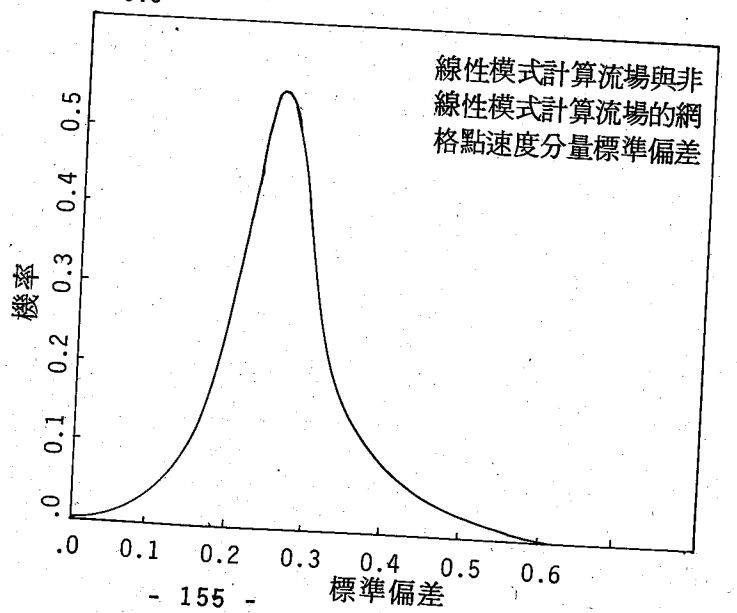

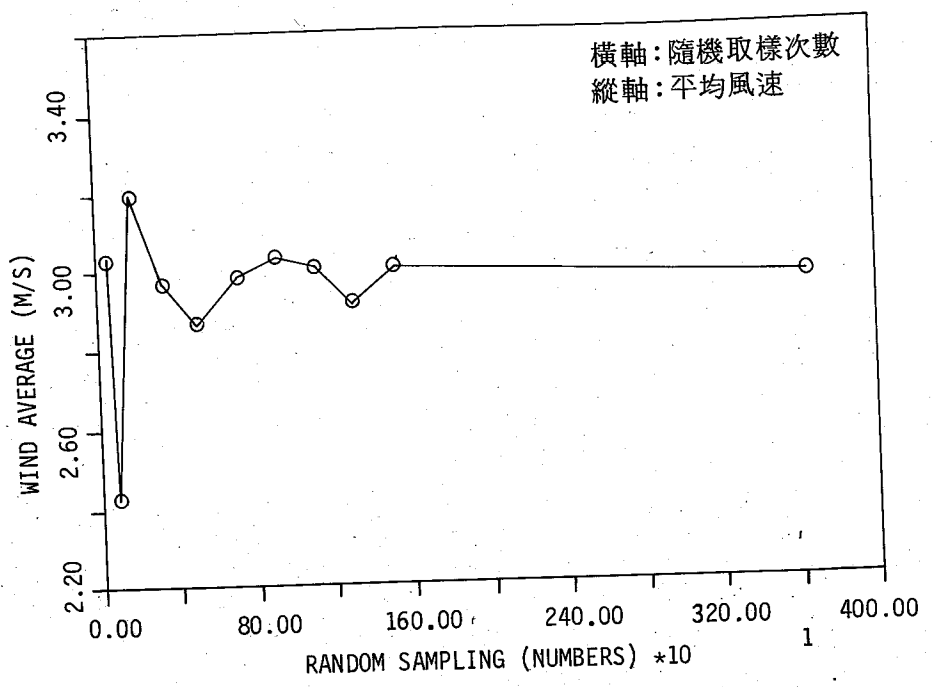

圖8：網格點（２，５）隨機取樣平均風速，圖中顯示取樣次數增加後平均風速逐漸趨近於穩定值

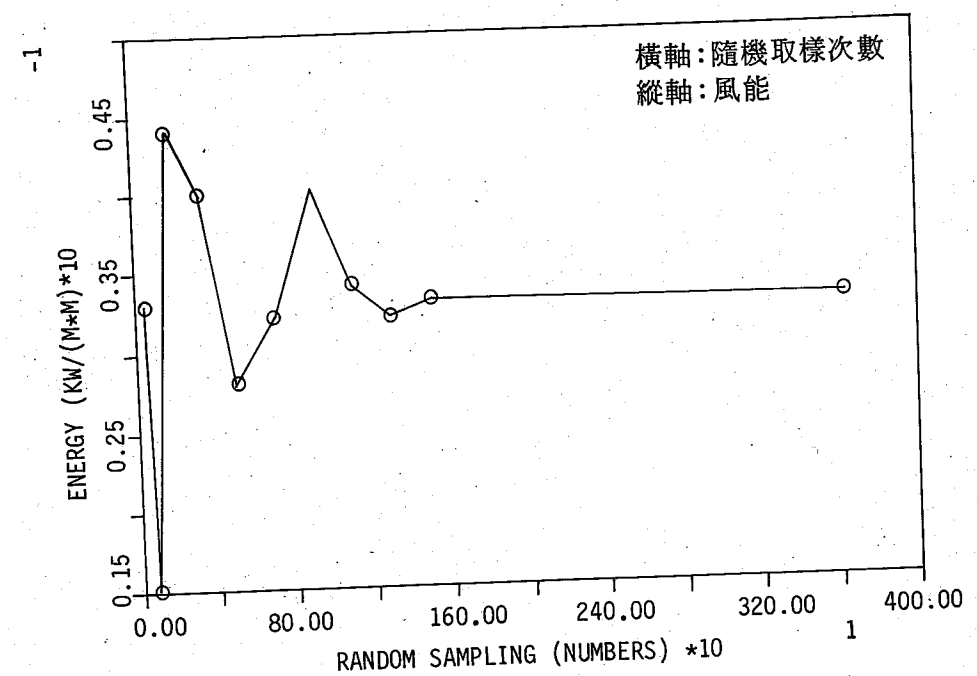

圖9：網格點（２，５）隨機取樣風能密度

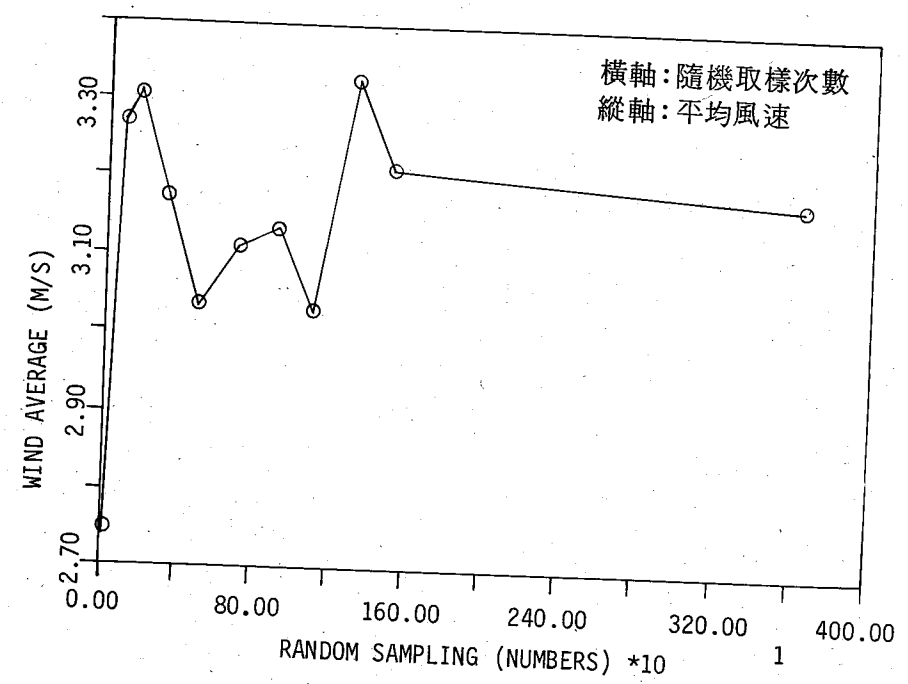

圖10：網格點（7,10）隨機取樣平均風速

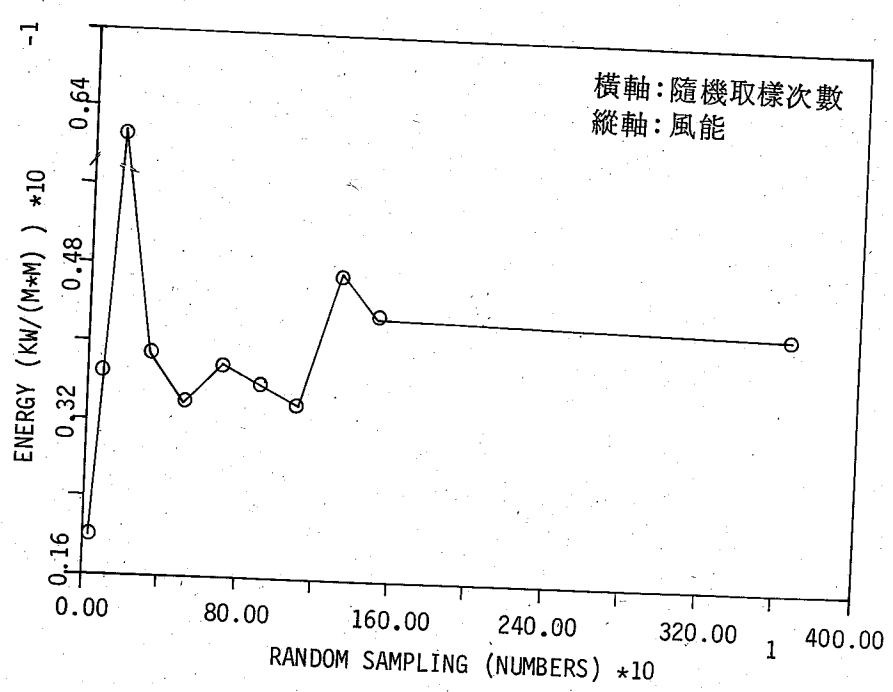

圖11：網格點（7,10）隨機取樣風能密度

網格點距離：2 公里　　單位：公尺／秒

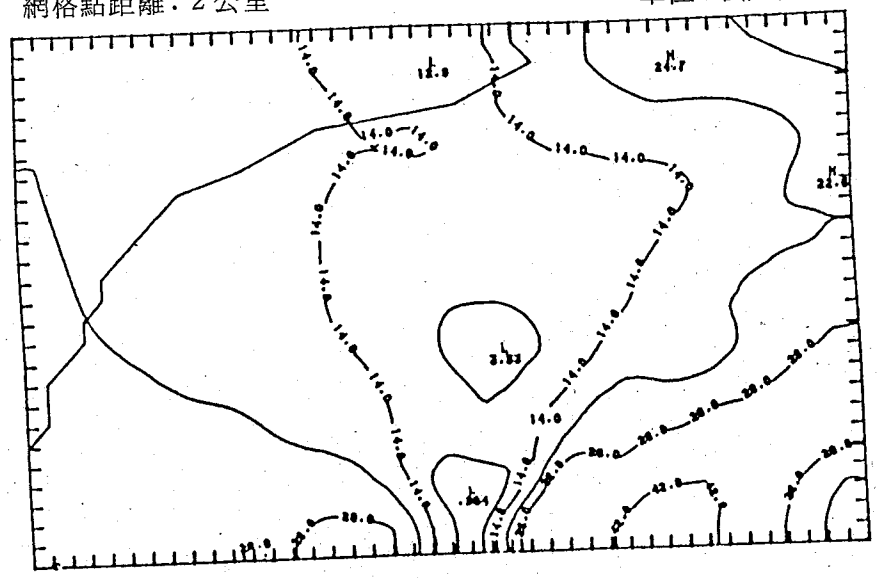

圖 12：全年最大風場分佈圖

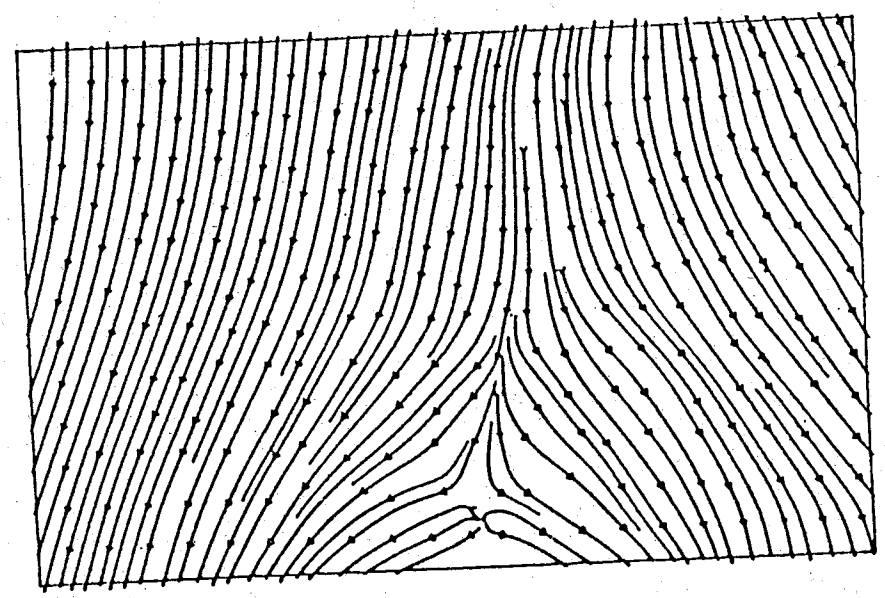

圖 13：全年最大風場流線圖

網格點距離：2 公里　　單位：公尺／秒

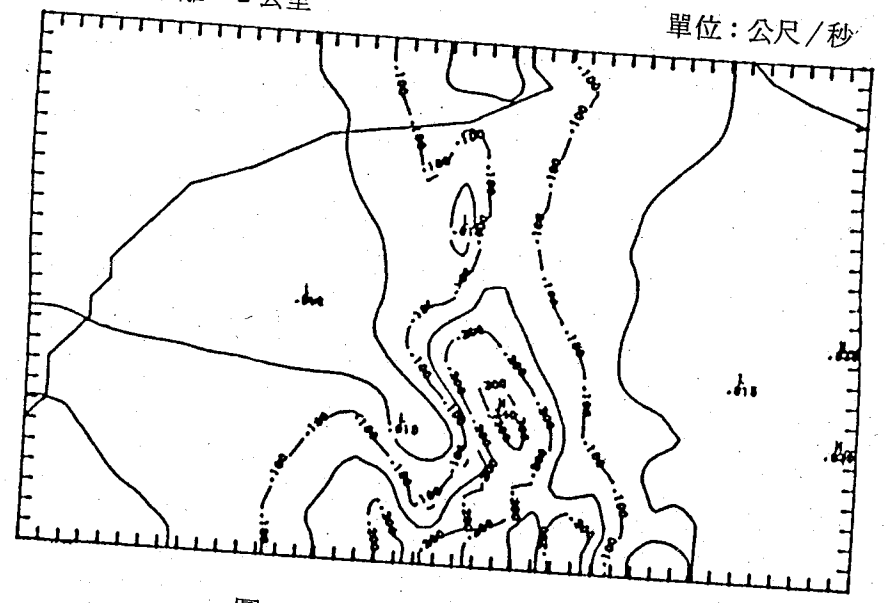

圖 14：全年最小風場分佈圖

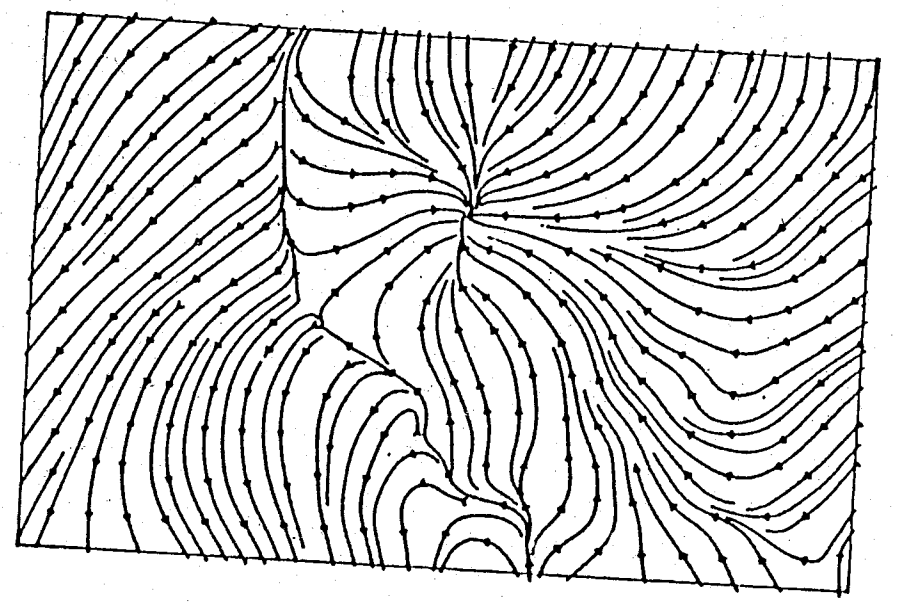

圖 15：全年最小風場流線圖

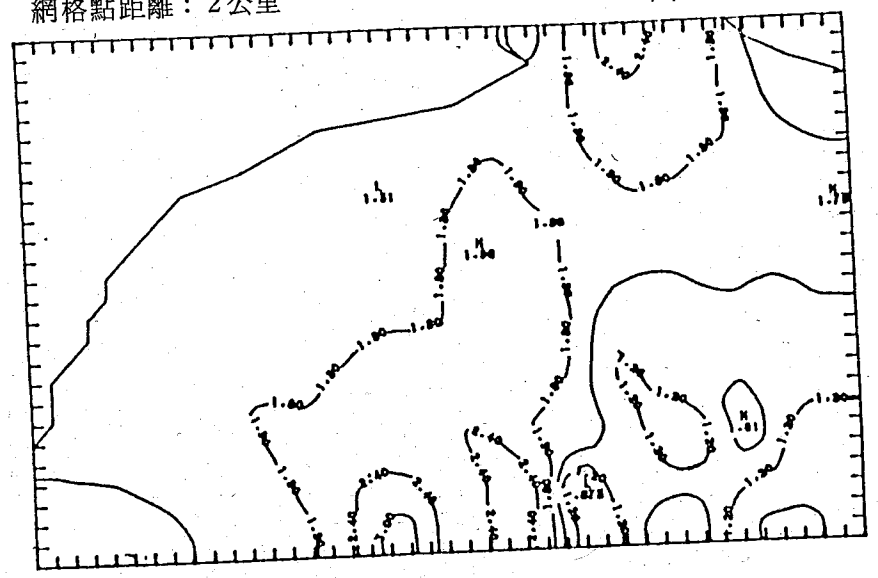

圖 16： 全年風場向量平均分佈圖

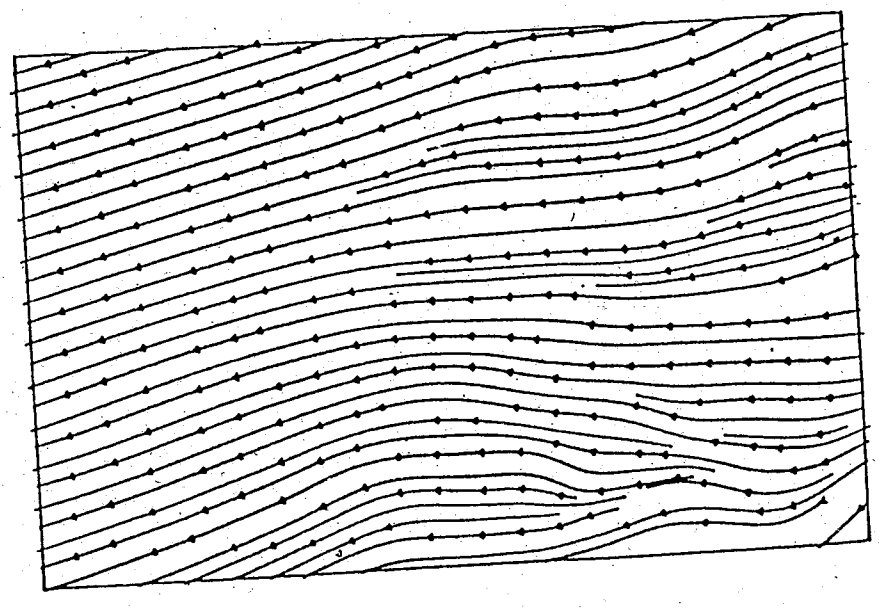

圖 17： 全年風場向量平均流線圖

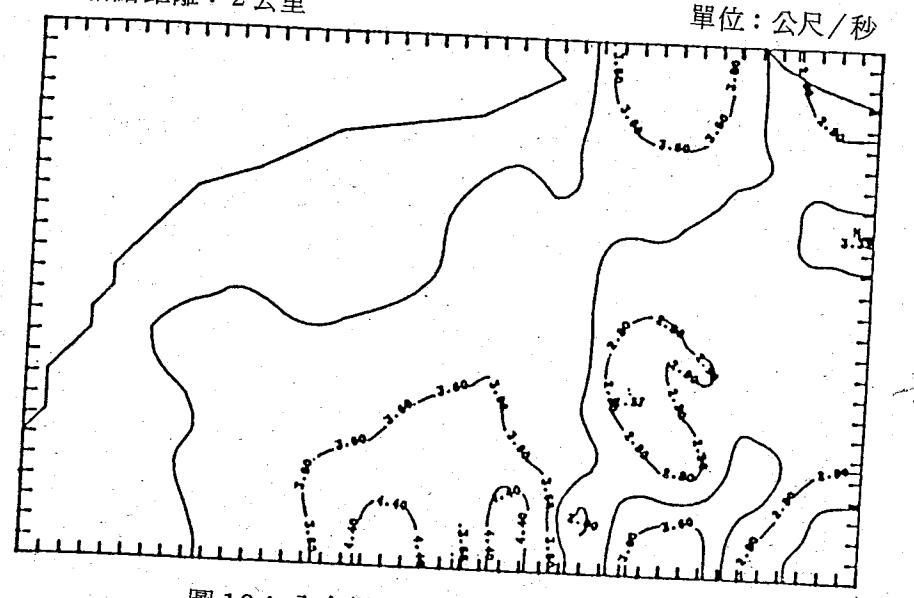

圖 18： 全年風場絕對值平均分佈圖

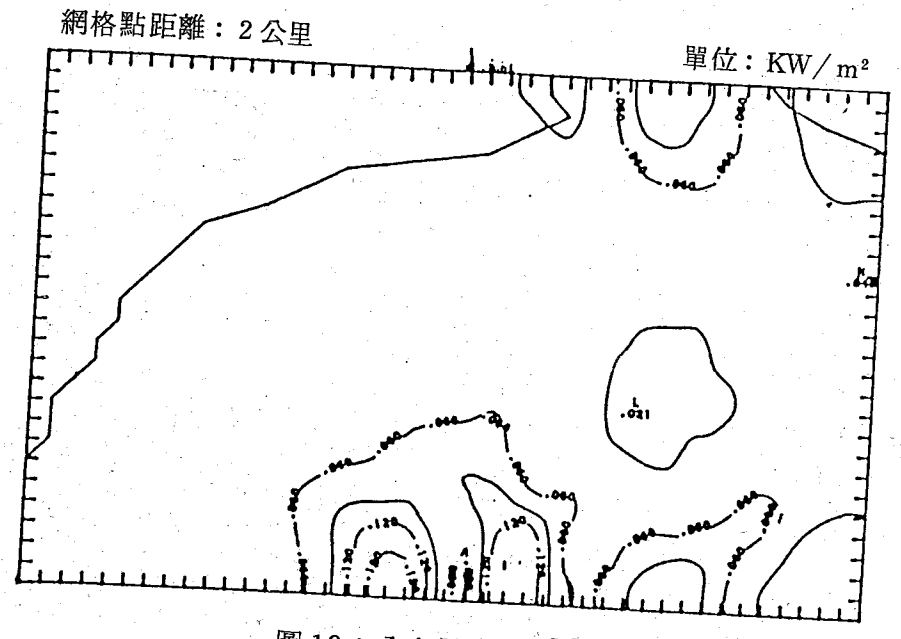

圖 19： 全年風能密度分佈圖

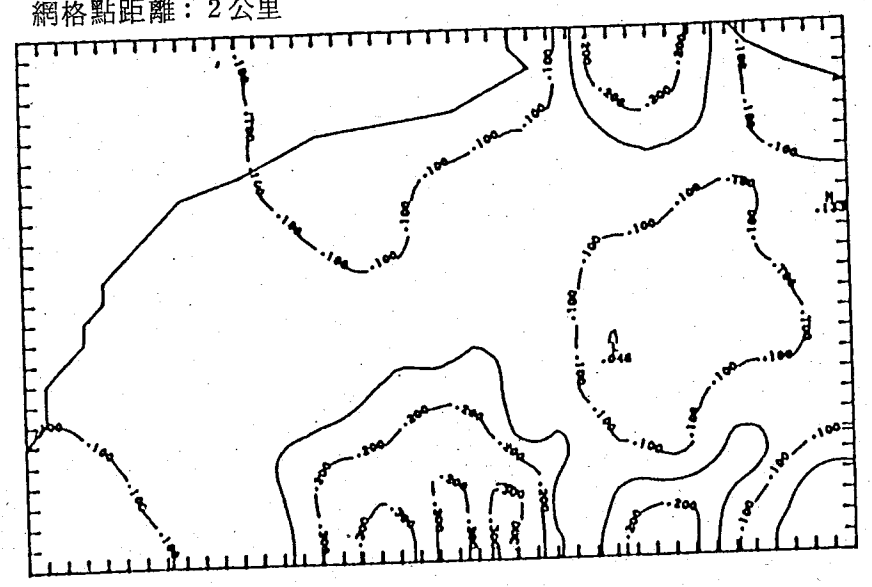

圖 20：全年等容量因子分佈圖

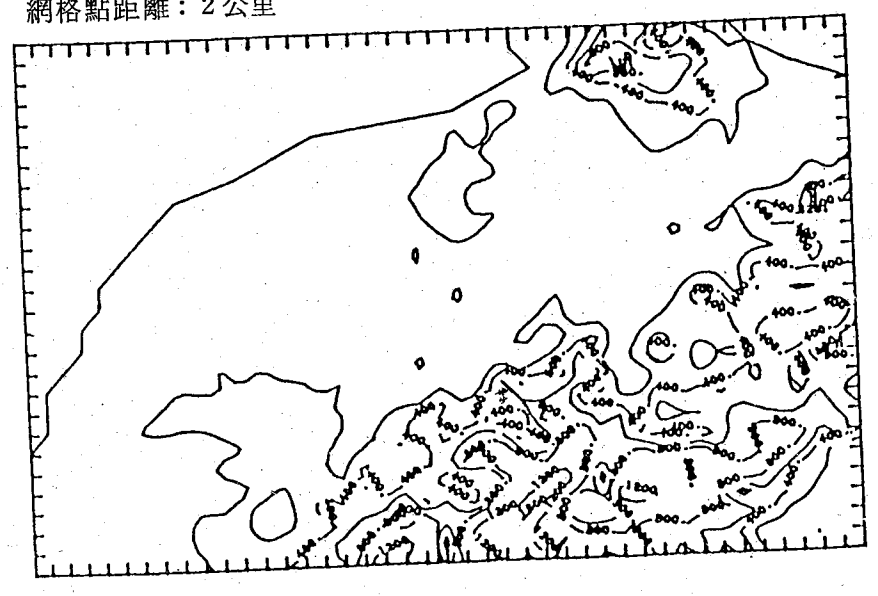

圖 21：台灣北部地區西海岸地形圖

THE THEORY AND APPLICATION OF EMPIRICAL ORTHOGONAL FUNCTION USE FOR WIND ENERGY ASSESSMENT

ABSTRACT

The theory of wind energy assessment is developed based on empirical orthogonal functions. The real field data over northern Taiwan are applied to verify the plausibility of the theory. This theory is useful to manage large amount of sampling data and large number of repeat computation of a mathematical model.

A sequence of sets of sampling data can be decomposed into the multiplication of coefficient matrix and empirical orthogonal function matrix. The empirical orthogonal functions are the eigenvecters of the corelation matrix of sampling data.

Empirical orthogonal function method is applicable to any model if relationships between inputs and outputs are linear. This paper linearizes Fosberg's mathematical model of terrain flow. With the help of empirical orthogonal functions, the total sets of terrain flow patterns corresponding to all data of observation stations for a long period (a year here) are calculated. The analysis of wind characteristics and the assessment of wind energy are performed after the whole sets of flow patterns are calculated.

This paper estimates the difference between linear mathematical model and nonlinear mathematical model to preserve the accuracy of linear mathematical model. In order to realize the benifit of empirical orthogonal function method, the results of the random sampling method and those of the empirical orthogonal function method are compared. It shows that the theory of wind energy assessment based on empirical orthogonal functions is economical, accurate, plausible and powerful.

大氣層變流中浮昇效應對跡流之影響

黃　榮　鑑

中央研究院物理研究所

陳　虞　修

中央研究院物理研究所

摘　要

本文爲研究穩定溫度層變流體通過薄板以及薄板上下爲兩種不同溫度的均質流場，其浮昇效應對於跡流產生的物理現象及影響。由流體力學的動量方程式經微分轉換成流線函數—旋量方程式，配合連續方程式及能量方程式，利用有限差分法的數值解以瞭解流線函數、旋量、速度及溫度在流場中的變化。

壹、前　言

大氣層變流通過障礙體的研究爲地球物理研究中基本及重要的問題。在重力場中，溫度層變之流體通過障礙體後，流場除了受邊界體因剪力所產生的旋量干擾外，尚有因密度之變化所產生的浮昇效應的作用，故所形成的物理現象，異於均質流場（ Hwang, 1982 ）。流場中的浮昇效應受上游邊界層作用產生的浮昇以及跡流中溫度差異形成的浮昇所共同影響。爲瞭解跡流中之浮昇效應對流場的影響，本文導引此一問題於最簡單的流型：溫度層變之流體通過有限薄板之效應，以探討浮昇效應對跡流之影響。

有關這方面的研究最早由Long（1959,1962 ）開始，他利用實驗觀察層變流體通過平板產生的流況變化，並由理論解釋上游端所發生的跡流現象。Martine （ 1968 ）研究薄板在線性密度層變之流場中運動產生的流況變化，經由實驗得知若層變不大或流速極大，則層變產生的影響極小；如果層變加大，則在平板上由於干擾波發生而影響界面層厚度的形成，使其最大值不發生於板尾。若流速極慢同時又有適當的層變作用，則板上游端有跡流發生。Pao（1968）也以實驗及理論探討在密度層變流場中一均勻流速通過平板的流場情形，其研究指出當流場之重力作用大於慣性作用時，則在平板上游端會有跡流（ upstream wake）發生，同時上游端的速度分佈及平板上方的界面層厚度將呈不規則變化。Kelly 及Redekopp（1970）研究層變流體的界面層問題，並引用盧斯爾數（ Russell number ）；$R_{UL}=(NL/U_0)^2$，爲指標參數得出當$R_{UL}>O(R_L^{1.2})$，界面層厚度由往下游增加改變成往上游增加，同時在上游端出現跡流。

上述的這些研究都在探討穩定層變流在板上及其前端上游區造成的影響，對於浮昇

作用單純影響下游跡流區的研究，則未有探討。本文利用數值模式研討層變流體通過薄板後，尾端跡流受浮昇效應影響的一些特性。所討論的流場有兩種，一爲穩定的溫度層變流體通過薄板，另一爲薄板上下爲兩種不同溫度的均質流場通過薄板等問題。

貳、基本方程式

爲了探討流體通過有限長平板受浮昇影響的流場特性，將流場按其受浮昇影響之不同分別加以研討如圖一所示，其一爲流場內之溫度爲線性穩定層變；其二爲薄板上下爲兩種不同溫度的均質流場。流場處於均勻重力場作用之二維溫度層變平流中，流體之粘滯係數及熱傳導係數爲常數經由波氏近似（Boussinesq approximation），則控制流場的連續方程式、運動方程式及能量方程式分別爲：

$$\frac{\partial \tilde{u}}{\partial \tilde{x}}+\frac{\partial \tilde{v}}{\partial \tilde{y}}=0 \tag{1}$$

$$\rho_0\left(\frac{\partial \tilde{u}}{\partial \tilde{t}}+\tilde{u}\frac{\partial \tilde{u}}{\partial \tilde{x}}+\tilde{v}\frac{\partial \tilde{u}}{\partial \tilde{y}}\right)=-\frac{\partial \tilde{p}}{\partial \tilde{x}}+\mu\left(\frac{\partial^2 \tilde{u}}{\partial \tilde{x}^2}+\frac{\partial^2 \tilde{u}}{\partial \tilde{y}^2}\right) \tag{2}$$

$$\rho_0\left(\frac{\partial \tilde{v}}{\partial \tilde{t}}+\tilde{u}\frac{\partial \tilde{v}}{\partial \tilde{x}}+\tilde{v}\frac{\partial \tilde{v}}{\partial \tilde{y}}\right)=\frac{\partial \tilde{p}}{\partial \tilde{y}}-\rho g+\mu\left(\frac{\partial^2 \tilde{v}}{\partial \tilde{x}^2}+\frac{\partial^2 \tilde{v}}{\partial \tilde{y}^2}\right) \tag{3}$$

$$\rho_0 C_p\left(\frac{\partial \tilde{T}}{\partial \tilde{t}}+\tilde{u}\frac{\partial \tilde{T}}{\partial \tilde{x}}+\tilde{v}\frac{\partial \tilde{T}}{\partial \tilde{y}}\right)=k\left(\frac{\partial^2 \tilde{T}}{\partial \tilde{x}^2}+\frac{\partial^2 \tilde{T}}{\partial \tilde{y}^2}\right)+\Phi \tag{4}$$

式中，$\tilde{u}$，$\tilde{v}$分別$\tilde{x}$及$\tilde{y}$向之速度分量，μ及k爲流體之粘滯係數及熱傳導係數，ρ_0爲參考密度，$\tilde{T}$爲流體之溫度。

爲分析方便起見，將(2)、(3)式分別對$\tilde{y}$及$\tilde{x}$取微分相減消去壓力項，並定義旋量，$\tilde{\zeta}=\partial\tilde{v}/\partial\tilde{x}-\partial\tilde{u}/\partial\tilde{y}$，則可得旋量方程式：

$$\frac{\partial \tilde{\zeta}}{\partial \tilde{t}}+\tilde{u}\frac{\partial \tilde{\zeta}}{\partial \tilde{x}}+\tilde{v}\frac{\partial \tilde{\zeta}}{\partial \tilde{y}}=-\frac{g}{\rho_0}\frac{\partial \rho_0}{\partial \tilde{x}}+\nu\left(\frac{\partial^2 \tilde{\zeta}}{\partial \tilde{x}^2}+\frac{\partial^2 \tilde{\zeta}}{\partial \tilde{y}^2}\right) \tag{5}$$

當壓力的變化不很大時，流體的密度，$\tilde{\rho}$與溫度$\tilde{T}$的關係爲

$$\tilde{\rho}=\rho_0\left[1-\alpha_0\left(\tilde{T}-T_0\right)\right] \tag{6}$$

式中，ρ_0及T_0分別爲參考密度及溫度，α_0爲熱脹係數，經對$\tilde{x}$取微分可得：

$$\frac{1}{\rho_0}\frac{\partial \tilde{\rho}}{\partial \tilde{x}}=-\alpha_0\frac{\partial \tilde{T}}{\partial \tilde{x}}$$

(5)式之旋量方程式可寫爲

$$\frac{\partial \tilde{\zeta}}{\partial \tilde{t}}+\tilde{u}\frac{\partial \tilde{\xi}}{\partial \tilde{x}}+\tilde{v}\frac{\partial \tilde{\zeta}}{\partial \tilde{y}}=\alpha_0 g\frac{\partial \tilde{T}}{\partial \tilde{x}}+\nu\left(\frac{\partial^2 \tilde{\zeta}}{\partial \tilde{x}^2}+\frac{\partial^2 \zeta}{\partial \tilde{y}^2}\right) \tag{7}$$

爲使方程式無因次化，取平板長度L，均勻流速U，高度L距離的溫差ΔT分別爲特性長度、速度及溫度定義無因次參數如下：

$$u=\tilde{u}/U,\quad v=\tilde{v}/U,\quad t=\tilde{t}U/L,\quad \zeta=\tilde{\zeta}L/U$$
$$x=\tilde{x}/L,\quad y=\tilde{y}/L,\quad T=(\tilde{T}-T_0)/\Delta T,\quad \phi=\tilde{\phi}/(UL) \tag{8}$$
$$R_L=UL/\nu,\quad R_I=gL\Delta T/(U^2T_0),\quad P_r=\nu/k$$

則控制方程式經無因化後，可作簡爲：

$$\frac{\partial \zeta}{\partial t}+\frac{\partial \phi}{\partial y}\frac{\partial \zeta}{\partial x}-\frac{\partial \phi}{\partial x}\frac{\partial \zeta}{\partial y}=R_I\frac{\partial T}{\partial x}+\frac{1}{R_L}\left(\frac{\partial^2 \zeta}{\partial x^2}+\frac{\partial^2 \zeta}{\partial y^2}\right) \tag{9}$$

$$\frac{\partial^2 \phi}{\partial x^2}+\frac{\partial^2 \phi}{\partial y^2}=-\zeta \tag{10}$$

$$\frac{\partial T}{\partial t}+\frac{\partial \phi}{\partial y}\frac{\partial T}{\partial x}-\frac{\partial \phi}{\partial x}\frac{\partial T}{\partial y}=\frac{1}{P_r R_L}\left(\frac{\partial^2 T}{\partial x^2}+\frac{\partial^2 T}{\partial y^2}\right)+\Phi \tag{11}$$

流場速度　$u=\partial\phi/\partial y$及$v=-\partial\phi/\partial x$ (12)

上述之控制方程式經給予適當邊界條件後，可用來探討流場的流況及溫度變化。

參、數值解析

利用有限差分法以求解上述控制方程式組，數值之解析爲對時間變化項以前進差分，對空間之變則項採用中心差分如圖二所示，並運用變向隱式之雙向掃描法將偏微分方程式化爲差分方程式如下：

$$\frac{2}{\Delta t}\zeta_{i,j}^{n+1}+\frac{\left[k_j^2\phi_{i,j+1}^n-k_{j+1}^2\phi_{i,j-1}^n-\left(k_j^2-k_{j+1}^2\right)\phi_{i,j}^n\right]}{k_jk_{j+1}\left(k_j+k_{j+1}\right)}$$
$$\times\frac{\left[h_i^2\zeta_{i+1,j}^{n+1}-h_{i+1}^2\zeta_{i-1,j}^{n+1}-\left(h_i^2-h_{i+1}^2\right)\zeta_{i,j}^{n+1}\right]}{h_ih_{i+1}\left(h_i+h_{i+1}\right)}$$
$$-\frac{1}{R_L}\frac{h_i\zeta_{i+1,j}^{n+1}+h_{i+1}\zeta_{i-1,j}^{n+1}-\left(h_i+h_{i+1}\right)\zeta_{i,j}^{n+1}}{h_ih_{i+1}\left(h_i+h_{i+1}\right)/2}=$$

對y一向掃描：

$$\frac{2}{\Delta t}T_{i,j}^{n+1}-\frac{\left[h_i^2\phi_{i+1,j}^n-h_{i+1}^2\phi_{i-1,j}^n-\left(h_i^2-h_{i+1}^2\right)\phi_{i,j}^n\right]}{h_ih_{i+1}\left(h_i+h_{i+1}\right)}$$
$$\times\frac{\left[k_j^2T_{i,j+1}^{n+1}-k_{j+1}^2T_{i,j+1}^{n+1}-\left(k_j^2-k_{j+1}^2\right)T_{i,j}^{n+1}\right]}{k_jk_{j+1}\left(k_j+k_{j+1}\right)}$$
$$-\frac{2}{P_rR_L}\frac{\left[k_jT_{i,j+1}^{n+1}+k_{j+1}T_{i,j-1}^{n+1}-\left(k_j+k_{j+1}\right)T_{i,j}^{n+1}\right]}{k_jk_{j+1}\left(k_j+k_{j+1}\right)}$$

$$=-\frac{\left[\,k_j^2\psi^n_{i,j+1}-k_{j+1}^2\psi^n_{i,j-1}-(k_j^2-k_{j+1}^2)\psi^n_{i,j}\,\right]}{}$$

$$\times\frac{\left[\,h_i^2T^n_{i+1,j}-h_{i+1}^2T^n_{i-1,j}-(h_i^2-h_{i+1}^2)T^n_{i,j}\,\right]}{h_ih_{i+1}(h_i+h_{i+1})}$$

$$+\frac{\left[\,h_iT^n_{i+1,j}+h_{i+1}T^n_{i-1,j}-(h_i+h_{i+1})T^n_{i,j}\,\right]}{h_ih_{i+1}(h_i+h_{i+1})}\frac{2}{P_rR_L}+\frac{2}{\Delta t}T^n_{i,j}\qquad(13)$$

$$\frac{2}{\Delta t}\zeta^{n+1}_{i,j}-\frac{\left[\,h_i^2\psi^n_{i+1,j}-h_{i+1}^2\psi^n_{i-1,j}-(h_i^2-h_{i+1}^2)\psi^n_{i,j}\,\right]}{h_ih_{i+1}(h_i+h_{i+1})}$$

$$\times\frac{\left[\,k_j^2\zeta^{n+1}_{i,j+1}-k_{j+1}^2\zeta^{n+1}-(k_j^2-k_{j+1}^2)\zeta^{n+1}_{i,j}\,\right]}{k_jk_{j+1}(k_j+k_{j+1})}$$

$$-\frac{2}{R_L}\frac{k_j\zeta^{n+1}_{i,j+1}+k_{j+1}\zeta^{n+1}_{i,j-1}-(k_j+k_{j+1})\zeta^{n+1}_{i,j}}{k_jk_{j+1}(k_j+k_{j+1})}$$

$$=-\frac{\left[\,k_j^2\psi^n_{i,j+1}-k_{j+1}^2\psi^n_{i,j-1}-(k_j^2-k_{j+1}^{22})\psi^n_{i,j}\,\right]}{}$$

$$\times\frac{\left[\,h_i^2\zeta^n_{i+1,j}-h_{i+1}^2\zeta^n_{i-1,j}-(h_i^2-h_{i+1}^2)\zeta^n_{i+j}\,\right]}{h_ih_{i+1}(h_i+h_{i+1})}$$

$$+\frac{2}{R_L}\frac{h_i\zeta^n_{i+1,j}+h_{i+1}\zeta^n_{i-1,j}-(h_i+h_{i+1})\zeta^n_{i,j}}{h_ih_{i+1}(h_i+h_{i+1})}$$

$$+R_I\frac{h_i^2T^n_{i+1,j}-h_{i+1}^2T^n_{i-1,j}-(h_i^2-h_{i+1}^2)T^n_{i,j}}{h_ih_{i+1}(h_i+h_{i+1})}+\frac{2}{\Delta t}\zeta^n_{i,j}\qquad(14)$$

對 x 一向掃描：

$$\frac{2}{\Delta t}T^{n+1}_{i,j}+\frac{k_j^2\psi^n_{i,j+1}-k_{j+1}^2\psi^n_{i,j-1}-(k_i^2-k_{i+1}^2)\psi^n_{i,j}}{k_jk_{j+1}(k_j+k_{j+1})}$$

$$\times\frac{h_i^2T^{n+1}_{i+1,j}-h_{i+1}^2T^{n+1}_{i-1,j}-(h_i^2-h_{i+1}^2)T^{n+1}_{i,j}}{h_ih_{i+1}(h_i+h_{i+1})}$$

$$-\frac{2}{P_rR_L}\frac{\left[\,h_iT^{n+1}_{i+1,j}+h_{i+1}T^{n+1}_{i-1,j}-(h_i+h_{i+1})T^{n+1}_{i,j}\,\right]}{h_ih_{i+1}(h_i+h_{i+1})}$$

$$=\frac{\left[\,h_i\psi^n_{i+1,j}-h_{i+1}\psi^n_{i-1,j}-(h_i-h_{i+1})\psi^n_{i,j}\,\right]}{h_ih_{i+1}(h_i+h_{i+1})}$$

$$\times\frac{\left[\,k_i^2T^n_{i,j+1}-k_{j+1}^2T^n_{i,j-1}-(k_j^2-k_{j+1}^2)T^n_{i,j}\,\right]}{k_jk_{j+1}(k_j+k_{j+1})}$$

$$+\frac{2}{P_rR_L}\frac{\left[\,k_jT^n_{i,j+1}+k_{j+1}T^n_{i,j-1}-(k_j+k_{j+1})T^n_{i,j}\,\right]}{k_jk_{j+1}(k_j+k_{j+1})}+\frac{2}{\Delta t}T^n_{i,j}\qquad(15)$$

$$\frac{2}{\Delta t}\zeta^{n+1}_{i,j}+\frac{\left[\,k_j^2\psi^n_{i,j+1}-k_{j+1}^2\psi^n_{i,j-1}-(k_j^2-k_{j+1}^2)\psi^n_{i,j}\,\right]}{k_jk_{j+1}(k_j+k_{j+1})}$$

$$\times\frac{\left[\,h_i^2\zeta^{n+1}_{i+1,j}-h_{i+1}^2\zeta^{n+1}_{i+1,j}-(h_i^2-h_{i+1}^2)\zeta^{n+1}_{i,j}\,\right]}{h_ih_{i+1}(h_i+h_{i+1})}$$

$$-\frac{2}{R_L}\frac{\left[\,h_i\zeta^{n+1}_{i+1,j}+h_{i+1}\zeta^{n+1}_{i-1,j}-(h_i+h_{i+1})\zeta^{n+1}_{i,j}\,\right]}{h_ih_{i+1}(h_i+h_{i+1})}$$

$$=\frac{\left[\,h_i^2\psi^n_{i+1,j}-h_{i+1}^2\psi^n_{i-1,j}-(h_i^2-h_{i+1}^2)\psi^n_{i,j}\,\right]}{h_ih_{i+1}(h_i+h_{i+1})}$$

$$\times\frac{\left[\,k_j^2\zeta^n_{i,j+1}-k_{j+1}^2\zeta^n_{i,j-1}-(k_j^2-k_{j+1}^2)\zeta^n_{i,j}\,\right]}{k_jk_{j+1}(k_j+k_{j+1})}$$

$$+\frac{2}{R_L}\frac{k_j\zeta^n_{i,j+1}+k_{j+1}\zeta^n_{i,j-1}-(k_j+k_{j+1})\zeta^n_{i,j}}{k_jk_{j+1}(k_j+k_{j+1})}$$

$$+R_I\frac{h_i^2T^n_{i+1,j}-h_{i+1}^2T^n_{i-1,j}-(h_i^2-h_{i+1}^2)T^n_{i,j}}{h_ih_{i+1}(h_i+h_{i+1})}+\frac{2}{\Delta t}\zeta^n_{i,j}\qquad(16)$$

方程式(10)以 SOR 連續疊代法求解之如下：

$$\psi^{K+1}_{i,j}=\psi^K_{i,j}+\frac{\omega}{(1+\frac{k_{j+1}}{k_j})(1+\frac{k_jk_{j+1}}{h_ih_{i+1}})}\left[\,\psi^K_{i,j+1}+\frac{k_{j+1}}{k_j}\psi^{K+1}_{i,j-1}+\right.$$

$$+\frac{k_{j+1}(k_j+k_{j+1})}{h_{i+1}(h_i+h_{i+1})}\psi^K_{i+1,j}+\frac{k_{j+1}(k_j+k_{j+1})}{h_i(h_i+h_{i+1})}\psi^K_{i-1,j}$$

$$\left.+\frac{1}{2}k_{j+1}(k_j+k_{j+1})\zeta_{i,j}-(1+\frac{k_{j+1}}{k_j})(1+\frac{k_jk_{j+1}}{h_ih_{i+1}})\psi^K_{i,j}\right]\qquad(17)$$

流場中之速度由下式求得：

$$u^{n+1}_{i,j}=\frac{k_j^2\psi^{n+1}_{i,j+1}-k_{j+1}^2\psi^{n+1}_{i,j-1}-(k_i^2-k_{i+1}^2)\psi^{n+1}_{i,j}}{k_jk_{j+1}(k_j+k_{j+1})}$$

$$v^{n+1}_{i,j}=-\frac{h_i^2\psi^{n+1}_{i+1,j}-h_{i+1}^2\psi^{n+1}_{i-1,j}-(h_i^2-h_{i+1}^2)\psi^{n+1}_{i,j}}{h_ih_{i+1}(h_i+h_{i+1})}\qquad(18)$$

上列式中，n 爲時間之增量，i 表 x 一向之格點，j 表 y 一向之格點，其增量 $h_i=x_i-x_{i-1}$，$k_j=y_j-y_{i-1}$ 爲不等距之增量。ω 爲收斂參數，本文取值爲 1.8，第 k＋1 次及第 k 次疊代之收斂臨界標準爲：

$$|\psi^{k+1}_{i,j}-\psi^k_{i,j}|/|\psi^k_{i,j}|\le 10^{-4}\qquad(19)$$

由於旋量方程式及流場溫度擴散方程式爲拋物線型方程式，利用變向隱式法以雙向掃描，將其有限差分化分別得(13)、(14)、(15)及(16)式。流函數—旋量關係式爲 Poisson型方程式，採用 SOR 方法由疊代程序求解流函數。流場中之速度則由(18)式之有限左分方程式解出。

肆、邊界條件及數值運算程序

流場之邊界條件，如圖三所示，就其探討之流場分別列述如下：

㈠流場A：流函數之起始條件由勢能流決定，旋量除在平板AB表面外，各處皆爲零。流場之邊界條件，在離平板AB遠處四周圍多不受平板AB干擾之流場爲均勻流，其旋量爲零，流函數則爲勢能流。在平板AB上之旋量ζ_b，可由其鄰近點之流函數，經泰勒級數對平板面展開化簡得之，即

$$\zeta_{i,0} = -\frac{2\left[(k_1+k_2)^3\phi_{i,1} - k_1^3\phi_{i,2}\right]}{k_1^2(k_1+k_2)^2k_2} \qquad (20)$$

㈡流場B：如圖所示，流體的溫度在平板上下各爲均勻的溫度分佈，流場中溫度的浮昇效應始於平板尾端之下游區，因而所探討之流場以板尾之斷面爲上游邊界，有關在此邊界之流函數及旋量等值皆由流場A之運算求得，下游邊界之邊界條件則以浮動特性，即$\partial/\partial x = 0$，表之。

起始條件及邊界條件決定後，控制方程式之求解由下列步驟經數值差分化之方程式寫成電腦程式後，利用高速電腦之運算解出。

(1)由流函數之拉普拉方程式解出勢能流流場。

(2)利用起始條件及邊界條件，由溫度擴散差分方程式(13)與(15)分別對y及x一向雙向掃描之運算以得出新時段之T^{n+1}值。

(3)由(20)式求得在平板表面上旋量，ζ值。

(4)解旋量差分方程式(14)與(16)分別對y及x一向雙向掃描之運算，加入邊界條件求得新時段之旋量，ζ^{n+1}。

(5)由求得之旋量ζ^{n+1}代入流函數—旋量關係式差分方程式(17)，利用SOR法循序收斂以求出該新時段的流函數，收斂之是否完成，則由滿足(20)式之判斷爲依據。

(6)新時段之速度則利用(18)式求得。

(7)重複步驟(2)至(6)以求解各個時段中流場的變數值。

流場中格點之分割，從板首到板尾的適當距離屬於流況變化較大之區域。本文之計算，從板首往下游6倍長的區域內，x方向之水平格點，$\Delta x_1 = L/20$，其餘區域，$\Delta x_2 = 1.5\Delta x_1$。垂直方向，由於界面層厚度遠小於平板長度，而界面層外之流場趨近於勢能流。因而在界面層內要有適當的格點才能描述流況的變化，本文在y一向的格點以下式形式表示之，

$$\Delta y_j = \frac{L}{150}\exp(0.15.N_j)$$

時間增量Δt的變化如下：

$$\Delta t = \begin{cases} 0.005 & \text{當 } t = 0 \\ 2x\Delta t_f & 0 < t < 0.2 \\ 0.2 & t > 0.2 \end{cases}$$

式中Δt_f爲前一時段所用之Δt，時間的增量Δt，曾取0.01,0.02,0.05,0.1及0.2比較之，當$t > 0.2$以後取$\Delta t = 0.2$，其誤差尚可容忍。

伍、結果與討論

爲印證本文數值模式之準確性，先用探討均勻流通過一有限長度板之尾端跡流的流場計算，所得結果與Goldstein解析解比較，如圖四所示。跡流中心軸速度的比較結果相當吻合。圖五爲均質流場通過有限長度平板之速度及流域分佈情形。

5.1 穩定溫度層變流體通過平板(流場A)

當流場爲一線性穩定層變時，流場受到干擾，則流線首先因旋量的影響，在垂直方向改變位置，此時水平方向之密度已不爲常數，而有$\partial\rho/\partial x$變化影響產生旋量的變化。圖六爲$R_L = 1000$，$R_I = 68$時的流場，圖中可看出流線的最高峯在$x = 0.8$，而通過薄板後在$x = 1.8$處流線有一近似射流的形式，和圖五的流場比較，在平板上游端其流線微高於均質流場，而在板尾附近則較均質流場爲低。當雷查遜數，$R_I = 136$時，如圖七所示，平板上游的波已可明顯的看出，波的最高峯約位於$x = 1.7$和$R_I = 68$的流場比較，波的高峯較大，在$x = 1.2$時，$R_I = 136$的流場其流域低於$R_I = 68$流場，因而此處有較大的流速。圖八爲$R_I = 200$的流場，其波峯約在$x = 0.4$，其高度遠大於其它三種流場，而在$x = 1.1$處流域下降有造成射流形狀的傾向，在板首附近由於波面形成的影響有產生另一個內界面層流(internal boundary layer)的傾向。由界面層理論，在均質流場的界面層厚度其形成由板首沿流向往下游處增加，而溫度層變流場，由於受層變的影響有不同的情形。如圖九所示，在位置的雷諾數，R_x大於500以後界面層厚度隨層變的增大而減小。R_x小於400以前層變流場的界面層厚度都要大於均質流場。

板尾跡流區速度的變化，由於在板尾端受不滑動條件的限制，速度爲零，而後逐漸增大，經適當距離後，回復至自由流速。層變流場中因受溫度層變的影響，在板尾跡流之流速要比均質流場爲大，由上述圖五至圖八的結果可看出跡流的長度也顯著的變小，也就是在較短的距離內，跡流的速度就回復至自由流速，這個結果也可由圖十中跡流的旋量變化看出。

5.2 平板上下爲兩種不同溫度的均質流場(流場B)

爲考慮浮力在跡流中對流場變化的影響，本文探討兩種不同的溫度變化情形：其一爲穩定狀況，即平板上方之均勻溫度大於下方之均勻溫度；其二爲不穩定狀況，即上方的均勻溫度小於下方之均勻溫度而有浮力的效應。在前述的研究結果可得知穩定的溫度層變對於通過平板尾端的跡流發展有穩定及壓抑的效應，也就是跡流的混合層(mixing layer)受到層變的影響使混合層的寬度及距離都變小，這個現象在這一種的穩定

狀況（上方溫度高，下方溫度低）研討中亦得出相同的結果，亦即流體的穩定層變對於尾端跡流的發展有壓抑的作用。

在第二種的不穩定溫度分佈則有不同的情形發生，當上下流場有一微小的不穩定溫度差，此時因受浮力的作用而在平板後的流場因密度的差異而產生旋量，因而使流線回復均勻流的高度，其距離要比均勻流場爲遠，如圖十一之系列結果所示。當溫度差加大時，在板尾附近會有一類似分離區出現，加大溫度差之分佈，則分離區的長度及範圍增加，中心線近板尾附近形成一極端不穩定的區域。

板尾附近的流線除了受平板上剪力效應而生的旋量影響外，尚有因密度差異的浮力作用而產生的干擾，由流線的分佈可知，在板尾中心線附近溫度差異之流場，其流線間距要比均質流場大，故速較慢，且當溫度差大於某一值後，中心線的速度有反向的現象發生。圖十二爲$R_L = 10^3$之流在不同溫度差異分佈時，其中心速度分佈的情形。在板尾適當距離內（$x/L < 1.8$），中心軸的速度隨著溫度差異的增大而減小，同時和均質流場中心線速度相合的位置亦因溫度差異的增大而增長。當溫度差大於1.5°C時，板尾附近的速度呈現反向的分佈。圖十三爲在各種溫度差異流場，板尾後的斷面速度剖面之比較。圖十四爲溫差1.5°C時，板尾後各斷面的速度分佈。旋量是造成流線改變的主要因素之一，均質流場中，板尾後端因無障礙物影響，所以旋量逐漸減小，到適當距離後爲零，成爲均勻流，而當溫度差異時，因密度的差異，流場內會有旋量發生，而使流場中旋量的分佈異於均質流場，圖十五爲不同的溫度差異在板尾的旋量分佈情形。板尾各斷面的旋量由於溫度差異產生的旋量逐漸加大，而後又逐漸減小回復到自由流速的勢能流。

陸、結　論

本文利用數值方法探討流場中密度層變對於通過有限長度平板的流場變化以及對板尾跡流的影響，經數值模擬之計算，獲致下列之結果：

(1)在線性穩定層變流體通過薄板之流場，由於層變的影響，在平板上游區有引生重力波的趨勢。

(2)平板上界面層的形成受層變的影響，由上游往下游減少，與均質流場中隨距離的增加而增大有所不同。

(3)穩定的層變效應對平板尾端之跡流發展有壓抑的作用。

(4)不穩定的溫度分佈，其浮力作用則有增大其跡流形成之效應，同時引生渦旋分離之現象。

參考文獻

1. Hwang, R.R. 1982: Viscous flows of stably stratified fluide over semi-circular obstacles, Proc. of the NSC, Vol. 6, No. 1, pp. 1-8.
2. Hwang, R.R. & S.W. Jang, 1982: Laboratory on the two-dimensional flows of stratified fluids over barriers, J. of the Chinese Institute of Engineers, Vol. 5, No. 3, pp. 167-177.
3. Kelly, R.E. & L.G. Redekopp, 1970: The development of horizental boundary layers in stratified flow, J. Fluin Mech., 42, pp. 497-511.
4. Long, R.R. 1959: The motion of fluid with density stratification, J. Geophys. Res., 64, pp. 2151-2161.
5. Long, R.R. 1962: Velocity distributions in stratified fluids, J. Hydraulic Divison, ASCE, pp. 9-26.
6. Martine, S. & R.R. Long, 1968: The slow motion of a flat plate in a viscous stratified fluid, J. Fluid Mech., 31, pp. 669-688.
7. Pao, Y.H. 1968: Laminar flow of a stably stratified fluid past a flat plate, J. Fluid Mech., 34, pp. 795-808.
8. Peyret, R. & T.D. Taylor, 1983: Computational Methods for Fluid Flow, Springer-Verlag.
9. Turner, J.S. 1973: Buoyancy Effect in Fluids, Cambridge.

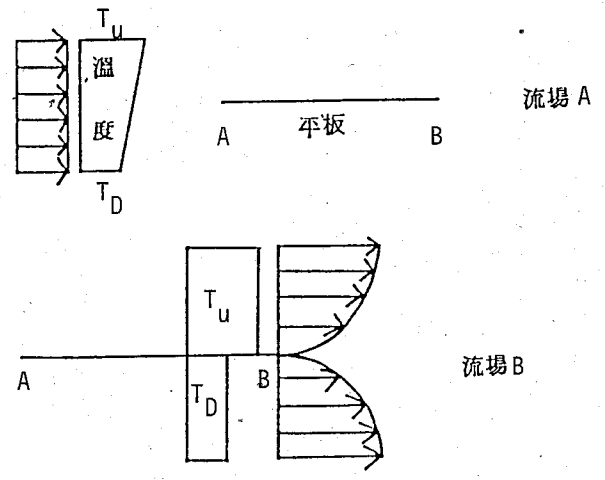

圖一　兩種流場問題

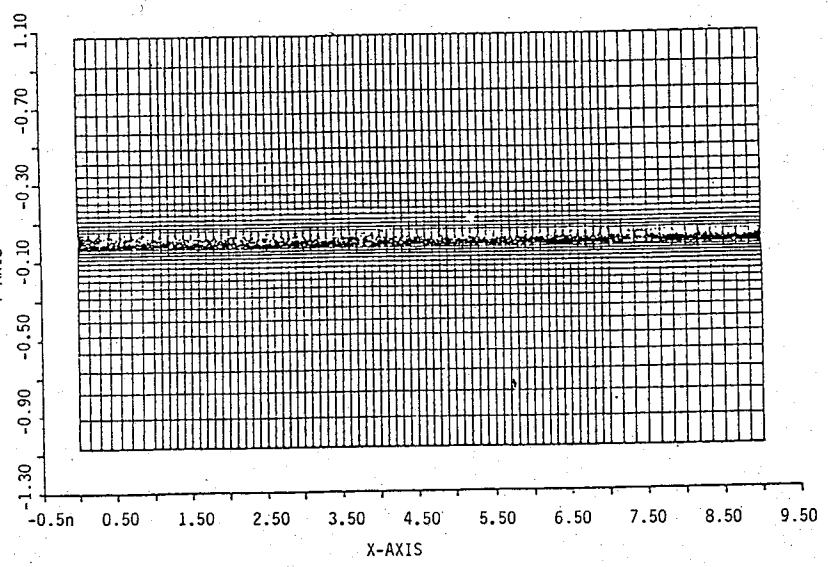

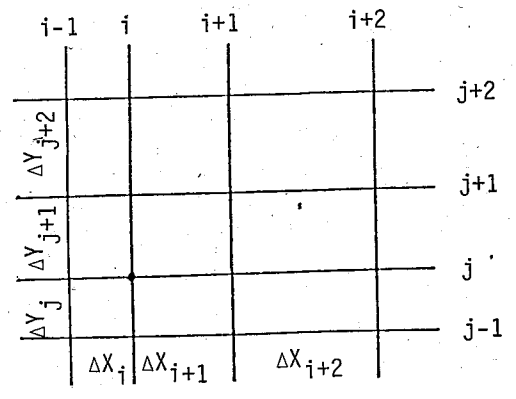

圖二　流場網格點分佈

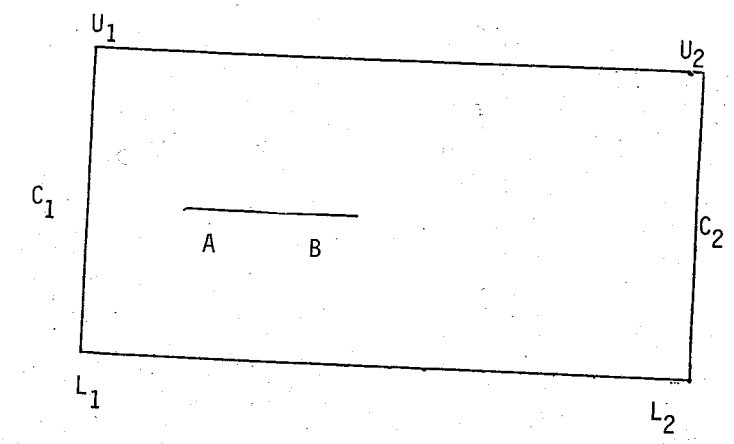

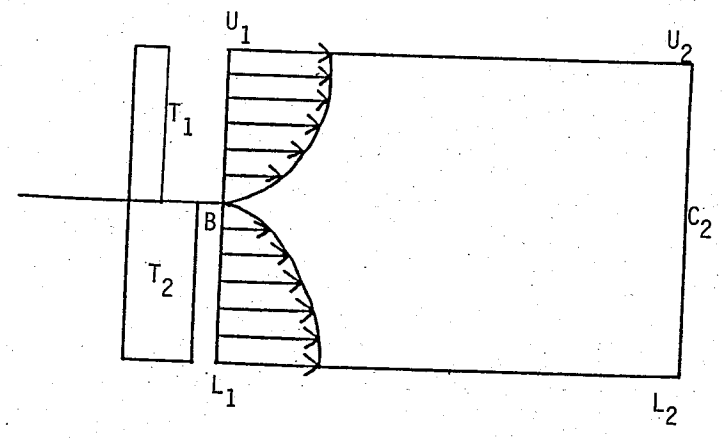

圖三　流場邊界

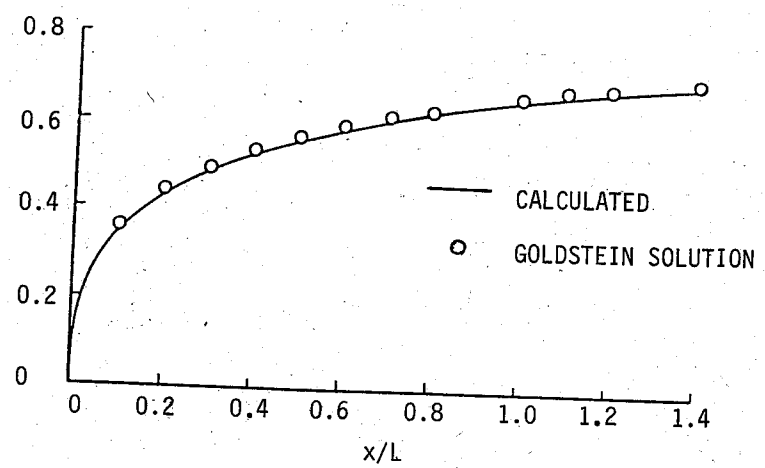

圖四　均質流場尾端計算之速度分佈與解析解比較

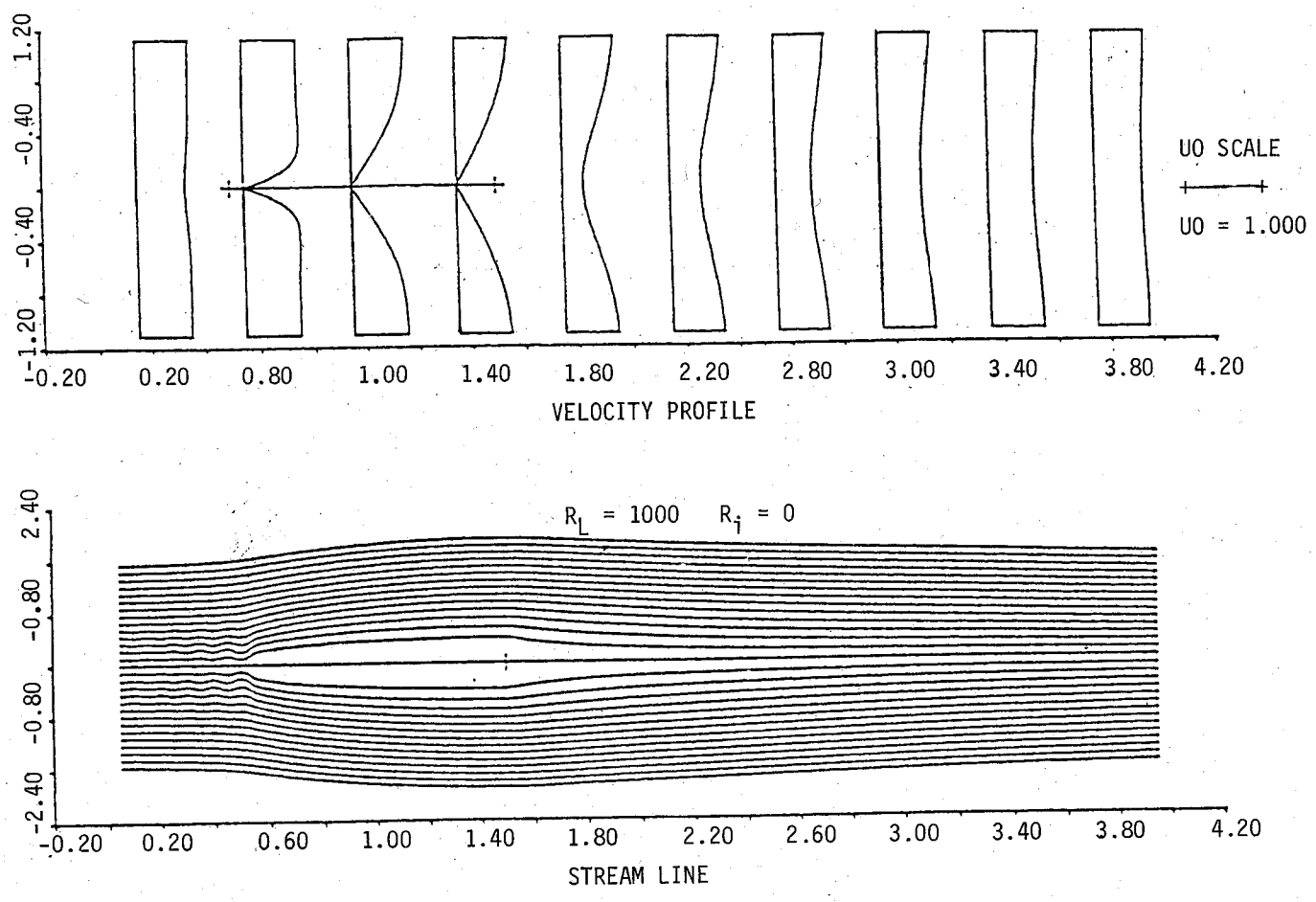

圖五　$R_L = 10^3$，均質流場速度及流綫分佈

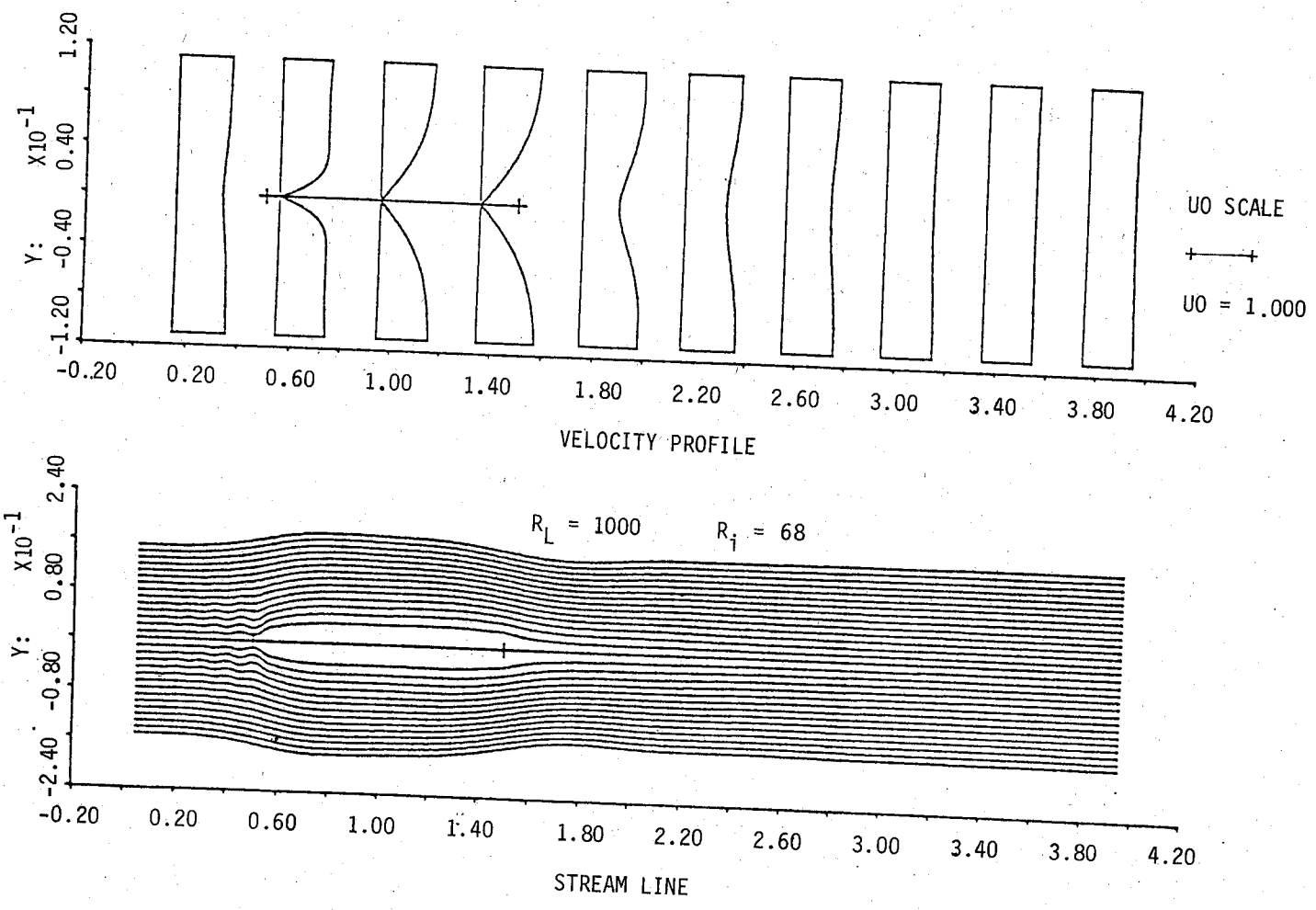

圖六　$R_L = 10^3$，$R_I = 68$，層變流場速度及流綫分佈

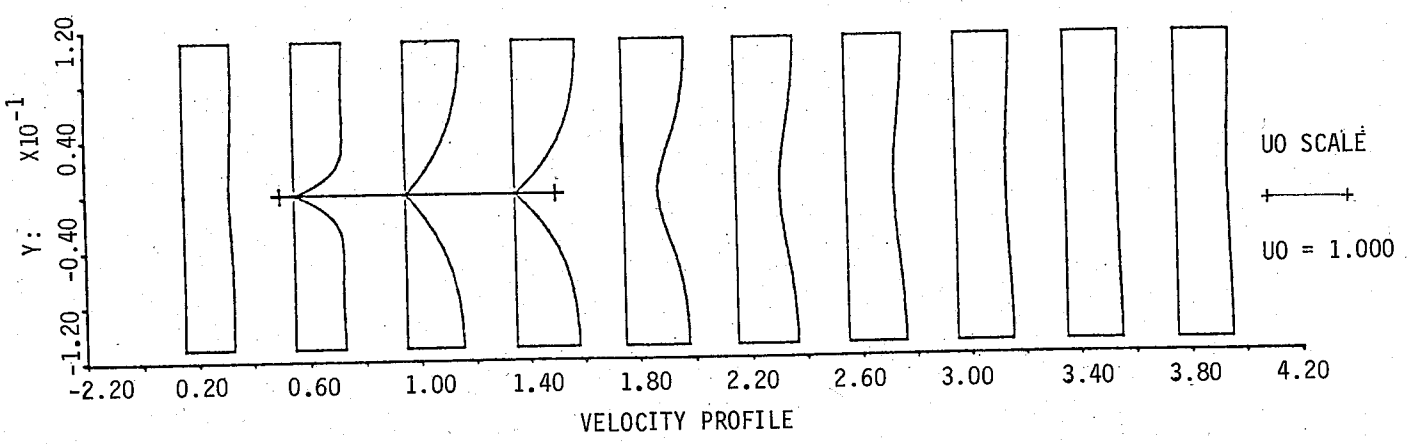

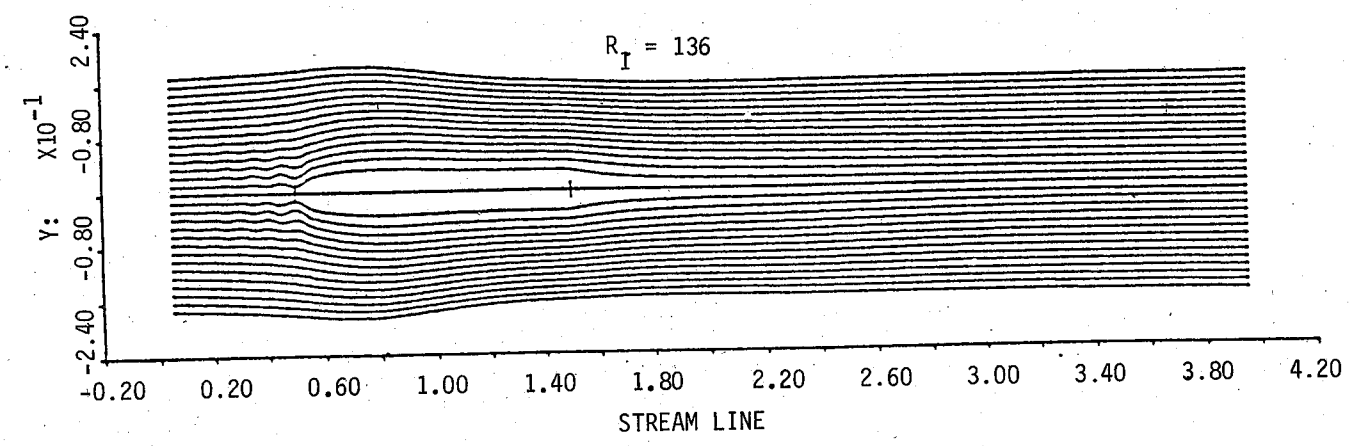

圖七　$R_L = 10^3$ ，$R_I = 136$ ，層變流場速度及流綫分佈

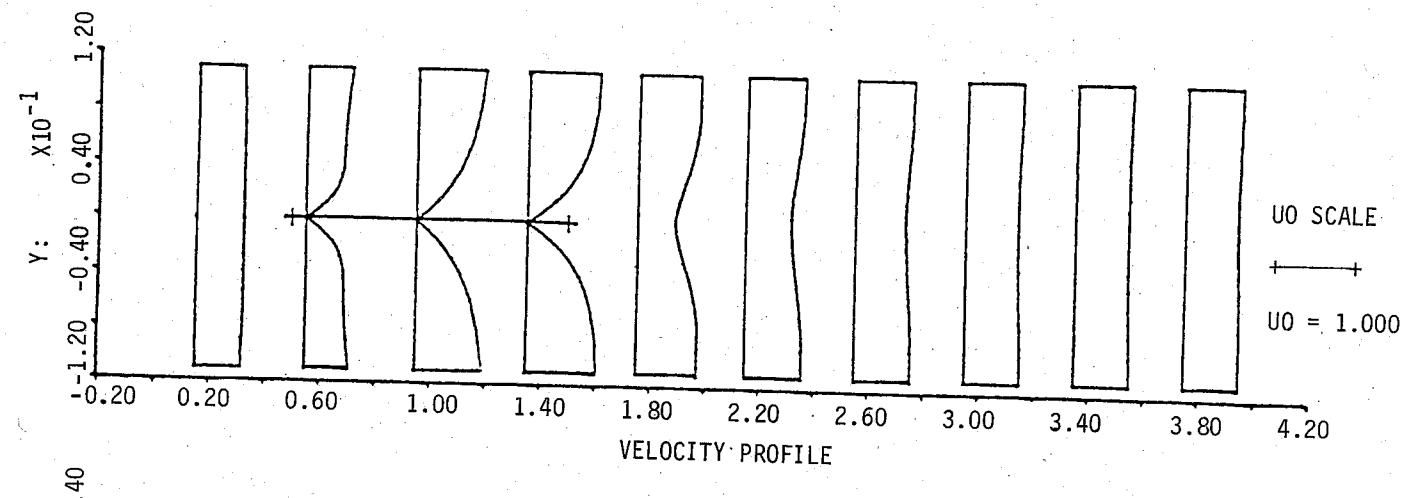

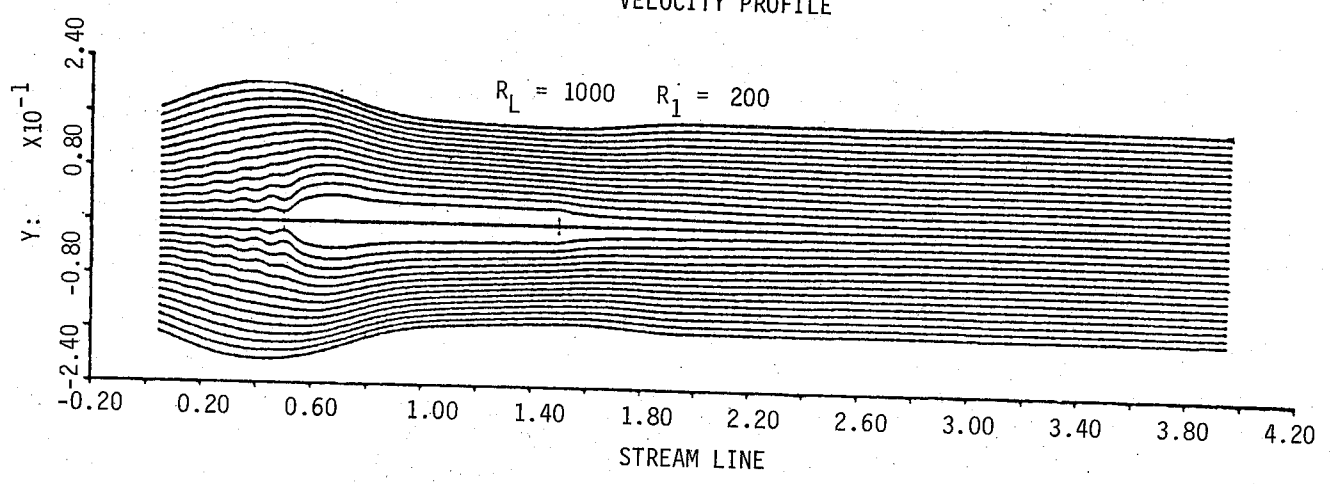

圖八　$R_L = 10^3$ ，$R_I = 200$ ，層變流場速度及流綫分佈

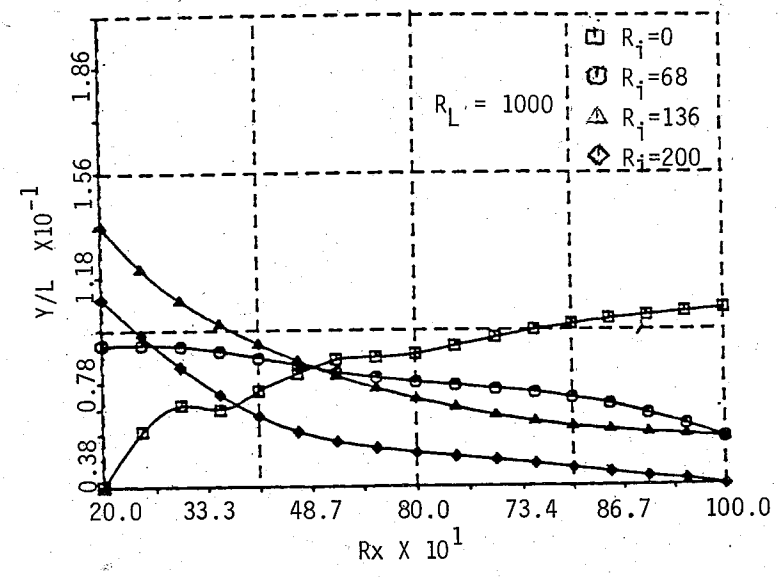

圖九、層變差異平板上界面層原度之變化

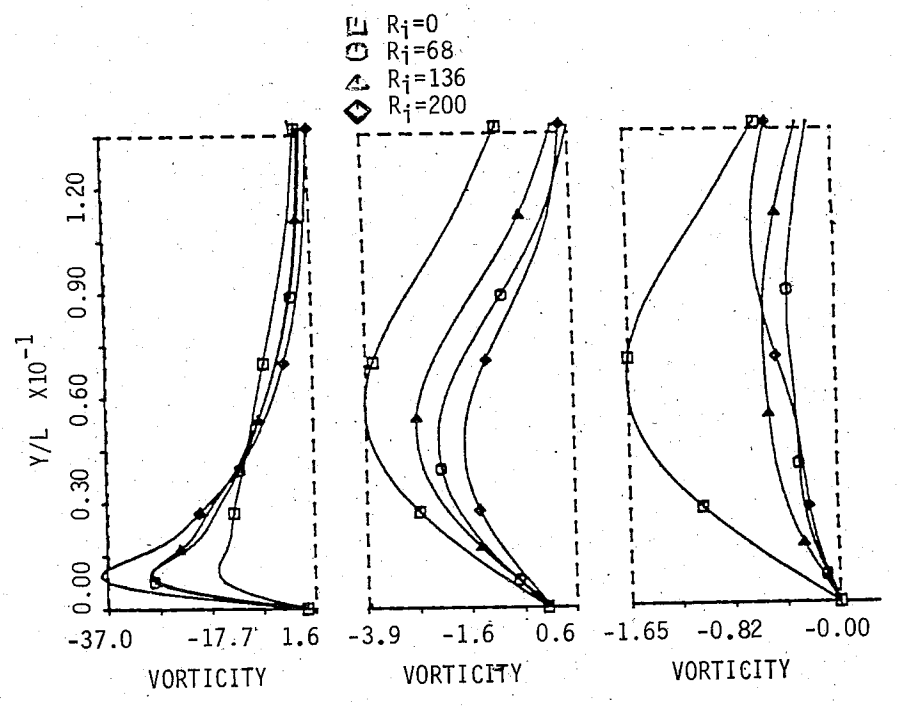

圖十、$R_L = 10^3$，板尾後端斷面旋量分佈

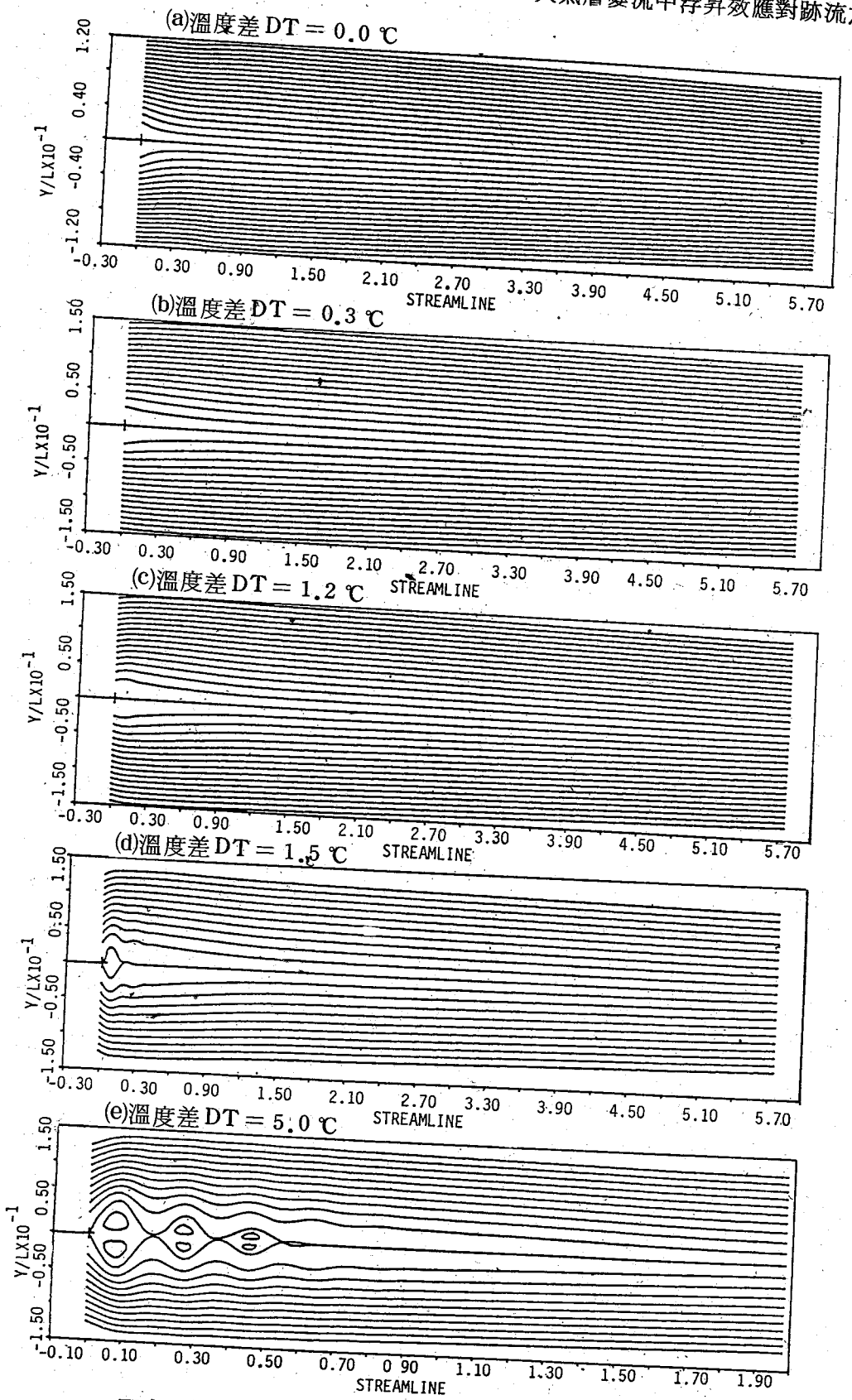

圖十一　流場雷諾數$R_L = 1000$，板尾後流線分佈

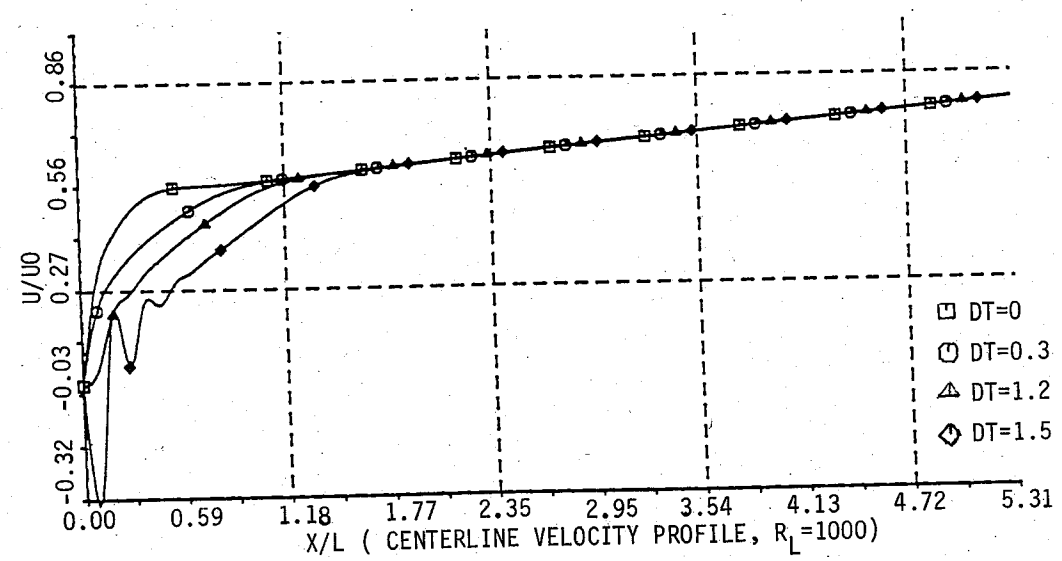

圖十二　板尾後中心線速度分佈比較

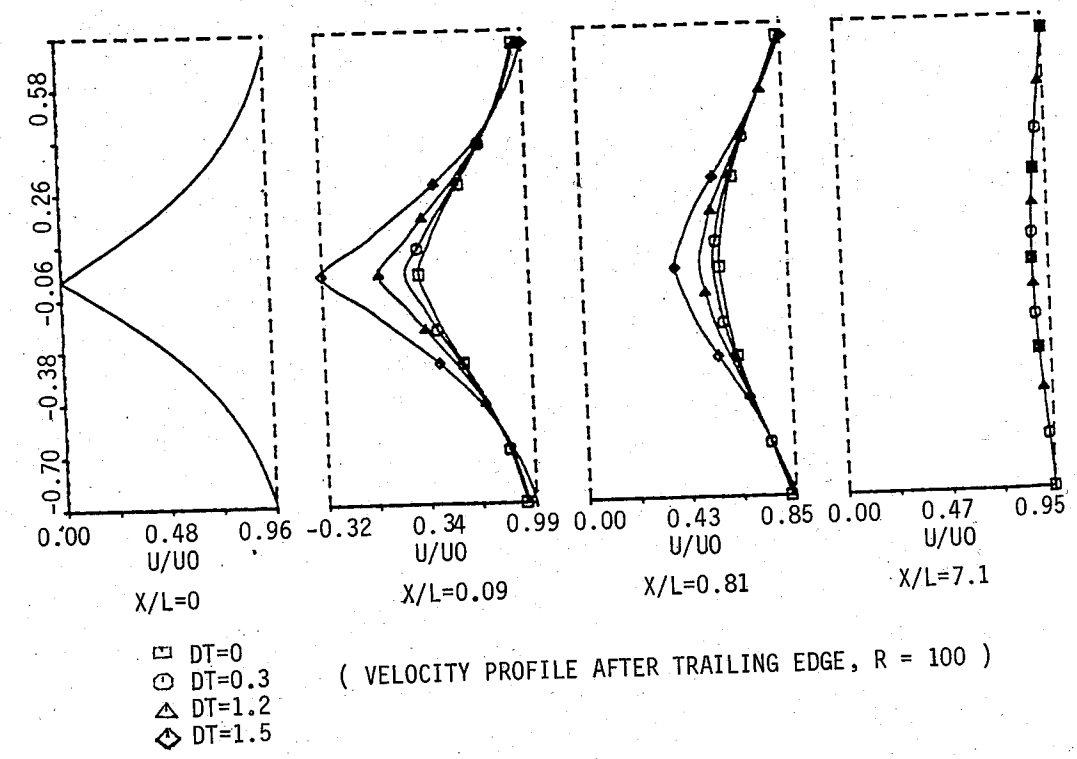

圖十三　板尾後各斷面速度分佈比較

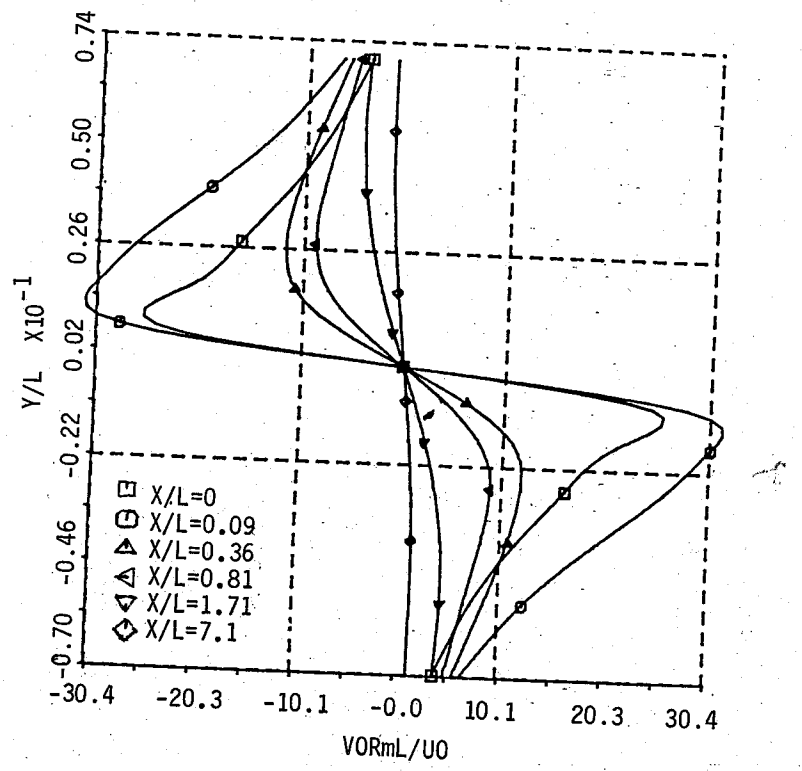

圖十四　溫度差 1.5 ℃，$R_L = 10^3$ 板尾後各斷面旋量分佈

Annual Report of the Institute of Physics, Academia Sinica, Vol. 14, 1984

BYOYANCY EFFECT ON THE DEVELOPMENT OF WAKE FLOW OF ATMOSPHERIC STRATIFIED FLUIDS

Robert R. Hwang and Y. S. Chen
Institute of Physics, Academia Sinica
Nankang, Taipei, R.O.C.

ABSTRACT

The thermal effect on wake flow is an important problem in heat trasnfer research. In this study, a numerical algorithm of integrating the equations of continuity, momentum and energy incorporately is applied to analyze the buoyancy effect on the development of wake flow behind a flat plate. Traditional wake-flow studies, the plate or an object is either heated or cooled and the wake developmetn is affected not only by the buoyancy effects which occur in the wake region, but also by the buoyancy effects produced in the upstream boundary layer flows. Both of these byoyancy effects are complex and from a fundamental point of view, it is desirable that these two effects be studied seperately so that better physical insight can be gained for an overall understanding of the wake development process under the influence of buoyancy. Results of the study will isolate the important physical mechanism of buoyancy effects on wake development without upstream contaminations.

平板尾端紊流跡流之數值研究

黃　榮　鑑
中央研究院物理研究所
蕭　葆　義
中央研究院物理研究所

摘　要

本文主要是研究平板尾端紊流跡流之物理現象。採用邊界層理論（boundary layer theory）近似後之連續及動量方程式（continuity & momentum equations）配合雙尺度K - ε紊流模式（two scale K - ε turbulente model），共同聯立求解，並與實驗數據比較，以證實雙尺度K - ε紊流模式及瞭解紊流跡流之流場變化。

研究的方法係利用有限差分做數值解，運用變換方向顯示及隱式法（ADE & ADI）求解，即動量方程式、K方程式、ε方程式之x方向採用顯示法而y方向採用隱式法解方程式。

數值研究結果與Chevray & Kovasznay之實驗數據比較驗證，結果良好，證實雙尺度K - ε紊流模式應用於平面跡流之可靠性。同時數值計算結果顯示隨著遠離平板尾端紊流跡流之中心軸向平均流速遞增；而紊流動能k（tubulent kinetic energy）、紊流消能ε（turbulent energy dissipation）則遞減；而跡流寬度則遞增。另外跡流之紊流剪應力（Reynolds stress）分佈最大值隨遠離平板尾端而減小且愈偏離跡流中心軸；k，ε之分佈也有相同之趨勢。

壹、前　言

跡流（wake flow）發生在許多實際的物理及工程問題上，常見的例如飛機、潛水艇、透平機旋葉等尾區跡流，大氣層中氣流越過各種地形障礙物尾區跡流，通過平板、圓柱體尾區跡流等等。在這些物理上的或工程上的跡流問題中，以紊流（turbulent flow）發生的情況較層流（laminar flow）爲普遍。雖然紊流較層流流況複雜且難解，但紊流卻較接近眞實流況。

本文就通過平板尾區紊流跡流問題進行研究，控制方程式利用邊界層理論（boundary layer theory）近似後之連續及動量方程式（continuity & momentum equations），動量方程式中之紊流應力項則採用雙尺度K - ε模式（two scale K-ε model）

閉合，運用數值方法求解紊流跡流流場變化，分析探討紊流跡流特性，再與實驗資料比較，以驗證雙尺度 K－ε 紊流模式模擬紊流跡流之可靠性，並提供進一步研究紊流模式之參考。

關於紊流跡流之研究文獻，數學模式均側重於紊流應力之決定。早期有簡單之紊流一階閉合（ first order closure ），皆是經驗式，不同的問題有不同的模式，例如 Prandtl mixing length model 〔1〕，Karman mixing length model 〔2〕，此等紊流模式只適用於非常簡單的流況，且爲後測（ postdiction ）而非預測（ prediction ）。近年來之研究則趨於二階閉合（ second order closure ），由紊流傳輸方程式（ turbulent transport equation ）出發，藉著各種假設達到簡化傳輸方程式形成各類紊流模式，例如K方程式〔 3 〕，K－ε 模式〔 4 〕等等。

通過平板尾區跡流屬於自由剪力流（ free shear flow ）。Prandtl 〔 5 〕曾提出在跡流中之渦粘性係數 ν_t 爲常數；接著Kolmogorov 〔 6 〕又提出 ν_t 爲紊流動能（ turbulent kinetic energy) K之函數，K由K方程式求得。然而由實驗及自然物理現象知悉 ν_t 非單純一常數或只是K之函數，故繼而有K－ε 模式〔 4 〕之出現。K－ε 紊流模式預測平面射流，混合層（ mixing layer ）結果良好〔 7 〕，但預測平面跡流則不理想，故本研究針對K－ε 模式中之 ε 方程式加以改進〔 8 〕，即 ε 方程式參數化時除考慮大渦流尺度外，加入小渦流尺度（ small eddy scale ），稱爲雙尺度K－ε 紊流模式，用來模擬預測通過平板尾區跡流之流場變化狀況，並分析探討紊流跡流。

貳、控制方程式

考慮二維不可壓縮流體（ two dimensional incompressible fluid) 通過光滑平板（ smooth flat plate ），在平板尾端跡流區中，沿主流（ main flow ）方向壓力均勻分佈，即零壓力梯度（ zero pressure gradient ）；紊流應力（ Reynolds' stress ）甚大於粘滯力（ viscous force ），即略去粘滯力；採邊界層理論近似；故連續方程式及動量方程式分別簡化如下：

連續方程式（ continuity equation ）

$$\frac{\partial U}{\partial x}+\frac{\partial V}{\partial y}=0$$

動量方程式（ momentum equation ）

$$U\frac{\partial U}{\partial x}+V\frac{\partial U}{\partial y}=-\frac{\partial}{\partial y}(\overline{uv})$$

式中 U：x 方向（主流方向）之平均流速

V：y 方向（垂直主流方向）之平均流速

$-\overline{uv}$：紊流應力（ Reynolds' stress ）

上述控制方程式有二個，未知數有三個，即 U，V，$-\overline{uv}$；是故 $-\overline{uv}$ 項必須閉合

方能求解。

叁、紊流模式

爲閉合 $-\overline{uv}$ 項，引入 Boussinesq 渦粘性概念（ eddy-viscosity concept ），即 $-\overline{uv}$ 爲平均主流速度梯度與渦粘性係數之乘積：

$$-\overline{uv}=\nu_t\frac{\partial U}{\partial y} \tag{3}$$

式中 ν_t 爲渦粘性係數或稱紊流粘性係數（ turbulent viscosity coefficient）。ν_t 不是流體之性質（ property of the fluid ），而隨所在點位置之紊流結構（ structure of turbulence ）而變化，亦即 ν_t 爲紊流動能（ turbulent kinetic energy) K，紊流消能（ dissipation ）ε 之函數，由因次分析 ν_t 表示如下：

$$\nu_t=C_\mu\frac{K^2}{\varepsilon} \tag{4}$$

式中 K：紊流動能

ε：紊流消能

C_μ：無因次係數，由實驗決定

紊流動能及紊流消能分別由紊流動能方程式、紊流消能方程式決定。此二方程式可由紊流傳輸方程式（ turbulent transport equation ）模式化求得。

紊流傳輸方程式之一般式爲：

$$\frac{D\overline{u_iu_j}}{Dt}=\frac{\partial}{\partial x_l}\left[-\overline{u_iu_ju_l}-\overline{\frac{P}{\rho}(\delta_{jl}u_i+\delta_{il}u_j)}+\nu\frac{\partial\overline{u_iu_j}}{\partial x_l}\right]-\left(\overline{u_iu_l}\frac{\partial U_j}{\partial x_l}+\overline{u_ju_l}\frac{\partial U_i}{\partial x_l}\right)-2\nu\overline{\frac{\partial u_i}{\partial x_l}\frac{\partial u_j}{\partial x_l}}+\overline{\frac{P}{\rho}\left(\frac{\partial u_i}{\partial x_j}+\frac{\partial u_j}{\partial x_i}\right)} \tag{5}$$

傳輸方程式等號右側之擴散項（ diffusion term ）、生成項（ production term ）、消能項（ dissipation term ）、壓力應變項（ pressure strain term) 經模式化如下：

$$\frac{D\overline{u_iu_j}}{Dt}=\frac{\partial}{\partial x_l}\left[C_K\left[\frac{\ell_2}{t}\right]\frac{\partial\overline{u_iu_j}}{\partial x_l}+\nu\frac{\partial\overline{u_iu_j}}{\partial x_l}\right]-\left(\overline{u_iu_l}\frac{\partial U_j}{\partial x_l}+\overline{u_ju_l}\frac{\partial U_i}{\partial x_l}\right)-\frac{2}{3}\delta_{ij}\varepsilon+\frac{1}{4\pi}\int_{vol}\left[\overline{\frac{\partial^2u_lu_m}{\partial x_l\partial x_m}}+2\overline{\frac{\partial U_l\partial u_m}{\partial x_m\partial x_l}\left(\frac{\partial u_i}{\partial x_j}+\frac{\partial u_j}{\partial x_i}\right)}\right]\frac{dVol}{d\vec{r}^2} \tag{6}$$

式中 ℓ：長度尺度

t：時間尺度

ϵ：紊流消能 $\quad \epsilon = \nu \overline{\frac{\partial u_i}{\partial x_l} \frac{\partial u_j}{\partial x_l}}$

Vol：體積

令 i = j，$K = \overline{u_i u_j} / 2$，取 $\ell = K^{\frac{3}{2}} / \epsilon$，$t = K / \epsilon$

則上式壓力應變項因 $\partial u_j / \partial x_i = 0$ 而爲零，故簡化爲K方程式如下：

$$\frac{DK}{Dt} = \frac{\partial}{\partial x_l}\left[C_\kappa \frac{K^2}{\epsilon} \frac{\partial K}{\partial x_l} + \nu \frac{\partial K}{\partial x_l} \right] - \overline{u_i u_j} \frac{\partial U_i}{\partial x_l} - \epsilon \tag{7}(7)$$

ϵ 方程式之一般式爲

$$\frac{D\epsilon}{Dt} = \frac{\partial}{\partial x_l}\left[-\overline{\epsilon u_l} - \frac{2\nu}{\rho} \overline{\frac{\partial u_l}{\partial x_j} \frac{\partial P}{\partial x_j}} + \nu \frac{\partial \epsilon}{\partial x_l} \right] - 2\nu \frac{\partial U_i}{\partial x_j} \left(\overline{\frac{\partial u_l}{\partial x_i} \frac{\partial u_i}{\partial x_j}} + \overline{\frac{\partial u_i}{\partial x_l} \frac{\partial u_j}{\partial x_l}} \right) - 2\nu u_l \overline{\frac{\partial u_i}{\partial x_j}} \frac{\partial^2 U_i}{\partial x_l \partial x_j} - 2\nu \overline{\frac{\partial u_i}{\partial x_j} \frac{\partial u_j}{\partial x_l} \frac{\partial u_j}{\partial x_l}} - 2\left(\nu \overline{\frac{\partial^2 u_i}{\partial x_l \partial x_j}} \right)^2 \tag{8}$$

式中各項模式化爲

$$\frac{D\epsilon}{Dt} = \frac{\partial}{\partial x_l}\left[C_\epsilon' \left[\frac{\ell^2}{t} \right] \frac{\partial \epsilon}{\partial x_l} + \nu \frac{\partial \epsilon}{\partial x_l} \right] - C_{\epsilon 1}' \left[\frac{1}{t} \right] \overline{u_i u_l} \frac{\partial U_i}{\partial x_l} - C_{\epsilon 2}' \left[\frac{\epsilon}{t} \right] \tag{9}$$

C.J. CHEN〔8〕認爲紊流動能包含大渦流尺度（large eddy scale），即擴散項採用 $\ell = K^{3/2} / \epsilon$，$t = K / \epsilon$；而紊流能量消散包含小渦流尺度（small eddy scale），即生成項、消能項採用 $t = (\nu / \epsilon)^{1/2}$，上式化爲：

$$\frac{D\epsilon}{Dt} = \frac{\partial}{\partial x_l}\left[C_\epsilon' \frac{K^2}{\epsilon} \frac{\partial \epsilon}{\partial x_l} + \nu \frac{\partial \epsilon}{\partial x_l} \right] - C_{\epsilon 1}' \sqrt{\frac{\epsilon}{\nu}} \overline{u_i u_l} \frac{\partial U_i}{\partial x_l} - C_{\epsilon 2}' \sqrt{\frac{\epsilon}{\nu}} \epsilon \tag{10}$$

在二維不可壓縮紊流邊界層流中，K方程式及 ϵ 方程式分別寫成：

$$\frac{DK}{Dt} = \frac{\partial}{\partial y}\left[C_\kappa \frac{K^2}{\epsilon} \frac{\partial K}{\partial y} \right] - \overline{uv} \frac{\partial U}{\partial y} - \epsilon \tag{11}$$

$$\frac{D\epsilon}{Dt} = \frac{\partial}{\partial y}\left[C_\epsilon' \frac{K^2}{\epsilon} \frac{\partial \epsilon}{\partial y} \right] - C_{\epsilon 1}' \sqrt{\frac{\epsilon}{\nu}} \overline{uv} \frac{\partial U}{\partial y} - C_{\epsilon 2}' \sqrt{\frac{\epsilon}{\nu}} \epsilon \tag{12}$$

式中 C_κ，C_ϵ'，$C_{\epsilon 1}'$，$C_{\epsilon 2}'$ 係數，分別由實驗決定(1)式、(2)式、(3)式、(11)式、(12)式聯立即構成了紊流跡流之控制方程組，配合適當之邊界條件，利用數值方法可求解出平板尾端紊流跡流流場之變化情形。

肆、邊界條件及紊流模式中各係數

流場邊界參見圖 —a，由於流場對稱，在中心軸處：

$$\frac{\partial}{\partial y}\{ U, K, \epsilon \} = 0, \quad y = 0 \tag{13}$$

在流場側邊界處：

$$\frac{\partial}{\partial y}\{ U, K, \epsilon \} = 0, \quad y = 0 \tag{14}$$

$$V = 0$$

在流場上游邊界處（upstream），U之分佈，K之分佈均 $-\overline{uv}$ 分佈均由實驗求得。(4)式之係數 C_μ 由實驗定之取 0.09。(11)式之係數 C_κ 亦由實驗定之，採用 0.09。(12)式之 C_ϵ' 由實驗定爲 2.19；而 $C_{\epsilon 1}'$ 與 $C_{\epsilon 2}'$ 亦由實驗定爲 $18.9/\sqrt{Re}$，其中 $Re = K^2 / \epsilon\nu$。ν 爲流體之粘性係數（kinematic viscosity）。

伍、差分方程式

利用差分方法，將上述偏微分控制方程式以差分方程式近似求解。各控制方程式之位變項採上風差分（upwind difference），時變項採用前進差分；其他各項對空間之變化採用中心差分（central difference）；各差分近似如下：

$$\frac{\partial f}{\partial t} = \frac{f_{ij}^{n+1/2} - f_{ij}^{n}}{\frac{\Delta t}{2}}$$

或 $$\frac{\partial f}{\partial t} = \frac{f_{ij}^{n+1} - f_{ij}^{n+1/2}}{\frac{\Delta t}{2}}$$

$$\frac{\partial f}{\partial y} = \frac{f_{ij+1}^{n} - f_{ij-1}^{n}}{2\Delta Y}$$

$$U \frac{\partial f}{\partial x} = \begin{cases} U_{ij}^{n} \dfrac{f_{ij}^{n} - f_{i-1j}^{n}}{\Delta x} & U_{ij}^{n} > 0 \\ U_{ij}^{n} \dfrac{f_{i+1j}^{n} - f_{ij}^{n}}{\Delta x} & U_{ij}^{n} < 0 \end{cases} \quad \text{若} \tag{15}$$

$$V\frac{\partial f}{\partial y}=\begin{cases} V^n_{ij}\dfrac{f^n_{ij}-f^n_{ij-1}}{\Delta Y} & \text{若 } V^n_{ij}>0 \\ V^n_{ij}\dfrac{f^n_{ij+1}-f^n_{ij}}{\Delta Y} & \text{若 } V^n_{ij}<0 \end{cases}$$

有限差分網格分割情形，示如圖一 b 。

利用(15)式之差分體系，(2)式可寫成：

$$U^{n+1/2}_{ij}=\frac{1}{\frac{2}{\Delta t}+\frac{U^n_{ij}}{\Delta x}}\left[\left(\frac{U^n_{ij}}{\Delta x}\right)U^{n+1/2}_{i-1j}+\frac{2}{\Delta t}U^n_{ij}-V^n_{ij}\frac{U^n_{ij}-U^n_{ij-1}}{\Delta Y}+\right.$$
$$\left.C_\mu\frac{1}{\Delta Y}\left(\frac{(K^n_{ij+1/2})^2}{\epsilon^n_{ij+1/2}}\frac{(U^n_{ij+1}-U^n_{ij})}{\Delta Y}-\frac{(K^n_{ij-1/2})^2}{\epsilon^n_{ij-1/2}}\frac{(U^n_{ij}-U^n_{ij-1})}{\Delta Y}\right)\right]$$
；若 $V^n_{ij}>0$ (16.a)

$$U^{n+1/2}_{ij}=\frac{1}{\frac{2}{\Delta t}+\frac{U^n_{ij}}{\Delta x}}\left[\left(\frac{U^n_{ij}}{\Delta x}U^{n+1/2}_{i-1j}+\frac{2}{\Delta t}U^n_{ij}-V^n_{ij}\frac{U^n_{ij+1}-U^n_{ij}}{\Delta Y}+\right.\right.$$
$$\left.\left.C_\mu\frac{1}{\Delta Y}\left(\frac{(K^n_{ij+1/2})^2}{\epsilon^n_{ij+1/2}}\frac{U^n_{ij+1}-U^n_{ij}}{\Delta Y}-\frac{(K^n_{ij-1/2})^2}{\epsilon^n_{ij-1/2}}\frac{(U^n_{ij}-U^n_{ij-1})}{\Delta Y}\right)\right]\right.$$
；若 $V^n_{ij}<0$ (16.b)

式中 $\frac{(K^n_{ij+1/2})^2}{\epsilon^n_{ij+1/2}}=\left[\frac{(K^n_{ij+1})^2}{\epsilon^n_{ij+1}}+\frac{(K^n_{ij})^2}{\epsilon^n_{ij}}\right]/2$

$\frac{(K^n_{ij-1/2})^2}{\epsilon^n_{ij-1/2}}=\left[\frac{(K^n_{ij-1})^2}{\epsilon^n_{ij-1}}+\frac{(K^n_{ij})^2}{\epsilon^n_{ij}}\right]/2$

$$\left[\frac{V^n_{ij}}{\Delta Y}+\frac{C_\mu}{\Delta Y}\left(\frac{(K^n_{ij-1/2})^2}{\epsilon_{ij-1/2}}\frac{1}{\Delta Y}\right)\right]U^{n+1}_{ij-1}+\left\{-\frac{2}{\Delta t}-\frac{V^n_{ij}}{\Delta Y}+\frac{C_\mu}{\Delta Y}\left[\right.\right.$$
$$\left.\left.\frac{(K^n_{ij+1/2})^2}{\epsilon_{ij+1/2}}\frac{-1}{\Delta Y}-\frac{(K^n_{ij-1/2})^2}{\epsilon_{ij-1/2}}\frac{1}{\Delta Y}\right]\right\}U^{n+1}_{ij}+\left[\frac{C_\mu}{\Delta Y}\left(\frac{(K^n_{ij+1/2})^2}{\epsilon_{ij+1/2}}\right)\right.$$
$$\left.\frac{1}{\Delta Y}\right]U^n_{ij+1}=\frac{-2}{\Delta t}U^{n+1/2}_{ij}+U^{n+1/2}_{ij}\frac{U^{n+1/2}_{ij}-U^{n+1/2}_{i-1j}}{\Delta x}$$
；若 $V^n_{ij}>0$ (17.a)

$$\left[\frac{C_\mu}{\Delta Y}\left(\frac{(K^n_{ij-1/2})^2}{\epsilon_{ij-1/2}}\right)\frac{1}{\Delta Y}\right]U^{n+1}_{ij-1}+\left\{-\frac{2}{\Delta t}+\frac{V^n_{ij}}{\Delta Y}+\frac{C_\mu}{\Delta Y}\left[\left(\frac{(K^n_{ij+1/2})^2}{\epsilon_{ij+1/2}}\right)\right.\right.$$
$$\left.\left.-\frac{1}{\Delta Y}-\left(\frac{(K^n_{ij-1/2})^2}{\epsilon_{ij-1/2}}\right)\frac{1}{\Delta Y}\right]\right\}U^{n+1}_{ij}+\left[-\frac{V^n_{ij}}{\Delta Y}+\frac{C_\mu}{\Delta Y}\left(\frac{(K^n_{ij+1/2})^2}{\epsilon_{ij+1/2}}\right)\right.$$
$$\left.\frac{1}{\Delta Y}\right]U^{n+1}_{ij+1}=-\frac{2}{\Delta t}U^{n+1/2}_{ij}+U^{n+1/2}_{ij}\frac{U^{n+1/2}_{ij}-U^{n+1/2}_{ij}}{\Delta x}$$
；若 $V^n_{ij}<0$ (17.b)

(11)式差分式寫成：

$$K^{n+1/2}_{ij}=\frac{1}{\frac{2}{\Delta t}+\frac{U^{n+1}_{ij}}{\Delta x}}\left[\left(\frac{U^{n+1}_{ij}}{\Delta x}\right)K^{n+1/2}_{i-1j}+\frac{2}{\Delta t}K^n_{ij}-V^{n+1}_{ij}\frac{K^n_{ij}-K^n_{ij-1}}{\Delta Y}+\right.$$
$$\frac{C_K}{\Delta Y}\left[\left(\frac{(K^n_{ij+1/2})^2}{\epsilon_{ij+1/2}}\frac{K^n_{ij+1}-K^n_{ij}}{\Delta Y}-\frac{(K^n_{ij-1/2})^2}{\epsilon_{ij-1/2}}\frac{K^n_{ij}-K^n_{ij-1}}{\Delta Y}\right]\right.$$
$$\left.+C_\mu\frac{(K^n_{ij})^2}{\epsilon^n_{ij}}\left(\frac{U^{n+1}_{ij+1}-U^{n+1}_{ij-1}}{2\Delta Y}\right)^2-\epsilon^n_{ij}\right]$$
；若 $V^n_{ij}>0$ (18.a)

$$K^{n+1/2}_{ij}=\frac{1}{\frac{2}{\Delta t}+\frac{U^{n+1}_{ij}}{\Delta x}}\left[\left(\frac{U^{n+1}_{ij}}{\Delta x}\right)K^{n+1/2}_{i-1j}+\frac{2}{\Delta t}K^n_{ij}-V^{n+1}_{ij}\frac{K^n_{ij+1}-K^n_{ij}}{\Delta Y}+\right.$$
$$\frac{C_K}{\Delta Y}\left[\left(\frac{(K^n_{ij+1/2})^2}{\epsilon_{ij+1/2}}\frac{K^n_{ij+1}-K^n_{ij}}{\Delta Y}-\frac{(K^n_{ij-1/2})^2}{\epsilon_{ij-1/2}}\frac{K^n_{ij}-K^n_{ij-1}}{\Delta Y}\right]\right.$$
$$\left.+C_\mu\frac{(K^n_{ij})^2}{\epsilon^n_{ij}}\left(\frac{U^{n+1}_{ij+1}-U^{n+1}_{ij-1}}{2\Delta Y}\right)^2-\epsilon^n_{ij}\right]$$
；若 $V^n_{ij}<0$ (18.b)

$$\left[\frac{V^{n+1}}{\Delta Y}+\frac{C_K}{\Delta Y}\frac{(K^n_{ij-1/2})^2}{\epsilon^n_{ij-1/2}}\frac{1}{\Delta Y}\right]K^{n+1}_{ij-1}+\left\{\frac{-2}{\Delta t}-\frac{V^{n+1}}{\Delta Y}+\frac{C_K}{\Delta Y}\left[\right.\right.$$
$$\left.\left.\frac{(K^n_{ij+1/2})^2}{\epsilon^n_{ij+1/2}}-\frac{1}{\Delta Y}+\frac{(K^n_{ij-1/2})^2}{\epsilon^n_{ij-1/2}}-\frac{1}{\Delta Y}\right]\right\}K^{n+1}_{ij}+\left[\frac{C_K}{\Delta Y}\frac{(K^n_{ij+1/2})^2}{\epsilon^n_{ij+1/2}}\frac{1}{\Delta Y}\right]$$
$$K^{n+1}_{ij+1}=-\frac{2}{\Delta t}K^{n+1/2}_{ij}+U^{n+1}_{ij}\frac{K^{n+1/2}_{ij}-K^{n+1/2}_{i-1j}}{\Delta X}-C_\mu\frac{(K^n_{ij})^2}{\epsilon^n_{ij}}$$
$$\left(\frac{U^{n+1}_{ij+1}-U^{n+1}_{ij-1}}{2\Delta Y}\right)^2+\epsilon^n_{ij}$$
；若 $V^n_{ij}>0$ (19.a)

$$\left[\frac{C_K}{\Delta Y}\frac{(K^n_{ij-1/2})^2}{\epsilon^n_{ij-1/2}}\frac{1}{\Delta Y}\right]K^{n+1}_{ij-1}+\left\{\frac{-2}{\Delta t}+\frac{V^{n+1}_{ij}}{\Delta Y}+\frac{C_K}{\Delta Y}\left[\frac{(K^n_{ij+1/2})^2}{\epsilon^n_{ij+1/2}}\right.\right.$$
$$\left.\left.\frac{-1}{\Delta Y}+\frac{(K^n_{ij-1/2})^2}{\epsilon^n_{ij-1/2}}\frac{-1}{\Delta Y}\right]\right\}K^{n+1}_{ij}+\left[\frac{-V^{n+1}_{ij}}{\Delta Y}+\frac{C_K}{\Delta Y}\frac{(K^n_{ij+1/2})^2}{\epsilon^n_{ij+1/2}}\frac{1}{\Delta Y}\right]$$
$$K^{n+1}_{ij+1}=\frac{-2}{\Delta t}K^{n+1/2}_{ij}+U^{n+1}_{ij}\frac{K^{n+1/2}_{ij}-K^{n+1/2}_{i-1j}}{\Delta x}-C_\mu\frac{(K^n_{ij})^2}{\epsilon^n_{ij}}$$
$$\left(\frac{U^{n+1}_{ij+1}+U^{n+1}_{ij-1}}{2\Delta Y}\right)^2+\epsilon^n_{ij}$$
；若 $V^{n+1}_{ij}<0$ (19.b)

(11)式差分式寫成：

$$\epsilon^{n+1/2}_{ij}=\frac{1}{\frac{2}{\Delta t}+\frac{U^{n+1}_{ij}}{\Delta x}+C'_{\epsilon 2}\sqrt{\frac{\epsilon^n_{ij}}{\nu}}}\left[\frac{U^{n+1}_{ij}}{\Delta x}\epsilon^{n+1/2}_{i-1j}+\frac{2}{\Delta t}\epsilon^n_{ij}-V^{n+1}_{ij}\right.$$

$$\frac{\epsilon^n_{ij}-\epsilon^n_{ij-1}}{\Delta Y}+\frac{C'_\epsilon}{\Delta Y}\left(\frac{(K^n_{ij+1/2})^2}{\epsilon^n_{ij+1/2}}\frac{\epsilon^n_{ij+1}-\epsilon^n_{ij}}{\Delta Y}-\frac{(K^n_{ij-1/2})^2}{\epsilon^n_{ij-12}}\right.$$

$$\left.\frac{\epsilon^n_{ij}-\epsilon^n_{ij-1}}{\Delta Y}\right)+C'_{\epsilon 1}\sqrt{\frac{\epsilon^n_{ij}}{\nu}}\,C_\mu\frac{(K^{n+1}_{ij})^2}{\epsilon^n_{ij}}\left(\frac{U^{n+1}_{ij+1}-U^{n+1}_{ij-1}}{2\Delta Y}\right)^2\Big]$$

；若 $V^n_{ij}>0$ (20.a)

$$\epsilon^{n+12}_{ij}=\frac{1}{\frac{2}{\Delta t}+\frac{U^{n+1}_{ij}}{\Delta x}+C'_{\epsilon 2}\sqrt{\frac{\epsilon^n_{ij}}{\nu}}}\Big[\frac{U^{n+1}_{ij}}{\Delta x}\epsilon^{n+1/2}_{i-1j}+\frac{2}{\Delta t}\epsilon^n_{ij}-$$

$$V^{n+1}_{ij}\frac{\epsilon^n_{ij+1}-\epsilon^n_{ij}}{\Delta Y}+\frac{C'_\epsilon}{\Delta Y}\left(\frac{(K^{n+1}_{ij+1/2})^2}{\epsilon^{n+1}_{ij+1/2}}\frac{\epsilon^n_{ij+1}-\epsilon^n_{ij}}{\Delta Y}-\frac{(K^{n+1}_{ij-1/2})^2}{\epsilon^n_{ij-1/2}}\right.$$

$$\left.\frac{\epsilon^n_{ij}-\epsilon^n_{ij-1}}{\Delta Y}\right)+C'_{\epsilon 1}\sqrt{\frac{\epsilon^n_{ij}}{\nu}}\,C_\mu\frac{(K^{n+1}_{ij})^2}{\epsilon^n_{ij}}\left(\frac{U^{n+1}_{ij+1}-U^{n+1}_{ij-1}}{2\Delta Y}\right)^2\Big]$$

；若 $V^n_{ij}<0$ (20.b)

式中 $\frac{(K^{n+1}_{ij+1/2})^2}{\epsilon^n_{ij+12}}=\Big[\frac{(K^{n+1}_{ij+1})^2}{\epsilon^n_{ij+1}}+\frac{(K^{n+1}_{ij})^2}{\epsilon^{n+1}_{ij}}\Big]/2$

$$\frac{(K^{n+1}_{ij-1/2})^2}{\epsilon^n_{ij-12}}=\Big[\frac{(K^{n+1}_{ij-1})^2}{\epsilon^n_{ij-1}}+\frac{(K^{n+1}_{ij})^2}{\epsilon^{n+1}_{ij}}\Big]/2$$

$$\Big[\frac{V^{n+1}_{ij}}{\Delta Y}+\frac{C'_\epsilon}{\Delta Y}\frac{(K^{n+1}_{ij-1/2})^2}{\epsilon^{n+12}_{ij-1/2}}\frac{1}{\Delta Y}\Big]\epsilon^{n+1}_{ij-1}+\Big\{\frac{-2}{\Delta t}-\frac{V^{n+1}_{ij}}{\Delta Y}+\frac{C'_\epsilon}{\Delta Y}\Big[\frac{(K^{n+1}_{ij+1/2})^2}{\epsilon^{n+1/2}_{ij+1/2}}$$

$$\frac{-1}{\Delta Y}+\frac{(K^{n+1}_{ij-1/2})^2}{\epsilon^{n+1/2}_{ij-1/2}}\frac{-1}{\Delta Y}\Big]-C'_{\epsilon 2}\sqrt{\frac{\epsilon^{n+1/2}_{ij}}{\nu}}\Big\}\epsilon^{n+1}_{ij}+\Big[\frac{C'_\epsilon}{\Delta Y}\frac{(K^{n+1}_{ij+1/2})^2}{\epsilon^{n+1/2}_{ij+1/2}}$$

$$\frac{1}{\Delta Y}\Big]\epsilon^{n+1}_{ij+1}=\frac{-2}{\Delta t}\epsilon^{n+1/2}_{ij}+U^{n+1}_{ij}\frac{\epsilon^{n+1/2}_{ij}-\epsilon^{n+1/2}_{i-1j}}{\Delta x}-C'_{\epsilon 1}\sqrt{\frac{\epsilon^{n+1/2}_{ij}}{\nu}}$$

$$C_\mu\frac{(K^{n+1}_{ij})^2}{\epsilon^{n+1/2}_{ij}}\left(\frac{U^{n+1}_{ij+1}-U^{n+1}_{ij-1}}{2\Delta Y}\right)^2\quad；若 V^n_{ij}>0 \qquad (21.a)$$

$$\Big[\frac{C'_\epsilon}{\Delta Y}\frac{(K^{n+1}_{ij-1/2})^2}{\epsilon_{ij-1/2}}\frac{1}{\Delta Y}\Big]\epsilon^{n+1}_{ij-1}+\Big\{\frac{-2}{\Delta t}+\frac{V^{n+1}_{ij}}{\Delta Y}+\frac{C'_\epsilon}{\Delta Y}\Big[\frac{(K^{n+1}_{ij+1/2})^2}{\epsilon^{n+12}_{ij+1/2}}\frac{-1}{\Delta Y}$$

$$+\frac{(K^{n+1}_{ij-1/2})^2}{\epsilon^{n+12}_{ij-1/2}}\frac{-1}{\Delta Y}\Big]-C'_{\epsilon 2}\sqrt{\frac{\epsilon^{n+1/2}_{ij}}{\nu}}\Big\}\epsilon^{n+1}_{ij}+\Big[\frac{-V^{n+1}_{ij}}{\Delta Y}+\frac{C'_\epsilon}{\Delta Y}\frac{(K^{n+1}_{ij+1/2})^2}{\epsilon^{n+1/2}_{ij+1/2}}\Big]$$

$$\epsilon^{n+1}_{ij+1}=\frac{-2}{\Delta t}\epsilon^{n+1/2}_{ij}+U^{n+1}_{ij}\frac{\epsilon^{n+1/2}_{ij}-\epsilon^{n+1/2}_{i-1j}}{\Delta x}-C'_{\epsilon 1}\sqrt{\frac{\epsilon^{n+1/2}_{ij}}{\nu}}\,C_\mu\frac{(K^{n+1}_{ij})^2}{\epsilon^{n+1/2}_{ij}}$$

$$\left(\frac{U^{n+1}_{ij+1}-U^{n+1}_{ij-1}}{2\Delta Y}\right)^2\quad；若 V^n_{ij}<0 \qquad (21.b)$$

(1)式之差分式寫成：

$$V^{n+1}_{ij-1}=V^n_{ij}+\frac{\Delta Y}{2\Delta Y}\left(U^{n+1}_{i+1j}-U^{n+1}_{i-1j}\right) \qquad (22)$$

邊界條件(13)式(14)式，以Taylor Series展開化簡得

$$\begin{aligned}
&U_{i,1}=(4U_{i,2}-U_{i,3})/3\\
&K_{i,1}=(4K_{i,2}-K_{i,3})/3 \quad ；y=0\\
&\epsilon_{i,1}=(4\epsilon_{i,2}-\epsilon_{i,3})/3
\end{aligned} \qquad (23)$$

$$\begin{aligned}
&U_{i,nj}=(4U_{i,nj-1}-U_{i,nj-2})/3\\
&V_{i,nj}=0\\
&K_{i,nj}=(4K_{i,nj-1}-K_{i,nj-2})/3\\
&\epsilon_{i,nj}=(4\epsilon_{i,nj-1}-\epsilon_{i,nj-2})/3
\end{aligned} \qquad (24)$$

陸、演算方法及結果與討論

上節之差分方程式可運用變換方向顯示及隱式方法(alternating direction explicit & implicit)求解。即對x方向掃描採用顯示法，對y方向掃描採用隱式法。先解動量方程式，求出變數U；再由連續方程式解變數V；次由K方程式解變數K；由ϵ方程式解變數ϵ；如此完成一次疊代；重覆上述步驟解U，V，K，ϵ，至前後二次數值相近，即趨於穩定，演算終止。

利用上述差分方程模式，演算平板尾端紊流跡流。演算之流場上游邊界條件由實驗值決定，取Chevray & Kovasznay〔9〕之實驗值：平均流速剖面及紊流速度擾動量強度u′，v′，紊流壓力$-\overline{uv}$。平均流速剖面可以下式表之：

$$\frac{u}{U_0}=0.16\ell n\frac{y}{\delta}+1.0 \qquad (25)$$

式中 $\delta=\dfrac{0.37L}{\left(\frac{U_0L}{\nu}\right)^{1/5}}$

u′ x方向速度擾動量

v′ y方向速度擾動量

U_0 自由流速(free stream velocity)

L：平板長

而

紊流動能 $K=\dfrac{\overline{u'^2}+\overline{v'^2}}{2}$ (26)

紊流消能 $\epsilon=C_\mu\dfrac{K^2}{-\overline{uv}}\dfrac{\partial U}{\partial y}$ (27)

演算結果取平板尾端後20cm，50cm，150cm之平均流速分佈計算值與Chevray & Kovaszay實驗值〔9〕比較，結果吻合。示之圖二。由圖中，很明顯地看出紊流跡

流在平板尾端後之平均流速剖面變化，尤其近中心軸速度梯度較大。圖三爲平板尾端紊流跡流中心軸平均流速之分佈變化情形。圖中顯示計算值與實驗值相吻合，且由圖中可以看出紊流跡流中心軸平均流速在接近平板尾端變化劇烈，此與跡流之物理現象符合。圖四爲平板尾端後 5cm, 20cm, 50cm, 150cm之紊流應力（雷諾應力）之分佈情形。圖中顯示計算值與實驗值之比較，結果良好，從該圖可以明顯地得知各斷面紊流應力最大值均隨遠離平板尾端而遞減。近平板尾端之各斷面，如 5cm, 20cm, 50cm 斷面之紊流應力，分佈均爲尖峰形，亦即紊流應力較集中，且近中心軸，此現象與圖二近中心軸平均流速梯度較大之現象相符合，蓋平均流速梯度正比於紊流應力，此由式(3)可以得知。在 150cm 斷面之紊流應力分佈則較扁平，即紊流應力分佈較寬廣，且最大紊流應力值亦較近平板尾端各斷面之最大紊流應力值爲小。從各斷面紊流應力分佈形狀隨著遠離平板尾端愈扁平之現象可以推知紊流動量在 y 方向之傳輸，隨著離平板尾端距離之增加而愈明顯。圖五爲平板尾端後跡流寬度變化。其中跡流寬度 $\delta 1/2$定義爲：當 $U = 1/2(U_c + U_o)$ 時，所對應之 y 。U_c 爲中心軸平均流速，U_o 爲自由流速 ，y 爲 y 軸方向距離，θ_o 爲邊界層動量厚度（ momentum thickness），圖中顯示計算值與實驗值比較，結果良好。跡流寬度隨遠離平板尾端而增加，且近平板尾端處變化較大。圖六爲紊流動能沿中心軸之變化。由圖上可以明顯地看出紊流動能在平板尾端 $X/\theta_o = 0$ 處爲零，離開平板尾端後突然變爲最大，之後隨著遠離平板尾端紊流動能遞減，遞減情形在 $x/\theta_o = 50$之前相當顯著。圖七爲紊流消能沿中心軸之變化。紊流消能亦隨遠離平板尾端而遞減。圖八爲各斷面之紊流動能分佈情形，由該圖可知各斷面紊流動能最大值並非在中心軸；且愈下游斷面之紊流動能最大值愈遠離中心軸。此外由該圖亦可看出愈上游斷面紊流動能分佈形狀愈集中，亦即愈近平板尾端紊流愈强。圖九爲紊流消能在各斷面之分佈情形。圖中顯示各斷面最大紊流消能並不在中心軸，且愈下游斷面其紊流消能最大值愈遠離中心軸。愈下游之斷面紊流消能分佈形狀愈緩和，與紊流動能分佈形狀有相似之處，此即說明了愈遠離平板尾端紊流强度愈小，該趨勢與 Chevray & Kovaznay 之實驗現象趨勢吻合。

柒、結　　論

綜合以上計算結果與討論，得以下結論：

1. 本文所採用雙尺度 $K-\epsilon$ 紊流模式經差分方程數值計算平板尾端紊流跡流結果與 Chevray & Kovasznay 實驗值比較，結果良好。證實雙尺度 $K-\epsilon$ 紊流模式應用於紊流跡流之可靠性。
2. 平板尾區跡流中心軸流速隨著遠離平板尾端而增大；中心軸紊流動能 k 與紊流消能 ϵ 均隨遠離平板尾端而減小；尾區跡寬度亦隨遠離平板尾端而增加。
3. 平板尾區跡流各斷面之紊流應力最大值隨著距平板尾端距離之增加而遞減且偏離跡流中心軸；而紊流動能與紊流消能亦有同樣趨勢。

參考文獻

1. Prandtl, L., Über die ausgebilclete Turbulenz, ZAMM, 5, p. 136, (1925).
2. Von Karman, Th. Mechanische Ähnlichkeit und Turbulenz, Nach, Ges. Wiss. Guttingen, Math. Phy. Klasse, 58, (1930) und NACA TM 611, (1931).
3. Ozaki's review report CRIEPI 1983.
4. Rodi, W. "Turbulence Models and Their Applications in Hydraulics" IAHR Publications 1980.
5. Prandtl, L. Bemerkungen zur Theorie der freien Turbulenz, ZAMM, 22, pp. 241-243, 1942.
6. Kolmogorov, A.N., Equations of Turbulent motion of an incompressible fluid: Imperical College, Mech. Eng. Dept. Rept. ON/6, 1968.
7. Launder, B.E. Morse, A.P., Rodi W. and Splading, D.B., The Prediction of free-shear flows - a comparison of the performance of six turbulence models, Proc. NASA Longley Free Turbulent Shear Flows Conf., Vol. 1, NASA sp 320, 1973.
8. Ching Jen Chen, Turbulence Modeling and Its Application, hand-written manuscript, June 1983, pp. III25-III26.
9. Rene Chevray and Leslie S.G. Kovasznay. Turbulence Measurements in the Wake of a Thin Flat Plate, Journal of AIAA, August 1969, pp. 1641-1642.
10. Paul K. Chang, Seperation of Flow, Pergamon Press New York, 1970, pp. 365-382b.

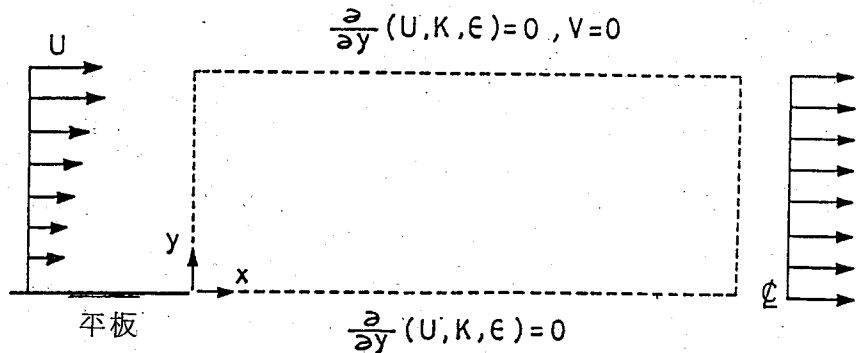

圖一(a) 流場邊界條件示意圖

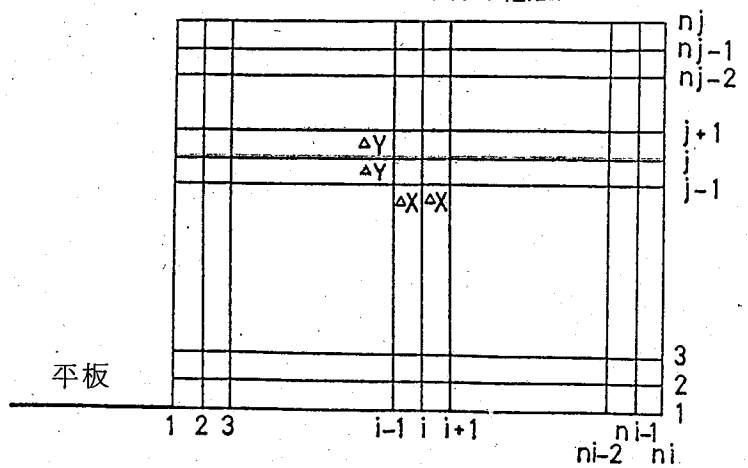

圖一(b) 流場網格分割示意圖

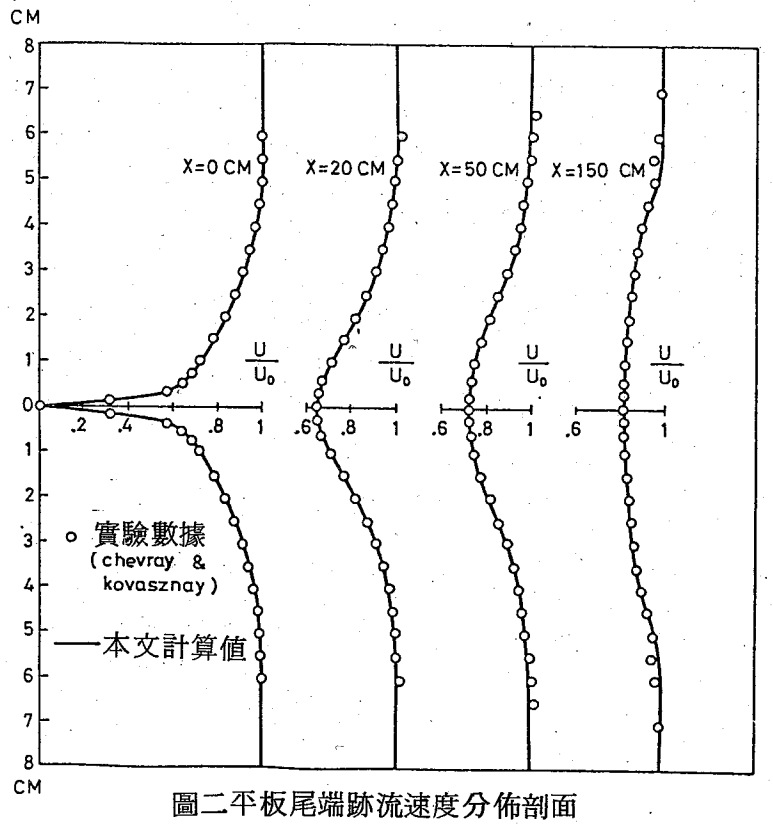

圖二平板尾端跡流速度分佈剖面

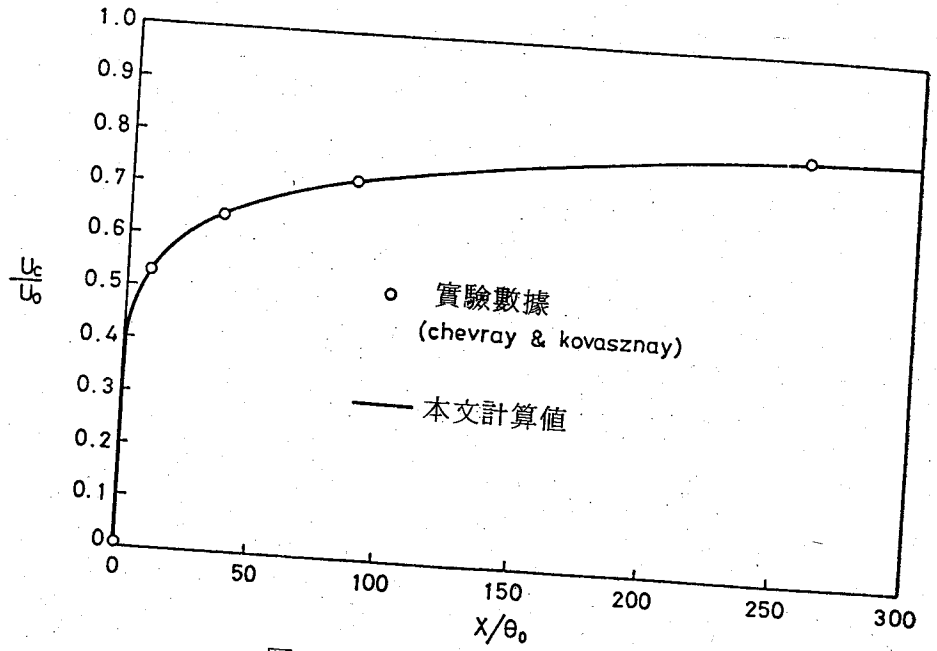

圖三 平板尾端跡流中心軸向速度之變化

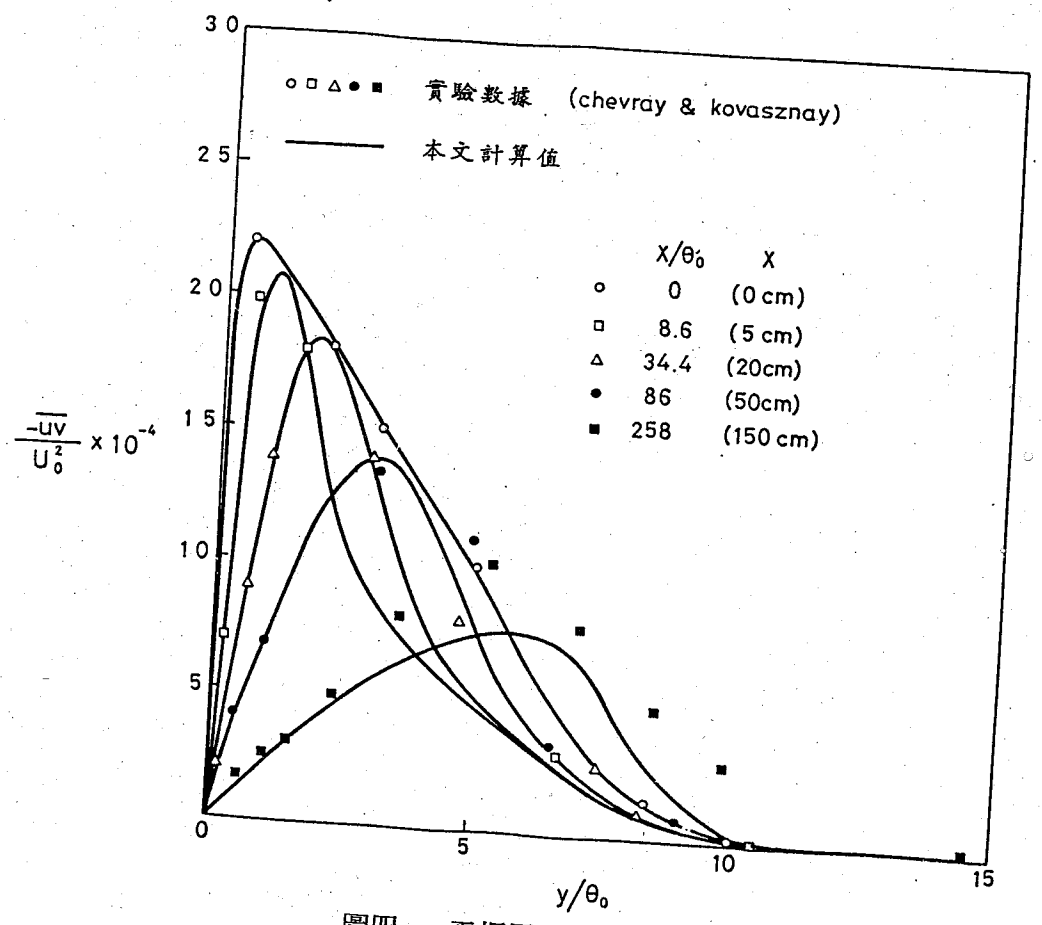

圖四 平板尾端跡流之剪應力分佈剖面

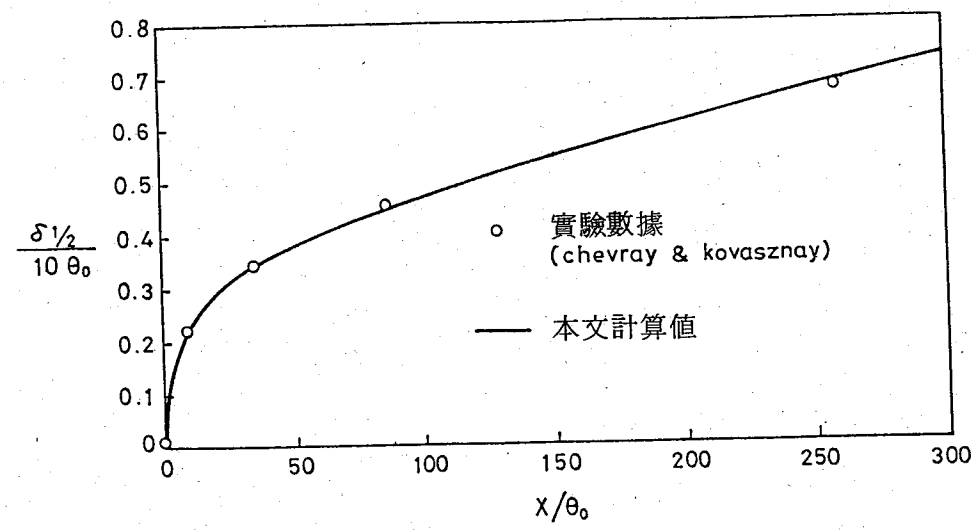

圖五　平板尾端跡流寬度之變化

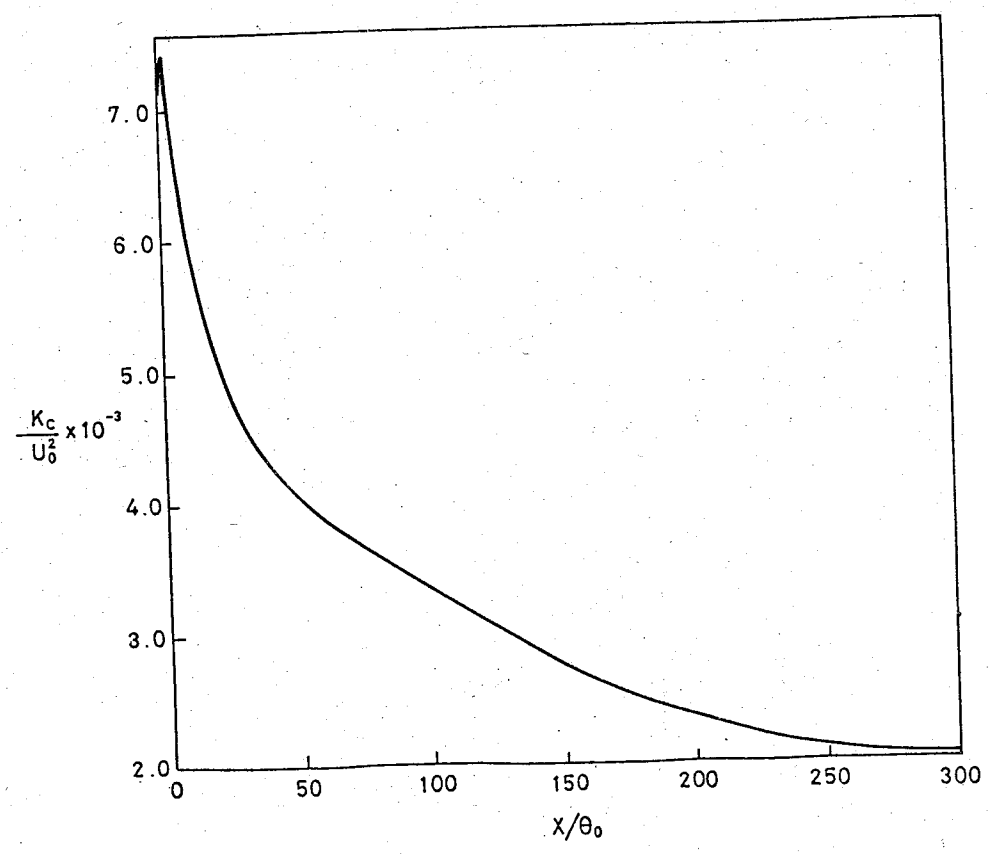

圖六　平板尾端跡流中心軸向紊流動能之變化

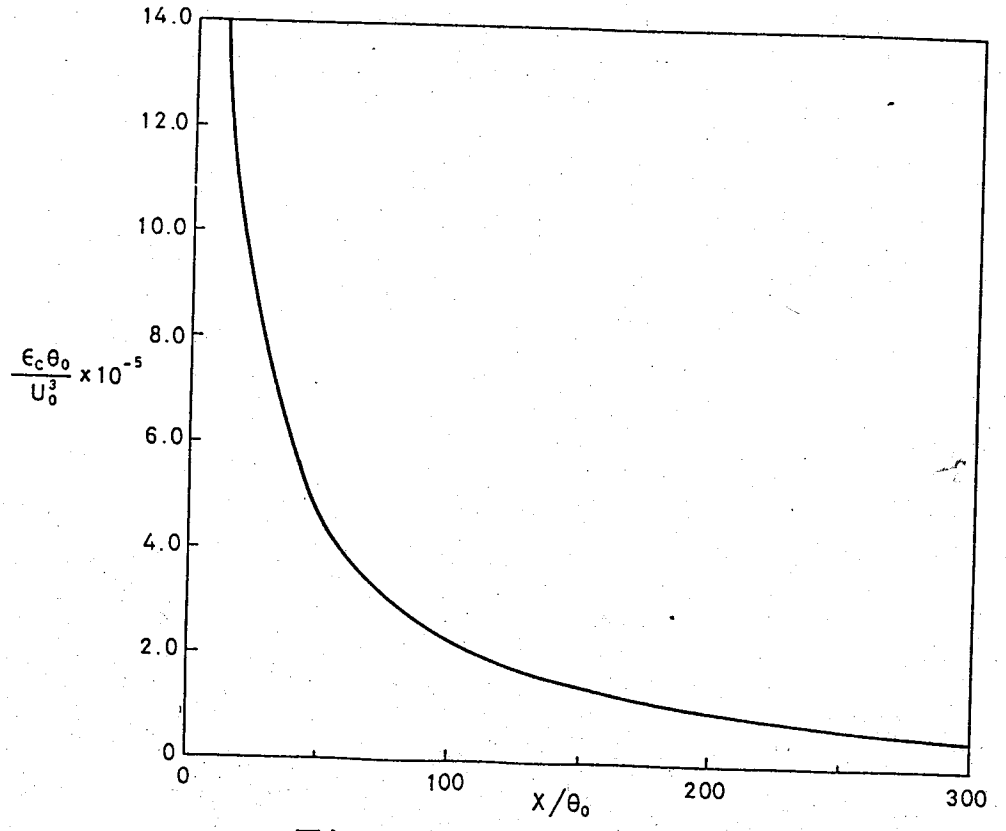

圖七　平板尾端跡流中心軸向紊流消能之變化

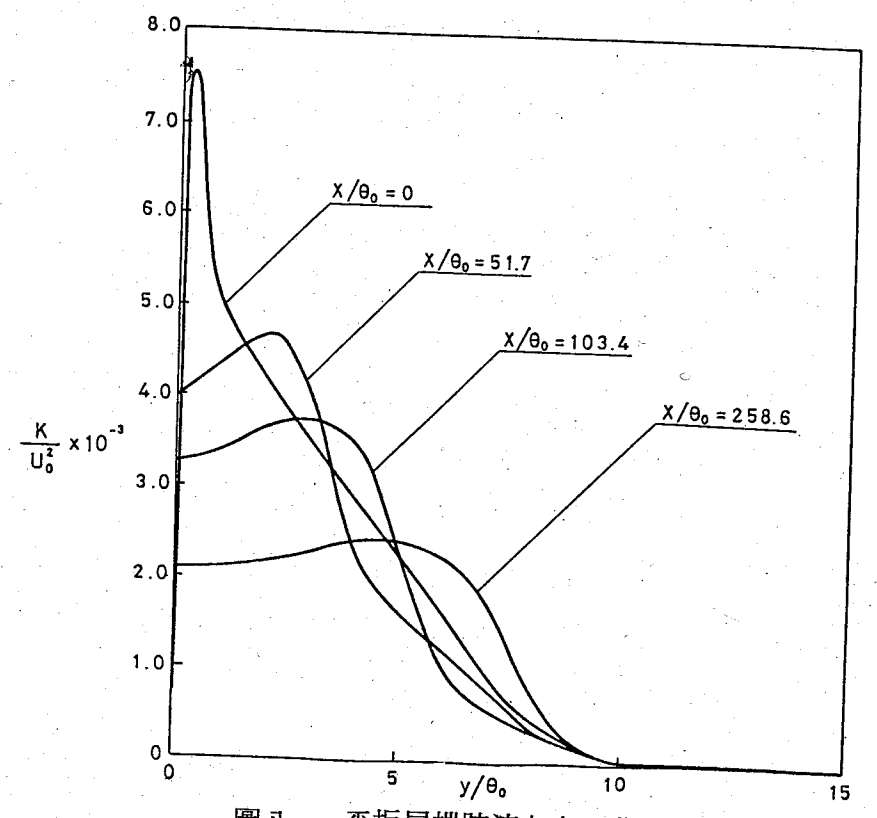

圖八　平板尾端跡流之紊流動能分佈剖面

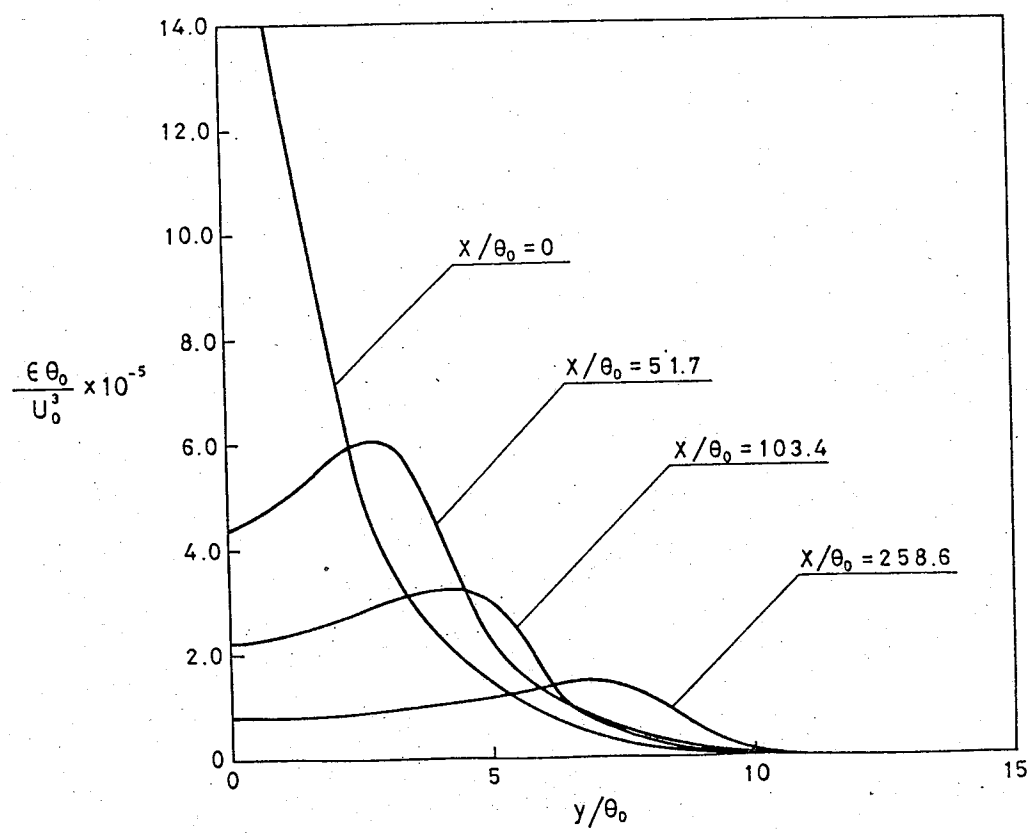

圖九　平板尾端跡流之紊流消能分佈剖面

MULTISITE-CORRELATED PERCOLATION AND ISING MODELS WITH MULTISPIN INTERACTIONS*

Chin-Kun Hu（胡進錕）
Institute of Physics, Academia Sinica
Nankang, Taipei, Taiwan 115
Republic of China

ABSTRACT

We extend the concept of site percolation and bond percolation to multisite percolation in which each active element in the random process involves more than two sites. We show that the partition function of the Ising model with multisite interactions of strength J_m is the generating function of a multisite-correlated percolation model. From this connection, we conclude that the phase transition of the Ising model with multispin interactions is also a percolation transition.

---

* Presented at Workshop on Statistical Physics, June 28-30, 1984 at Institute of Physics, Academia Sinica, Taipei, Taiwan, R.O.C.

PERCOLATION THEORY OF PHASE TRANSITIONS IN SPIN MODELS*

Chin-Kun Hu (胡進錕)
Institute of Physics, Academia Sinica
Nankang, Taipei, Taiwan, 115
Republic of China

ABSTRACT

The phase transition in the spin model and the percolation transition in the lattice percolation model have many characteristics in common which have motivated researchesr to explore whether the former is a percolation transition of a correlated percolation model. Previous attemps to draw such a connection have been either unsuccessful or unsatisfactory. This paper briefly reviews a new approach which not only solves the problem but also provides a new avenue to understand the behavior of phase transitions in spin models.[1-3]

1. C.K. Hu, Phys. Rev. *29*, 5103 and 5109 (1984); Physica *119*A, 609 (1983).
2. C.K. Hu, Chin J. Phys. (Taipei) Vol. 22, No. 1, 1 (1984); C.K. Hu and H.Y. Lee, ibid, No. 3 (1984).
3. C.K. Hu, J. Phys. A Vol. 16, L321 (1983).

* Presented at Workshop on Statistical Physics, June 28-30, 1984 at Institute of Physics, Academia Sinica, Taipei, Taiwan, R.O.C.

REPRESENTATION OF SU(n) GROUP AND A THEORY OF RAMAN SCATTERING*

Chin-Kun Hu
Institute of Physics, Academia Sinica
Nankang, Taipei, Taiwan 115
Republic of China

ABSTRACT

The representation of SU(n) group with $n \geq 3$ has been used to formulate a theory of Raman scatterings[1] based on the idea that N molecules within a small portion of the wavelength of the incident light should be considered as a single quantum mechnical system. For such a system, at zero temperature, i.e. T = 0, if the final level involved in the Raman scattering is populated by the stimulated absorption or earlier scattering so that Ne molecules are in the excited state, the theory predicts that the scattering cross section would be enhanced by a factor (1 – Ne/N) (Ne + 1) due to the cooperative effect. The extension of the result to finite temperatures is also discussed.

1. C.K. Hu and C.Y. Huang, Optics Communications *43*, 395 (1982).

* Presented at the 13th International Colloquium on Group Theoretical Methods in Physics on 21-25 May, 1984 at University of Maryland, Maryland, U.S.A.

Annual Report of the Institute of Physics, Academia Sinica, Vol. 14, 1984

CORRELATED PERCOLATION AND THE PHASE TRANSITIONS IN ISING-LIKE SPIN MODELS*

Chin-Kun Hu
Institute of Physics, Academia Sinica
Nankang, Taipei, R.O.C.

ABSTRACT

Considering each lattice site with a spin occupied and the lattice site without a spin unoccupied, we could formally show that the partition functions of many Ising-like spin models are the generating functions of correlated percolation models. Each correlated percolation model has the same critical properties as the corresponding spin model. From such connections, we could physically understand many properties of spin models. In this paper, we first formally show that the partition function of the q-state Potts model (QPM) is the generating function of a q-state bond-correlated percolation model (QBCPM) which has the same critical point and exponents as those of the QPM. From this connection, we propose a geometrical condition of phase transitions and give geometrical reasons for the variation of the critical exponent α with q, the changeover from second-order to first-order phase transition as q increases, and the finite-size scaling and broadening at theremal and magnetic first-order phase transitions. Similar analyses for other spin models will be presented in other papers.

---

*Published in Chinese J. Phys. (Taipei) Vol. 22, No. 1, 1 (1984).

Annual Report of the Institute of Physics, Academia Sinica, Vol. 14, 1984

EXACT RESULTS FOR AN ONE DIMENSIONAL q-STATE BOND-CORRELATED PERCOLATION MODEL

Chin-Kun Hu (胡進錕) and Hong-Yuh Lee (李宏裕)
Institute of Physics, Academia Sinica
Nankang, Taipei, Taiwan 115
Vepublic of China

ABSTRACT

Based on the connection between the q-state Potts model (QPM) and the q-state bond-correlated percolation model (QBCPM), we present a new way to calculate the exact partition function of the one-dimensional QPM. We write down an exact formula for the geometrical factor $g_f(q, R)$, $0 \leq R \leq 1$, of the one dimensional QBCPM and present numerical evidence to support Hu's idea that the average number of occupied bonds of the QBCPM, which corresponds internal energy of the QPM, is determined by the peak of $g_f(q, R)\, U_K(R)$, where $U_K(R)$ is the known interaction factor.

Published in Chinese J. Phys. (Taipei), Vol. 22, No. 3, (1984).

CORRELATED PERCOLATION AND THE SCALING RELATION OF CRITICAL EXPONENTS*

Chin-Kun Hu (胡進錕)
Institute of Physics, Academia Sinica
Nankang, Taipei, R.O.C.

ABSTRACT

Based on the connection between the Ising-like spin model and the correlated percolation model established recently by us, we propose a formula for the singular part of the free energy for the spin model. Such free energy is a generalized homogeneous function of the reduced temperature and the magnetic field. Therefore, the critical exponents derived from the free energy satisfy the scaling relations. The method that may be used to test our formulation is also discussed.

---

* Presneted at the Annual Meeting of the Physical Society of the Republic of China, January 19, 1984.

RENORMALIZATION-GROUP STUDY OF A SIMPLE CUBIC ISING MODEL WITH FOUR-SPIN INTERACTIONS

Chin-Kun Hu and Hong-Yuh Lee
Institute of Physics, Academia Sinica
Nankang, Taipei, Taiwan 115
Republic of China

ABSTRACT

The modified Kadanoff variational method has been used to study a simple cubic Ising model with the nearest-neighbor two-spin interactions of strength J_2 and the four-spin interactions of strength J_4. The free energy f, spontaneous magnetization M, magnetic susceptibility χ, internal eneryg U, and the specibic heat C_h are calculated and plotted. The results indicate that for $0 \leq J_4/J_2 \leq 4$, the phase transitions are second-order.

Published in Chinese J. Phys. (Taipei) Vol. 22, No. 3, (1984).

^{9}Be(p, p α)^{5}He CLUSTER KNOCKOUT REACTION WITH POLARIZED BEAM AT 150 MeV

*C. W. Wang,† P. G. Roos, N. S. Chant, G. Ciangaru,**
F. Khazaie, and D. Mack
Department of Physics and Astronomy
University of Maryland, College Park, Maryland 20742

A. Nadasen
Department of Natural Sciences
University of Michigan-Dearborn, Dearborn, Michigan 48128

S. J. Mills
CSIR, Faure, South Africa

R. E. Warner
Oberlin College, Oberlin, Ohio 44074

ABSTRACT

The (p, Pα) cluster knockout reaction on ^{9}Be has been investigated with polarized beam. Coincident data for 8 quasifree angle pairs were obtained at a bombarding energy of 150 MeV. Both energy sharing distribution and analyzing power were measured. Distorted wave impulse approximation (DWIA) calculations indicate that the reaction is dominated by quasifree process, and that the D-state component of the cluster-core wave function is important for larger momentum transfer. Absolute spectroscopic factors for the S- and D-state extracted are in good agreement with theoretical predictions. The analyzing power follows the trend of the free p-^{4}He scattering and agrees with DWIA calculation reasonably well. The spin-orbit interaction in the distorted waves plays little role around the quasifree peaks.

---

† On leave of absence from Institute of Physics, Academia Sinica, Taipei, Taiwan 115, and partly supported by by NSF, R.O.C.

EXCITATION SPECTRA OF GROUP-II ACCEPTORS IN Ge: Ge(Be^{0}), Ge(Be^{-}), AND Ge(Mg^{0})

J. W. Cross, L. T. Ho, and A. K. Ramdas
Department of Physics, Purdue University,
West Lafayette, Indiana 47907

R. Sauer
Physikalisches Institut Teilinstitut 4, Universitat Stuttgart,
Federal Republic of Germany

E. E. Haller
Department of Materials Science and Mineral Engineering and Lawrence Berkeley Laboratory,
University of California, Berkeley, California 94720
(Received 1 August 1983)

ABSTRACT

Substitutional Mg and Be impurities in Ge bind two holes and are solid-state analogs of neutral helium. A high-resolution Fourier-transform spectrometer, a liquid-helium optical cryostat, and a liquid-helium-cooled germanium bolometer were employed in the study of Ge(Mg^{0}), Ge(Be^{0}), and Ge(Be^{-}). The excitation lines of the neutral double acceptors represent one-hole excitations from the $\{\Gamma_8 \times \Gamma_8\} = \Gamma_1 + \Gamma_3 + \Gamma_5$ $(1s)^2$ ground state to the $\Gamma_8 \times \Gamma_8$, $\Gamma_8 \times \Gamma_7$, and $\Gamma_8 \times \Gamma_6$ $(1s)$ (np) excited states. The binding energies of the excited states show excellent agreement with those of other group-II and group-III acceptors as well as with those calculated in the effective-mass theory of Baldereschi and Lipari. The spectrum of Ge(Be^{0}) shows a doublet structure which can be attributed to the splitting of the ground-state multiplet into a $\Gamma_1 + \Gamma_5$ state. When Ge(Be^{0}) is suitably compensated with a group-V impurity or with Li, the resulting Ge(Be^{-}) exhibits lines in its excitation spectrum representing $\Gamma_8 \rightarrow \Gamma_8$, Γ_7, or Γ_6 transitions, the binding energies of the excited states being four times larger than those of neutral acceptors. The excitation lines of Ge(Be^{-}) show the characteristic broadening and asymmetry caused by charged impurities.

Published in Phys. Rev. B28, 6953 (1983).

SPECTROSCOPY OF IMPURITIES IN SEMICONDUCTORS

L. T. Ho
Institute of Physics, Academia Sinica

ABSTRACT

Many chemical impurities can be introduced into semiconductors in a deliberate and controlled manner. Under suitable circumstances these impurities can bind electrons or holes with bound states having binding energies small compared to the intrinsic energy gap of the host. A series of excitation lines in absorption can be observed for these donor and acceptor impurities in the infrared region. In this review talk, the role and the behavior of various chemical impurities in semiconductors will be discussed based on the experimental results on the spectroscopy of donors and acceptors. Effects of external perturbation on the excitation spectra will also be mentioned.

Invited talk at the Annual Meeting of The Physical Society of The Republic of China, February 19, 1984.

MAGNETORESISTANCE OF $(Fe\text{-}M)_{80}B_{14}Si_6$ GLASSES WITH M = Mn, Mo AND V*

Y. D. Yao, B. J. Wen and S. T. Lin+
Institute of Physics
Academia Sinica
Taipei, Taiwan, R.O.C.

ABSTRACT

In recent years there has been an increased interest in the magnetoresistance as well as the ferromagnetic anisotropy of the electrical resistance (FAR) of amorphous ferromagnetic alloys. FAR is an inherent property of ferromagnetic materials and does not depend on the initial domain configuration in the demagnetized state. Previous studies have suggested that $FAR = A\bar{\mu}^n$, where $\bar{\mu}$ is the averaged magnetic saturation moment per iron atom at 0 K, and A and n are constants at room temperature.

In this investigation we report measurements on the magnetoresistance of amorphous $Fe_{30-x}Mn_xB_{14}Si_6$ (x = 0, 2, 4, 6, 10, 12), $Fe_{80-x}Mo_xB_{14}Si_6$ (x = 2, 4, 6, 8) and $Fe_{30-x}V_xB_{14}Si_6$ (x = 2, 4, 6, 8) alloys at both 300 K and 77 K in an applied magnetic fields up to 6 KG.

If FAR(T) is the value of FAR at absolute temperature T and $\bar{\mu}(T)$ is the averaged magnetic saturation moment per iron atom at T K, then our experimental results suggest that:

$FAR(300) = A\bar{\mu}^m(0)$; with $A = 1.1 \times 10^{-5} \pm (0.2 \times 10^{-5})$, $m = 7.9 \pm 0.1$
$FAR(77) = A\bar{\mu}^m(0)$; with $A = 1.2 \times 10^{-4} \pm (0.2 \times 10^{-4})$, $m = 5.3 \pm 0.1$
$FAR(T) = A\bar{\mu}^m(T)$; with $A = 3.8 \times 10^{-4} \pm (0.3 \times 10^{-4})$, $m = 3.7 \pm 0.2$

---

* To be published.

+ Physics Department, Cheng Kung University, Tainan, Taiwan, R.O.C.

ITINERANT FERROMAGNETISM AND VALENCE FLUCTUATION OF $RE_{0.5}Rh_3B_2$ (RE = La, Ce) WITH THE NEW $La_{1-x}Rh_3B_2$-TYPE STRUCTURE*

H. C. Ku, Y. P. You, L. J. Ma and H. Y. Chao
Department of Physics, National Tsing Hua University,
Hsinchu, Taiwan 300, Republic of China

Y. D. Yao
Institute of Physics, Academia Sinica,
Taipei, Taiwan 115,
Republic of China

ABSTRACT

Ternary borides with the new disordered $La_{1-x}Rh_3B_2$-type structure ($0 < x \leq 0.5$) are reported with the general formula $RE_{0.5}Rh_3B_2$ (RE = La, Ce, Pr or Nd). Unit cell volume data indicate that $Ce_{0.5}Rh_3B_2$ exhibits valence fluctuation. High temperature resistivity measurements on itinerant ferromagnetic compound $La_{0.5}Rh_3B_2$ exhibit abrupt drop around 950K, which indicate that these new compounds are high-temperature metastable compounds.

---

* Presented at 4th Int. Conf. Val. Fluc., West Germany, Aug. (1984).

ELECTRICAL RESISTIVITY OF AMORPHOUS AND CRYSTALLIZED $(Fe\text{-}Mn)_{80}B_{14}Si_6$ BETWEEN 300 AND 1200 K†

Y. D. Yao, M. M. Yih** and S. T. Lin****
** Institute of Physics, Academia Sinica, Taipei, Taiwan, R.O.C.*
*** Physics Department, Tamkung University, Taipei, Taiwan, R.O.C.*
**** Physics Department, Chengkung University, Tainan, Taiwan, R.O.C.*

ABSTRACT

Electrical resistivity ρ of amorphous and crystallized $Fe_{80-x}Mn_xB_{14}Si_6$ alloys (x = 0, 2, 4, 6, 10, 12, 14, 16, 20) has been studied as a function of temperature T between 300 and 1200 K. Using heating rates of $\sim$ 2 K/min., the slopes of the ρ vs T curves are positive ofr all the alloys below the crystallization temperature. Near the crystallization temperature the quantity of ρ decreases abruptly for these alloys with the Mn content $<$ 16 at.%, and this decrease decreases with increasing the Mn content. However, for the alloys with x = 16 and 20, the quantity of ρ increases abruptly near the crystallization temperature; and then followed by an abruply decreasing. At high temperatures ($\geqq$ 1100 K), the electrical resistivity of these alloys with the Mn content $\geqq$10 at.% shows an anomalous increase; this is explained by the fast diffusibility of the alloys near the melting point. The electrical resistivity of the alloys with x = 0 and 2 does not show any anomalous increase for temperatures $\sim$ 1250 K. This suggests that the melting point of the alloys is decreased with increasing the Mn content from 2 to 10 at.%. In the crystalline state, our data show that ρ is a monotonically increased function of T between 300 and 1100 K. Each of the ρ vs T curves exhibits a well-defined knee around the Curie temperature T_c. T_c of these alloys is determined by the $d\rho/dT$ vs T analysis. Our Our data shows that the values of T_c are decreased with increasing the Mn content.

---

* Published in Proc. Fifth Int. Conf. Rapidly Quenched Metals, West Germany (1984).

LATTICE DYNAMICS OF SOLID HYDROGEN CHLORIDE

W. S. Tse
Institute of Physics, Academia Sinica
Taipei, Taiwan (115), R.O.C.

ABSTRACT

Lattice dynamics of solid hydrogen cholride is studied, assuming a rigid molecule, in the harmonic and pair potential (Lennard-Jones interaction) approixmation between atoms with the inclusion of electrostatic interactions between point dipoles placed on atomic centres. The potential parameters for each of the different non-bonded atom pairs were obtained by means of an optimization routine to give a least-squares fit to observed zone centre (k = 0) frequencies, equilibrium conditions and lattice energy of the lattice.

To be published in Chemical Physics Letters. (1984).

RAMAN SPECTRA OF CRYSTALLINE SILICON AND TIN TETRACHLORIDES

Wan-Sun Tse
Institute of Physics, Academia Sinica
Taipei, Taiwan (115), R.O.C.

The high resolution Raman spectra of the solid tetrachlorides of tin and silicon at 80K and 18K have been reinvestigated. Previous studies obtained the Raman spectra of polycrystalline $SnCl_4$ and $SiCl_4$ at 80K [1] and that the factor-group splittings of the $\nu_1(A_1)$ fundamental as reported by Shurvell [2] on $SnCl_4$ at 30K were not observed. Besides, the isotopic structure of the $\nu_1(A_1)$ band of $SiCl_4$ did not reflect the relative abundance of the various isotopic species. The present work reported a comprehensive study of the Raman spectra of both samples down to 18K and try to gain further insight into these problems.

Proceedings of the Ninth International Conference on Roman Spectroscopy, Tokyo, Japan (1984).

COMMENT ON "THRESHOLD SWITCHING IN CHALCOGENIDE-GLASS THIN FILMS"*

Chun Chiang
Institute of Physics, Academia Sinica, Nanking,
Taipei, Taiwan, Republic of China

ABSTRACT

D. Adler, M. S. Shur, M. Silver, and S. R. Ovshinsky [J. Appl. Phys. 51, 3289 (1980)] propose that field-induced filling of traps may lead to S-shaped negative differential conductance (SNDC), and use the existence of two solutions of electron concentration for a given applied field as evidence for it. We comment on the conditions for this existence of two solutions and its significance to the SNDC.

* Published in J. Appl. Phys. *56*, 578 (1984).

PHOTO-ILLUMINATION AND CURRENT EXCITATION OF SWITCHING IN AMORPHOUS THIN FILMS*

Chun Chiang
Institute of Physics, Academia Sinica, Nankang,
Taipei, Taiwan 115, Republic of China

ABSTRACT

Smith and Henisch have observed that under illumination, the threshold current for switching in amorphous thin films has changed appreciably, yet the threshold voltage remains approximately the same. Using Chiang's switching theory, this phenomenon may be explained by assuming that not all the free carriers generated by photo-illumination have been used to excite the switching. In fact, we may use this technique to probe the current excitation process of switching in amorphous thin films.

* Published in Phys. Stat. Sol. *(a)84*, K189 (1984).

ATOMIC AND ELECTRONIC PROCESSES OF SWITCHING IN AMORPHOUS THIN FILMS*

Chun Chiang
Institute of Physics, Academia Sinica, Nan kang,
Taipei, Taiwan, Republic of China

ABSTRACT

It is proposed that the conversion of C_3^0 from C_2^0 leads to switching. Since C_3^0 has more connection points, the conductivity of C_3^0 is higher and large current favours the C_3^0 species; thus increasing the current increases the C_3^0 density and less voltage is needed to sustain the same amount of current. This explains the S-shaped negative resistance. The concept is simple and the mathematics for for quantitative calculation is manageable.

*Published in Physics Letters *101A*, 106 (1984).

河口及港灣流場傳輸及擴散之數值模擬

黃 榮 鑑*
中央研究院物理研究所
梁 興 杰**
中央研究院物理研究所

摘 要

風力與潮汐在河口及港灣引生之流場傳輸運動及擴散研究最初僅由水工模型試驗方法以觀測瞭解其現象，近年由於電子計算機之快速發展，純理論之偏微分聯立方程式，即連續方程式（continuity equation）、運動方程式（equation of motion）及擴散方程式（diffusion equation），可藉電子計算機進行數值計算；本文即以有限元素法進行二維度流體動力模式及擴散模式之研究，利用葛拉金近似將垂直積分後之控制方程式轉換爲有限元素方程式，再對時間積分求解時變微分代數式，以探討流場之傳輸、水位、流速之變化及污染質之擴散。

ABSTRACT

The flows in the estuary and coastal sea are governed by the shape of the estuary and its boundaries at sea and the inland ends, as well as by the tides, wind blowings and the river discharges. In this study, hydrodynamics circulation and pollutant dispersion in the estuary are formulated in terms of mathematical models. The relevant equations of continuity, momentum and pollutant diffusion are combined to set up a numerical model of the physical flow for a particular domain of known geometry. The solution of the formulated problem is achieved by using numerical techniques of the Galerkin finite-element method.

In the model, velocities and concentration of the water in the region are computed together with the water levels. In order to verify the validity of the model, this study has been applied to study the motion of standing waves in a semi-finiti channel in which the analytical solution could be obtained theoretically. Results show that the comparison between the numerical calculations and the theoretical solutions are favorable.

本文發表於土木水利，第十一卷，第二期，民國七十三年八月，第3～16頁。
(J. of Civil and Hydraulic Engineering, Vol. 11, No. 2, August 1984, pp. 3-16).

AUTHOR INDEX

本集刊每年出版一次

非 賣 品

中 央 研 究 院

物 理 研 究 所 集 刊

第 十 四 卷

發行人：林 爾 康

編輯者：中央研究院物理研究所集刊編輯委員會

出版者：中央研究院物理研究所 臺北市南港區

印刷者：萬 達 打 字 印 刷 有 限 公 司

電 話：三 九 四 〇 七 一 八

中華民國七十三年十二月出版